

Universidade de São Paulo
Instituto de Astronomia, Geofísica e Ciências Atmosféricas
Departamento de Geofísica

Irfan Ullah

Near-surface characterization from the H/V spectral curves along with the joint inversion of the ellipticity and dispersion curves.

SÃO PAULO
2017

Irfan Ullah

Near-surface characterization from the H/V spectral curves along with the joint inversion of the ellipticity and dispersion curves.

Tese apresentada ao Departamento de Geofísica do Instituto de Astronomia, Geofísica e Ciências Atmosféricas da Universidade de São Paulo como requisito parcial para obtenção do título de Doutor em Ciências

Área de Concentração: Geofísica Aplicada

Orientador: Prof. Dr. Renato Luiz Prado

Versao corrigida. O original encontra-se disponivel na unidadae.

SÃO PAULO
2017

Acknowledgement

Firstly, I would like to express my sincere gratitude to my advisor Prof. Renato Luiz Prado for the continuous support of my Ph.D. study and related research, for his patience, motivation, and immense knowledge. His guidance helped me in all the time of researching and writing of this thesis. I am really indebted to his kindness.

Besides my advisor, I would like to thank my co-advisor and progress report evaluator Prof. Marcello Assumpção for his insightful comments and encouragement and also for the hard question which incited me to widen my research from various perspectives. He also provided me the seismometers for the seismic noise data recording. I am also thankful to Marcello Bianchi for his help in computational aspects.

My sincere thanks to the development team and the contributors of the free tool package Geopsy. I would also like to thank, Dr. Manuel Hobiger and Prof. Francisco J. Sánchez-Sesma for his code sharing and explanation about various aspects via emails. I am also indebted to Luis Galhardo and Felipe Neves for preparing and checking the seismometers prior to the field and their help in the noise recording. I want to thank to my friends and colleagues Dr. Asif Iqbal, Dr. Taj Ali Khan, Dr. Abdu Raheem, Dr. Hanif Ur Rehman, Aamir Rana, Usama Bilal and Saqib for their moral support.

I wish to thank TWAS-CNPq for the fellowship grant number 190038/2012-8 (CNPq/TWAS - Full-Time Ph.D. Fellowship - GD 2012) and the financial support.

The last but not the least, I would like to thank my wife and family who constantly encouraged me to complete the tasks. I will never forget and will always feel my inability for not going to welcome my son (Muhammad Arish Khan) when he was born.

Abstract

The destruction caused by an earthquake at a site depends on many factors like source characteristics such as magnitude, epicentral distance from the site, depth of the source, and on the geological setting of the area. The destruction caused due to the geological setting of an area is termed as site effect. To model the site effect of an area is to determine the shaking level longevity and its displacement amplification. The elastic properties (shear and compressional wave velocities, density, thickness of soil layer, etc.) of the site are required to find out by employing various geophysical procedures. The knowledge of these elastic properties help in better designing the infrastructure, which reduces the chances of destruction caused by a local geological setting due to an earthquake occurrence. This procedure is widely termed as microzonation. The most important parameters for the microzonation are the thickness of soft sediments over the seismic bedrock and its shear wave velocity profile. These two parameters are properly characterized by employing various geophysical techniques like borehole measurement, seismic reflection and seismic refraction. The conventional geophysical methods bring some hindrance to the picture such as, the drilling of a borehole and artificial seismic sources deployment for the reflection and refraction survey, which are both expensive and time consuming, difficult or even in some case impossible to implement in urbanized environment, the investigation is depth limited to few tens of meter. The methods which replaced this conventional geophysical method from the last decades or so is the analysis of Earth vibration caused by the seismic noise which is produced by both natural and cultural sources. This ambient seismic noise can be recorded with less cost and effort with good lateral coverage. Various seismic noise techniques are employed for this job; however, the one which got the most attention in recent years is the horizontal over vertical spectral ratio (H/V) technique. The H/V spectral ratio curve is a fast easy and cheap tool for the near-subsurface characterization. There are various study performed on the topic which has tried to cover almost all the aspects and problems associated with the method. Here in this study, we try to detail the aspects of this technique, which are not been evaluated fully. The different modelling procedures presented to model and physically link the H/V curve with some physical phenomenon will be discussed and its numerical result with the experimental H/V curve will be compared for a borehole test site. The peak and the shape of the H/V curve will be modelled to find its peak frequency deviation from the shear wave resonance frequency by considering different wave-field around the peak. Similarly, the shape dominance of the H/V curve linkage will be find out. The peak frequency of the H/V curve is used to estimate the thickness-frequency relation by regression analysis. Here we will show that the dispersion curve obtained from multi-channel analysis of surface waves (MASW) can be used to estimate the velocity at one meter and the shear wave velocity increase trend with depth. These values can be used to estimate the thickness frequency relation for an area and its result will be compared with the experimentally derived thickness-frequency relationship for the same area. The sensitivity of the H/V curve shape to the subsurface velocity structure will find out for two main modelling techniques (Rayleigh wave ellipticity and diffused field based H/V curve). The different parts of the H/V curve are inverted (back modelled) to find

out the part of H/V curve which is carrying the most important information about the subsurface structure. The lesson learned from all this analysis will be applied to experimental data of three different sites. The Love waves might contaminate the result of the H/V curve. Two different techniques to remove their effects will be discussed. Then, the joint inversion result of the dispersion and this Love effect removed H/V for more precisely ellipticity curve is discussed. Some new aspects of the H/V curve technique are also discussed at the end.

Key Words. (Microzonation, Earthquake mitigation, Seismic noise, Horizontal-over-Vertical spectral ratio, Modeling of H/V curve, Ellipticity curve, Dispersion curve, Joint inversion of ellipticity and dispersion curve).

Caracterização da subsuperfície rasa através da curva da razão espectral H/V e da inversão conjunta das curvas de dispersão e de elipticidade

Resumo

A destruição causada por um terremoto depende de muitos fatores, como características e profundidade da fonte, magnitude, distância epicentral e da configuração geológica da área. A destruição causada devido à configuração geológica da área é denominada como efeito local. A modelagem do efeito local implica na determinação do tempo e nível de vibração e do efeito de amplificação do deslocamento. As propriedades elásticas dos materiais geológicos (velocidade das ondas de compressão e de cisalhamento, densidade, espessura da camada de solo, etc.) podem ser obtidas por diversos métodos geofísicos. O conhecimento dessas propriedades elásticas ajuda a melhor projetar as infraestruturas e reduzir as chances de danos. Este procedimento é denominado de microzoneamento. Os parâmetros mais importantes para realizar o microzoneamento são as espessuras dos sedimentos que recobrem o embasamento e o perfil das velocidades das ondas S (cisalhamento). Esses dois parâmetros são adequadamente caracterizados pelo uso de várias técnicas geofísicas como perfilagens em furos de sondagem, reflexão e refração sísmica. Esses métodos geofísicos trazem algumas restrições como a necessidade da execução de um furo, emprego de fontes sísmicas artificiais que muitas vezes são dispendiosas e por vezes de uso restrito em áreas urbanas, além de muitas vezes estarem limitadas a investigações de apenas algumas dezenas de metros. Os métodos que substituíram esses métodos geofísicos convencionais nas últimas décadas são a análise do ruído sísmico produzido por fontes naturais e culturais. Este ruído sísmico ambiental pode ser registrado com menor custo e esforço e com boa cobertura lateral. Várias técnicas que se utilizam do ruído sísmico podem ser empregadas, no entanto, aquela que obteve maior atenção nos últimos anos é a técnica da razão do espectro horizontal sobre o espectro vertical da onda de superfície (H/V). A curva da razão espectral H/V é uma ferramenta rápida, fácil e de baixo custo para a caracterização da subsuperfície rasa. Existem vários estudos realizados sobre o tema que tentaram cobrir todos os aspectos e problemas associados ao método. Aqui neste estudo são aprofundados alguns aspectos ainda não avaliados em detalhe. Diferentes procedimentos para a modelagem e as associações entre os fenômenos físicos envolvidos e as características da curva H/V são discutidos e os resultados numéricos desses estudos são comparados com informações extraídas de perfis de sondagens de um dos locais estudados. O pico e a forma da curva H / V são modelados para encontrar o desvio na frequência de pico a partir da frequência de ressonância da onda de cisalhamento considerando diferentes campos de onda em torno do pico, assim como sua relação com a forma dominante da curva. A frequência de pico das curvas H/V é utilizada para estimar a relação entre a frequência a espessura através de análise de regressão. O estudo mostra que a curva de dispersão obtida a partir de um ensaio MASW pode ser usada para estimar a velocidade da onda S a um metro de profundidade e sua tendência de aumento com a profundidade. Esses valores podem ser usados para estimar a relação frequência-espessura para uma área. Esses resultados são comparados com a relação frequência-espessura derivada experimentalmente para a mesma área. A sensibilidade da forma da curva H/V à estrutura de velocidade do meio é analisada através de duas técnicas de modelagem (elipticidade da onda Rayleigh e campo difuso baseado na curva H/V). Diferentes partes da curva H/V são invertidas visando avaliar qual a parte da curva H/V contém as informações mais importantes sobre a estrutura subterrânea. As lições aprendidas dessas análises são aplicadas a três dados

experimentais de locais distintos. As ondas Love podem contaminar o resultado da curva H/V. Duas técnicas diferentes para remover o efeito das ondas amorosas são discutidas. Em seguida, são discutidos os resultados da inversão conjunta das curvas de dispersão e da curva H/V após remoção do efeito da onda Love, ou seja, a curva de elipticidade. Alguns aspectos novos da técnica H/V são discutidos no final.

Palavras-chave: microzoneamento, ruído sísmico, razão espectral das componentes horizontais e vertical, curva H/V, curva de elipticidade, curva de dispersão, inversão conjunta das curvas de elipticidade e dispersão

Contents

Chapter 1: Introduction to the study	1
1. Introduction	1
1.1 The objective of the study	1
1.2 Organization of the thesis	3
2. Introduction.....	4
2.1 Seismic noise	4
2.2. Seismic sources of noise	5
2.3 The composition of noise wavefield	6
2.4 Techniques used for seismic noise.....	11
2.4.1 Spatial autocorrelation (SPAC) method.....	11
2.4.2 Frequency-wavenumber analysis	14
Chapter 3: Review of the H/V spectral curve method	18
3.1 Historical overview of the H/V curve	18
3.2 Formula of the H/V curve	19
3.3 The experimental procedure for the H/V measurement.....	25
Chapter 4: Array technique of active source.....	32
4.1 Introduction.....	32
4.2 SASW (Spectral Analysis of Surface Waves)	33
4.3 MASW (Multichannel Analysis of Surface Waves).....	35
4.3.1 MASW data acquisition procedure	35
4.3.2 Length of the geophones spread.....	36
4.3.4 The effect of topography on MASW acquisition.....	38
4.4 Dispersion analysis of the acquired data.....	38
4.4.1 Swept-frequency technique.....	39
4.4.2 Phase-shift method.....	42
4.6 Advantage of MASW method.....	44
4.7 Inversion of dispersion curve.....	45
5.1 The forward and inversion problem.....	48
5.2. Surface wave curves inversion strategies.....	51
5.2.1 Iterative method (Linearized inversion).....	52
5.2.2 Monte Carlo inversion strategies	53

5.2.2.1 Simulated Annealing	53
5.2.2.2 Genetic Algorithm.....	54
5.2.2.3 Neighborhood algorithm	54
5.3 Brief inversion procedure of neighbourhood algorithm.....	56
5.4. The parameter setting for the inversion	58
Chapter 6: Modelling of the H/V curve	60
6. Introduction.....	60
6.1 Nakamura explanation of the H/V curve	60
6.2 Rayleigh wave ellipticity modelling of H/V curve	64
6.3 H/V modelling on the basis of surface wave	69
6.4 Diffuse field assumption technique.....	73
Chapter7: The peak frequency (f₀) and shape of the H/V curve	78
7. Introduction.....	78
7.2 Peak frequency (f₀) of the H/V curve.....	79
7.3 Sensitivity analysis of the peak frequency f₀ for ellipticity and DFA H/V curves.....	83
7.3.1 Thickness (h), density, P-wave and S-wave velocities effects on the peak frequency	86
7.4 The shape of the H/V curve	92
7.5 The numbers of layers and effect on the shape of H/V curve	94
Chapter 8: The use of peak frequency of the H/V curve.....	97
8. Thickness frequency relation	97
8.1 How to estimate the value of V₀, x	100
8.2 Thickness frequency relation for the Bebedouro area.....	103
8.3 V₀, x values estimation for the Bebedouro area from MASW dispersion curve	104
8.4 Deviations in thickness estimates among the three equations	111
Chapter 9: Part of ellipticity and misfit function	112
9.1 Which part of ellipticity curve should be used for inversion?	112
9.2 Inversion of the ellipticity curve with velocity trend and thickness information.....	116
9.6 Misfit function for the joint inversion.....	123
Chapter 10: The inversion of ellipticity and dispersion curves.....	129
10.1 Inversion of the experimental data.....	129
10.2 Data acquisition parameters	132
10.3 The retrieval of ellipticity from single 3c-station recording	136

10.3.1 Time-frequency analysis	139
10.3.2 Random decrement technique (RayDec)	142
10.5 The application of H/V curve for some new aspects	150
Chapter 11: Conclusions	156
Articles	160
References	161
Index A : The forward computation procedure of the ellipticity curve (courtesy to Piccozi, 2005)	173

List of figures

Fig.2. 1 Deep-to-surface noise Fourier spectra amplitude ratio (vertical component) as a function of period (taken from Douze, 1964).7

Fig.2. 2 Recording of seismic noise (left) and earthquake signals (right) at the surface and at different depth levels of a borehole (from Bormann 2012).7

Fig.2. 3 Velocity power density spectra as obtained for noise records at the surface (top) and at 300 m depth in a borehole (below) near Gorleben, Germany (taken from Bormann, 2012).....8

Fig.2. 4 Velocity power density spectra as obtained for noise records at the surface (top) and at 300 m depth in a borehole (below) near Gorleben, Germany (taken from Bormann, 2012).....9

Fig.2. 5(a) Velocity profiles used by Tokimatsu (1997) to compute Rayleigh waves dispersion curves numerically. The corresponding dispersion curves (dots) computed from noise synthetics in case 1 (b), case 2 (c) and case 3 (d) are compared with theoretical dispersion curves of higher mode Rayleigh waves (after Tokimatsu 1997).10

Fig.2. 6 The shape of the spatial correlation function. The function shows a constant value and abruptly decreases with increase in frequency in the propagation direction (from Okada 2003).13

Fig.2. 7 Diagram of a circular array with an incident plane wave arriving under an azimuth angle (from Hobiger 2011).....13

Fig.3. 1 H/V-ratio of Rayleigh waves as a function of Poisson’s ratio (modified from Malischewsky et al., 2004)..22

Fig.3. 2 Shows the shape of H/V (Eq.2.20) for a layer over the half-space (with vs contrast 6) for a model taken from Malischewsky et al. (2004) shown in Fig 3.3.24

Fig.3. 3 Shows the Vs and Vp profiles of the model used to produced Fig.3.2 from Eq.3.20. (taken from Malischewsky et al., 2004).24

Fig.3. 4 Shows one-hour seismic ambient noise record at IAG site: (a) shows the windows (each of 50 sec) selected for the H/V analysis; (b) shows the smoothed spectral amplitude of all the three components; (c) the average H/V curves of all the 64 windows (upper lower limit indicates the 95% confidence interval around mean H/V curve values); (d) show the criteria of reliable H/V curve SESAME 2004, reliability of clear peak, SESAME 2004.27

Fig.3. 5 Shows the spectrogram of the three component, both the horizontal components show stationarity at 2 Hz for all the seismic noise record.29

Fig.3. 6 Shows the spectrogram of the three component, both the horizontal components show stationarity at 2 Hz for all the seismic noise record.30

Fig.3. 7 Shows the arrangement of urbanization around the recording (taken from Google earth. Imagery date April 2015. Access at March 2017)30

Fig.3. 8 Show the directional H/V with azimuth for IAG site for 19 hours of seismic noise record.31

Fig.3. 9 Show the directional H/V with azimuth for IGC site, for 23 hours of seismic noise recording.31

Fig.4. 1 The schematic describing the overall procedure of the SASW method.34

Fig.4. 2 A overview of the MASW method: (a) Geophones are lined up on the surface of the test site. A wave is generated and the wave propagation is recorded; (b) A dispersion image (c) is obtained from the recorded surface wave data. The high amplitude bands display the dispersion characteristics and is used to construct the fundamental mode dispersion curve (d). A theoretical dispersion curve is obtained based on assumed layer thicknesses and material parameters for each layer and compared to the experimental dispersion curve (e). The shear wave velocity profile and the layer structure that result in the best fit are taken as the result of the survey (f) (taken from Ólafsdóttir, 2016).....35

Fig.4. 3 Shows a sketch of receiver profile for acquisition (taken from www.masw.com)38

Fig.4. 4 Show the sketch of swept frequency procedure (modified from Ólafsdóttir ,2016).39

Fig.4. 5 Shows the swept frequency record for a trace of impulsive source (from a short gather) by convolution with stretch function $s(t)$ of changing frequency ($f_1=5$ Hz $[f]$ $f_2=30$ Hz) (Ólafsdóttir ,2016).....40

Fig.4. 6 Swept-frequency record obtained from an impulsive shot gather. Red markers identify the local maxima of each trace that are parts of linear events that are considered reliable for further analysis. Local maxima that are not used for analysis are shown with blue markers (taken from Ólafsdóttir, 2016).	41
Fig.4. 7 Linear events extracted from a swept-frequency record. Red markers identify the local maxima of each trace that are used for identification of linear events. Two linear events corresponding to frequencies (f) of 11.3 Hz and 18.8 Hz are indicated by black Lines (Ólafsdóttir, 2016).	41
Fig.4. 8 A sketch of phase-shift (Ólafsdóttir, 2016)	42
Fig.4. 9 Shows the basic principle behind the phase-shift method: (a) Normalized sinusoid curves with the frequency of 20 Hz and phase velocity of 140 m/s; (b) Normalized summed amplitude as a function of frequency for a different number of traces (www.masw.com)	44
Fig.4. 10 Show the frequency-phase velocity plot as function summed amplitude (dispersion image for BEB4a, Bebedouro area).....	44
Fig.5.1 Shows the illustration of inversion and forward problems (from Scales & Snieder, 2000).	48
Fig.5.2 Shows the least-squares misfit function for a linear problem. (b) The conventional view of the misfit function for a nonlinear inverse problem (Menke, 2012).	50
Fig.5.3 A schematic representation of various search/optimization algorithms in terms of exploration and exploitation of the information. Shaded borders indicate a deterministic (not–Monte Carlo) method (Sambridge and Mosegaard, 2002).	51
Fig.5.4 Shows the example of Voronoi cells drawn around the points (model) of parameter space for a simple 2-D problem.....	55
Fig.5.5 Shows Voronoi cells for a two-dimensional parameter space (from Sambridge, 1999a). (a) is an example of a two-dimensional parameter showing the models (black dots) and the limits of the Voronoi cells. (b) depicts the Voronoi geometry after the first iteration (from Wathelet, 2005)	57
Fig.6. 1 Horizontal and vertical transfer functions for horizontal and vertical motion of IAG borehole model. The vertical line shows the fundamental frequency where the maximum application of bedrock motion occurs.	62
Fig.6. 2 Show the comparison of experimental H/V theoretical ellipticity curve of Rayleigh wave and QTS of Eq6.9.	63
Fig.6. 3 Shows the schematic one-dimensional model defined by a stack of (n+1) layers. z_i are the depths of the top of each layer (modified from Aki and Richard, 2002).	66
Fig.6. 4 Show the ellipticity curve for the first four mode of IAG bore model, yellow line show the experimental H/V recorded at site.	68
Fig.6. 5 Shows the geometry of (a) soil layer and (b) microtremor source models to formulate the theoretical H/V spectrum of surface waves considering the effects of fundamental and higher modes (from Arai and Tokimatsu, 2004).	69
Fig.6. 6 Top panel show S-wave velocity profiles based on the results of PS logs at two sites A and B in Tokyo. Comparison of the H/V spectra of microtremors ($(H/V)_m$) (open circles) with those of fundamental-mode Rayleigh wave and surface waves, $(H/V)_R$ and $(H/V)_S$ (broken and solid lines), respectively, computed for the soil profiles at sites A and B (Arai & Tokimatsu, 2004).	72
Fig.6. 7 Shows the IAG model curve by considering the contribution of surface waves (Rayleigh and Love waves) using Arai & Tokimatsu (2004) procedure, red line show the experimental H/V recorded at the borehole site (IAG).	73
Fig.6. 8 Shows the H/V curve for the IAG borehole model by using full wavefield under diffused field assumption.	75
Fig.6. 9 Shows the imaginary part of Green function for both horizontal component <i>ImG11</i> , <i>ImG22</i> in blue, and imaginary part of Green function for vertical component for <i>ImG33</i>	76
Fig.6. 10 Show different curve comparison with that of H/V obtained from the noise data recorded at IAG borehole site.	76

Fig.7. 1 Shows the comparison of H/V curve and the theoretical borehole ellipticity curve for the IAG site; the blue shows the experimental H/V curve, while black line shows the borehole ellipticity curve.	79
Fig.7. 2 Shows the (a) V_p and (b) V_s profiles for six different models. The corresponding dispersion curves are also given for the six models (c).	80
Fig.7. 3 Shows the H/V curve obtained via ellipticity (a) and DFA approach (b) for six different models shown in Fig.7.2.....	80
Fig.7. 4 Shows (a) the change in Poisson values by changing V_{s0} value of soil layer by considering Rayleigh waves (a) ; (b) Surface wave contribution only ; (b) shows the peak frequency of all wave.	82
Fig.7. 5 Shows the (a) the peak frequencies deviation from S-wave resonance; (b) the relative error between different wave contributed H/V curve and S-wave resonance.....	82
Fig.7. 6 Shows the (a) V_p and V_{s0} of the soil layer changing which corresponded to Poisson ratio variation (b) the peak frequencies as a function of Poisson ratio (c) the relative error between different wave contributed H/V curve and S-wave resonance.	83
Fig.7. 7 Model used by Xia (1999) for finding out the sensitivity of Rayleigh wave dispersion curve for different parameters (solid line shows the profile of V_s , while dotted line the V_p profile).	84
Fig.7. 8 Shows the contributions to Rayleigh-wave phase velocity by 25% changes in each model parameter (V_s , V_p , ρ and h). The solid black line (not visible clearly due to overlapping of density and P-wave change based dispersion curve) is Rayleigh-wave phase slowness attributed to the Earth model. The dispersion of each parameter change is shown in with different colours (modified from Xia 1999).	85
Fig.7. 9 Shows IAG-and Hobiger models, (a) and (c); solid line shows V_s profiles, while dashed lines show V_p profiles. (b) and (d) are the IAG and Hobiger models reduced to one layer above the bedrock (V_s profiles only). ...	86
Fig.7. 10 Shows the thickness variation for IAG and Hobiger models.....	87
Fig.7. 11 Shows changes in thickness vs change in frequency peak of ellipticity curve; the peak shifted toward the lower and high frequencies with increase and decrease of thickness, respectively, for both ellipticity DFA approaches. Colours are assigned to each increase and decrease along with V_s profile.	87
Fig.7. 12 Shows the deviation from fundamental frequencies of S-wave with that of ellipticity curve and DFA based H/V curve. (a) IAG model, (b) Hobiger model and (c) IAG with high V_s -contrast 3.6.	88
Fig.7. 13 Shows the V_p , V_s and density profiles of IAG-borehole.	88
Fig.7. 14 Shows H/V curve obtained via Rayleigh wave ellipticity (a) and DFA approaches (b) against density changes between soil and rock interface.....	89
Fig.7. 15 Shows the V_p velocity contrast profile of IAG-borehole.	89
Fig.7. 16 H/V curve obtained via Rayleigh wave ellipticity (a) and DFA approaches (b) against P-wave velocity contrast changes between soil and rock interface.	89
Fig.7. 17 Shows the V_s profile along with V_s velocity contrast profile with V_s contrast among soil and bedrock: (a) IAG-model; (b) Hobiger model.	90
Fig.7. 18 Shows the shape of the H/V curve obtained via Rayleigh wave ellipticity for IAG model (a), for Hobiger model (c), and DFA approach for IAG (b) and for the Hobiger model (d), against S-wave velocity contrast changes between soil and rock interface.	91
Fig.7. 19 (a) shows the plot of ellipticity peak frequency shift with V_s contrast increase; (b) shows the ratio of trough frequency to that of peak frequency of ellipticity; (c) shows the combined plot; the vertical black line shows the V_s ratio 2.6 from where the effect V_s contribute smoothly.	91
Fig.7. 20 Shows the combined plot of ellipticity peak frequency shift with V_s contrast increase (green) and the ratio of peak to trough frequency (red). The vertical bar indicates the V_s contrast 2.61 from where both curve stabilize. ...	92
Fig.7. 21 Shows the V_s profiles of the models used for the comparison of H/V curve for Rayleigh wave ellipticity modeling and Diffuse field assumptions modeling for Green function. (a) Model Jose Pina-Flores (2016); (b) IAG borehole generic model; (c) Greece model (Lontsi, 2015); (d) Piccozi (2005) model; (e) Hobiger model (2013). ...	93

Fig.7. 22 Shows the H/V curve obtained for different models through the ellipticity of Rayleigh wave (blue line), Diffuse field assumption (red line) .The vertical lines indicate the peak and trough of the curve as indicated by the ellipticity.....	93
Fig.7. 23 Shows the IAG and Greece models with a different number of layers.....	95
Fig.7. 24 Shows IAG model with a different number of layers for both ellipticity (a) DFA H/V modelling approaches (b) with corresponding shape deviation from one layer model in (c) and (d).....	95
Fig.7. 25 Shows Greece model with a different number of layers for both ellipticity and DFA H/V modelling approaches (b) with corresponding shape deviation from one layer model in (c) and (d).....	96
Fig.8.1 Model A and B. (a) and (b) show V_s profiles (solid lines) while dash line show average S-velocity trend obtained from best-fitting; (c) shows fundamental mode dispersion curve for models A and B; (d) shows the fundamental mode ellipticity curve for both models.	101
Fig.8.2 The best-fit line through V_s -depth plot for model A (top) and (B) bottom; the rate of increase of average shear wave velocity obtained is $b=0.35$ for A (top); the same procedure is done for model B which result in $b =0.40$ (bottom).	102
Fig.8.3 Shows the H/V curves measured at borehole sites given in Table 8.1.	103
Fig.8.4 Shows the regression plot for H/V curve peaks and depth to bedrock (sandstone) in Bebedouro area (x is resonance frequency, R-Square is the coefficient of determination, $f(x)$ thickness to soil deposit.....	104
Fig.8.5 (a) The location of the seismic stations in Bebedouro area. The triangles show the location of seismic sensors where the noise measurement are made for the H/V analysis, black lines show the MASW profiles. (b) The stars show the location of water wells; the wells used for a thickness frequency relationship are shown in Table 8.1s.	105
Fig.8.6 Shows the dispersion images of all the MASW profiles (Fig.8. 5) black lines.	105
Fig.8.7 Shows V_s -depth data fit for the three curves (a) active 30 meter forward (b) 15 m reverse, and (c) passive source curve; on the lower right statistical robustness and values of data fit are given. The values of (V_0) and x are same as all these curves are taken from same site MASW.	106
Fig.8.8 Shows the effect of Poisson ratio changes on velocity increase trend with depth for different Poisson ratios. The black dots shows the V_s -depth data while the blue line shows the best fit to the data. The value of x remains constant at 0.3369.	106
Fig.8.9 Shows the IAG model and the corresponding velocity increase trend ($x= 0.42$) for different Poison ratio (ν) of the soil layer. The V_0 values as a function of Poison ratio are given in (b).	107
Fig.8.10 Shows the velocity-depth increase trend for different source intervals a) 30 meter forward, (b) 30-meter reverse, (c) 10 meter forward and (d) 10-meter reverse. The value of in power law relationship obtained from Fig. 8.7 is kept constant at $a=137$	108
Fig.8.11 Shows the velocity-depth increase trend for BEB 1, BEB 4a, BEB 7 and BEB 11; shear wave velocity increase trend with depth are kept constant at $x=0.3369$; the value of a are shown in each case.	108
Fig.8.12 Shows the plot of all the three thickness-frequency relationships obtained for the Bebedouro area.....	109
Fig.8.13 Shows the plot of thickness estimate vs. frequency with an error bar of \pm one standard deviation. The plot is reproduced for various frequency ranges to clearly view the deviation in thickness estimate.	110
Fig.8.14 Shows the relative error plot of thickness relationship of travel time based (dashed line) and Tuan relation based (solid line).....	110
Fig.9.1 Shows the distribution of the misfits as a function of the surface velocity (v_0) and layer thickness (d). The upper panel corresponds to the dispersion curve misfits while the lower panel corresponds to the ellipticity misfits (Scherbaum, 2003).....	113
Fig.9.2 Shows the four models and their corresponding ellipticity curves. The same model of the IAG borehole by considering one, two, three and four layers above the bedrock.	114

Fig.9.3 Showing joint inversion of ellipticity and dispersion curves. The black dotted line shows the IAG borehole data ellipticity and dispersion curve. On the right, the result of inversion is shown; the black line shows the true model.	115
Fig.9.4 Shows the shear wave velocity vs. depth trend for the theoretical model dispersion curve of IAG borehole curve.	116
Fig.9.5 Shows the inversion of ellipticity curve along with S-velocity increase trend and thickness information....	118
Fig.9.6 Shows the inversion of a left limb of ellipticity curve along with S-velocity increase trend and thickness information.	120
Fig.9.7 Shows the inversion of a left-peak-right limb of ellipticity curve along with S-velocity increase trend and thickness information.	120
Fig.9.8 Shows the inversion of right limb of ellipticity curve along with S-velocity increase trend and thickness information.	121
Fig.9.9 Shows the inversion of beyond the trough of ellipticity curve along with S-velocity increase trend and thickness information.	121
Fig.9.10 Shows the inversion result of Picozzi model: (a) ellipticity curve along (b) shows the proximity value is given with narrow black line the dispersion curve of the original model; (c) shows the inversion results; the dotted line shows the velocity increase trend obtained from dispersion curve, dashed line shows Parolai (2002) velocity trend for the area, and the narrow black line shows the original model.	122
Fig.9.11 Shows the inversion result of Greece model (Lontsi, 2015) from full ellipticity curve along with S-velocity increase trend; dash line show the velocity increase trend for the model, at the center the proximity value is given with narrow black line.	122
Fig.9.12 Shows the inversion results for misfit function defined in Eq.9.9 for a different number of data points for ellipticity and dispersion curves. Shear wave velocity profiles of all the generated models are shown; the original model has included (black line).	127
Fig.9.13 Shows the inversion results for misfit function defined in Eq 9.9 for a different number of data points for ellipticity and dispersion curves. Shear wave velocity profiles of all the generated models are shown; the original model has included (black line).	127
Fig.10.1 Shows the boundary (in red) of Sao Paulo state. Locations where the MASW and H/V analysis were made are shown in the red circles ((taken from Google earth. Imagery date April 2015. Access at March 2017).	130
Fig.10.2 Location (left) and geological map of the Colonia structure. The black thick lines indicate the locations of MASW tests, while thin line indicates reflection line (modified from Riccomini et al., 2011).....	131
Fig.10.3 Shows the geological map of the NE region of São Paulo State. The area is dominated geologically by the sedimentary rocks of the Bauru Group and basalts.....	132
Fig.10.4 Shows the locations of IAG-IGC-USP site where the MASW (in red) and H/V analysis were made (triangle) (taken from Google earth. Imagery date April 2015. Access at March 2017).....	133
Fig.10.5 Shows the detailed location map of IAG site; legends explain the different symbols (modified from Porsani 2004).....	133
Fig.10.6 Shows the H/V curve of IAG and IGC sites.	134
Fig.10.7 Shows the elevation contour map of the Colonia area; the red triangle shows the location of seismic noise recordings.	135
Fig.10.8 Shows the H/V curves obtained for the Colonia site (Fig 10.7).	135
Fig.10. 9 Shows the H/V curves of Bebedouro area next to each MASW profile.....	136
Fig.10.10 The comparison between H/V curve and the theoretical borehole ellipticity curve for the same site. The H/V curve in case of equal contribution of Rayleigh and Love waves as $(H/V)/2$	138
Fig 10.11 A graphic outline of the time-frequency method showing the CWT results of the vertical (top) and combined horizontal (bottom) signals from noise record. The plus sign is taken as an example of maxima on the vertical component for Rayleigh wave detections. The ellipticity of these detected Rayleigh waves is estimated using the ratio between the horizontal and vertical maxima at this time and frequency, \pm shifting the horizontal component by a quarter period at each analyzed frequency f.	140

Fig.10.12 Shows the ellipticity (H/V) obtained from continuous wavelet transformation CWT for different duration of the signal with value of $m=2$; a histogram is drawn for each frequency; the colour within the histogram indicates the energy level; curly line shows the ellipticity obtained from CWT while solid smooth line shows the ellipticity curve obtained from the borehole data at the same location (IAG site).....	141
Fig.10.13 Shows the ellipticity (H/V) obtained from the continuous wavelet transformation (CWT) for different values of m for one hour signal. The curly line shows ellipticity obtained from CWT while solid smooth line shows the ellipticity curve obtained from the borehole data at the same location (IAG site).....	141
Fig.10.14 Shows the ellipticity obtained via RayDec technique; (a) shows the effect of recorded signal duration on ellipticity retrieval $df=0.2$ and $\delta=20/f$; (b) shows the effect of δ on ellipticity retrieval for $T=1$ hour and for $df=0.2$; (c) shows the effect of filtering for different df values with $T=1$ hour and $\delta=20/f$; (d) shows the ellipticity for six 10 minutes windows, the result is averaged out and compared with the borehole ellipticity.....	143
Fig.10.15 Shows the dispersion image of MASW recording line (Fig10.5). The dotted line shows the dispersion curve obtained from dispersion image while the dashed line shows the borehole's model dispersion curve.	144
Fig.10.16 The inversion result of ellipticity and dispersion curves at IAG site; (a) shows the fitting ellipticity curve of IAG site with the dotted line while the black line shows the lower misfit ellipticity curve model; (b) shows the fitting to the experimental curve with the dotted line and lower misfit model dispersion curve with the black line; (c) shows all the generated models, the black line shows the lower misfit model.	145
Fig.10.17 Shows the lower misfit Vs model (solid line) of the joint inversion (Fig.10.16) and borehole Vs model (dashed line).	145
Fig.10.18 Shows the inversion result of the ellipticity and dispersion curves at IGC site; (a) shows the fitting ellipticity curve of IGC.....	146
Fig.10.19 Shows the velocity increase trend via best-fit through shear wave velocity and depth which give value of $V_0 = 50 \text{ m/s}$ and $x=0.45$ (b here is x in other relation of chapter 7).	147
Fig.10.20 Shows the inversion of ellipticity curve supplemented by the sediment thickness and velocity increase trend shown in dashed line.	148
Fig.10.21 Shows the inversion results of the dispersion and ellipticity curves for Bebedouro site, areas Beb1 and Beb 4a.	149
Fig.10.22 Shows the inversion results of the dispersion and ellipticity curves for Bebedouro site, areas Beb7 and Beb 11.	149
Fig.10.23 Shows the inversion results of the dispersion and ellipticity curves for Bebedouro site, areas Beb 4b and Beb 16.....	150
Fig.10.24 Shows the inversion results of ellipticity curves supplemented with velocity trend (shown in dashed line of all models) for Bebedouro site, areas Beb 13, Beb 17, Beb 17 and Beb 19.	150
Fig.10.25. Shows the shift of the peak frequency of H/V curves for rotating horizontal components for IAG site. .	151
Fig.10.26 Shows the shift of peak frequency with the azimuth (left), while on the right shows the thickness of sediment package estimated from the peak frequency shift with azimuth (for IAG site).	151
Fig.10.27 Shows the shift of the peak frequency of H/V curves for rotating horizontal component for IGC site.	152
Fig.10.28 Shows the shift of peak frequency with the azimuth (left), while on the right shows the thickness of sediment package estimated from the peak frequency shift with azimuth (for IGC site).	152
Fig.10.29 Shows the topographical map of USP (the boundary of campus are shown in dotted line); filled arrow shows IAG site while two-headed arrow show IGC site.	153
Fig.10.30 Shows the dispersion images of six locations at Bebedouro area.	154
Fig.10.31 . Shows the dispersion images (a) IAG site (b) IGC site (c) Colonia 1 and (d) Colonia 2	154
Fig.10.32 Shows the H/V curve for IAG, IGC and Colonia sites of the MASW profiles shown in Fig 10.31.....	155

List of Tables

Table 2. 1: Summary of noise sources according to frequency after	5
---	---

Table 2. 2 Summary conclusions about the proportion of.	8
Table.3. 1 The definition of terms appeared in Fig.3.4 (e-f) (SESAME 2004).....	28
Table.3. 2 : Shows the threshold values for stability conditions.....	28
Table.4. 1 Summary of the acquisition parameter (more detailed parameter setup for 24 and 48 geophones for various depth can be found on www.masw.com).	38
Table.4.2 MASW acquisition parameters for IGC and IAG (geophones 4,5 Hz).	46
Table.4.3 MASW acquisition parameters for Bebedouro area (BEB4A, BEB7, BEB11, BEB1; geophones 14Hz).46	46
Table.4.4 MASW acquisition parameters for Bebedouro area (BEB 16b, BEB 4b; geophones 4.5 Hz).....	47
Table.4.5 MASW acquisition parameters for Colônia area at site A and site B (geophones 4.5Hz).....	47
Table 8. 1 Peak frequencies of noise recording made next to water wells.	103
Table 9. 2 Shows the misfit and T values for the ellipticity different part inversions.	119
Table 10. 1 Shows the fundamental frequency of each station and their	147

Chapter 1: Introduction to the study

1. Introduction

The level of damage and destruction caused by an earthquake in developed area, like Mexico City, Loma Prieta, Kobe and Izmit, followed a complicated pattern. This localized destruction is attributed to longer shaking and higher amplification of seismic motion caused by the geological and geotechnical setting of the area. It is also termed as local site effect. To model the site effect of an area is to determine the shake level longevity and its displacement amplification. For this, is required to find the elastic properties (shear and compressional wave velocities, densities, the thickness of soil layer, etc.) of the site which are inferred by employing various geophysical procedures. This reduces the chances of destruction by an earthquake, that was caused by a local geological setting. This procedure is widely termed as microzonation.

The two very important parameters of the microzonation studies are the thickness of the sediment cover and, most importantly, the shear wave velocity profile of the site. Both these parameters hold the capacity to estimate the amplification caused by soft soil cover in case of motion triggered at its base due to the earthquake. To map out these important parameters, some conventional geophysical techniques are employed such as downhole measurement, seismic reflection and refraction. The conventional geophysical methods bring some hindrances to the picture such as drilling borehole and artificial seismic sources required for the reflection and refraction survey, which are both expensive, time consuming and difficult or even, in some cases, impossible to implement in urbanized environment. The investigation depth is limited to few tens of meter. The method that replaced these conventional geophysical methods from last decades or so is the analysis of earth vibration caused by the seismic noise which is produced by both natural and cultural sources. This ambient seismic noise can be recorded with less cost and effort with a good lateral coverage. Due to its large usage and importance for geological investigation and seismic hazard prevention, it was necessary to define the standard operation protocol for the seismic noise data acquisition, processing and interpretation. A project initiated to design experimental, processing and interpretative protocol with the collaboration of the 14 European research institutes in the years of 2001-2004 (SESAME European Project) provided the guidelines for the researchers involved with this theme, reported and are used extensively afterward.

1.1 The objective of the study

The survey of seismic noise methods specially performed to estimate shear wave velocity profile and thickness are done with a single 3 component seismometer, an array of 3c or one component vertical sensors. The single station measurement is used to obtain a horizontal over vertical Fourier spectral ratio while the array method is used to retrieve the dispersion curve which is combined with H/V curve and jointly inverted for the shear wave velocity profile estimation of

deep soil packages. Many studies performed on this topic have shown the results in a good agreement with borehole techniques. The basic assumption of those methods are that surface wave are dominating the seismic noise wavefield and the shape of the H/V curve are mostly dominated by fundamental mode of Rayleigh wave ellipticity. The seismic noise wavefield also contains the fraction of Love and body waves which contaminate the H/V curve and deviates its shape from Rayleigh wave ellipticity.

The two most important features of the H/V curve are the peak frequency and the shape of the curve. The peak frequency is used for the unconsolidated sediments thickness estimation of a site while the shape of the H/V curve, with some supplementary information, is utilized for the shear wave velocity profile retrieval through inversion. In this study we are going to investigate the aspects of joint inversion on H/V and dispersion curves which have not been evaluated in detail yet, such as it is usually whispered that the peak of H/V provides a good estimative of the shear wave resonance frequency, even when the H/V curve is considered a proxy for Rayleigh wave ellipticity. If this is the case, we will try to check the deviation of shear wave resonance frequency deviation from the H/V peak frequency by forward modeling, considering the noise wavefield as completely dominated by Rayleigh waves, surface waves (both Love and Rayleigh waves) and equal contribution of body and surface waves (diffuse field). We will also try to list all the parameters (shear wave velocity, primary wave velocity, thickness and density of mass) which affect the shift of the peak frequency from the shear wave resonance frequency.

The other important use of the peak frequency is to derive a thickness-peak frequency regression relationship of an interest area. This thickness-peak frequency relationship can be used to obtain the soil deposit thickness by measuring seismic noise at a site and inputting the peak frequency of the H/V to the derived relationship. To obtain this thickness-peak frequency relationship, we must have some borehole control points where the detailed information of the soil deposit is available. The H/V curves are obtained at each control site and then the peak frequency is related to the soil thickness through the regression relationship. However, in the field it is difficult to have the borehole as a control point for calibration. We will try to use dispersion curve of Rayleigh wave and derived thickness-peak frequency relationship to analyze the role of borehole control points if not available in the investigation area.

The H/V curve shape deviates from the Rayleigh wave ellipticity due to the presence of the fraction Love and body waves in the noise wavefield. We will try to remove or minimize the effect of the Love and body waves presence on the noise wavefield and make the shape of the H/V curve closer to the Rayleigh ellipticity shape. The inversion of the H/V curve alone for the shear wave velocity retrieval always had a trade-off between S-wave velocity and thickness estimative. To overcome this trade-off some prior information is needed. The dispersion curve will be analyzed to obtain the velocity increase trend which can be used to overcome this trade-off between thickness and S-wave velocity by inverting the ellipticity alone. The part of the H/V curve which carries the most important information regarding the subsurface ground structure is necessarily analyzed. The most ambiguous problem in all the surface wave inversion problem is

how to fix the subsurface layers prior to the inversion. This is very tricky to answer, however, we tried to find the sensitivity of ellipticity (H/V) curve shape deviation to layers within the earth.

The joint inversion of the H/V for the deep soil S-wave velocity profile retrieval is also very necessary. Usually, there is no role to define weight of misfit for this two different targets. We will try to design a weight function for both targets to find the misfit of the joint inversion in a way to account the number of sample data available for each target (dispersion and H/V curves). All the observation of the analysis will be tested on three different sites in São Paulo state, Brazil, to jointly invert the H/V and dispersion curves.

1.2 Organization of the thesis

The thesis is organized in two main sections. One (Chapters 2-5) dealing with the theoretical background from literature, while the second section (Chapters 6-10) is the analysis and the results of the study. Chapter 1 describes the general introduction, objectives and the organization of the thesis. Chapter 2 is about the origin of seismic noise, techniques used for its analysis and its application for near surface are highlighted. Chapter 3: a brief introduction to the H/V methods, it has a theoretical summary and the practical aspects of the data analysis are discussed. Chapter 4: The array technique used for surface wave, especially Rayleigh wave analysis, is described in detail for the SASW and MASW. Chapter 5: the inversion algorithm used for the study is explained briefly (how the parameter space is modeled and how the new model is generated). The modeling technique of the H/V curve is described in Chapter 6, where the noise wavefield is considered to be dominated by the Body waves, Rayleigh waves, only considering the effect of both Love and body waves, and by the diffused wave field situation.

The analysis of the peak frequency of H/V curve is discussed in Chapter 7 by the forward modeling. The sensitivity of the peak frequency against Poisson ratio, V_s , V_p , thickness (h) and density (ρ) is analyzed, so is the sensitivity of the H/V curve for different number of layers. Chapter 8 describes the thickness-peak frequency relation for the 7 borehole sites at the Bebedouro area (one of the study areas). The MASW dispersion curves are used to obtain the shear wave velocity increase trend of the area. These information are used to obtain the thickness-frequency relation and then compared with the borehole and H/V peak-frequency relation experimentally derived. Chapter 9 is about the analysis of part of ellipticity which is carrying the most relevant information regarding the subsurface structure. The misfit function is discussed and defined for the joint inversion of ellipticity and dispersion curve. Finally, Chapter 10 describes the results of the joint inversion on three studied sites: IAG, Colônia and Bebedouro.

Chapter 2: A review of seismic noise

2. Introduction

The term microzonation is a very familiar expression frequently used in seismology and earthquake engineering for seismically active area classifications. The microzonation is actually the characterization and division of the seismically active area into sub-regions on the basis of predicted risk in case of earthquake damage. This analysis is made as precautions to mitigate hazard and safely design of the infrastructure and dwelling (water and gas pipelines, electricity distribution, schools, hospitals and roads/bridges infrastructures). For the microzonation studies, the velocity model, especially shear wave velocity structure, has a great importance, since it is actually responsible for the major destruction. This velocity model helps in quantifying how destructive the effect of the surface wave will be in the case of an earthquake occurrence. So, the velocity model of the structure information is the prime interest for the microzonation. Unfortunately, this microzonation is desired to be performed on the urbanized area where it is difficult to employ conventional geophysical techniques. To overcome this problem, passive and non-destructive active methods, like spectral analysis of surface waves (SASW) and multichannel analysis of surface waves (MASW), are developed, which are based on the ambient seismic noise recording and hammer seismic, respectively, and can be easily implemented on urbanized area. Prioritizing to describe that technique, in brief, we present a review of the nature of seismic noise. First, an attempt will be made to explain the term seismic noise, its nature and its different aspects. Later, the techniques that use seismic noise for the geophysical and engineering applications.

2.1 Seismic noise

The scientists that deals with measured/recorded data such as seismologists often use the term noise for the unwanted portion of data. The seismic noise is considered as a random and non-deterministic process in nature. It is considered non-deterministic because it is very difficult to mathematically formulate the randomness of the process that generates it or, as we may say, it seems random to us because we do not know all the processes which contribute in the generation of it.

The main signal in seismology is the earthquake record, which is used to model the earth properties from the mechanical vibration signal produced by the earthquake. The dynamic nature of the Earth is supported by the fact that its surface is constantly modified by some of its internal and external processes along the geologic time scale. The earthquake is one of the main evidence presented to support this claim, however, an earthquake is not the only proof of its vibrant nature. There is a permanent small amplitude vibration that causes very small displacements. This permanent vibration on the surface of the Earth could not be related to the earthquake, so it is termed as seismic noise by the seismologists. So our first goal, here, is: try to

understand the origin of the seismic noise from the literature review. Before the advent of standard instrumentation for the recording of earthquakes, the studies made on the analysis of seismic noise were mainly qualitative, however, soon after the development of instrumentation and technical facilities such as the computers, Kanai (1954), Aki (1957) and Akamatsu (1961) were the first researchers who pointed out that the soil characteristics can be inferred from the analysis of seismic ambient noise. This opened a corridor toward the precise understanding of nature of the seismic noise wavefield and its use for the subsurface information retrieval. This reminds an old saying “*One man noise is another man signal*”. Scales & Snieder (1998) consider the transcription “*noise is that part of the data that we choose not to explain*”.

2.2. Seismic sources of noise

Generally, the seismic noise wavefield is the superposition of many seismic signals generated by various natural and man-made sources. The seismic noise wavefield is unpredictable because we do not know the different sources, and if the sources are known, then we are unaware of each source contribution to the noise wavefield. The natural sources of seismic noise, in general, are ocean tides, water-waves striking the coast, standing water waves in the open seas due to storm systems, air pressure changes, turbulent wind or wind-induced vibrations of trees or tall buildings and man-made sources such as car and train traffic, industrial machines, explosions or the exploitation of underground reservoirs e.g. hydrocarbons, geothermal (Sesame, 2004).

A comprehensive and complete literature review of the current knowledge about the seismic noise wave field is given by Bonnefoy-Claudet et al. (2004, 2006a). They have shown that although many kinds of noise sources exist, they can be easily classified in a simple term: the natural and anthropogenic sources. Concerning the origin of the noise, Gutenberg (1958) lists the different types of sources according to the frequency of the relevant seismic motion. Several years later, other authors got the same conclusions (Asten, 1978; Asten & Henstridge, 1984). A summary about the frequency dependency of noise sources is shown in Table 2.1

	Gutenberg 1958	Asten 1978-1984
Waves striking at Coast	0.01-0.5Hz	0.5-1.2Hz
Large scale metrological perturbation	0.1-0.25 Hz	0.16-0.5
Cyclone over ocean	0.3-1Hz	0.5-3Hz
Local metrological conditions	1.4-5Hz	-----
Volcanic tremor	2-10 Hz	-----
Urban	1-100 Hz	1.3-30 Hz

Table 2. 1: Summary of noise sources according to frequency after Gutenberg (1958) and Asten (1978, 1984) (from SESAME Project, report WP08, 2003).

Almost all the authors working on the problem of understanding the nature of seismic noise wavefield agreed that the boundary between man-made noise and natural noise is around 1 Hz. Below one Hz (<1Hz ⇒ Long-period) noise is termed as microseism and above one Hz (>1Hz ⇒ short-period) noise is termed as microtremor. The term microseism and microtremor are not

fully used in the literature of seismology. We will try to use these both terms for seismic noise wave-field equally in some places at this study. Information listed in Table 2.1 can be described in terms of frequency. It is possible to see from this short summary that surface waves are an essential component of seismic noise. In fact, even if their importance decrease with the increase of frequency, their role is always significant from the Table 2.1. It can be observed that, at frequencies below 0.5 Hz, the sources are natural (ocean, large-scale meteorological conditions). So, at low frequencies, seismic noise is generally stable, it has high coherence, and consists mainly of surface waves. In the intermediate frequency range between 0.5 to 1 Hz, sources are both natural (local meteorological conditions) and anthropogenic (urban). Thus, in this case, the noise is less stable and the fraction of the surface waves is variable. Finally, for frequencies higher than 1 Hz, sources are essentially anthropogenic. As a consequence of the elevated variability of the anthropogenic sources, at high frequencies, the seismic noise is extremely unstable both in amplitude and in terms of the ratio between body and surface waves.

2.3 The composition of noise wavefield

The seismic noise field is assumed to be dominated by surface wave field as demonstrated by some studies (Douze, 1964; Bormann 2012). Bonnefoy-Claudet et al. (2006a) made an extensive review of the composition of the noise wavefield. Here, the developments made in this direction are listed and discussed, such as their uses for the engineering applications. The seismic noise wavefield was believed, and it is still the case, to be dominated by the fundamental mode of Rayleigh waves. The ocean generated double frequency noise wavefield, that is considered to be the main source of seismic noise wavefield (Gutenberg, 1911; Longuet-Higgins, 1950). The dominance of noise field by the Rayleigh wave fundamental mode is considered true for the most cases of ocean-generated noise wave field within a period of 5-20 s (Brooks et al., 2009). The characteristic of this important noise generated source is assigned to be the same for the shortest and longest period dominated by this noise generation sources.

Due to the development of seismic noise wavefield recording sensors (3component seismometer) and processing ease due to the modern computer, it is observed that seismic noise field contain both body and surface waves. At lower frequencies (0.04 to 0.15 Hz) the noise wavefield is dominated by Rayleigh and Love waves fundamental modes (Lacoss et al. 1969; Kurrle & Widmer, 2008). Generally, for the natural sources of seismic noise wavefield, it consists on higher mode of Rayleigh waves, along with dominated fundamental mode (Brooks et al., 2009), Love waves (Saito, 2010) and a fraction of body waves (Koper et al., 2010). So, noise wavefield composition is debatable and one can simply narrow down its nature search by asking and finding some answers to the questions likes (SESAME, 2004): 1. What is the proportion of body and surface wave energies in noise wavefield? If dominated by a surface wave then, 2. What are the relative fractions of the Rayleigh and Love waves in noise wavefield? 3. If the seismic wave noise wavefield is dominated by Rayleigh waves then what is the relation of fundamental mode to higher mode Rayleigh wave energy?

The answer to the question 1 can be sought out from two study analysis (Douze, 1964; Bormann, 2012) carried out with seismic noise and earthquake recording analysis done with sensors installed both at the surface and in the boreholes at different depth levels. The surface-wave nature of seismic noise is the reason for the exponential decay of noise amplitudes with depth, which is not the case for body waves (Fig.2.1). Douze (1964) analyzed the noise measurement in an abandoned oil well at the surface and at different depths with a vertical short period seismometer. The ratio of Fourier spectral amplitude at depth over the surface spectral amplitude ratio decreased significantly at 0.25-3 s period (Fig.2.1), which suggests the surface wave dominance of noise wavefield. Above the 3s period, the ratio of spectral amplitude for depth to surface are nearly 1, which suggests that for those frequencies decay should occur at higher depth (Fig.2.1). Another study (Bormann, 2012) performed with the same propose to check the nature of noise wavefield was done with recording at the surface and depth (Fig 2.2).

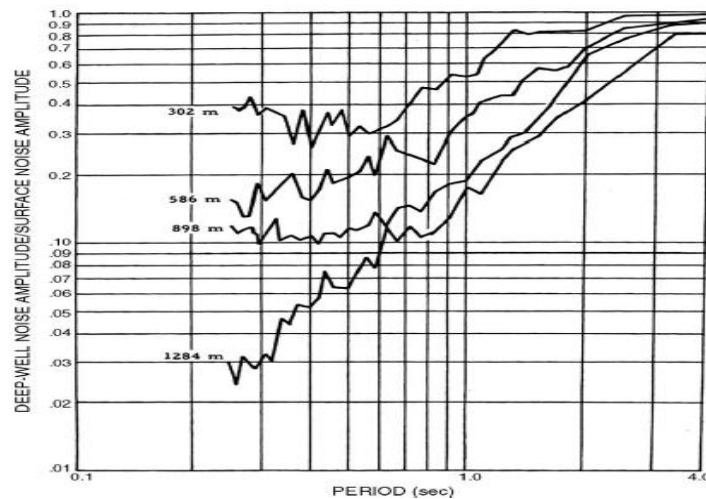


Fig.2. 1 Deep-to-surface noise Fourier spectra amplitude ratio (vertical component) as a function of period (taken from. Douze, 1964).

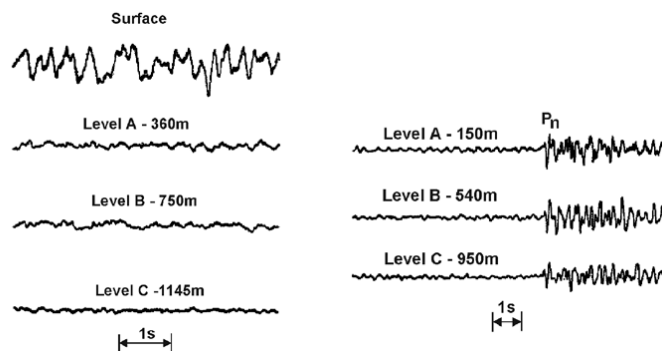


Fig.2. 2 Recording of seismic noise (left) and earthquake signals (right) at the surface and at different depth levels of a borehole (from Bormann 2012).

Similarly, the penetration depth of surface waves increases with wavelength and high-frequency noise attenuates more rapidly with depth. In the case of (Fig.2.3) the noise power at 300m depth in a borehole was reduced, as compared to the surface, by about 10 dB at $f = 0.5$ Hz, 20 dB at 1

Hz and 35 dB at 10 Hz. This continuous amplitude decline with frequency is in accordance with the surface waves nature of seismic noise. However, the noise amplitude drop, as well as the signal behavior, with depth and it also depended on the local geological conditions. Withers et al. (1996) found that for frequencies between 10 to 20 Hz, the SNR (signal to noise ratio) could be improved between 10 to 20 dB and for frequencies between 23 and 55 Hz as much as 20 to 40 dB by deploying a short-period sensor at only 45m below the surface.

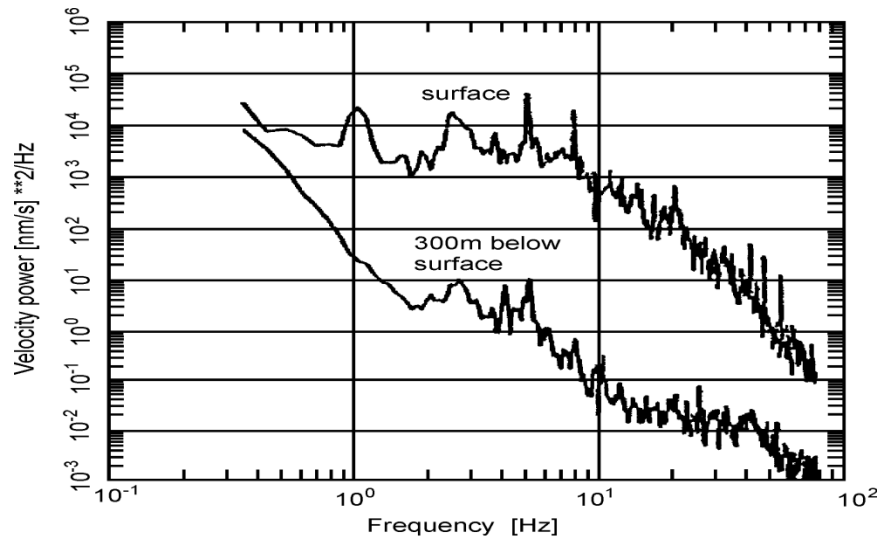


Fig.2. 3 Velocity power density spectra as obtained for noise records at the surface (top) and at 300 m depth in a borehole (below) near Gorleben, Germany (taken from Bormann, 2012)

To deal with the second question, some empirical studies were done seeking to find the fraction energy of the Rayleigh and Love waves in noise field. As early as 1980, most of the researchers focused their attention to find the fraction of Rayleigh to Love ratio from the analysis of noise wavefield recorded on vertical component (Li et al., 1984; Horike, 1985; Yamanaka et al., 1994). The results of these studies showed an agreement in one aspect that microseism (<1Hz) are mainly dominated by Rayleigh waves, and at high frequency (> 1Hz) a combination of Love and Rayleigh waves exists. However, two other studies (Arai et al., 1998 and Yamamoto, 2000) performed on the same subject have shown very unclear results about the fraction of Rayleigh-to-Love waves (see for example Table 2.2). The outcome of their analysis is that at anthropogenic region (urban site) the fraction of Love energy is more than Rayleigh energy (Table 2.2).

	Rayleigh waves(%)	Love waves(%)	Frequency range(%)
Chouet et al.,1998	30%	70%	>2Hz
Yamamoto, 2000	<50%	>50%	3-10 Hz
Arai et al., 1998	30%	70%	1-12 Hz
Cornou, 2002	60%	40%	< 1 Hz
Okada (2003)	<50%	>=50%	0.4-1 HZ
Köhler(2006)	10-35%	65-90%	0.5-1.3 Hz

Table 2. 2 Summary conclusions about the proportion of Rayleigh and Love waves in noise wave field.

The three component sensor array analysis, frequency-wavenumber (F-K) and spatial autocorrelation (SPAC) analysis helps to identify the fraction of Rayleigh to Love wave in noise wavefield (Arai and Tokimatsu, 1998-2000; Köhler et al., 2007; Endrun et al., 2010). Arai and Tokimatsu (1998, 2000) tried to find the comparative fraction of Rayleigh and Love waves and this fraction dependence on frequency from 3-c sensor array analysis for four sites in Japan A: Yumenoshima (Tokyo), B: Rokko Island (Kobe), C: Asahi (Kushiro), D: Kotobuki (Kushiro). They applied both the frequency-wave-number (F-K) and spatial auto-correlation method (SPAC) approach (Fig.2.4). The ratio of $(\text{Rayleigh/Love})_{\text{FK}}$ and $(\text{Rayleigh/Love})_{\text{SPAC}}$ is 0.4 to 1 for the period 0.1-5 s. The fraction of the ratio is concluded to be 0.7 (0.41/0.59). Hence, for frequencies higher than 1 Hz (cultural noise), the noise wavefields consists around 60% Love waves and 40% Rayleigh waves in that area. Another study done by Cornou (2002) showed from the 3-c array data analysis that the energy ratio for each radial and transverse component is around 50% each. She estimated that the proportion of energy carried by Rayleigh waves through the ratio of the energy carried by radial and transverse components is around 50% of Rayleigh waves for frequency range from 0.2 to 1 Hz.

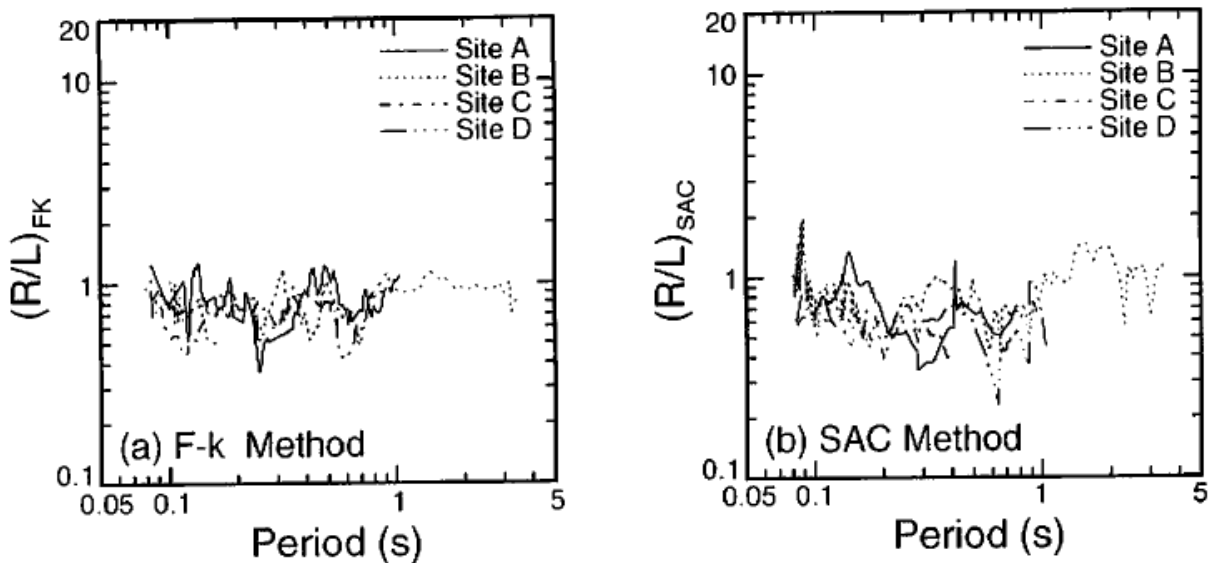


Fig.2. 4 Rayleigh to Love waves fraction for four sites, from 3-c array data for FK (a) and for SAC (b) analysis (Arai and Tokimatsu, 1998).

About the third question, the actual energy distribution for various modes of Rayleigh waves is almost impossible to predict due to the heterogeneous ground conditions (Bonney-Claudet et al., 2006). The Rayleigh wave higher modes existences in the seismic noise wavefield are not very well investigated. Indirect information of Rayleigh wave higher modes dominancy can be achieved from the Horizontal-over-Vertical spectral ratio (H/V) method. Yamanka et al. (1994) performed a study with continuous noise recording in Japan (Kanto plain). They observed that H/V closely match with the fundamental mode of Rayleigh wave ellipticity, which lead them to

conclude that noise wavefield is dominated by fundamental mode of Rayleigh waves. Two other studies, Stephenson (2003) and Konno & Ohmachi (1998) concluded that if the noise wavefield is dominated by fundamental mode of Rayleigh wave then the H/V curve should have a clear peak and trough for the site.

Tokimatsu (1997) analyzed the Rayleigh wave displacement equation for synthetic noise at a simple model (horizontal layered, elastic and homogeneous medium over a half space), theoretical dispersion curve was estimated for the model. He characterized the model by 3 different S-wave velocity profiles for different stiffness values with depth, stiffness changing regularly (increases and decreases cases Fig. 2.5 a). Tokimatsu observed that in case 2 and case 3 the computed dispersion curve (obtained from synthetic noise) does not perfectly match the theoretical one for fundamental mode, however in case 1 (increasing velocity with depth), the theoretical and computed curves for the model match very reasonable. He observed that one higher mode or multiple higher modes played a significant role in various frequency ranges. Hence, depending on the geological characteristics of the soil (especially due to the presence of velocity inversions at depth) higher modes can be excited in seismic noise (if mainly made of surface wave).

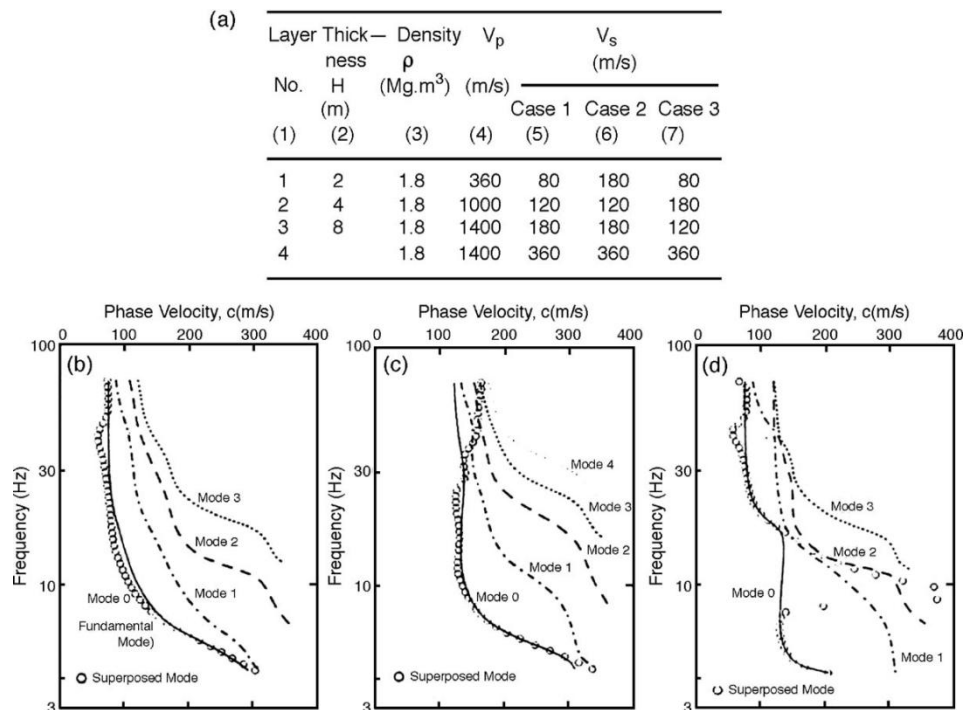


Fig.2. 5(a) Velocity profiles used by Tokimatsu (1997) to compute Rayleigh waves dispersion curves numerically. The corresponding dispersion curves (dots) computed from noise synthetics in case 1 (b), case 2 (c) and case 3 (d) are compared with theoretical dispersion curves of higher mode Rayleigh waves (after Tokimatsu 1997).

2.4 Techniques used for seismic noise

The seismic noise wavefield is utilized for different purposes at different levels. The first real techniques, which were developed for the seismic noise analysis, are array analysis like Spatial Autocorrelation (SPAC), Aki (1957-1965), and the frequency-wavenumber analysis technique, F-K, (Capon et al., 1967-1969). We can also cite the single 3 component method introduced by Nogoshi & Igrashi (1971) to estimate the site effect properties for the mechanical vibration like an earthquake, and very recently, the Green function is used for the same purpose of the site effect fundamental period and shear wave velocity estimation (Sanche Sesma, 2011; Pina Flores, 2017). We briefly explain the F-K and SPAC in coming section. In seismology, a 2D array (SPAC and F-K method) of seismic sensors is used to capture the full wave field for the velocity and azimuth information retrieval at an investigated site. 1D array of sensors only records the wave field that is on the direction of the array line while fail to capture both the velocity and azimuth information. To resolve the azimuth, the horizontal component of the wave field should be properly resolved. For each array technique, the basic principle is to find the arrival delay at each station for an incident wavefront. Each wavefront reaches different sensors at a different time. From this time delay, the slowness or the velocity information are obtained. In the case of vertically incident wavefield, a 2D array will record the apparent velocity or slowness and this apparent velocity is strongly affected by the incidence angle from the vertical. Therefore, a 3D array is needed to capture the velocity, azimuth and incidence angle information. This 3D array is usually achieved by installing sensors in a borehole at a depth equivalent to the length of the 2D array on the surface. To the surface wave (both Love and Rayleigh waves) that travels along the horizontal direction, a 2D array is sufficient to analyzed surface waves.

2.4.1 Spatial autocorrelation (SPAC) method

SPAC method was developed by Aki (1957, 1965) for seismic noise analysis which helps in characterizing the nature of the noise wavefield and wave propagation characteristics of a site. Aki considered the seismic noise wave as a stationary and random process both in time and space. Hence, two further assumptions are made that the wave field is made of superimposed isotropic waves propagating with same phase velocities for certain frequency, but with different powers in all directions, in a horizontal plane. The second assumption is that waves with different frequencies and propagation directions are independents. Taken all these assumptions into consideration the spatial correlation of ground motion at two location $u(a,t)$ and $u(b,t)$ is given by Aki (1957) as:

$$\phi(r, \varphi) = \langle u(a, b, t)u(a + r\cos\varphi, b + r\sin\varphi, t) \rangle \quad (2.1)$$

Here $u(a, b, t)$ is the recorded signal at location (a,b), t is time, φ is azimuth and r is the distance. The time and space spectrum relation for a wavefront of single mode traveling along the azimuth θ is given as:

$$\phi(\mathbf{r}, \varphi) = \frac{1}{\pi} \int_0^\infty \Phi(\omega) \cos \left[\frac{\omega r}{c(\omega)} \cos(\theta - \varphi) \right] d\omega \quad (2.2)$$

$\Phi(\omega)$ is the power spectrum of the wave in time, $c(\omega)$ is the phase velocity, ω is the angular frequency. A power spectrum term, $\Phi(\omega)$, which can be filtered with band filter at a central frequency ω_o is given as:

$$\Phi(\omega) = P(\omega_o) \delta(\omega - \omega_o) \quad (2.3)$$

where $P(\omega_o)$ is spectral power density, δ is dirac function. Using these values in Eq.2.2 result as:

$$\phi(\mathbf{r}, \varphi, \omega_o) = \frac{1}{\pi} P(\omega_o) \cos \left[\frac{\omega_o r}{c(\omega_o)} \cos(\theta - \varphi) \right] \quad (2.4)$$

This spatial correlation in Eq.2.4 is normalized by the autocorrelation of a central station and a new spatial correlation is given as:

$$\rho(\mathbf{r}, \varphi, \omega_o) = \frac{\phi(\mathbf{r}, \varphi, \omega_o)}{\phi(0, \varphi, \omega_o)} \quad (2.5)$$

upon putting its value will reduce Eq.2.5 to

$$\rho(\mathbf{r}, \varphi, \omega_o) = \cos \left[\frac{\omega_o r}{c(\omega_o)} \cos(\theta - \varphi) \right] = \cos(\omega_o \tau(\mathbf{r}, \varphi, \omega_o)) \quad (2.6)$$

In Eq.2.6 $\frac{r}{c(\omega_o)} \cos(\theta - \varphi) = \tau(\mathbf{r}, \varphi, \omega_o)$ shows the time delay between different sensors. The shape of spatial-correlation function, ρ , can easily sketch the wave propagation direction (Fig2.6).

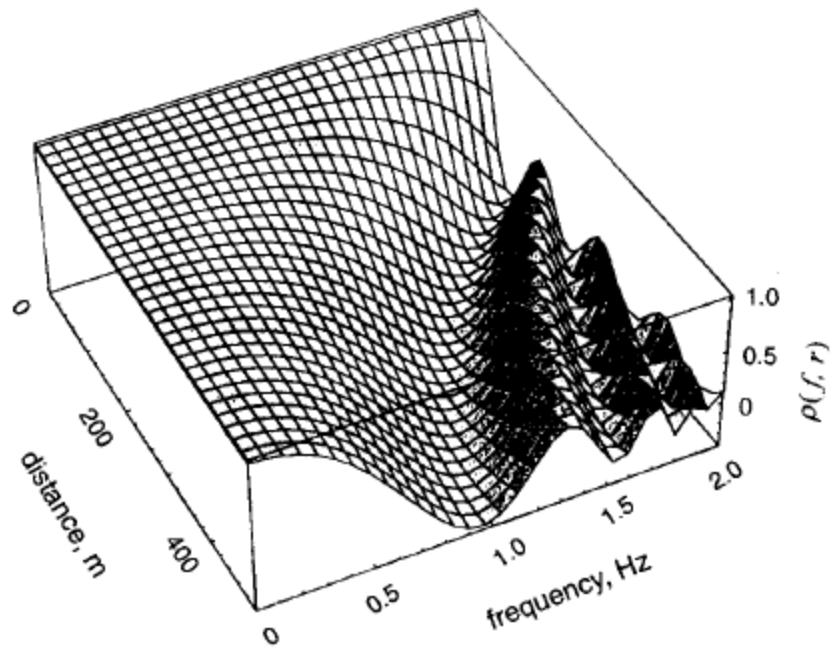


Fig.2. 6 The shape of the spatial correlation function. The function shows a constant value and abruptly decreases with increase in frequency in the propagation direction (from Okada 2003).

For experimental point of view, Aki (1957) suggested to use a circular array of radius r and install the station at regular space with respect to the central station (Fig.2.7).

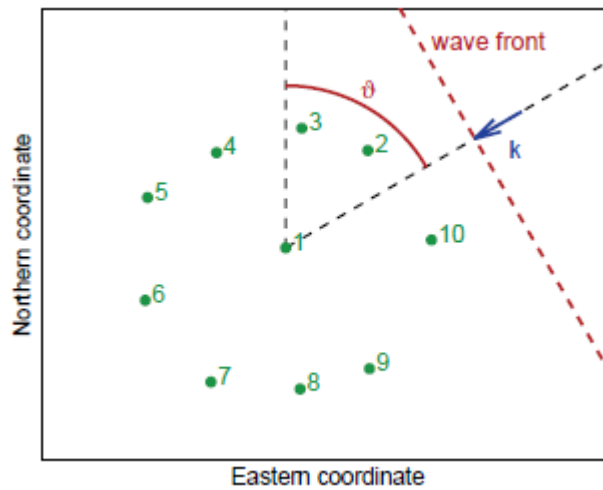


Fig.2. 7 Diagram of a circular array with an incident plane wave arriving under an azimuth angle (from Hobiger 2011).

The function for this circular array is azimuthally average as

$$\bar{\phi} = \frac{1}{\pi} \int_0^{\pi} \phi(r, \varphi) d\omega \quad (2.7)$$

and in more general form Okada (2003) expressed Eq.2.7 as

$$\bar{\varphi} = \frac{1}{\pi} \int_0^{\infty} \Phi(\omega) \int_0^{\pi} \cos \left[\frac{\omega r}{c(\omega)} \cos(\theta - \varphi) \right] d\varphi d\omega \quad (2.8)$$

the term in Eq.2.8 $\int_0^{\pi} \cos \left[\frac{\omega r}{c(\omega)} \cos(\theta - \varphi) \right] d\varphi$ is the Bessel function first kind of zero order J_0 . Then Eq.2.8 can reduced to

$$\bar{\varphi} = \frac{1}{\pi} \int_0^{\infty} \Phi(\omega) J_0 \left(\frac{\omega r}{c(\omega)} \right) d\omega \quad (2.9)$$

Similar like Eq.2.5 the normalized spatial correlation function is given as

$$\rho(r, \omega_o) = J_0 \left(\frac{\omega_o r}{c(\omega_o)} \right) \quad (2.10)$$

This derivation is detailed in Aki (1957). Eq.2.10 provides a way to compute the phase velocity when the average of the spatial-correlation function is made for fixed r . Naturally, if data recorded on several circles with different radio are available, an azimuthally average can be computed for each circle, and for a fixed frequency f , using r as the independent variable (Chavez-Garcia,2005). This Eq.2.10 provides a dispersion curve which can be inverted to obtain the ground structure.

2.4.2 Frequency-wavenumber analysis

Frequency wave number method was developed by Capon et al. (1967) and Lacoss et al. (1969). This method was initially developed to detect nuclear explosion using seismic network LASA (large aperture seismic array) which has a diameter of 200 km (Okada 2003). This helps out to single out a predominant seismic wave from a mixture of other waves disregarding its nature. This method works for both body and surface wave analysis. Applying to the surface wave analysis, in the case of seismic noise, the main assumption is made that wave field is dominated by surface waves.

To describe the kernel of this procedure let assumed a single incident plane wave arriving at N sensors with its position as \mathbf{r}_i and the corresponding slowness vector for delay arrival at all sensors is given as product of slowness vector with the positions vector within array. The first sensor position of the array system is considered as the origin. In this situation, the recording for a single-component for all the sensors is given as:

$$x_i(\mathbf{t}) = \int_0^{\infty} \mathbf{C}(f) e^{i2\pi f(t-s_0(f)r_i)} d\mathbf{f} \quad (2.11)$$

where $\mathbf{C}(f)$ is wave complex amplitude (frequency dependant). The signal vector of the array can be define as

$$\mathbf{x}_i(t) = \begin{pmatrix} x_1 \\ x_2 \\ \vdots \\ x_N \end{pmatrix} = \int_0^\infty \mathbf{C}(\mathbf{f}) e^{i2\pi\mathbf{f}(t-s_0(\mathbf{f})\mathbf{R})} d\mathbf{f} \quad (2.12)$$

Where, in 2.12, \mathbf{R} are the sensors locations given as a matrix (the size of \mathbf{R} is $N \times 3$). By taking the Fourier transform of signal vector yield as:

$$\begin{aligned} \mathbf{X}(\mathbf{f}) &= \frac{1}{\sqrt{2\pi}} \int_{-\infty}^{\infty} \int_{-\infty}^{\infty} \mathbf{C}(\mathbf{f}') e^{i2\pi\mathbf{f}'(t-s_0(\mathbf{f}')\mathbf{R})} e^{-2\pi\mathbf{f}t} d\mathbf{f}' dt \\ &= \frac{1}{\sqrt{2\pi}} \int_{-\infty}^{\infty} \mathbf{C}(\mathbf{f}') e^{-i2\pi\mathbf{f}'s_0(\mathbf{f}')\mathbf{R}} \int_{-\infty}^{\infty} \mathbf{C} e^{2\pi(\mathbf{f}'-\mathbf{f})t} d\mathbf{f}' dt \\ &= \frac{1}{\sqrt{2\pi}} \int_{-\infty}^{\infty} \mathbf{C}(\mathbf{f}') e^{-i2\pi\mathbf{f}'s_0(\mathbf{f}')\mathbf{R}} \delta(\mathbf{f}' - \mathbf{f}) d\mathbf{f}' \\ &= \frac{1}{\sqrt{2\pi}} \mathbf{C}(\mathbf{f}) e^{-i2\pi\mathbf{f}s_0(\mathbf{f})\mathbf{R}} \end{aligned} \quad (2.13)$$

if $\frac{\mathbf{C}(\mathbf{f})}{\sqrt{2\pi}} = \mathbf{s}_0(\mathbf{f})$ is the origin sensor Fourier transform and the wave vector is given as $\mathbf{k}_0(\mathbf{f}) = 2\pi\mathbf{f}s_0(\mathbf{f})$ then 2.13 reduced to

$$\mathbf{X}(\mathbf{f}) = \mathbf{s}_0(\mathbf{f}) e^{-i\mathbf{k}_0(\mathbf{f})\mathbf{R}} \quad (2.14)$$

$\mathbf{X}(\mathbf{f})$ is multiplied by a steering vector $\mathbf{a}(\mathbf{k}) = (\mathbf{1}/\sqrt{N}) e^{-i\mathbf{R}\mathbf{k}}$ which takes all the element of $\mathbf{X}(\mathbf{f})$ in phase and then sum it.

Application of seismic noise $\mathbf{X}(\mathbf{f})\mathbf{a}(\mathbf{k})$ energy is estimated as:

$$\mathbf{E}(\mathbf{k}) = |\mathbf{X}(\mathbf{f})^t \mathbf{a}(\mathbf{k})|^2 \quad (2.15)$$

$$= \left| \mathbf{s}_0(\mathbf{f}) e^{i\mathbf{k}_0(\mathbf{f})\mathbf{R}} \frac{1}{\sqrt{N}} e^{-i\mathbf{R}\mathbf{k}} \right|^2 \quad (2.16)$$

$$= |\mathbf{s}_0(\mathbf{f})|^2 \left| \frac{1}{N} \sum_{i=1}^N e^{-ir_i(\mathbf{k}-\mathbf{k}_0(\mathbf{f}))} \right|^2 \leq |\mathbf{s}_0(\mathbf{f})|^2 = E_f(\mathbf{k}_0) \quad (2.17)$$

A grid search is performed for all values of \mathbf{k} and trying to recognize the maximum energy for a correct wave vector. The second term in 2.17 is known as an array response function which corresponds to a zero vector incident wave or, more simply, the wave is arriving at an incident angle of zero which corresponds to infinite velocity. Frequency wave number method characterized the seismic noise wave field by determining the apparent velocity and direction of maximum propagating waves. FK method is used mainly to determine the Rayleigh wave dispersion curve with vertical seismic sensors because in 3 component sensors case, horizontal

component requires a rotation for radial and transverse component which is not an easy task (Lacoss et al., 1969 Fah et al 2008). There is one other technique that uses seismic noise for site investigation. It is the H/V spectral curve technique. The H/V will be explained in detail in separate chapters (chapter 3).

There is a variety of seismic noise application ranging for environmental applications to earthquake engineering and oil and gas exploration. The most common techniques utilized for these purposes are a single sensor and the array techniques. The main feature of seismic noise, on which most of these techniques are based, is the spectral analysis of seismic noise and its variation both in space and time.

For the environmental studies, the main application of seismic noise is its use for the environmental monitoring. The global climate changes and tried to observe the temporal variation of seismic noise (Grevemeyer, 2000; Aster et al., 2008), as one of the main sources of seismic noise are an ocean related process like ocean swell and tides, and all these processes are directly related to the climatic condition. The change in global climate is observed with the temporal variation of continuous seismic noise recording. Gross et al. (2009) utilized seismic noise for local and regional scale metrological variation like air pressure and wind speed changes. Burtin et al. (2008) analyzed seismic noise spectral amplitude variation with time and space to observe the hydrodynamics of the river to its transported bedload. The use of seismic noise for seismic interferometry is another important application. This interferometric study is performed by measuring the Green function from the cross-correlation of coherent wave field between any two receivers of seismic noise recording and trying to observe its variation with time. This approach is used for the analysis of seismic velocities changes at fault zones (Breguier et al., 2008b) and at volcanoes sites (Breguier et al., 2008a). The cross-correlation of the seismic noise recording converges to Green function when the seismic noise wavefield is assumed to be equipartitioned (equal contribution of surface and body waves) (Gouédard et al., 2008a).

In earthquake engineering, seismic noise is often used to analyze the site based specific properties like shear wave velocity, which is the most important parameter in microzonation for earthquake hazard mitigation. The other applications are an estimative guess of the thickness of soil package, the direction of maximum slope inland sliding prone areas and site based vibration amplification. The retrieval of the 1D shear wave velocity profile with depth are achieved through array techniques like SPAC, multi-channel analysis of surface waves (MASW), spectral analysis of surface wave (SASW) and frequency-wavenumber (FK) method. In all these methods, dispersion curves are obtained and later, they are inverted to obtained the S-wave velocity profile. H/V is another very important technique used to study the frequencies around, the maximum amplification of the bedrock motion is expected to occur at a local site (will be discussed in detail in next chapter).

The most commercialized application of seismic noise is its utilization in the hydrocarbon industry. Some studies have shown the possibility of using seismic noise analysis as direct hydrocarbon indicator (DHI) for hydrocarbon reservoir (Mohammed et al., 2007). It is observed that within the frequency ranges of 1 to 4 Hz, the H/V ratio and spectral amplitude of recorded seismic noise changes with the presence of hydrocarbon reservoir in the subsurface. However, there is no univocal agreement among the researcher for this specific usage. A study over the hydrocarbon reservoir concluded that the variation in H/V and spectral amplitude variation at the site are more affected by seismic noise produced by local sources like hydrocarbon exploitation activity and not as DHI (Hanssen & Bussat 2008). However, this seems a very interesting application and may need further study for the detailed insight.

Chapter 3: Review of the H/V spectral curve method

H/V (horizontal-to-vertical) spectral ratio is a fast way to characterize a site for engineering application from the ambient noise measurement with a single 3-component sensor on the Earth surface. The method is used for a rapid estimation of fundamental resonance frequency of a site around which the maximum displacement amplification is expected to occur in case of shakes induced by an earthquake. The technique can be summarized as: a three-component sensor (seismometer) used to record the ground motion induced by natural seismic noise. The Fourier spectra of all the three (east-west, north-south and vertical) components are find out. The horizontal (east-west, north-south) components are averaged out and divided by the vertical one.

$$(H/V) = \sqrt{\frac{P(\omega)_{NS} + P(\omega)_{EW}}{P(\omega)_{UD}}} \quad (3.1)$$

where $P(\omega)_{UD}$ is the Fourier amplitude spectra of the vertical motion and $P(\omega)_{NS}$ and $P(\omega)_{EW}$ are the spectra of two horizontal components at frequency ω . Both the horizontal components are averaged either by geometrical mean or quadratic mean.

This spectral amplitude ratio (Eq.3.1) is plotted as a function of frequency which usually results in a peak (depending on the subsurface configuration). This peak corresponds to the S-wave resonance frequency of the site. The shear wave resonance frequency within a layer of thickness h is one-quarter of the wavelength of shear wave within the layer (Mooney et al 1966; Malischewsky & Sherbaum, 2004). This peak of the H/V curve is used extensively for the site effect characterization and for quick estimation of its fundamental resonance (Sing, 2014-2015 and 2017; Shokry, 2016). The advantage of this method is that it can be used in the areas where the earthquake seismic activity is not so frequent, in such case, the recording of the seismic noise achieved the required goal.

Here, in this chapter, it will be given the historical overview of the method. And later a brief outline of the H/V formula derived by Malischewsky & Sherbaum (2004) from the wave equation for homogeneous half space and a layer over half space situation, following by the processing of seismic noise from the SESAME (2004) recommendations to get the reliable H/V curve.

3.1 Historical overview of the H/V curve

Kanai and Tanaka (1961) were the first researchers to use the seismic noise horizontal component Fourier spectra for the subsurface characterization. Their conclusion was that seismic natural noise properties depend both on the mechanical properties of a site and sources of seismic noise. Later, Nogoshi and Igarashi (1971) used the horizontal over vertical spectral ratio

to infer the site properties, however, their work was published in Japanese so the rest of the scientific community did not notice it. This method was familiarized by Nakamura in 1989, which is actually the reason that some of the researchers called it Nakamura method.

The H/V curve methods are extensively used for various purposes. Harutoonian (2012) used it for the soil compaction evaluation. Stankoe et al. (2017) showed that directional analysis of the H/V might provide the link to the presence of near subsurface faults. Mohammed et al. (2007) and Saenger et al. (2009) used this method to link it to the presence of hydrocarbon within the subsurface. Though all these applications of the H/V spectral curve seem very intriguing, the most commonly adopted application of the H/V curve is its utilization for the near subsurface characterization. The H/V curve is used very extensively to retrieve 1D shear wave velocity profile by the joint inversion with the dispersion curve (Scherbaum et al., 2003, Arai & Tokimatsu 2004, Parolai et al., 2005, Piccozi et al., 2005 and Hobiger et al., 2013). Scherbaum et al. (2003) showed that dispersion curve inversion can be improved by the inclusion of the peak of the H/V curve for deeper soil deposit. Arai & Tokimatsu (2004) showed that thickness of the soft sediments can be retrieved if the absolute shear wave velocity of the site is known in priority. Parolai et al. (2005) showed a very similar result that dispersion and Rayleigh wave ellipticity have a different sensitivity to the soil layers.

The two most important features of the H/V curve often used for the near-subsurface application is the peak and the shape of the curve. The peak frequency is used for the fundamental resonance frequency, thickness and the average shear wave velocity estimation of the soil package, while the shape of the H/V curve, along with some supplementary information, is utilized for the shear wave velocity profile retrieval through inversion. In this study, we are going to investigate the aspect of joint inversion of the H/V and dispersion curves which have not been evaluated in detail yet (discussed in objectives and summary of the thesis in detail). For example, it is usually whispered that the peak of H/V provides a good estimative of shear wave resonance frequency even when H/V curve is considered as proxy for the Rayleigh wave ellipticity. If this is the case, we will try to check the deviation between shear wave resonance frequency from the H/V peak frequency by forward modeling.

3.2 Formula of the H/V curve

The first attempt to model and formulate the H/V curve mathematically was made by Malischewsky et al., (2004, 2008). Malischewsky tried to explicitly derive a formula for the H/V curve from the wave equation, for the Rayleigh wave traveling through different situations like in homogeneous half-space, and a layer of thickness d over the half-space. The complete algebraic derivation of the formula is lengthy, especially for a layer over the half-space, and can be found in Malischewsky et al. (2004). Here it will be listed briefly.

The propagation of Rayleigh wave along homogeneous and inhomogeneous surfaces of half space is a well-understood phenomenon. The displacement of particles under the influence of Rayleigh waves has two orthogonal components, one horizontal along the direction of propagation while the other component is directed downward along the depth axis. The ratio of these two displacements eigenfunctions at the surface of homogeneous or inhomogeneous half-space is termed as ellipticity of Rayleigh wave. The shape of the ellipticity is linked to an elastic parameter of the subsurface and it is therefore considered an important parameter for engineering problems.

To derive the formula of the H/V for the homogenous half-space we are using the notation of Malischewsky et al. (2004, 2008). Consider a homogeneous half-space in a Cartesian coordinate system, where the origin of a two-dimensional Rayleigh wave motion is located on the surface of half space. The wave motion direction assumed is from left to right, the horizontal displacement in the x-direction is given by x_1 , while vertical component of displacement x_3 is directed into the half-space (z-direction). The displacement u_i in case of no-body forces for homogenous, elastic and isotropic medium can be characterized by Lamé parameter μ, λ and density ρ as

$$\mu \frac{\partial^2 u_i}{\partial x_j \partial x_j} + (\lambda + \mu) \frac{\partial^2 u_j}{\partial x_i \partial x_j} = \rho \ddot{u} \quad (3.2)$$

where \ddot{u} denotes double derivative with respect to time. For a plane wave the depth dependant harmonic displacement eigenfunctions for Rayleigh wave are given as

$$\mathbf{u}_1 = \mathbf{U}_1(x_3) e^{ik(x_1 - ct)} \quad (3.3)$$

$$\mathbf{u}_3 = \mathbf{0} \quad (3.4)$$

$$\mathbf{u}_3 = \mathbf{U}_3(x_3) e^{ik(x_1 - ct)} \quad (3.5)$$

where k is the wave number, c is phase velocity, ω is angular frequency and t is the time. The term in 3.3 and 3.5 ($\mathbf{U}_1(x_3), \mathbf{U}_3(x_3)$) are given as

$$\begin{aligned} \mathbf{U}_1(x_3) &= ikAe^{-px_3} + qBe^{-qx_3} \\ \mathbf{U}_3(x_3) &= -pAe^{-px_3} + ikBe^{-qx_3} \end{aligned} \quad (3.6)$$

$k \left(1 - \frac{c^2}{\alpha^2}\right)^{1/2}$, $q = k \left(1 - \frac{c^2}{\beta^2}\right)^{1/2}$ where α is P-wave velocity and β is the shear wave velocity by putting the value of \mathbf{u}_1 and \mathbf{u}_3 in 3.2 and on simplification it result the two differential equation of second order as

$$\gamma U_1''(x_3) + ik(1 - \gamma)U_3'(x_3) - PU_3(x_3) = 0, \quad U_3''(x_3) + ik(1 - \gamma)U_1'(x_3) - QU_3(x_3) = 0 \quad (3.7)$$

here $P = p^2$ and $Q = q^2$, $\gamma = \alpha^2 / \beta^2$, dash signifies the derivative of $\mathbf{u}_i = \mathbf{U}_i(x_3) e^{ik(x_1 - ct)}$ ($i = 1, 3$) with respect to the depth (x_3). The general solution of (3.7) can be written as

$$\begin{aligned}
U_1(x_3) &= C_1 e^{-px_3} + C_2 e^{px_3} + C_3 e^{-qx_3} + C_4 e^{qx_3} \\
U_3(x_3) &= i \left(\frac{p}{k} C_1 e^{-px_3} - \frac{p}{k} C_2 e^{px_3} + \frac{p}{k} C_3 e^{-qx_3} - \frac{p}{k} C_4 e^{qx_3} \right)
\end{aligned} \tag{3.8}$$

where C_1, C_2, C_3, C_4 are integration constants whose values are found from the boundary condition, which are for half space $C_2, C_4 = 0$ $x_3 = \infty$ and the other two constants C_1, C_3 are found from the stress-free condition at the surface of half-space ($x_3 = 0$). The values of stresses $\tau_{i3}, i = 1, 3$ from hook law are given as

$$\begin{aligned}
\tau_{13} &= S_{13}(x_3) e^{ik(x_1-ct)} \\
\tau_{33} &= S_{33}(x_3) e^{ik(x_1-ct)}
\end{aligned} \tag{3.9}$$

where $S_{i3}, i = 1, 3$ are depth depended stress tensors given as

$$\begin{aligned}
S_{13} &= \rho \beta^2 (U_1'(x_3) + ik U_3(x_3)) \\
S_{33} &= \rho \beta^2 (U_3'(x_3) + ik(1 - 2\gamma) U_1(x_3))
\end{aligned} \tag{3.10}$$

setting the determinant of $S_{i3} = 0, i = 1, 3$ for C_1 and C_3 to be zero results in famous Rayleigh wave equation with phase velocity $c = \omega/k$

$$4pq - k \left(2 - \frac{\alpha^2}{\beta^2} \right) = 0 \tag{3.11}$$

with

$$C_3 = -\frac{2pq}{q+k^2} C_1 \tag{3.13}$$

by putting the values of p and q in 3.11 it take the form on the simplification as

$$4 \sqrt{1 - \frac{c^2}{\beta^2}} \sqrt{1 - \frac{c^2}{\alpha^2}} - \left(2 - \frac{c^2}{\beta^2} \right)^2 = 0 \tag{3.14}$$

The simple formula derived by Malischewsky et al (2004, 2008) for the H/V at homogeneous half-space is given as

$$\frac{H}{V} = \frac{U_1(0)}{U_3(0)} = 2 \frac{\sqrt{1 - \frac{c^2}{\beta^2}}}{2 - \frac{c^2}{\beta^2}} \tag{3.15}$$

The ratio of displacement (ellipticity) 3.15 as function of Poisson ratio is given as

$$\frac{H}{V}(\nu) = \frac{\sqrt{1 - 2g_4(\nu)}}{1 - g_4(\nu)} \tag{3.16}$$

the function of $g_4(\nu)$ is defined as

$$g_4(\nu) = \frac{1}{3} \left[4 + \frac{2(1-3\bar{\nu})}{\sqrt[3]{g_3(\nu)}} - \sqrt[3]{g_3(\nu)} \right] \quad (3.17)$$

$$g_3(\nu) = 17 + \sqrt[3]{33 - 24\bar{\nu}^3 + \frac{321}{4}\bar{\nu}^2 - 93\bar{\nu} - \frac{45}{2}\bar{\nu}} \quad (3.18)$$

$$\bar{\nu} = 1 - \frac{\nu}{1-\nu} \quad (3.19)$$

The shape of $\frac{H}{V}(\nu)$ (3.16) as function of Poisson ratio (0 to 0.5) on the surface of the half-space, given in Fig.3.1.

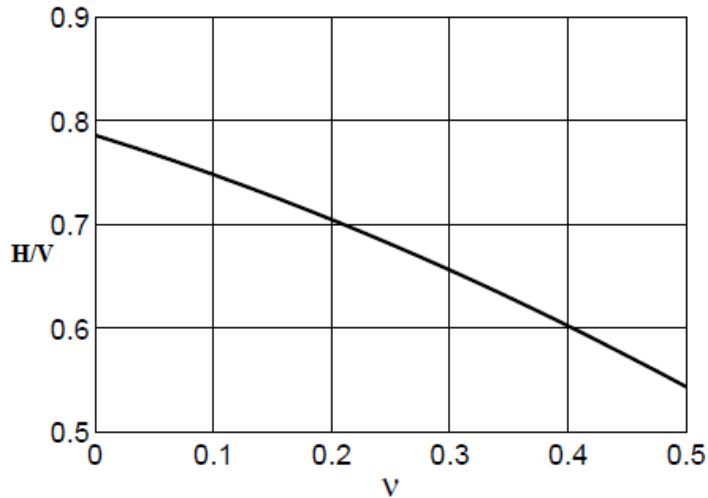


Fig.3. 1 H/V-ratio of Rayleigh waves as a function of Poisson's ratio (modified from Malischewsky et al., 2004).

shows that the H/V ratio is positive for all range of Poisson ratio and have no clear peak over homogeneous half space. Similarly, the expression of the H/V for a layer over the half space is derived by the Malischewsky et al. (2004 & 2008). The derivation detail of the formula of H/V, in the case of a layer over half-space, is lengthy and algebraically complicated, and can be found in Malischewsky et al. (2004, 2006, 2008). The expression for the final formula of a layer with thickness d characterized by the properties such as P-wave velocity, S-wave velocity, density of mass and Poisson ratio $\alpha_1, \beta_1, \rho_1, \nu_1$ for layer and $\alpha_2, \beta_2, \rho_2, \nu_2$ for half space, is given as

$$\frac{H}{V} = \left(1 - \frac{c^2}{2\beta_1^2}\right) \times \frac{1}{\sqrt{1-c^2/\alpha_1^2}} \times \frac{1+y\tanh(dp_1)}{y+\tanh(dp_1)} \quad (3.20)$$

where the different term appearing in 3.20 are given below as

$$y = \frac{g_1 \cosh(dq_1) + g_2 \sinh(dp_1) + g_3 \sinh(dq_1)}{g_4 \cosh(dp_1) + g_5 \sinh(dq_1) + g_6 \sinh(dq_1)}$$

$$g_1 = p_2 q_1 k^2 (m_2 m_4 + 2f_1 m_1 m_3)$$

$$g_2 = -2k^2 p_1 q_1 (m_1 m_2 - 2m_3 p_2 q_2 \delta_\mu)$$

$$g_3 = k^2 (m_2 m_5 - 2f_1 p_2 q_2 m_3^2)$$

$$g_4 = 2k^2 p_1 q_1 (m_1 m_2 - 2m_3 p_2 q_2 \delta_\mu)$$

$$g_5 = -2k^2 p_1 q_1 (f_1 m_1^2 + m_4 p_2 q_2 \delta_\mu)$$

$$g_6 = 2k^2 p_1 q_2 (f_1 m_1 m_3 - m_5 \delta_\mu)$$

$$\delta_\mu = \rho_1 \beta_1^2 - \rho_2 \beta_2^2, \delta_\rho = \rho_1 - \rho_2$$

$$p_1 = \sqrt{k^2 - \omega^2 / \alpha_1^2}, p_2 = \sqrt{k^2 - \omega^2 / \alpha_2^2}$$

$$q_1 = \sqrt{k^2 - \omega^2 / \beta_1^2}, q_2 = \sqrt{k^2 - \omega^2 / \beta_2^2}$$

$$m_1 = 2k^2 \delta_\mu + \omega^2 \rho_2$$

$$m_2 = 2k^2 \delta_\mu + \omega^2 \delta_\rho$$

$$m_3 = 2k^2 \delta_\mu - \omega^2 \rho_1$$

$$m_4 = -4k^2 \delta_\mu + \omega^2 (\rho_1 - \rho_2) \frac{\beta_2^2}{\beta_1^2}$$

$$m_5 = 4k^4 \delta_\mu + \frac{\omega^4 \delta_\rho}{\rho_1} + 2k^2 \omega^2 \delta_\mu (\rho_2 \left(\frac{\beta_2^2}{\beta_1^2} + 1 \right) - 2\rho_1).$$

The shape of the H/V formula (Eq. 3.20) for a model of one layer over a half-space (Fig 3.3) is given in Fig.3.2 as function of dimensionless constant $d/\lambda\beta$, where λ is the wavelength of the shear wave velocity in layer of thickness d . The result of a layer over half-space (Fig.2.2) shows that the shape of ratio of the displacement eigenfunction at surface ($x_3=0$) has a peak following by a trough. This is the first formal formulation solved from the wave equation to model the H/V spectral curve.

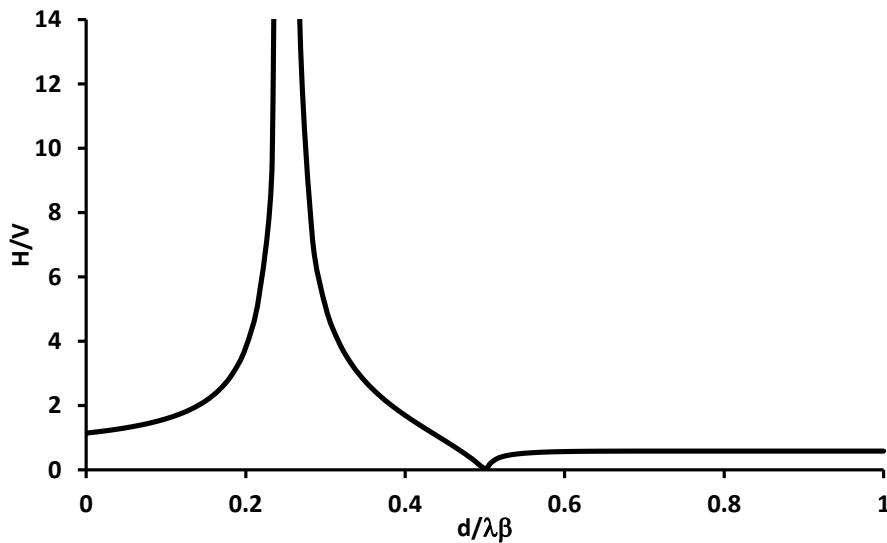


Fig.3. 2 Shows the shape of H/V (Eq.2.20) for a layer over the half-space (with v_s contrast 6) for a model taken from Malischewsky et al. (2004) shown in Fig 3.3.

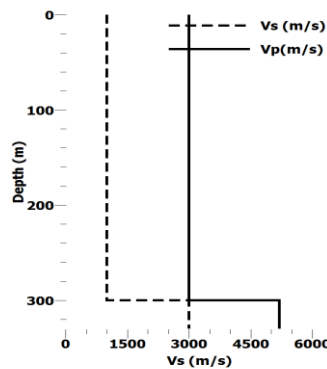


Fig.3. 3 Shows the V_s and V_p profiles of the model used to produced Fig.3.2 from Eq.3.20. (taken from Malischewsky et al., 2004).

3.3 The experimental procedure for the H/V measurement

The experimental procedure for the H/V curve analysis is quite simple. As discussed above, a three-component sensor is used to record the seismic ambient noise placed on the surface of the Earth at an investigated site. The type of sensor generally recommended is a short period sensor, as broadband sensor requires a large time for stabilization prior to the effective recording. The accelerometer is not recommended for the noise measurement as its response below 1 Hz is very unstable. If the investigated site has an expected frequency lower than the natural frequency of the short period sensor, the result might not be reliable. In such cases, a sensor with lower natural frequency is recommended for the larger duration. The recommendations for the experimental recording and processing procedure were firstly suggested by Mucciarelli (1998) and Bard (1999), later SESAME (Site EffectS assessment using AMbient Excitations 2004) refined the recording and processing protocol in a comprehensive way. Similarly, another reliability classification scheme was developed later by Albarello et al. (2011) to quality check the recorded noise data. This new classification includes some additional recommendations to that proposed by the SESAME. The data recorded with the three-component sensor is processed initially such as

1. Offset removal-means that the whole signal is deducted from the each sample;
2. The signal is divided into a number of windows (n windows), whose length is chosen such that the window must have 10 significant cycles for the frequency of interest $f_0 > \frac{10}{L_w}$, f_0 is the expected fundamental frequency of the site, L_w is the length of time window in seconds. The stable portion of the signal is chosen with the help of short time average (STA) and long time average (LTA), this helps to avoid choosing the transient portion of the signal. The following steps of the process are applied to the selected windows, as recommended by SESAME 2004:
 - (a) for all the components Vertical, North-South and East-West, a cosine taper of 5% is applied at each end of the window;
 - (b) FFT is performed for each window of all the three components and the spectral amplitudes are estimated at each frequency (0.2 to 20 Hz);
 - (c) the spectral of each component are smoothed by the Kohno and Ohmachi (1998) smoothing function of bandwidth 30;

(d) both the horizontal components (NS and EW) are averaged by quadratic, which means

$$\mathbf{H}(\omega) = \sqrt{\frac{(\mathbf{P}(\omega)_{NS})^2 + (\mathbf{P}(\omega)_{EW})^2}{2}} \quad (3.21)$$

(e) the merged horizontal component is divided by the vertical component for each frequency to obtain the H/V ratio amplitude. The H/V ratio amplitude is plotted as a function of frequency as shown in Fig 3.4 (Note: a sufficient number of windows are required for the good statistical control for all the process steps from (a) to (e). In each of the n windows the log of ratio of spectral amplitudes for merged horizontal and vertical is obtained as function of frequency);

3. The mean H/V ratio is obtained from all the windows selected by

$$\mathbf{H}/\mathbf{V}_{Avg} = \frac{\sum \log_{10}(\mathbf{H}/\mathbf{V})}{n(\text{windows})} \quad (3.22)$$

(Average standard deviation is estimated by the relation)

$$\sigma_{\mathbf{H}/\mathbf{V}} = \sqrt{\frac{\sum \log_{10}^2(\mathbf{H}/\mathbf{V}) - n(\text{windows}) \times \log_{10}^2(\mathbf{H}/\mathbf{V})_{Avg}}{n(\text{windows}) - 1}} \quad (3.23)$$

After this initial processing, a statistical analysis is performed to check the reliability of the H/V curve and peak clarity condition as suggested by SESAME (2004). The reliability criteria for the H/V curve were found (Fig 3.4e) which shows that whether the curve obtained with the analyzed recorded noise is the true representative of the site and another seismic noise record at the site will result in the same curve or not. By satisfying SESAME (2004) reliability conditions for H/V curve, the next stage is to pick the peak of it. It is essential to remember that the most important application of the H/V curve is its correct peak identification which corresponds to the shear wave resonance frequency for higher velocity contrast between soil and bedrock. Therefore, it is of great interest to pick the correct peak of the H/V curve. In most of the cases, when a high-velocity contrast exists at the subsurface, the picking of the peak frequency is quite easy and straightforward. However, sometimes there exists two velocity contrasts or an increasing gradient of velocity from the surface to the rock for which the H/V results in two or a broad peak, respectively. Therefore, to pick the peak of H/V curve, which should be closer to the shear resonance frequency, is quite tricky in both cases. Consequently, some criteria to clarify the peak are suggested to ensure the picking of the correct peak (Fig 3.4f, SESAME, 2004). The terms appearing in Fig.3.4e-f are given in Table 3.1 with its short definition. With the help of these criteria for the curve and peak, the margin of mistake of picking a wrong peak is very little.

To obtain the H/V curve, the Geopsy free package is a good tool, however the problem with Geopsy is that the SESAME (2004) criteria are not implemented there yet. For this purpose, we

analyzed our recorded noise data with Matlab, where the conditions for the reliability of the curve and peak can be easily implemented.

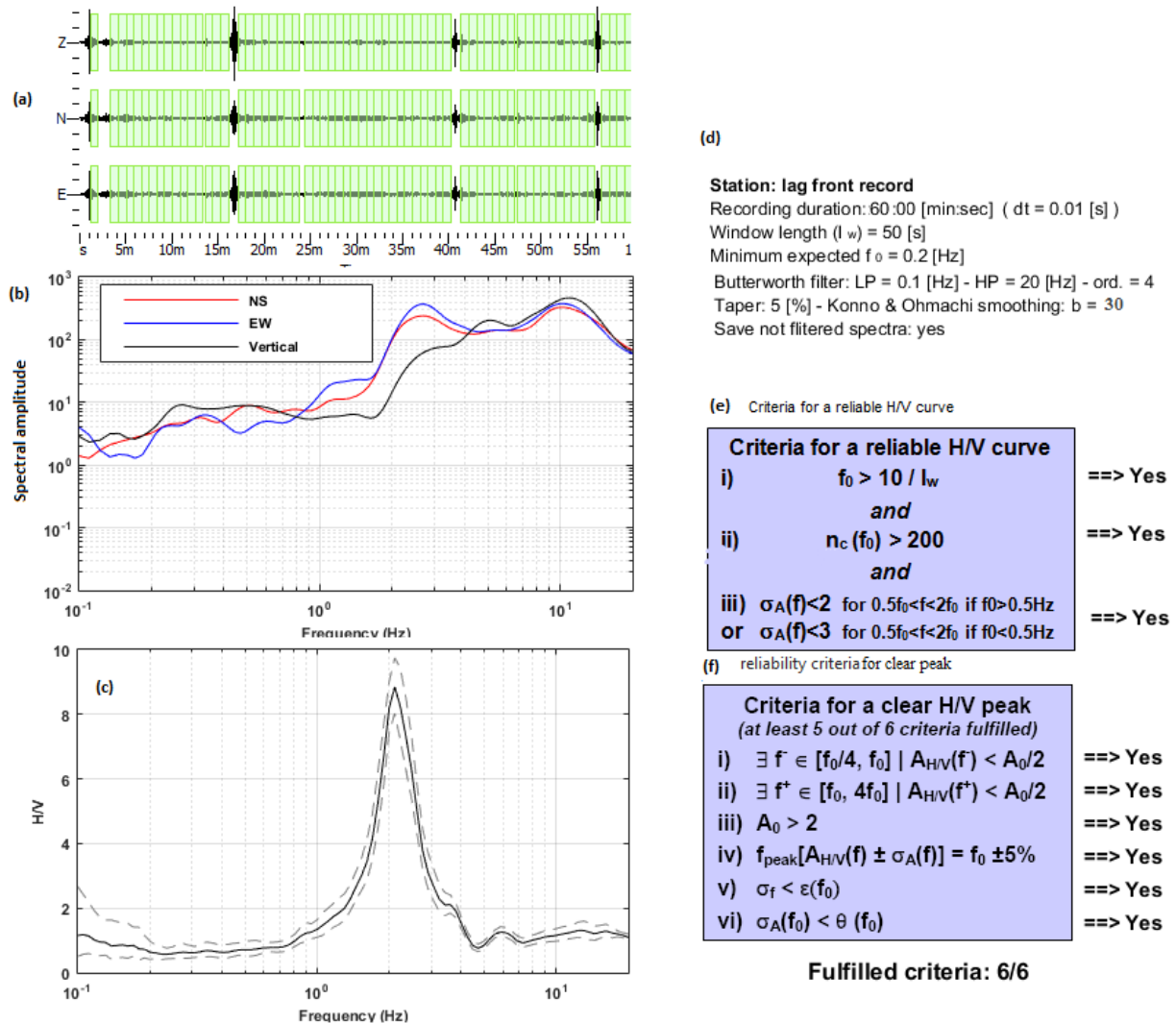


Fig.3. 4 Shows one-hour seismic ambient noise record at IAG site: (a) shows the windows (each of 50 sec) selected for the H/V analysis; (b) shows the smoothed spectral amplitude of all the three components; (c) the average H/V curves of all the 64 windows (upper lower limit indicates the 95% confidence interval around mean H/V curve values); (e-f) show the criteria of reliable H/V curve and reliability of clear peak, SESAME 2004.

<ul style="list-style-type: none"> ➤ n_w = number of windows selected for the average H/V curve ➤ $n_c = l_w \cdot n_w$. f_0 = number of significant cycles ➤ f = current frequency ➤ f_0 = H/V peak frequency ➤ σ_f = standard deviation of H/V peak frequency ($f_0 \pm \sigma_f$) ➤ $\varepsilon(f_0)$ = threshold value for the stability condition $\sigma_f < \varepsilon(f_0)$ ➤ A_0 = H/V peak amplitude at frequency f_0 ➤ $A_{H/V}(f)$ = H/V curve amplitude at frequency f ➤ f^- = frequency between $f_0/4$ and f_0 for which $A_{H/V}(f^-) < A_0/2$ ➤ f^+ = frequency between f_0 and $4f_0$ for which $A_{H/V}(f^+) < A_0/2$ ➤ $\sigma_A(f)$ = standard deviation of $A_{H/V}(f)$, $\sigma_A(f)$ is factor by which the mean $A_{H/V}(f)$ curve should be multiplied or divided ➤ $\theta(f_0)$ = threshold value for the stability condition $\sigma_A(f) < \theta(f_0)$

Table.3. 1 The definition of terms appeared in Fig.3.4 (e-f) (SESAME 2004).

Frequency range [Hz]	< 0.2	0.2 – 0.5	0.5 – 1.0	1.0 – 2.0	> 2.0
$\varepsilon(f_0)$ [Hz]	0.25 f_0	0.20 f_0	0.15 f_0	0.10 f_0	0.05 f_0
$\theta(f_0)$ for $\sigma_A(f_0)$	3.0	2.5	2.0	1.78	1.58

Table.3. 2 : Shows the threshold values for stability conditions.

As we will use the H/V curve, later, in this thesis for the inversion process, some additional criteria are implemented along with ones suggested by the SESAME (2004) for more robust H/V curve results. Albarello et al., (2011) defined the quality of seismic noise recorded data and the H/V curve in terms of three different classes, as: class A, trustworthy and interpretable H/V curve, it represents a reference measurement that can be considered by itself for the site of concern; class B, ambiguous H/V curve, that should be used with caution and in case of coherency with other measurements performed nearby; class C, poor quality H/V curve (hardly interpretable), to be discarded. The criteria used to classify measurements of class A are:

1. The duration of the noise record: the duration of the analyzed record should be more than 15 minutes (we choose 1 hour in our case, Fig. 3.4 (a))
2. The removal of artifact: the manmade disturbances (e.g. electromagnetic noise or peaks of industrial origin) could be recognized in the Fourier spectra as monochromatic disturbances such as the increase of spectral amplitude of all components;
3. Stationarity of H/V with time: the data should show a persistent shape for at least 30% of the duration of the record, Fig. 3.5.

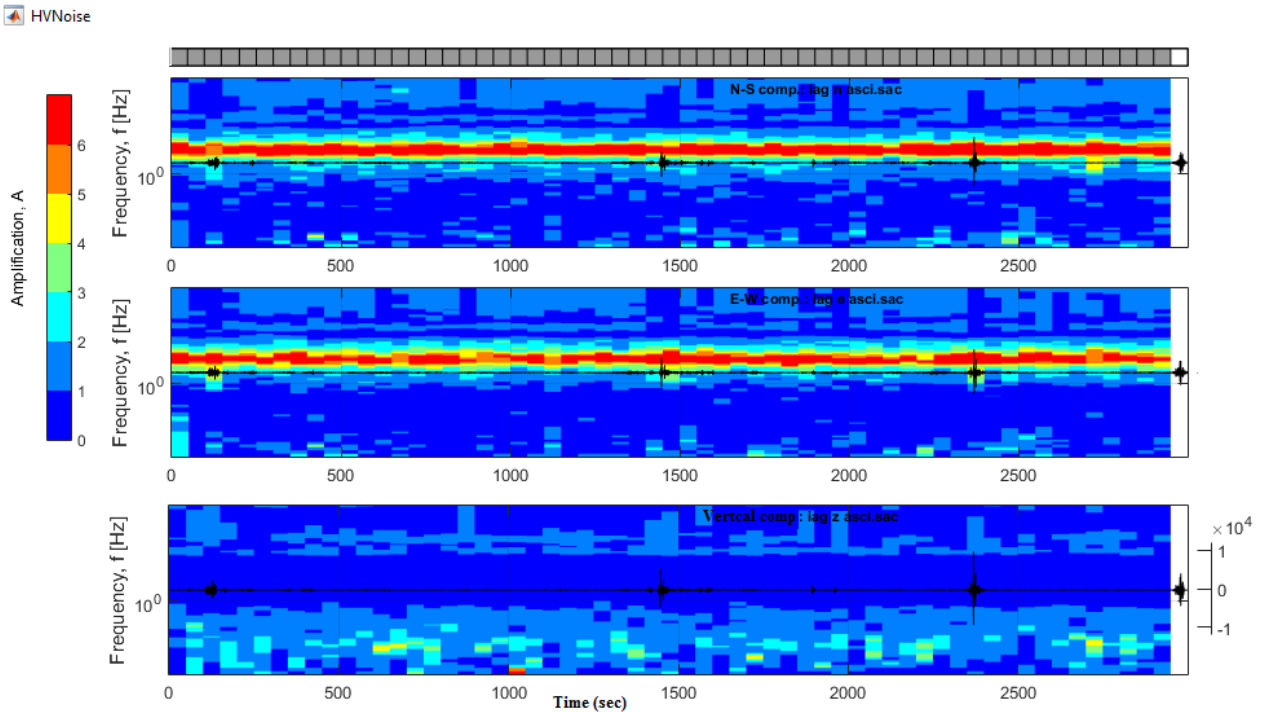


Fig.3. 5 Shows the spectrogram of the three component, both the horizontal components show stationarity at 2 Hz for all the seismic noise record.

4. The statistical robustness: SESAME (2004) criteria “for a reliable H/V curve and peak” should be fulfilled, Fig. 3.4(e-f).

A measurement belongs to class B if one or more of the previous conditions are not fulfilled. Class B measurements degrade to class C if: a rising drift exists from low to high frequencies that indicate a tilting of the instrument.

A new aspect of the H/V curve method, but not analyzed in detail, is to find the directivity effect of the H/V curve. The directivity effect of the H/V is trying to evaluate its links either with the subsurface geology or with the arrangement of local seismic noise sources. For this analysis the seismic noise recorded at the IAG and IGC sites were analyzed. The horizontal (east-west and north-south) components of the seismic noise are rotated, merged and its ratio is found with the vertical component. The amplitude of the H/V along with azimuth $0^{\circ} - 180^{\circ}$ is found. The H/V amplitude with azimuth $180^{\circ} - 360^{\circ}$ is similar because of the symmetry. The amplitude of the H/V between $65^{\circ} - 120^{\circ}$ decreased, which shows the less energetic arrival of seismic energy from this azimuth. However, a river and heavy traffic road presence, on both sides of the river, in the same azimuth suggest that the arriving seismic energy from this azimuth should be higher, which is not the case (Fig.3.6, page 30). To observe the direction of this low-energetic seismic noise sources distribution ($65^{\circ} - 120^{\circ}$) we map the locations where the noise recording are made along with its surrounding. It is shown in Fig.3.7.

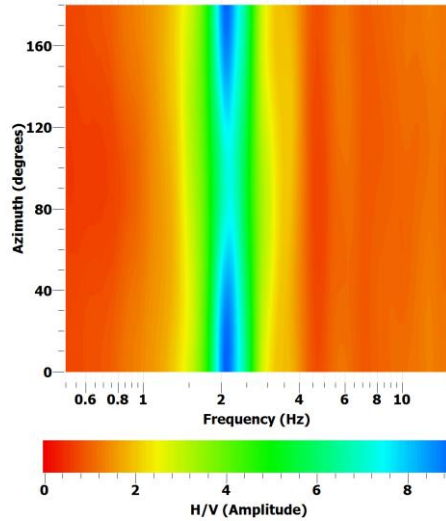


Fig.3. 6 Shows the spectrogram of the three component, both the horizontal components show stationarity at 2 Hz for all the seismic noise record.

We found no such clear source of noise generation in this predominant direction as most of urbanized part of the city surrounding the recording sites is almost equally (Fig 3.7). We believe this directivity is related to some subsurface characteristics rather than the distribution of noise sources around the recording sites. This will be investigated, later, in detail, for now, we compared the results of the two recording sites which are made in close proximity and tried to link the directivity effects for both sites for the whole length of its noise recording (Fig. 3.8 & Fig 3.9), which shows a similar trend.

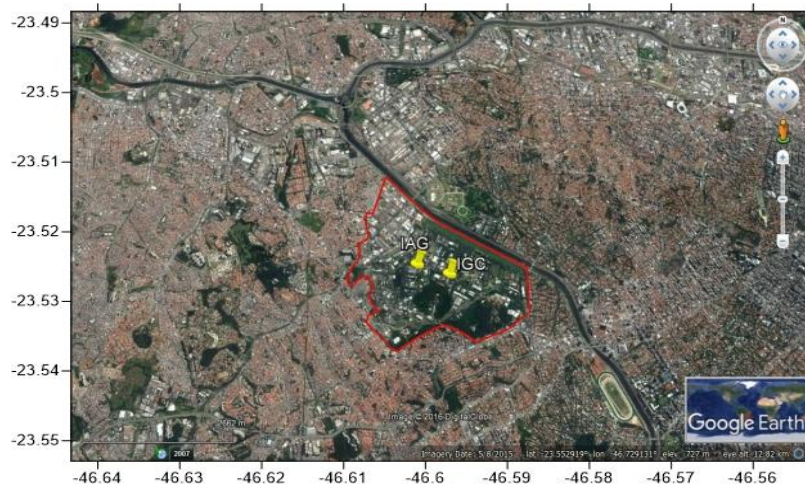


Fig.3. 7 Shows the arrangement of urbanization around the recording (taken from Google earth. Imagery date April 2015. Access at March 2017)

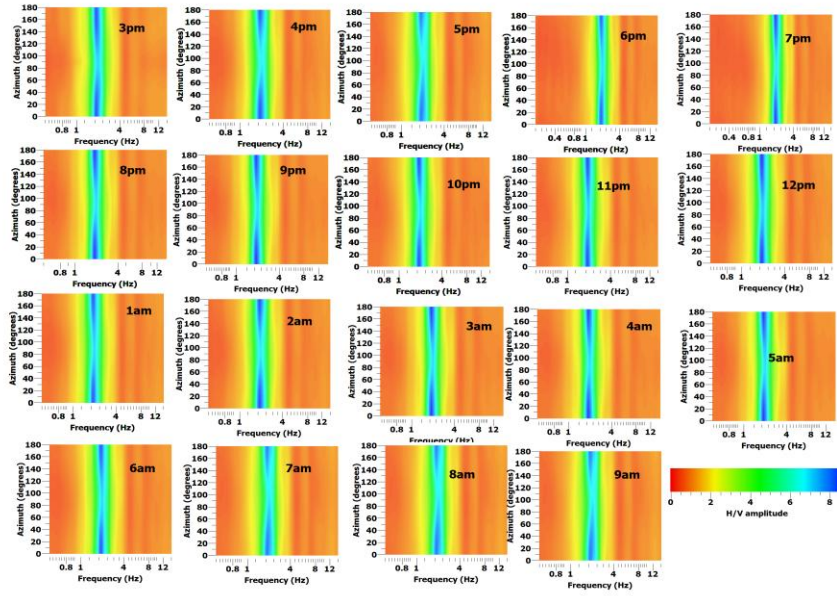


Fig.3. 8 Show the directional H/V with azimuth for IAG site for 19 hours of seismic noise record.

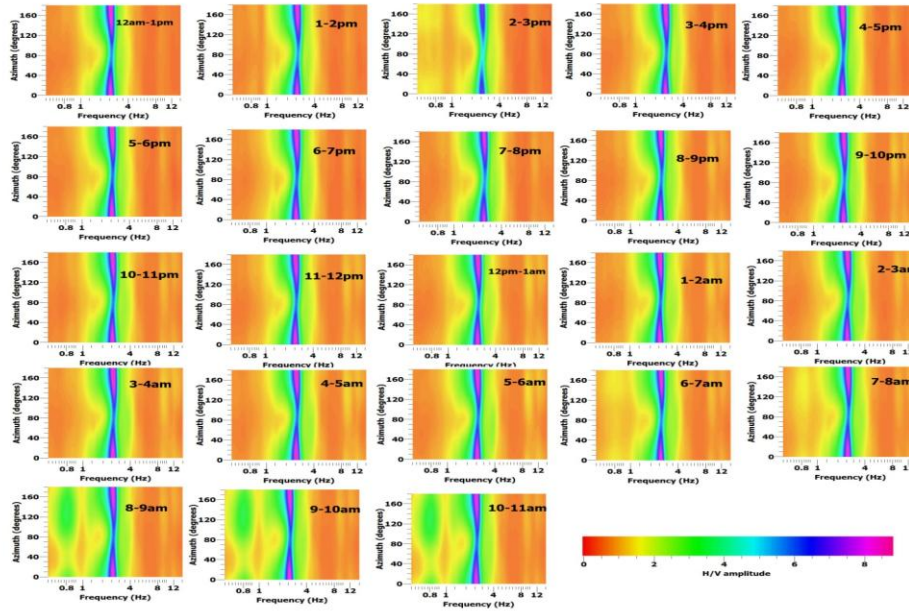


Fig.3. 9 Show the directional H/V with azimuth for IGC site, for 23 hours of seismic noise recording.

Chapter 4: Array technique of active source

4.1 Introduction

As discussed, one of the basic target in many earthquakes and civil engineering projects is to find the stiffness of the soil layer. Actually, there are two approaches to measuring these properties, one in the laboratory and the other in the field. The laboratory approach is to study the soil sample effect on different parameters of variation in a controlled environment (Kramer, 1996). The in situ (field) measurement has the benefit of studying the soil properties in its natural undisturbed state. Another advantage of in situ measurement is that a large area can be covered by this analysis. For the stiffness measurement in the field, many methods are employed. Among of these methods, the best one is the drilling method (downhole logging). Also, there are some methods which are used to estimate the stiffness of the soil regarding to the penetration resistance, such as cone penetration test (CPT) and standard penetration test (SPT). These methods provide excellent results; however, they are very expensive and time-consuming. The solution for this time consuming and cost effectiveness is the surface wave analysis. In the surface wave method, the earth is considered as a layered medium for which the shear wave velocity profile is obtained as a function of depth. The stiffness of a layer can be found from the shear wave velocity of the layer. The stiffness and shear wave velocity are directly related (Kramer, 1996). Rayleigh and Love waves are used to obtain the dispersion curve, which later are inverted to deduce the shear wave velocity profile of the soil. We will try to focus our attention on the surface wave analysis method used for the dispersion curve retrieval from the Rayleigh wave, and latter jointly, we will latter invert this phase velocity dispersion curve with Rayleigh ellipticity curve.

Rayleigh waves are dispersive in inelastic, isotropic and vertically heterogeneous material. The dispersion curve obtained for the Rayleigh waves provides information regarding the shear wave velocity, which in turn, it can be used for the stiffness measurement. Rayleigh wave's dispersion curve is a function of frequency, which means that different frequencies travel with different phase velocities. Rayleigh waves phase velocity is a complicated function of the shear wave velocity V_s , thickness h , primary wave velocity V_p and density ρ of soil layers. There are many methods used to retrieve Rayleigh wave's dispersion curve. Among these, the most popular for the active source case are SASW (spectral analysis of surface waves) and MASW (multi-channel analysis of surface waves) (Park et al., 1999). The MASW is widely used for the shear wave velocity estimation of a site for geophysical and engineering projects (Xia 2014). Xia et al. (2002) showed that the deviation between borehole and MASW result is only 15%. We will discuss the MASW method in detail but, before that, let's focus on some related features of Rayleigh waves.

Rayleigh waves are made from the interaction of P and Sv waves along the surface of the Earth (the interface between two media). The particle motion induced by Rayleigh waves has two components, horizontal and vertical. This interaction of vertical and horizontal components produce particle motion retrograde (anticlockwise) or prograde (clockwise), depending on the theoretical phase shift ($\pm\frac{\pi}{2}$) between the two respective components. The particle motion induced by Rayleigh waves varies with depth. Being retrograde at the surface and become prograde at greater depth. The Rayleigh waves are non-dispersive in homogeneous half space, however, they are dispersive in vertically heterogeneous materials (by dispersion it means, waves with different wavelengths travel with different velocities). A vibrating seismic source at the surface of a homogeneous elastic half-space produced, the energy whose 67% of its fraction is imparted to Rayleigh waves, 26% to S-waves and 7% to P-waves (Wood, 1968). When the waves travel away from the seismic source as a hemispherical wavefront, it encounters a larger area of material, the amplitude of the waves decrease, which is known as geometrical spreading or geometrical damping. The amplitude of Rayleigh waves decreases in elastic and homogeneous half space as $r^{-0.5}$, where r is the distance from the source. The body waves amplitude decrease in respective situation as r^{-2} along the surface and r^{-1} in the medium. As Rayleigh decay slower in comparison to body waves and 67% of energy is imparted to Rayleigh waves, the wave field is dominated by Rayleigh waves at very short distances from the impact source (Richard et al., 1970). The Rayleigh waves phase velocity curve (dispersion) are multimodal, which means that, each frequency component might have different propagation velocity. The curve with low phase velocity for all frequency components is known as the fundamental mode curve, while the rest all are termed as higher modes. Higher mode exists above a certain frequency. The two most commonly active source surface wave dispersion curve method used will be discussed here; both methods have the advantage that they can be easily employable in the urbanized environment.

4.2 SASW (Spectral Analysis of Surface Waves)

SASW was introduced in 1980 ((Heisey et al., 1982)) for the surface wave spectral analysis and Rayleigh wave dispersion retrieval. For the generation of seismic wave, an impulsive source is used, and the propagated waves are recorded with two, or in some cases, 12 geophones. To obtain the dispersion curve on the wide frequency range, impulsive sources of different impacts (hammer, weight drop) are used at various distances from the first geophone (sensor), with the purpose to excite waves of different frequency contents.

Data recorded by geophones are processed in the frequency domain for Rayleigh wave velocity retrieval. The schematic diagram describing the overall procedure of the SASW method is shown in Fig.4.1. Two sensors time series, i and k, are taken at a time. The source and first receiver distance, x_i , are kept equal to the distance between two receivers (x_k). Both of the sensors time series are transformed into frequency domain to calculate the corresponding spectral density, $P_{ik}(f)$, which gives the power of the signal as function of frequency.

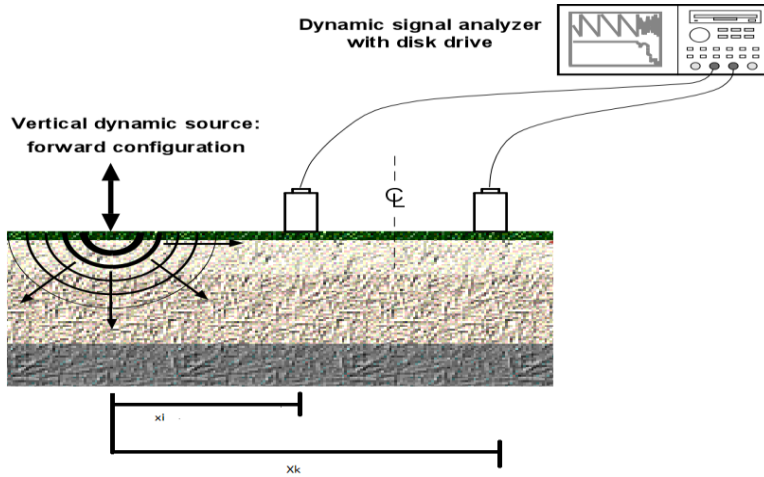


Fig.4. 1 The schematic describing the overall procedure of the SASW method.

To estimate the connection between two-time series as a function of frequency, the cross spectral density distribution is found out through Eq.4.1 as

$$P_{ik}(f) = M_{ik}(f)e^{i\vartheta_{ik}(f)} \quad (4.1)$$

where $M_{ik}(f)$ and $\vartheta_{ik}(f)$ are the magnitude spectrum and the phase spectrum of the cross spectral density, respectively, and $i = \sqrt{-1}$. The time taken by the Rayleigh waves to travel between the two sensors (geophones) is given by

$$t_{ik}(f) = \frac{\vartheta_{ik}(f)}{2\pi f} \quad (4.2)$$

where $t_{ik}(f)$ is the time taken through distance $x_k - x_i$ by the frequency component (f) of the Rayleigh waves. The Rayleigh waves phase velocity and wavelength at frequency (f) can be found out through equation 4.3 and 4.4 as

$$c_{ik}(f) = \frac{x_k - x_i}{t_{ik}(f)} \quad (4.3)$$

$$\lambda_{ik}(f) = \frac{c_{ik}(f)}{f} \quad (4.4)$$

This process is repeated with different impact sources and sensors distances $x_k - x_i$ and also for different source-receiver distances x_i . Later, the dispersion curve of the Rayleigh waves is obtained. Rayleigh wave phase velocity curve upper and lower bounds are found out using standard deviation for each frequency component, which is later used for inversion to retrieve shear wave velocity as a function of depth.

Spectral analysis of surface waves (SASW) are repeated for different receiver of pairs of distances in order to manually examine the quality of the result, so it is very time-consuming. Another error, which is often made during the SASW analysis, is the misidentification of surface

wave signal from noise (body wave or higher mode). If a noise (body waves) is taken as surface wave signal, it will compromise the quality of dispersion curve and also, the shear wave velocity (Park et al., 1999).

4.3 MASW (Multichannel Analysis of Surface Waves)

Multichannel Analysis of Surface Waves (MASW) was introduced by Park et al (1999). Like most of the geophysical methods, the MASW method can be divided into three steps: data acquisition, data processing, and inversion analysis. A brief description of each step will be given here, followed by the advantages of this method over the other surface wave method. The main procedures of the MASW are given in the schematic diagram shown in Fig.4.2.

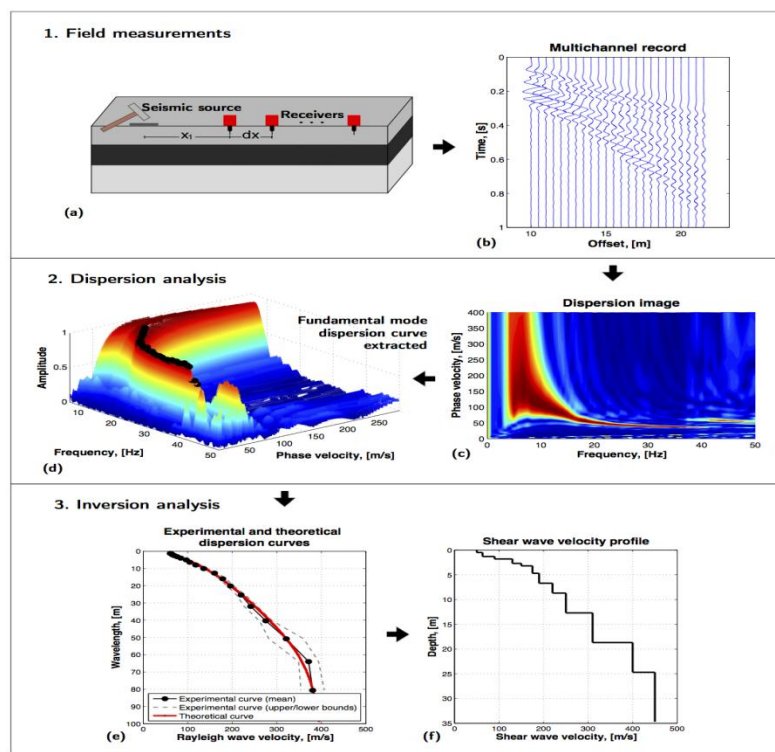


Fig.4. 2 A overview of the MASW method: (a) Geophones are lined up on the surface of the test site. A wave is generated and the wave propagation is recorded; (b) A dispersion image (c) is obtained from the recorded surface wave data. The high amplitude bands display the dispersion characteristics and is used to construct the fundamental mode dispersion curve (d). A theoretical dispersion curve is obtained based on assumed layer thicknesses and material parameters for each layer and compared to the experimental dispersion curve (e). The shear wave velocity profile and the layer structure that result in the best fit are taken as the result of the survey (f) (taken from Ólafsdóttir, 2016).

4.3.1 MASW data acquisition procedure

To acquire the MASW data, a set of 12, 24, 48 or even 96 geophones are usually used (Donohue, 2013). The geophones are vertically coupled to the ground on a line with equal geophone spacing

dx. All the geophones are connected to a separate channel and the whole system is analysed by a field computer, which has a data recording quality control software. Seismic waves are generated by an impact source at one end of the geophones array. The recorded data consist of time or time-offset histories in discrete form. The data (wave field) recorded is expressed as $u(x,t)$, where x is the distance from the source to a geophone and t is the time. The record $u(x,t)$ is digitized at a sampling interval dt , corresponding to sampling frequency f_s , which is the number of data points recorded in unit time. The usual sampling interval used for active MASW is 1 ms, which corresponds to a sampling frequency of 1000 Hertz. The sampling frequency in terms of angular frequency is defined as $\omega_s = 2\pi f_s$. The record length of one second is enough for MASW impact source (Park 2015). In case of using a vibrating seismic source (vibrator) a longer recording time (2 s) is required (Park 1999).

The maximum depth (Z_{max}) to which the MASW survey gives a reliable measure of shear wave depends on the characteristics of the site, sensors threshold frequency f_c and impact source type. A general rule of thumb for the depth of investigation is related with longest wavelength recorded during acquisition (Park & Carnevale, 2010).

$$Z_{max} = 0.5\lambda_{max} \quad (4.5)$$

The effects of the sensors used during the acquisition are not thoroughly investigated yet. Park and Miller (2002) pointed out that geophone sensors with threshold frequency f_c 10 and 40 Hz can be used to record the surface wave field up to 5 and 10 Hz. Xia (2009) noted that to retrieve shear wave velocity up to 30-50 m depth, the geophones with f_c 4.5 Hz are good choices. Another important aspect of data acquisition is the choice of the source to generate seismic waves. The most commonly used impact source for seismic wave generation is sledgehammer of 5 to 10 kg (Park, 2007). Another important seismic generating source for MASW is weight drop in which a heavy weight is drop from a crane. The source which can produce high impact on ground is capable of producing surface wave of low frequency (long-wavelength) and hence facilitate a deeper investigation. The use of a base plate (metallic or firm rubber) for hammer impact point helps in generating low frequency surface waves (Park, 2015). To overview the MASW setup parameter for the data acquisition a literature review was done. Here, the main practicing parameters of data recording such as profile length, receiver spacing and source offset were listed.

4.3.2 Length of the geophones spread

The spread of geophones (L) for data acquisition is connected with the maximum wavelength (λ_{max}) recorded during acquisition, which corresponds to the maximum investigation depth (Z_{max}). The general rule of thumb is the maximum wavelength is equal to the spread array (Park and Carnevale, 2010)

$$Z_{max} \approx L \quad (4.6)$$

The study of Park & Carnevale (2010) has shown that an error of 5% might occur if trying to analyse higher wavelength than the receiver spread $L \leq Z_{max} \leq 2L$. For practice, Park (2015) suggested that the spread of the geophones should lie with $Z_{max} \leq L \leq 3Z_{max}$, and Xia (2009) recommend a spread of $L = 2Z_{max}$. The seismic waves generated for the data acquisition in MASW by impact survey sources will attenuate below the detectable signal level until to the end of the large spread geophones, that's the reason why very long receiver spreads are avoided during the acquisition

4.3.3 Receiver spacing and source offset

The space between two receivers (dx) is associated with minimum wavelength (λ_{min}) which can be included in the Rayleigh wave phase velocity curve (dispersion curve). Xia (2009) pointed out that to avoid spatial aliasing the minimum wavelength should not be larger than $dx \leq \frac{1}{2} \lambda_{min}$. Another important aspect about the receiver spacing is regarding to the thickness of the topmost layer. Receiver spacing acts as a control parameter for the minimum thickness of layer which can be retrieved during the inversion: $h_1 \geq h_{min} \approx dx$, where h_1 is the thickness of top soil layer (Park et al., 1999; Xia et al., 2009).

There are two important features which are directly associated with source offset, near-field effect and far-field effect. The near field-effect situation occurs when the offset of the source (x) is not large enough to produce planar surface waves. To avoid the near-field effect, the source offset (x) should be in accordance with the maximum wavelength expected to be recorded in the acquisition. Generally, planar surface wave arrival occurs at the nearest receiver when the source offset is greater than half of the maximum wavelength λ_{max} (i.e, $x \geq 0.5L$ where x is the source offset). Far-field effect is the situation when attenuation of high-frequency components of waves travelling along the free surface causes body waves to dominate the wave field (Park and Shawver, 2009). The minimum (x_{min}) and maximum (x_{max}) source offsets for use in practice have been suggested (Park,2015)

$$x_{min} = 0.2 L \text{ and } x_{max} = L \quad (4.7)$$

The measurement profile setup parameters discussed in preceding sections are summarized in Table 4.1. The length of the receiver spread (L) and the length of the source offset (x) are given within a range, as indicated Table 4.1. The receiver spacing (dx) is calculated by assuming that N=24 receivers are used for data acquisition. The possible effects of surface wave attenuation, i.e., due to the length of the receiver spread or the length of the source offset, are not specifically considered in the Table 4.1.

Depth	Maximum wavelength	Receivers spread	Source offset	Receiver interval
z_{\max} [m]	λ_{\max} (m)	L (m)	x_1 (m)	dx (m)
5	10	5-15	1-15	0.4
10	20	10-30	2-30	0.9
20	40	20-60	4-60	1.7
30	60	30-90	6-90	2.6

Table.4. 1 Summary of the acquisition parameter (more detailed parameter setup for 24 and 48 geophones for various depth can be found on www.masw.com).

4.3.4 The effect of topography on MASW acquisition

The natural layout of the Earth's surface is termed as topography. Topography has an effect on the quality of the acquired surface wave data and therefore, on the quality of retrieved dispersion curve. The terrain on which the acquisition are made should be flat for the optimum results; within the receiver spread, the surface relief should be less than $0.1L$ (Park, 2015, Fig.4.3a,b). Zeng et al. (2012) pointed out that the slope of the surface along the receivers spread should be less than 10° . A steeper slope ($\theta \geq 10^\circ$; Fig.4.3d) leads to a significant error, compromising the quality of retrieved dispersion curve.

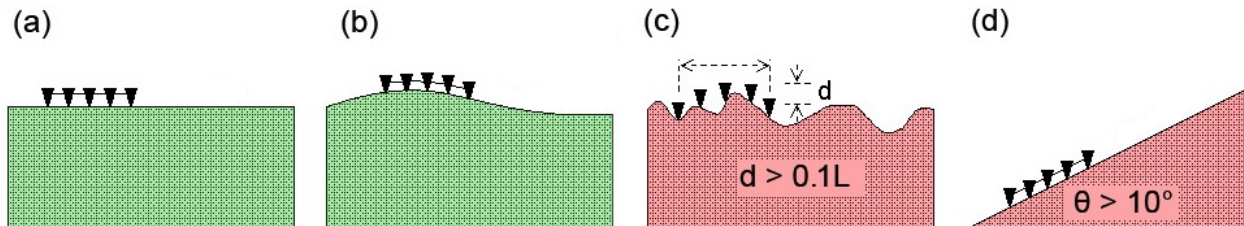


Fig.4. 3 Shows a sketch of receiver profile for acquisition (taken from www.masw.com)

4.4 Dispersion analysis of the acquired data

One of the most crucial steps of the MASW analysis is the retrieval of correct dispersion curve (Park et al., 1998). There are several methods employed for this task (McMechan & Yedlin, 1981; Park et al., 1998, 1999). Here in this section, we discuss the two most commonly used techniques for the dispersion curve retrieval (swept-frequency and phase shift method; Park et al., 1998, 1999).

4.4.1 Swept-frequency technique

Swept-frequency technique was first described by Park et al. (1999). It is used to extract the fundamental mode dispersion curve from the MASW recorded. The procedure of the method is to determine, trace to trace, the time arrival and amplitude coherence of the surface waves recorded.

In such procedure, the Rayleigh waves phase velocity of different frequencies is obtained by the slope of each frequency (Park et al, 1999). A little processing effort is required in swept frequency record to retrieve a dispersion curve from an active source recording (shot gather). The coherence of surface wave motion is used as a tool to neglect the noise source in the data, such as body waves and higher Rayleigh in arrival mode, causing a break in the coherence.

The procedure of swept frequency can be outlined in two-step, like as getting swept frequency record and determining the phase velocity curve from coherency of each frequency component of the record.

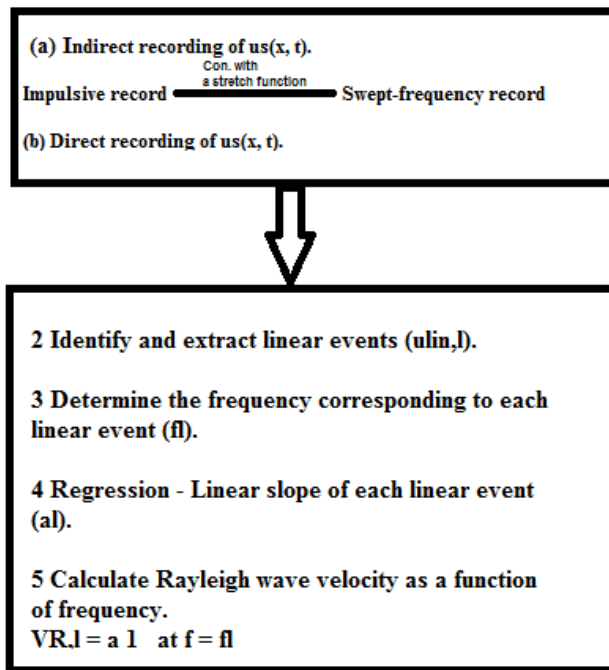


Fig.4. 4 Show the sketch of swept frequency procedure (modified from Ólafsdóttir ,2016).

The sketch of Fig.4.4 can be explained in the follow steps:

1. For n receivers, the indirect recording (impulsive source) and for direct source recording (a vibrating seismic source) a swept frequency record is obtained by transforming by convolution the swept-frequency with a stretch function .The indirect impulsive record are transformed to swept-frequency by the convolution of a stretch function $s(t)$ with the record $u(x, t)$ as

$$\mathbf{u}_s(\mathbf{x}, t) = \mathbf{u}(\mathbf{x}, t) * \mathbf{s}(t) \quad (4.8)$$

This process in Eq.4.8 is performed from trace to trace for total record of n traces such as

$$\mathbf{u}_{s,j}(\mathbf{x}, t) = \mathbf{u}_j(\mathbf{x}, t) * \mathbf{s}(t) \quad (4.9)$$

where $\mathbf{u}_{s,j}(\mathbf{x}, t)$ is swept-frequency for j-th trace; $\mathbf{u}_j(\mathbf{x}, t)$ is the impulsive record for j-th trace; $\mathbf{s}(t)$ stretch function (Eq.4.10 and Fig.4.5) is a function (sinusoidal) of changing frequency (f_1 to f_2) with time (T). Here f_1 and f_2 are the lowest and highest frequencies to be processed while T is the total length of the $\mathbf{s}(t)$.

$$\mathbf{s}(t) = \text{Sin}\left(2\pi f_1 t + \frac{\pi(f_2 - f_1)t^2}{T}\right) \quad (4.10)$$

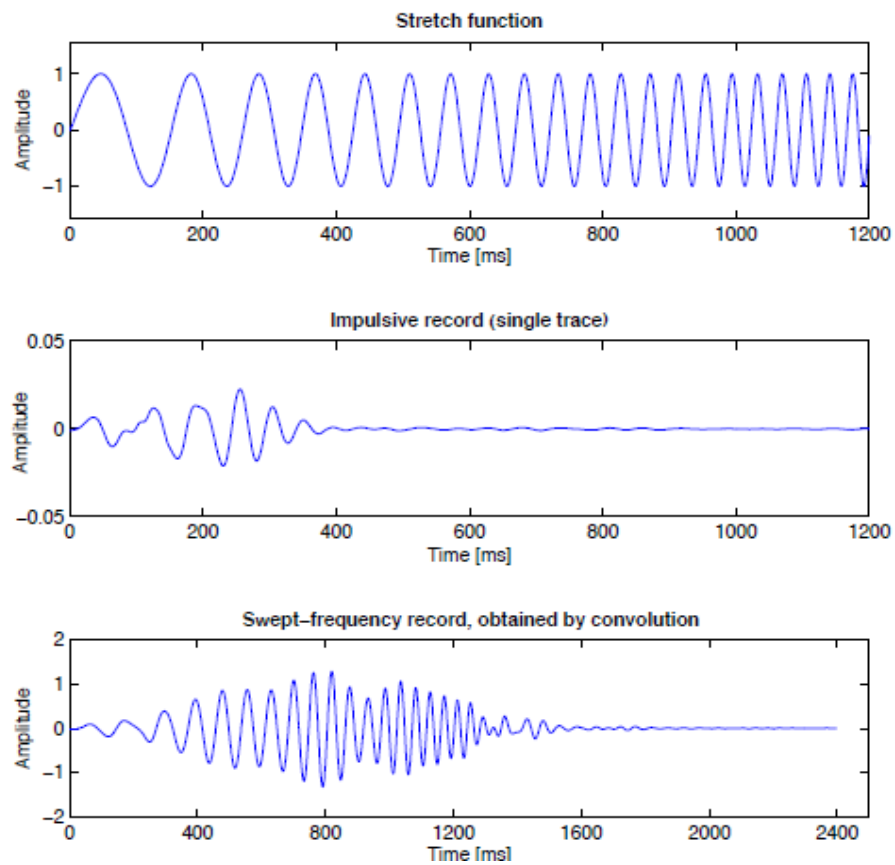


Fig.4. 5 Shows the swept frequency record for a trace of impulsive source (from a short gather) by convolution with stretch function $s(t)$ of changing frequency ($f_1=5$ Hz [,f] $f_2=30$ Hz) (Ólafsdóttir ,2016).

2. In the next step, after swept frequency record is obtained, the determination of trace to trace time arrival and amplitude coherency of the recorded surface waves are analysed on the swept-frequency recorded (Fig.4.6).

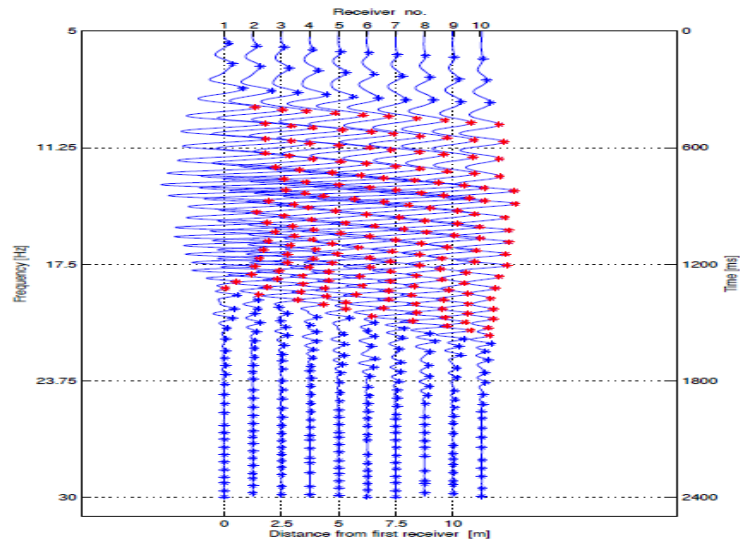


Fig.4. 6 Swept-frequency record obtained from an impulsive shot gather. Red markers identify the local maxima of each trace that are parts of linear events that are considered reliable for further analysis. Local maxima that are not used for analysis are shown with blue markers (taken from Ólafsdóttir, 2016).

3. Each linear event corresponds to a specific frequency. The frequency corresponding to each linear event is determined. The frequency corresponding to linear event l (f_l) is assumed to be the average frequency within the event.
4. The linear slope of each linear event is determined by using the method of least squares.
5. The Rayleigh wave velocity at the frequency representative of each linear event is determined. The Rayleigh wave velocity is taken dividing the slope of the least squares regression line. The process is repeated for the whole record and dispersion curve, and a function of frequency is obtained at the end.

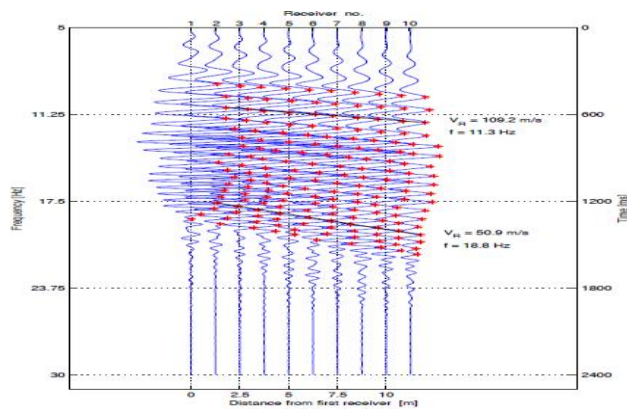


Fig.4. 7 Linear events extracted from a swept-frequency record. Red markers identify the local maxima of each trace that are used for identification of linear events. Two linear events corresponding to frequencies (f) of 11.3 Hz and 18.8 Hz are indicated by black Lines (Ólafsdóttir, 2016).

4.4.2 Phase-shift method

This procedure is actually a wave field transformation method termed as phase-shift technique. For a shot gather of an impulsive source record of MASW, the dispersion curve is obtained by dispersion image (phase-velocity spectra) (Park et al., 1998). Utilizing the phase shift technique, different mode of Rayleigh waves dispersion can be perceived from the frequency content and phase velocity at each frequency. The body wave and other scatter energy (reflected-refracted), which are considered as a noise, can be easily recognized by its frequency content and move-out. The dispersion curve of Rayleigh waves is extracted from the dispersion image (Park et al., 1998; Xia et al., 2003). The phase shift retrieval of dispersion curve processing is a tri-stage procedure, which is comprised of: Fourier transformation of the data, dispersion imaging, and retrieval of dispersion curve. A sketch like of the swept frequency method for the processing steps is shown in Fig.4.8.

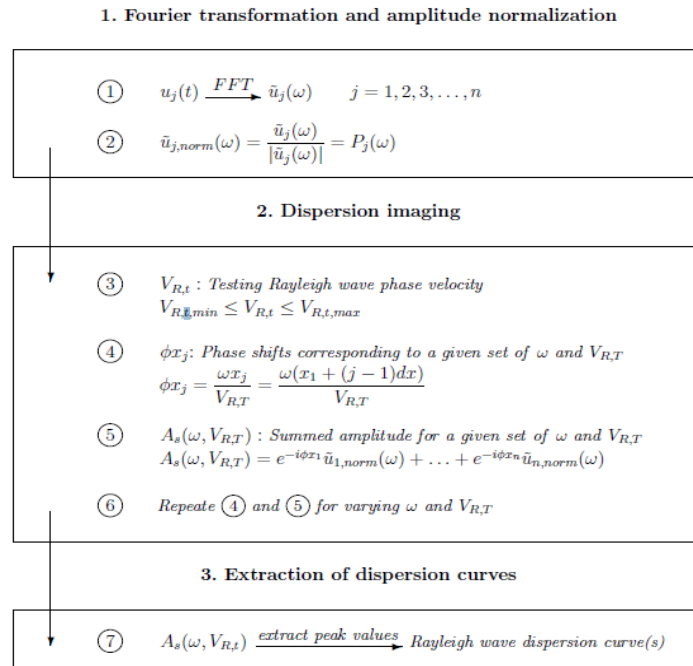


Fig.4. 8 A sketch of phase-shift (Ólafsdóttir, 2016)

The phase shift method outlined in Fig 4.8 can be detailed in steps as follows.

1. The acquired data is in time-space $\mathbf{u}(\mathbf{x}, \mathbf{t})$. It is transformed into Fourier domain along the time axis $\mathbf{u}(\mathbf{x}, \boldsymbol{\omega})$. As the acquired data is discrete both in time and in space, the Fourier transform is achieved for each trace, separately, along the time axis as discrete Fourier transformation (DFT).

$$\mathbf{u}(\mathbf{x}, \boldsymbol{\omega}) = \int_{-\infty}^{\infty} \mathbf{u}(\mathbf{x}, \mathbf{t}) e^{-i\boldsymbol{\omega}\mathbf{t}} d\mathbf{t} \quad (4.11)$$

$\mathbf{u}(\mathbf{x}, \boldsymbol{\omega})$ is represented as function of amplitude and phase $\{\mathbf{A}(\mathbf{x}, \boldsymbol{\omega}), \mathbf{P}(\mathbf{x}, \boldsymbol{\omega})\}$ as follow

$$\mathbf{u}(\mathbf{x}, \boldsymbol{\omega}) = \mathbf{A}(\mathbf{x}, \boldsymbol{\omega}), \mathbf{P}(\mathbf{x}, \boldsymbol{\omega}) \quad (4.12)$$

where

$$\mathbf{P}(\mathbf{x}, \boldsymbol{\omega}) = e^{-i\Phi(\boldsymbol{\omega})\mathbf{x}} \quad (4.13)$$

The dispersion related properties are sealed in the phase spectrum $\mathbf{P}(\mathbf{x}, \boldsymbol{\omega})$, while the amplitude spectrum carries the information regarding the attenuation and spherical divergence (Park et al., 1999). The term $\Phi(\boldsymbol{\omega})$ is defined as

$$\Phi(\boldsymbol{\omega}) = \frac{\boldsymbol{\omega}}{VR(\boldsymbol{\omega})} \quad (4.14)$$

and the term $\Phi(\boldsymbol{\omega})\mathbf{x}$ is determined at each frequency as

$$\Phi(\boldsymbol{\omega})\mathbf{x} = \frac{\boldsymbol{\omega}(\mathbf{x}_1 + (J-1)d\mathbf{x})}{VR(\boldsymbol{\omega})} \quad (4.15)$$

where \mathbf{x}_1 is the distance from the source to the first receiver and $d\mathbf{x}$ is the spacing between geophones.

2. As dispersion related properties are embedded in phase spectrum, amplitude spectrum in the frequency domain is normalized by dividing its absolute value without losing any information.

$$\mathbf{u}_{j-norm}(\boldsymbol{\omega}) = \frac{\mathbf{u}_j(\boldsymbol{\omega})}{|\mathbf{u}_j(\boldsymbol{\omega})|} \quad (4.14)$$

where $\mathbf{u}_{j-norm}(\boldsymbol{\omega})$ is the normalized amplitude of the j th trace .

3. A phase velocity range is selected for analysis, such as, $VR, T_{min} \leq VR, T \leq VR, T_{max}$ (for example, 10m/s to 2000 m/s).

4. For a given frequency and phase velocity, the time delay to balance the specific offset is found out in term of phase-shift.

5. The phase-shift calculated is applied to all separate traces of shot gather and later added to obtain the summed amplitude against each set of $\boldsymbol{\omega}$ and VR, T . Both of these steps (4 and 5) are repeated for different frequencies with a small incremental increase in test phase velocity (VR,T).

6. The Rayleigh wave phase velocity dispersion curve is obtained from the plot of summed amplitude of the slant-trace in frequency-phase velocity domain. The peak amplitude of the summed slant-trace displays the dispersion properties in term of color coding with normalized amplitude.

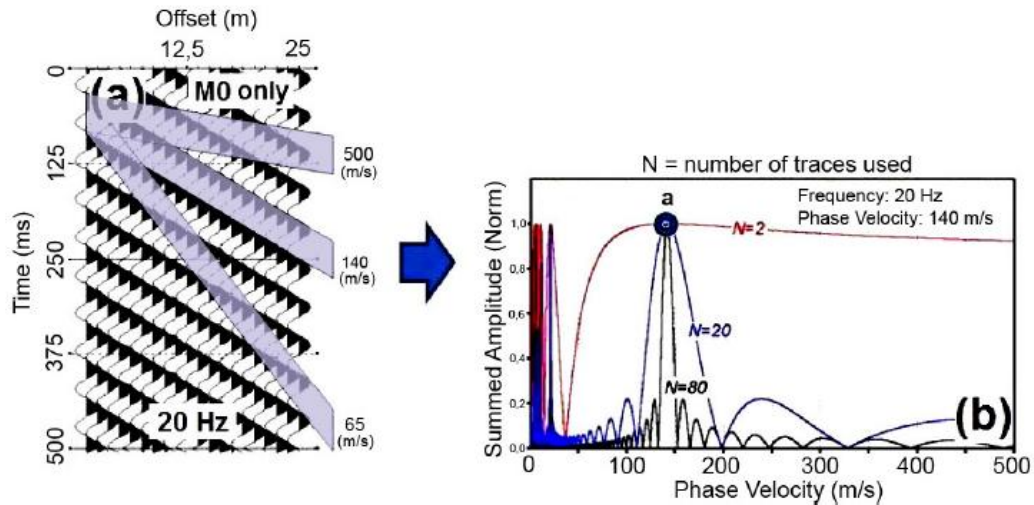


Fig.4. 9 Shows the basic principle behind the phase-shift method: (a) Normalized sinusoid curves with the frequency of 20 Hz and phase velocity of 140 m/s; (b) Normalized summed amplitude as a function of frequency for a different number of traces (www.masw.com)

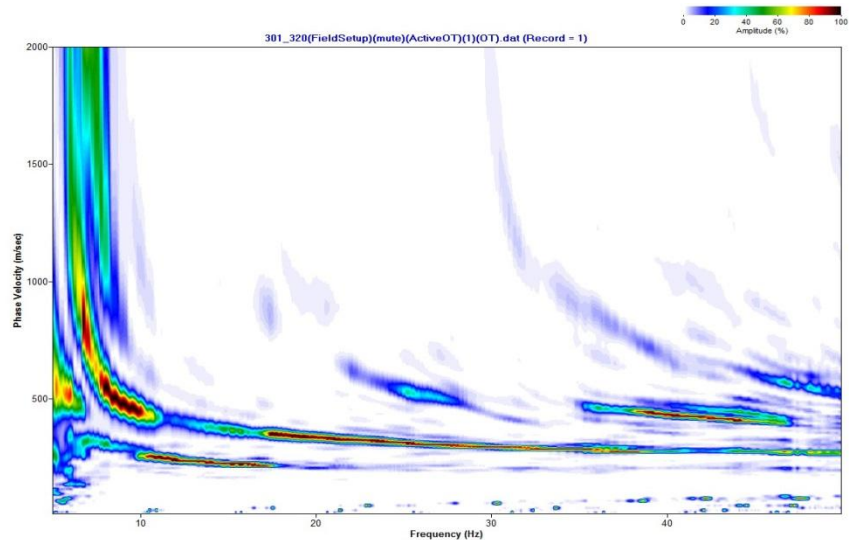


Fig.4. 10 Show the frequency-phase velocity plot as function summed amplitude (dispersion image for BEB4a, Bebedouro area).

4.6 Advantage of MASW method

The MASW method overcame the limitations of the SASW method initially introduced. SASW method data acquisition requires more effort when compared to MASW data acquisition, for

example, to cover a wide frequency range for dispersion analysis, SASW acquisition is repeated with different impact points and with diverse source-receivers intervals along with different sensors intervals. A single MASW measurement is sufficient for all this analysis which is done by multiple recording with different sources, variable source receiver intervals and different receivers spacing for SASW (Park et al, 1999). As the final goal of almost all surface wave based methods is to obtain the dispersion curve, the method which achieves it with less physical and computational effort will be considered better than the others. The dispersion curve retrieval in MASW cases is faster and can be effortlessly automated. The noise reduction (body or reflected/scattered waves) can be handled easily in MASW, when compared to SASW (Park et al., 1999). The investigation's depth of each technique is another way to eligible a better job over the other. For a given impact load, the investigation depth provided by MASW (generally 30-50 m) is greater than (Park et al., 2007) the achieved by SASW (20 m) (Bessason & Erlingsson, 2011). MASW method is handier in identifying the multimodal dispersion than the SASW (Xia & Miller, 2003). The last advantage to mention which interest in this study is also the possibility of measuring the dispersion curve analysis of passive surface wave generated by environmental and cultural noise. The lower frequency characteristics of passive surface wave helps to obtain dispersion curve for higher wavelengths which in turn it provides deeper investigation.

4.7 Inversion of dispersion curve

After obtaining the Rayleigh wave dispersion curve, the next step is to obtain the shear wave velocity profile by the inversion analysis of the retrieved experimental curve. The inversion process is based on Rayleigh waves propagation in a layered Earth model. The inversion process of surface wave is a non-linear operation. Several mathematical frameworks are used to estimate the fundamental and higher mode dispersion curve for the Rayleigh wave from an initial set of parameters. The initial set of these parameters is either assumed in priority or chosen randomly from the parameter space. These initial parameters are altered during the inversion process and for each change, the corresponding theoretical dispersion curve of the model is compared with the experimental curve. The inversion of surface wave is a multi-parameter optimization process. The general outline of an inversion process is usually divided into three steps: a computational algorithm computing the initial set of parameters; a mathematical procedure to estimate the theoretical dispersion curve for a computed set of parameters with assumption of layered Earth model; and a computation procedure to minimize the misfit, which is the deviation between theoretically estimated and experimental dispersion curves. The inversion algorithm and the procedure adopted for inversion of this work will be discussed in Chapter 5, the mathematical procedure will be given in chapter 6, as well as, the misfit function of the deviation between targets curves and the modelled curve.

4.8 MASW data acquisition for the study

Three locations were chosen for the experimental analysis for the application of the learned lessons from the theoretical analysis of the study (give in detail in Chapter 10). The first one are the borehole test sites in front of the Institute of Astronomy, Geophysics and Atmospheric Sciences, IAG, and Institute of Geosciences, IGC, both at the campus of University of São Paulo. The second is the Colônia site. Colônia, near to São Paulo city, is a circular structure, nearly swampy, is believed to be a crater site from the impact of a meteorite. The third site is Bebedouro area, São Paulo state, which remains under research due to the induced earthquake, reported in the area. The parameters of data acquisition of MASW profiles will be given in Tables for each site. The details of these sites will come in its respective sections. Here we list the parameters which were used during the MASW data acquisition.

Acquisition mode	Active	Passive
Source	Sledgehammer 10 kg	Cultural noise
Minimum offset (m)	10, 15, 20, 25, 30 and 40	_____
Geophone interval (m)	1.5	1.5
Number of Geophones	96	96
Length of the array (m)	142.5	142.5
Sampling interval (ms)	0.5	-----
Record length (s)	1,1	10,15

Table.4.2 MASW acquisition parameters for IGC and IAG (geophones 4,5 Hz).

Acquisition mode	Active	Passive
Source	Sledgehammer 10 kg	Cultural noise
Minimum offset (m)	2,50	_____
Geophone interval (m)	2	1
Number of Geophones	96	96
Length of the array (m)	190	190
Sampling interval (ms)	0.5	-----
Record length (s)	2	15, 20, 30

Table.4.3 MASW acquisition parameters for Bebedouro area (BEB4A, BEB7, BEB11, BEB1; geophones 14Hz).

Acquisition mode	Active	Passive
Source	Sledgehammer 10 kg	Cultural noise
Minimum offset (m)	5,15,30	_____
Geophone interval (m)	2	1
Number of Geophones	96	96
Length of the array (m)	190	190
Sampling interval (ms)	0.5	-----
Record length (s)	2	15, 20, 30

Table.4.4 MASW acquisition parameters for Bebedouro area (BEB 16b, BEB 4b; geophones 4.5 Hz)

Acquisition mode	Active	Passive
Source	Sledgehammer 10 kg	Cultural noise
Minimum offset (m)	5,10,15,30	_____
Geophone interval (m)	1	1
Number of Geophones	96	96
Length of the array (m)	95	95
Sampling interval (ms)	0.5	-----
Record length (s)	2	15, 20, 30

Table.4.5 MASW acquisition parameters for Colônia area at site A and site B (geophones 4.5Hz)

The sites were chosen keeping in mind some distinct properties of the other sites. The USP site (in front of the IAG - Instituto de Astronomia, Geofísica e Ciências Atmosféricas, cited here frequently as IAG-front) has the advantage of the borehole data availability for the calibration and the quality check of the result, the Colônia site was chosen due to its geological significance, its bowl shape structure is almost swampy and most of the conventional geophysical methods are difficult to employ there because of the surface water and mud (there are some small patches of dry land which make it possible to install a seismometer for noise recording and hence, the H/V analysis) , the Bebedouro area was chosen because of the availability of seismic noise data recording, as well as, the data about the multiple water wells subsurface interfaces, from which the information about the subsurface interfaces are accessible and it was easy to test thickness frequency relation over this site. Among all these three sites, the two IAG-IGC and Colônia has a strong bedrock laying below the unconsolidated soft sediments, being also true for the Bebedouro area, however, this area surface sediments are stronger when compared to the pre-mentioned sites. The detailed geological description of these sites are beyond the scope, however, a concise introduction will be presented for each of the sites prior to its inversion in the coming chapters.

Chapter 5: General inversion strategies for the surface waves analysis

5.1 The forward and inversion problem

Understanding the data is one of the basic starting steps in all the inverse problem cases. Data is simply the list of some numerical values, which is most conveniently represented as a vector. If N is the number (measurement) which an experiment is repeated, each result is an addition to data as element of data vector. After N performances, the data will have N elements. Noteworthy is that observations from an experiment (data) are not knowledge, the knowledge is gained from the analysis of data in general and inverse theory in particular. The knowledge can be obtained in many forms. Our knowledge will take the form of numerical value (s-wave velocity model).

The link between data and model can be defined in one line such that: data = what we have measured; model parameters = numbers that constitute knowledge; something distilled from the theory data or physical law is the link between the two, data and model parameter. To understand it, let's consider an example: if we want to find the density of rock from its mass and volume, the mass and volume measured are the data, having two elements $\{d_1 = \text{mass and } d_2 = \text{volume}\}$, with $N=2$ (d_1, d_2) and the unknown model parameter is one as $M=1$ (density as m_1). In this study, The physical law which link data and model would be the statement that the density multiplied by volume is equal to the mass and can be written in compact form by the vector equation as $d_2 m_1 = d_1$ (Menke 1989). There are two types of problem, one is known as forward problem (Fig.5.1), while the other is known as inverse problem, which are defined below.

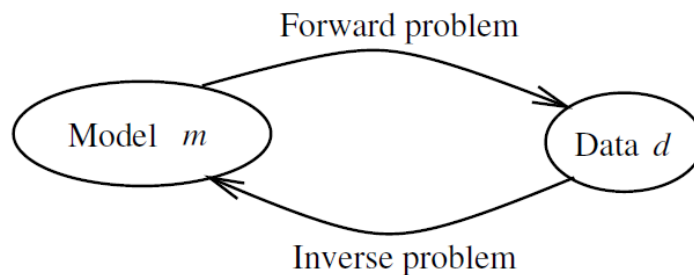


Fig.5.11 Shows the illustration of inversion and forward problems (from Scales & Snieder, 2000).

Forward problem is known as numerical models obtained on the basis of computation of theoretical values corresponding to experimental data measurement, d .

The inverse problem is where the information concerning of the physical properties of the model and the values to be assigned to the parameters have to be inferred from the data (Fig.5.1).

$$d_N = G_{N \times M} m_M \quad (5.1)$$

In Eq.5.1, where $\mathbf{G}_{N \times M}$, or \mathbf{G}_m in matrix notation, is a function that maps the model \mathbf{m}_M on the datum \mathbf{d}_N (Snieder, 1998), \mathbf{d}_N , $\mathbf{G}_{N \times M}$ and \mathbf{m}_M are in matrix form $\mathbf{d} = [d_1, d_2, \dots, d_N]^T$, $\mathbf{m} = [m_1, m_2, \dots, m_M]^T$ and $\mathbf{G} = [N \times M]$. \mathbf{G} is termed as data kernel matrix, \mathbf{d} is known and it is the column vector of the N data points. It is possible to solve this matrix equation to find the M model parameters of the vector \mathbf{m} . In another way, looking at Eq.5.1, if \mathbf{m} is known and utilize data kernel matrix to estimate \mathbf{d} , it is a forward problem and if \mathbf{d} is known, and use inverse of data kernel matrix to find the model parameters \mathbf{m} , is considered inverse problem. The linearity degree of $\mathbf{G}_{N \times M} \mathbf{m}_M$, is one of the most important aspect of an inverse problem. The geophysical observation $\mathbf{d} = [d_1, d_2, \dots, d_N]^T$ and model parameters $[m_1, m_2, \dots, m_M]^T$ relationship will be either linear (e.g., $f(x) = a + bx$) or nonlinear $\mathbf{f}(\mathbf{x}) = \mathbf{e}^{-\mathbf{a}\mathbf{x} + \mathbf{b}}$. As function of linearity, it will be more or less complex within the optimization procedure.

To summarize the inversion problem in geophysical perspective in one sentence might be said that “To make suggestions about the Earth model parameters from geophysical observations”. In the case of dispersion and ellipticity curves, the forward problem can be estimate the (dispersion and ellipticity) curves, while on the contrary, inversion problem estimates the medium properties (S-wave profile) from the experimentally obtained dispersion and ellipticity curves.

5.2 Global and local minimal solution of an inverse problem

One of the easiest and simplest approaches is to solve an inverse problem by data fitting, which involves minimizing the misfit $\mathbf{E}(\hat{\mathbf{m}})$ (also termed as the objective function, or squared error) among the set of estimated $\mathbf{G}_i(\hat{\mathbf{m}})$ and observed data (d_i). This approach is a function of joint estimated model \mathbf{m} through un-weighted least-squares misfit.

$$\mathbf{E}(\hat{\mathbf{m}}) = \sum_i (\mathbf{d}_i - \mathbf{G}_i(\hat{\mathbf{m}}))^2 \quad (5.2)$$

In case of linear forward problem the squared error $\mathbf{E}(\hat{\mathbf{m}})$ are estimated via Eq.5.2 to fit the data. The $\mathbf{E}(\hat{\mathbf{m}})$ dependence on the parameter has a parabolic shape containing a single minimum (unimodal). Any method employed to find out this minimum will be able to find it, which will correspond to the best model and will explain the data more closely than all other models (Press et al., 1992). However, most of the inversion problems in seismology are nonlinear. In such case $\mathbf{E}(\hat{\mathbf{m}})$ dependency on the parameter contain many peaks and it is termed as multimodal (Fig 5.2 b). Between these minima's there is one absolute minimum peak known as global minimum, which is linked to the best model to explain the data. The other minima's, apart from the global one, are known as local minima's and somehow, are linked to the best models.

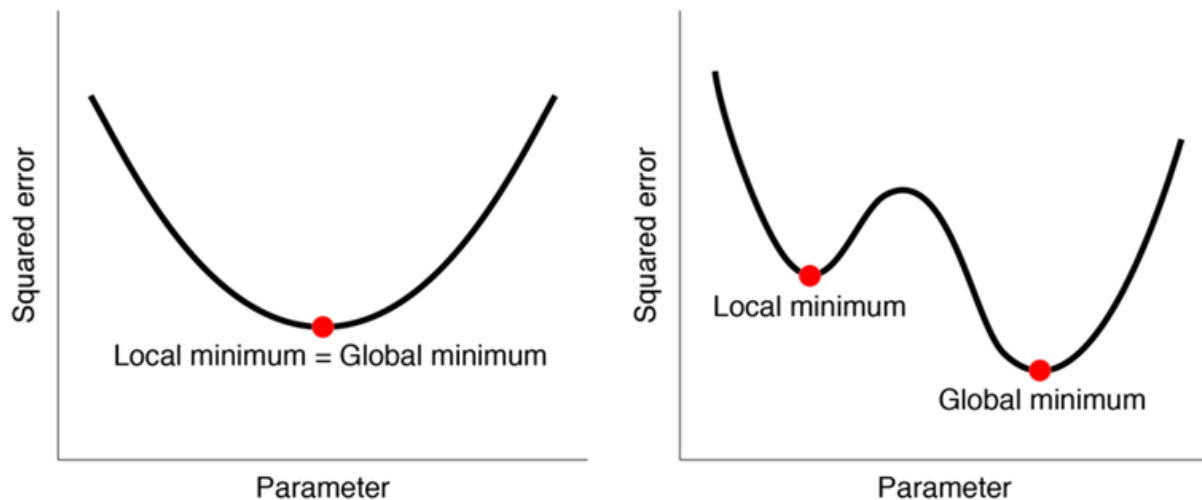


Fig.5.12 Shows the least-squares misfit function for a linear problem. (b) The conventional view of the misfit function for a nonlinear inverse problem (Menke, 2012).

There are two more commonly mistakes made during the inversion process; one is the consideration of local minima as a global one. In such situation, the data fit are not able to give the best data fit (Snieder, 1998). The second problem usually faced is the solution may not lie within the physical limits, although the data fit might be better. To handle such situation, the misfit function is made clearer to include extra conditions (limits) converging to the acceptable physical limits.

To find the minimum of the misfit function of an inverse problem is considered more an art than science, apart from all the mathematical development made in this regard (Snieder, 1998). This art foundation is based on the generalized inverse theory presented by Backus and Gilbert in the mid-sixties (e.g. Backus and Gilbert, 1967, 1968, 1970). They tried to retrieve the ground structure by data analysis strategies. This initial work opens up a new corridor which has been heavily studied since then, and several inversion strategies have been developed. The study of the performances of these developed inversion strategies are done by the analysis of exploration and exploitation criteria (Sambridge & Mosegaard, 2002). Exploration means the reducing of misfit function by a randomly trial basis on different region of parameter space, irrespective of what is already known from the previous samples. The exploitation criteria are the other way around, which where it is choosen the next sample by using the knowledge of previous samples, or the only best current fit sample. Keeping these two criteria as basis for the analysis, Sambridge & Mosegaard (2002) found out that in case of adopting an explorative strategy for the inversion like Tabu search, Uniform search, Importance sampling, Genetic Algorithms, Simulated annealing, Evolutionary programming and Neighbourhood algorithm are unlikely to trap in local minima, however, these are slower at convergence. In the case of using an exploitative strategy for inversion (e.g., Newton-Raphson, Steepest descent, and Amoeba search), they are very fast in converging to a specific area of parameter space but are more prone

to trap in local minima and inferred ground structure are more likely depended on the initial model considered for inversion.

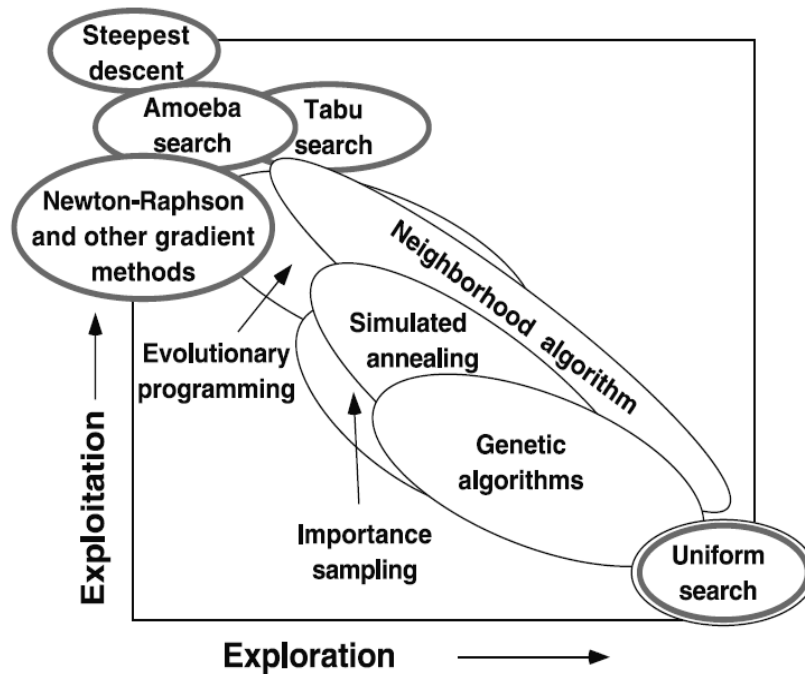


Fig.5.13 A schematic representation of various search/optimization algorithms in terms of exploration and exploitation of the information. Shaded borders indicate a deterministic (not-Monte Carlo) method (Sambridge and Mosegaard, 2002).

To draw a conclusion from the previous discussion, it can be said that an inversion strategy can be adopted depending on the basis of the goal of the study (quick convergence or global solution). As for our case, we will adopt an inversion strategy for the surface wave (dispersion and ellipticity). A combination of exploration and exploitation may be more suitable as surface wave inversion problems are highly non-linear and have many minima's in the misfit function, where each minimum fit the data with the same misfit.

5.2. Surface wave curves inversion strategies

Surface waves, especially Rayleigh waves analysis, are most commonly employed for the job of inferring the subsurface structure for engineering application. Rayleigh wave curves (dispersion and ellipticity) are greatly nonlinear function of S-waves velocity (V_s), thickness (h), P-waves velocity (V_p) and density (ρ), respectively. The inversion problem is termed as multimodal because of the existence of a large number of local minima's in the respective parameter space (Yamanaka and Ishida, 1996). Two main methodologies are applied to handle the non-linearity of surface wave inversion case. The first one is the nonlinear objective function (e.g. $f(x) = e^{-ax+b}$). This function is mathematically linearized by changing an appropriate variable (e.g $h(x) = \ln [f(x)] = -ax+b$) or first order Taylor expansion, and later, any linear inversion technique is applied for optimization procedure. In the second procedure no mathematical linearization is

performed to the solution of the inverse problem. It is find out with some deterministic or probabilistic approach. The following section will briefly outline the two strategies.

5.2.1 Iterative method (Linearized inversion)

The main theme of this class of inversion scheme is the fast convergence of the minimum of the misfit function by an iterative method through a gradual changing made on the properties of current model chosen prior to the inversion. The inversion strategies that fall in this category are damped least-square, steepest descendent, conjugate gradients and Newton-Raphson (Press et al., 1992). In the case of adopting all of these mentioned methods, it is possible to observe the convergence toward the solution by partial derivatives or Jacobian matrix. Jacobian matrix is a partial derivative matrix that contains the partial derivative of theoretical data of estimated model with respect to the model parameter. The partial derivatives computation allows the linearization of the non-linear inverse problem. The process is repeated many times (iteration) to converge to the minimum of misfit function. Another iterative method employed for the linearized inversion is the downhill simplex (Press et al. 1992). The downhill simplex requires function evaluations instead of derivatives, unlike Damped least-square, steepest descendent, conjugate gradients or Newton-Raphson.

This linearization class of inversion is used for the situation when the dimension of the space parameter is higher. This method converges quickly to the solution of the problem. As described above, in situation of high non-linearity of the problem, when there are many minima's in the misfit function, all these methods are prone to converge to one of the misfit minima regardless of the global minimum. The final obtained model will be highly dependent on the initial model. The non-unique solution of the surface wave inversion is very common (Sambridge, 2001). All these linearization strategies require a good initial model to start the inversion. The final model may lead to a starting model after a large number of iteration.

Making a conclusion about the linearized inversion strategies, these methods will give the best results in the case on the feebly non-linear problem. The methods shown can only be applied to a highly non-linear problem in a situation of sufficient previous information about the ground structure. However, in a surface wave inversion scenario, where the shear wave velocities are linked to surface wave velocities in a complicated way (highly non-linearity and multimodal misfit), mostly of the methods failed to find a global solution. The interested reader of the linearized inversion strategies is referred to Dorman and Ewing (1962), Herrmann (1994), Lai (1998) and Xia et al. (1999). Among the various procedures recommended for the inversion under linearized strategy, Singular Value Decomposition - SVD (Golub & Reinsch, 1970) is the most widely used. SVD is the best choice for producing a solution in the case of ill-condition matrices.

5.2.2 Monte Carlo inversion strategies

The main idea of these methods is originated from the experimental branch of mathematics which used random numbers to find a solution to a deterministic or probabilistic problem. The search of parameters space (predefined parameters upper and lower bounds) was initially achieved by uniform sampling for an optimal solution of an inverse problem under these inversion strategies. The parameter space search is done by the uniform sampling of the parameter space without taking any initial model to start the process. All these Monte Carlo methods, unlike linearized inversion strategies (which necessitate partial derivatives and matrix inversion which might cause numerical instabilities), require only forward model and misfit computation, that's why Monte Carlo inversion strategies are considered potentially stable techniques. The advantages of the Monte Carlo inversion strategies are: i) though the process is slow it still ensures the convergence to an optimal solution without any possibility to trap in local minima; (ii) it explores the whole parameter space, therefore, a best-fitted model of the data and the trade-off between various parameter can be evaluated (Sambridge & Mosegaard, 2002); (iii) it statistically treats the result of the inverse problem, which helps in cases of high non-linearity. The uniform sampling of the parameter space in case of a high dimensionality of parameter space makes it computationally ineffective. Because of this disadvantage of the uniform Monte Carlo inversion approach, different refined strategies were presented with pseudo-random sampling of parameter space (Simulated Annealing by Kirkpatrick et al., 1983; Neighborhood Algorithm by Sambridge, 1999, Yamanaka & Ishida, 1996). Below, we will briefly discuss Genetic algorithm and simulated annealing and then will discuss with details the Neighborhood Algorithm which is used for the inversion analysis in this thesis (Geopsy tool packages; <http://www.geopsy.org/>).

5.2.2.1 Simulated Annealing

This class of Monte Carlo inversion strategy method exploits a statistical mechanical analogy to search for the global minimum of a misfit function containing a large number of local minima's (Sambridge & Mosegaard, 2002). The fundamental thought is to simulate the physical

methodology of chemical annealing in which a liquefied crystalline material is cooled gradually towards the point of solidification and, consequently, a stable high ordered (low-energy) design. In similarity to this physical-chemical process, in the inversion plan, the objective function is related to the energy of the crystalline material, while suitable numerical standards are settled, simulating a "cooling" of the framework to be optimized (Sambridge & Mosegaard, 2002). When an appropriate cooling rate is used, the process is able to find, at least, the location of the parameter space near the global minimum, as well as, slow cooling results in low-energy crystal configurations.

5.2.2.2 Genetic Algorithm

The evolution of biological life is considered as a core theme for this kind of inversion strategy. The evolution is considered as an optimization process. A natural system like fauna adapts to its surrounding environment to survive. The genetic algorithm at first was developed by Holland (1975), which was later popularized by Wilson & Vasudevan, (1991), Gallagher et al. (1994), Stoffa & Sen (1991) and Sen & Stoffa (1992) for the different geophysical problems. There are many variants of genetic algorithm, however, the basic strategy is to compel a total population of models towards better data to fit at the same time. The genetic algorithm works on the sets of the parameters with stress placed on the particular parameter, however, the simulated annealing algorithm emphasises on a set of parameter which is continually updated. The iteration of the basic method involves three stages usually called selection, crossover and mutation. Each step of iteration in the genetic algorithm is controlled by a tuning parameter chosen by the user. In each iteration, all these three steps aim to generate a new offspring model population which, in a way, have survived (the models with lower misfit) among the previous models population. At each iteration, the misfit function is evaluated for all models previously generated. The criteria are set to select only those models which fulfil certain criteria (Survival of the fittest). This converge a new model generation toward a lower misfit region of the parameter space. The mechanisms used to implement selection, crossover, and mutation of the model population can be crucially important to the effectiveness of the algorithm. For a detail discussion the interested readers are referred to (Goldberg, 1989; Wilson & Vasudevan, 1991).

5.2.2.3 Neighborhood algorithm

As discussed above, both of the Monte Carlo approaches which utilize uniform pseudorandom sampling of the parameter space become impractical in the case of the high dimensionality of the problem due to its heavy computation. The solution to minimized this heavy computation was offered by Sambridge (1999) when seeking an answer to the question that "By what means can a search for new models be best guided by all the past models for which the forward problem has been solved (and hence the data misfit value are evaluated)?" Both genetic and simulated annealing methods utilize the information from the previous sample generated but in a complex way. The information deduced from previous samples may also be highly dependent on control

parameters (GA) or temperature profiles (SA), each of which must be tuned for each problem individually (Sambridge, 1999). On the other hand, neighborhood algorithm operated by four parameters is a self-adaptive search of parameter space. The parameter space of the inverse strategy is decomposed into cells based on the approximation of the misfit. These cells are known as Voronoi cell (Voronoi, 1908; Fig.5.4). The Voronoi cell for any distribution of points in any number of dimensions of parameter space is the region about a point, which is nearer to point under consideration than all other points of the distribution. The region of Voronoi cell around a point is defined by an appropriate norm distance (typically Euclidean). For Euclidean distance in 2D, they are polygons whose edges are perpendicular bisectors between pairs of points. In 3D they are convex polyhedra, in higher dimensions they are convex polytopes (Sambridge, 1998). This division of parameter space into Voronoi cells of neighborhoods region around a generated points (models) has a powerful property, which is, how irregular the initial points (models) distribution are and how high the dimensions of the parameter space is. It always converges to the part of the parameter space having the optimal solution.

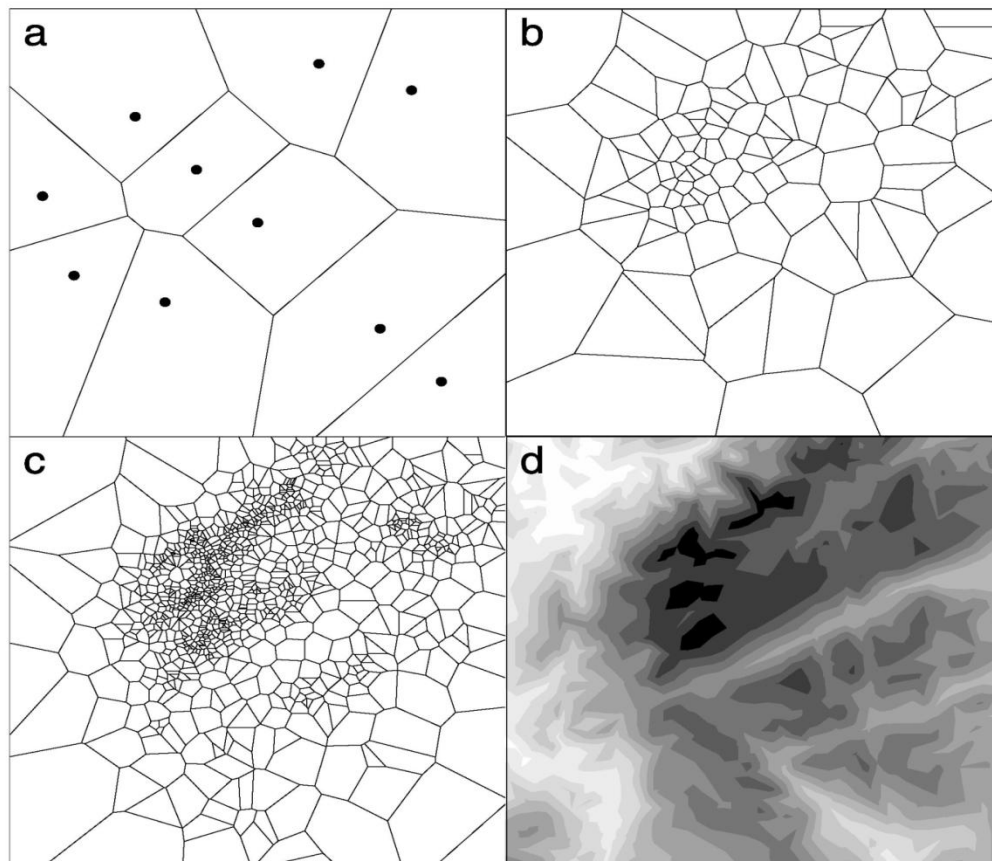


Fig.5.14 Shows the example of Voronoi cells drawn around the points (model) of parameter space for a simple 2-D problem. (a–c) Voronoi cells of about 10, 100, and 1000 generated model, respectively. Figure 5.4d shows the true fitness surface. As the algorithm proceeds, each Voronoi diagram is used to guide the sampling. Note how the Voronoi cells are more concentrated in the darker regions where the fit is high. (Sambridge & Mosegaard, 2002).

The neighborhood algorithm has two important aspects which guides the new generation of samples within the parameter space to the promising region of a lower misfit. The first one is the shape and size of the Voronoi cell, which it is not handled externally but operated and guided automatically by the previous sampling. Note that the boundaries of each Voronoi cell are determined by all previous samples, and regardless of how irregularly distributed the samples are, the Voronoi cell will be a ‘reasonable’ one, in the sense of an L-norm (Sambridge, 1999).

At each iteration step, the newly generated samples are concentrated in the neighborhoods surrounding the better data-fitting models. In this way, the algorithm exploits the information contained in the previous models to adapt the sampling. The second is the arrangement of the models generated to fit the data on the basis of misfit rank, which helps in identifying good models based on the data fit. All the generated models are rank on the basis of their misfit, which help in search the most promising area of the parameter space.

5.3 Brief inversion procedure of neighbourhood algorithm

The Neighborhood Algorithm - NA (Sambridge, 1999) is a standout amongst the latest MC direct search method for nonlinear inversion. The key idea of the NA is to make use of a simple geometrical concept to search the parameter space. In fact, new samples of parameter values are generated by randomly re-sampling within specific Voronoi cells with a locally uniform density. The power of this approach consists of the fact that at each iteration, the sampling is influenced by the size and distribution of the Voronoi cells, which are automatically controlled by all the previous samples (Sambridge, 2001). Thanks to the interesting properties of the Voronoi geometry, it seems that NA is able to sample the most promising regions of the solution space simultaneously (Whatelet, 2005). Therefore, at each iteration, the new samples tend to be concentrated in the neighborhood surrounding of the models better fitting the data.

The Voronoi decomposition of the parameter space is the base of an approximation of the misfit function which is progressively refined during the inversion process. The approximation is set as constant inside each cell and the misfit value calculated at the central point is affected to the whole cell. A two-dimensional parameter space is given as an example in Fig. 5.5. The black dots are some model points for which a misfit is calculated.

The neighbourhood algorithm needs four tuning parameters:

i_{\max}^t is the number of iteration to perform;

n_{s0} is the number of models chosen at random inside the parameter space at the beginning of the inversion;

n_s is the number of models generated at each iteration;

n_r is the number of best cells (with the lowest misfit) where the n_s models are generated.

The inversion process is composed of the following phases (described by Sambridge (1999a) and Wathelet, 2005, 2008):

1. A set of n_{s0} models is randomly generated with a uniform probability in the parameter space;
2. The misfit function is calculated for the most recently generated model;
3. The n_r models, with the lowest misfit of all models generated so far, are selected;
4. Generate an average of $\frac{n_s}{n_r}$ new samples with a uniform probability in each selected cell;
5. Add to the n_s new samples to the previous ensemble of models and go back to 2.

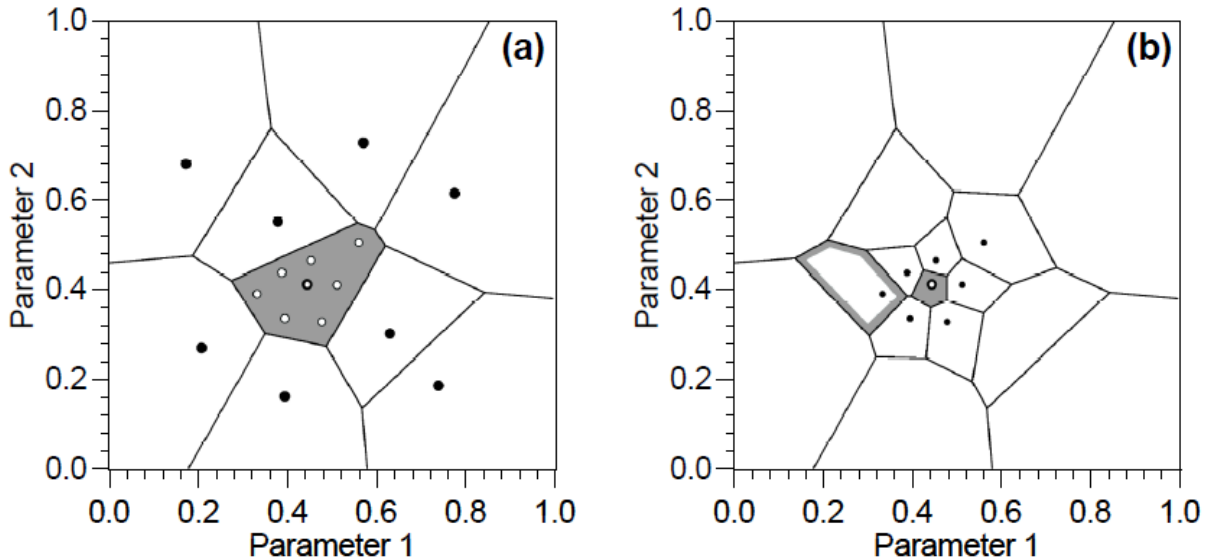


Fig.5.15 Shows Voronoi cells for a two-dimensional parameter space (from Sambridge, 1999a). (a) is an example of a two-dimensional parameter showing the models (black dots) and the limits of the Voronoi cells. (b) depicts the Voronoi geometry after the first iteration (from Wathelet, 2005)

In Fig 5.5 (a) $n_{s0} = 9$ (in this case) models are generated and the grey cell has the lowest misfit. In this example, seven new models are generated in one cell ($n_r = 1$, and $n_s = 7$). The size of the original cell decreases as the sampling rate increases. If the cell with the grey outline has the lowest misfit, the density of sampling will not decrease systematically after each iteration. This is an interesting property of the Voronoi geometry that allows the centre of sampling to jump from place to place, whilst always sampling the most promising n_r regions simultaneously.

In the neighborhood algorithm, a random walk (Gibbs sampler) is performed with a uniform probability density function inside the cell and zero outside. A walk is a sequence of perturbations of a model along with all the axis. The modified model is statistically independent of the original model. Asymptotically, the samples produced by this walk will be uniformly

distributed inside the cell regardless of its shape. To continue the random walk inside a particular cell, it is mandatory to calculate the multi-dimensional limits of the cell. Calculating the complete Voronoi geometry for high dimensional spaces becomes practically impossible when the number of models increases. Sambridge (1999) proposed an original algorithm to compute only the limits along lines, which are parallel to the axis, in a precise and efficient way. These lines support the successive segments of the random walks.

The exploration and exploitation are nicely handled by the neighborhood algorithm. The algorithm is more exploratory if the n_s new samples are distributed on many cells and it optimizes more quickly if they are restricted to the very few best cells. Typical values for the tuning parameters are 100 for n_{s0} , n_s , n_r . To force a better optimization, n_r may be set to 5, 10 or 50 (Wathelet, 2005). Tests had generally shown that better misfits are obtained with fewer iterations if n_r is low, but the inversion is more trapped in local minima. The exploratory mode (e.g. $n_r=100$ and $n_s=100$) usually provides better final misfits if the inversion is conducted with a great number of iterations. The number of iterations ranges from 50 to 200. This makes a total of 5,000 to 20,000 generated models. Compared to linearized methods, the number of forward computations is greater. Consequently, the forward computation has to be correct for each parameter set without a visual check, and it must be highly optimized to reduce the total computation time.

The neighborhood algorithm is used in different studies at different scale. Sambridge (1999) and Snoke (2002) employed it for the receiver function inversion at crustal scale, Wathelet (2005) refined it further and utilized it for the surface waves inversion at engineering scale. Recently the NA algorithm was used by Hobiger et al (2013) and Lontsi et al (2015) for ellipticity inversion with supplementary information. The interested reader is referred to the paper review for a very detailed procedure about neighborhood algorithm. (Sambridge, 1999a and 1999b also Wathelet, 2008)

5.4. The parameter setting for the inversion

For an Earth model made of homogeneous horizontal layers, four parameters (shear wave velocity V_s , thickness h , P-wave velocity V_p and density ρ) can fully describe the computation of both dispersion and ellipticity curves. The parameter listed above, which affect the shape of both dispersion and ellipticity curves, are given in decreasing order. Specially, the P-wave velocity and density have very little effect on dispersion curve (Xia et al 2002) and we will try to check its effect on ellipticity in next chapters. For linearized inversion, the ground structure is divided into layers of fixed thickness, while V_s are allowed to set as free parameter by fixing V_p or Poisson ratio for the whole structure. However, Wathelet (2008) pointed out that by taking V_p values for fixation from refraction data has its own uncertainties and, fixing V_p values from refraction survey will penalized the result at the end. Therefore, it is suggested to keep V_p and V_s as free parameters linked by Poisson ratio, and the density value are fixed to some value. Both V_p and V_s can be defined within a range for lower and upper bound, this sets the physical

range of parameter space. Taking a large number of layers above bedrock will be confined to concentrate the generated models around a median depth due to central limit theorem (Wathelet, 2008). Therefore, Wathelet suggested setting up the depth range of the bedrock instead of fixing the thickness of each layer so, in this way, thickness also becomes a free parameter. The presence of a low velocity zone in the subsurface complicates the forward model estimation because in the case of stochastic inversion, like neighborhood procedure, the random generation of a model would be impossible to generate a model for the target curve, which contains a low velocity zone (Wathelet, 2008). This problem is dealt with by trial and error, however, if the area for which the inversion is made has a linear velocity increase, then the models are generated without the LVZ. In all our three tested sites for the study we have assumed a linear velocity increase trend and have not included the presence of any low velocity layer in the inversion.

Chapter 6: Modelling of the H/V curve

6. Introduction

Amongst the researchers working with the H/V techniques the most debated question was how to model the H/V curve with respecting the wave field that contributes in its subsistence. The purpose is to pinpoint the phases of the elastic wave which might be considered as the major contributor in its shape. Initially, It was believed that the ratio (H/V) is mainly influenced by the SH resonance frequency within the surface layers of soil above the bedrock. However, other researchers showed (Nogoshi & Igarashi 1971, Fah et al., 2001, Fah et al., 2003, Scherbaum et al., 2003) that seismic noise is mainly dominated by a surface wave and the shape of the H/V curve is actually subjugated by the shape of the Rayleigh waves ellipticity. This interpretation got allot of attention because of the peak and trough points alignment between the experimental H/V curve and theoretical ellipticity. However, in the case of considering the H/V curve as a proxy for the Rayleigh wave ellipticity, the H/V curve mostly reproduce the peak and trough frequency of the ellipticity curve but failed to match the amplitude of the ellipticity curve. To explain this mismatch between the amplitude, some of the studies concluded that this deviation in shape of the H/V curve are due to the presence of body and Love waves on the horizontal component of noise wave field around the peak frequency f_0 (Arai & Tokimatsu, 2000 and Yamamoto, 2000). To incorporate the effect of body wave an effort was made by Sánchez-Sesma et al. (2010; 2011) who considered the noise wave field as a diffuse field and attributed the H/V curve to all the seismic phases present in the noise wave field. Here, in this chapter, it will be outlined the major theoretical developments used to numerically model the H/V curve by different assumptions of seismic noise wave field and will compare its results with experimental H/V recorded at same site, whose velocity model were used to numerically model the curve.

6.1 Nakamura explanation of the H/V curve

Nakamura (1989) gave an explanation that, actually, this (H/V) simple spectral ratio technique is a very good indicator of shear wave resonance frequency of a site. He explained the H/V curve for the vertically SH incident wave case. However, his initial interpretation was faced with many controversies and objections, such as that H/V curve is not dominated by body waves but it contains a major contribution from surface waves (Bard, 1999). Nakamura re-evaluated his technique and included the effect of surface waves in the H/V curve modelling (Nakamura, 2000). Here, a brief idea about his explanation is given. The explanation of wave amplification at the surface due to wave propagation from a hard rock through soil is achieved by the product of transfer function with the Fourier transform of the waves arriving at the bedrock. Therefore, the

motion produced at the surface by a horizontal motion at bedrock can be replicated by the transfer function multiplied to the Fourier transform of the horizontal motion at the bedrock and the Fourier transform of the surface wave as bellow.

$$\mathbf{H}_{FT(\omega)} = \mathbf{A}_H(\omega)\mathbf{H}_{FT-b(\omega)} + \mathbf{H}_{FT-s(\omega)} \quad (6.1)$$

$\mathbf{A}_H(\omega)$ is the horizontal transfer function between bedrock and soil surface (also known as frequency response), $\mathbf{H}_{FT-b(\omega)}$ is the Fourier transform of horizontal motion at bedrock surface due to the body waves, $\mathbf{H}_{FT-s(\omega)}$ is the horizontal motion Fourier transform at surface due to the surface wave. Similarly, the motion produced by vertical component at bedrock at soil surface is given as

$$\mathbf{V}_{FT(\omega)} = \mathbf{A}_V(\omega)\mathbf{V}_{FT-b(\omega)} + \mathbf{V}_{FT-s(\omega)} \quad (6.2)$$

the terms in Eq.6.2 are same as that of Eq.6.1 but for the vertical component of motion. The transfer function for the horizontal component of motion for a soil deposit over a bedrock, of velocity \mathbf{V}_s , thickness h and damping (ξ) is given as (Kramer, 1996)

$$\mathbf{A}_H(\omega) = \frac{1}{\cos(\omega h / \mathbf{V}'_s)} \quad (6.3)$$

where $\mathbf{V}'_s = \mathbf{V}_s \sqrt{1 + 2i\xi}$. The expression for vertical transfer is the same function as Eq 6.3 $\mathbf{A}_V(\omega)$, where \mathbf{V}'_s is replaced by \mathbf{V}'_p which is $\mathbf{V}_p \sqrt{1 + 2i\xi}$. To obtain natural frequency of the soil deposit the term in Eq 6.1 and Eq6.2 ($\mathbf{H}_{FT(\omega)}, \mathbf{V}_{FT(\omega)}$) cannot be used directly as it has the effect of sources that generated the waves. It is, therefore, common to take the ratio of $\mathbf{H}_{FT(\omega)}, \mathbf{V}_{FT(\omega)}$ for source effect removal such as

$$\mathbf{T}_H(\omega) = \frac{\mathbf{H}_{FT(\omega)}}{\mathbf{H}_{FT-b(\omega)}}, \quad \mathbf{T}_V(\omega) = \frac{\mathbf{V}_{FT(\omega)}}{\mathbf{V}_{FT-b(\omega)}} \quad (6.4)$$

where $\mathbf{T}_H(\omega)$ is the transfer function for horizontal component motion Fourier transform at the surface, while the $\mathbf{H}_{FT-b(\omega)}$ is the horizontal component Fourier transform at the rock due to body waves. The element of the transfer function for vertical motion, $\mathbf{T}_V(\omega)$, has the same definition as that of $\mathbf{T}_H(\omega)$. Nakamura's explanation of H/V is based on an assumption that the horizontal and vertical motion at the rock level, ($\mathbf{H}_{FT-b(\omega)}$ and $\mathbf{V}_{FT-b(\omega)}$) is equal such that their ratio is 1. To estimate the site frequency, Nakamura suggests to estimate the ratio, $\mathbf{T}_H(\omega) / \mathbf{T}_V(\omega)$, and called it Quasi Transfer function

$$\mathbf{T}_{QTS} = \frac{\mathbf{T}_H(\omega)}{\mathbf{T}_V(\omega)} \quad (6.5)$$

using the values of $\mathbf{T}_H(\omega), \mathbf{T}_V(\omega)$ from Eq6.4 in Eq6.5 results in

$$T_{QTS} = \frac{H_{FT(\omega)}}{V_{FT(\omega)}} \quad (6.6)$$

and putting the values of $H_{FT(\omega)}$ and $V_{FT(\omega)}$ from Eq.6.1, 6.2 and simplifying its results as

$$T_{QTS} = \frac{A_H(\omega)H_{FT-b}(\omega)+H_{FT-s}(\omega)}{A_V(\omega)V_{FT-b}(\omega)+V_{FT-s}(\omega)} \approx \frac{H_{FT-b}}{V_{FT-b}} * \left(\frac{A_H(\omega)+H_{FT-s}(\omega)/H_{FT-b}}{A_V(\omega)+V_{FT-s}(\omega)/V_{FT-b}} \right) \quad (6.7)$$

as $\frac{H_{FT-b}(\omega)}{V_{FT-b}(\omega)}$ is equal to 1 due to the assumption; the quasi transfer function (T_{QTS}) is equal to the

$$T_{QTS} = \left(\frac{A_H(\omega)+H_{FT-s}(\omega)/H_{FT-b}}{A_V(\omega)+V_{FT-s}(\omega)/V_{FT-b}} \right) \quad (6.8)$$

if the wave field is dominated by the body waves (such as $H_{FT-s}(\omega) \approx 0$ $V_{FT-s}(\omega) \approx 0$), Eq.6.8 simplify as

$$T_{QTS} = \left(\frac{A_H(\omega)}{A_V(\omega)} \right) \quad (6.9)$$

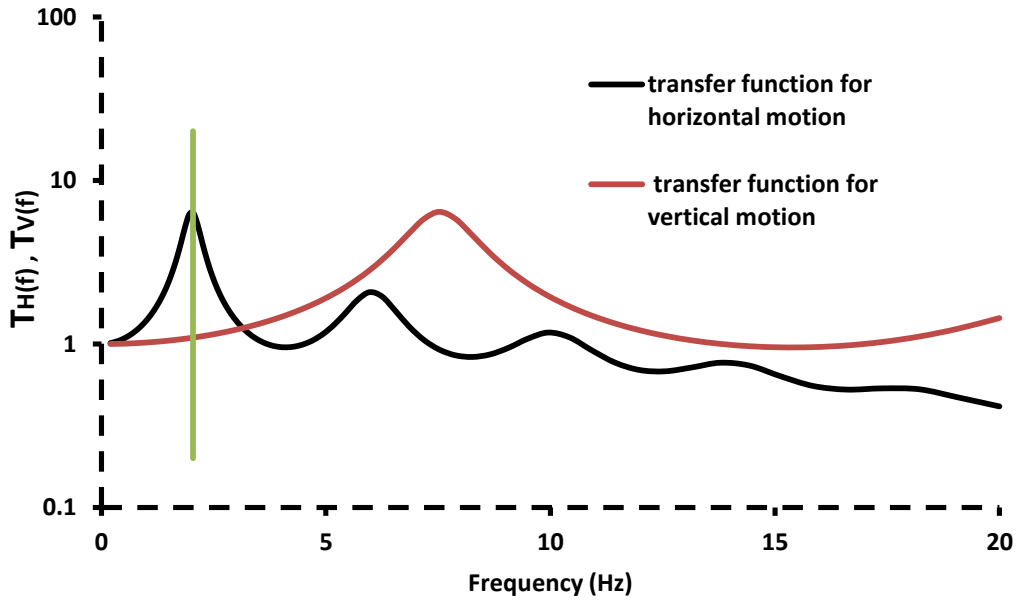


Fig.6. 1 Horizontal and vertical transfer functions for horizontal and vertical motion of IAG borehole model. The vertical line shows the fundamental frequency where the maximum application of bedrock motion occurs.

In Fig.6.1 it can be easily observed that for soil deposit of thickness h (55m), V_s (420m/s), V_p (1500m/s) and damping factor $\xi = 0.10$, the vertical transfer function $|A_V(\omega)|$ is around 1 (1.08 - Fig.6.1) at the fundamental peak frequency f_0 (1.99 Hz) of $|A_H(\omega)|$. This fact was first

observed by Nakamura (1989, 2000). Nakamura suggested that if the surface wave dominates the wave fields then the shape of Eq.6.8 can be simplified as

$$T_{QTF} = \left(\frac{H_{FT-s}(\omega)/H_{FT-b}}{V_{FT-s}(\omega)/V_{FT-b}} \right) = \frac{H_{FT-s}(\omega)}{V_{FT-s}(\omega) \frac{H_{FT-b}}{V_{FT-b}}} \quad (6.10)$$

Where $\frac{H_{FT-b}}{V_{FT-b}} = 1$ in Eq. 6.10 (Nakamura assumption, 1989).

It is assumed that in case of surface wave domination, the term $V_{FT-s}(\omega)$ around the peak frequency decreases which results in a peak around the fundamental frequency f_0 of the site. Therefore, even in case of the surface waves domination, the surface waves alone reproduced the transfer function. Comparing the result of Eq.6.9 with the H/V curve of recorded noise at the IAG borehole site, the peak frequency of the QTS match and has only a deviation of 4% from experimental H/V. A similar observation leads Nakamura (1989) to conclude that H/V basically gives the transfer function of a soil deposit. However, the amplitude of both H/V and result of QTS (Eq.6.9) rarely match. Another discrepancy of H/V curve is the difference in overall shape from QTS (Fig.6.2). That is why some of the authors concluded that the H/V basically serves as a proxy for the Rayleigh waves ellipticity rather than SH-transfer function (Nogoshi & Igarashi 1971, Fah et al., 2001, Fah et al., 2003, Scherbaum et al., 2003). Bard (1999) reviewed, in detail, the Nakamura (1989) theory and rejected the possibility of H/V linkage with SH-transfer function of a soil deposit. In next section, we will briefly outline the Rayleigh waves ellipticity explanation of the H/V modelling.

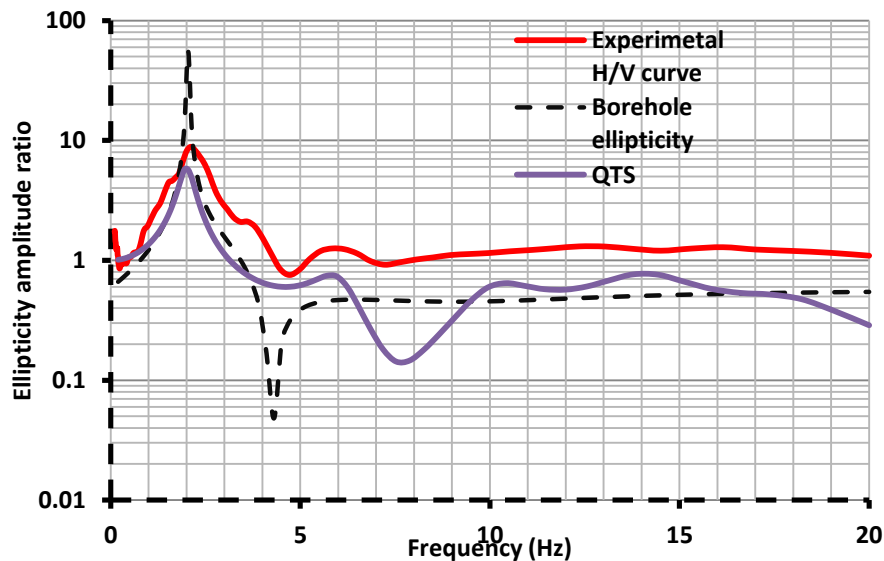


Fig.6. 2 Show the comparison of experimental H/V theoretical ellipticity curve of Rayleigh wave and QTS of Eq6.9.

6.2 Rayleigh wave ellipticity modelling of H/V curve

In 1885 Sir John Strutt, Lord of Rayleigh, first observed the presence of Rayleigh waves on the surface of an elastic half space. Rayleigh waves are formed by the linear pairing of P (primary waves) and SV (vertically polarized shear waves) waves (Aki, 2002). This pairing of vertical and horizontal components has a phase shift of $\pm \frac{\pi}{2}$. The particle motion induced by Rayleigh waves depicts an ellipse. This elliptical particle motion under the Rayleigh waves influence will be either retrograde or prograde depending on the sign of the phase shift. Similarly, Love waves are composed with horizontally polarized shear waves (SH). The horizontal over vertical displacement component at the surface, described by the particle motion under the Rayleigh waves influences results in a curve as function of frequency, which is termed as ellipticity (E) of Rayleigh waves. In the situation of homogeneous half-space the particle motion is retrograde at all frequencies and ellipticity is constant. However, in case of layered media (elastic, isotropic and vertically heterogeneous) ellipticity exhibits a peak followed by a trough, while the particle motion switch from retrograde to prograde and then to retrograde with the frequency, depending on the velocity contrast between the soil and bedrock (Konno & Ohmachi, 1998). Some researchers have shown that the H/V curve is actually depicting the Rayleigh waves ellipticity curve for a site (Nogoshi & Igarashi 1971, Fah et al., 2001, Fah et al., 2003, Scherbaum et al., 2003). Here, we will briefly outline this modelling prospective of the theoretical ellipticity curve. When the Rayleigh waves travel through a media, it produces displacement of particle in horizontal and vertical directions. This displacement can be described in the form as (Aki and Richard, 2002)

$$\begin{aligned} \mathbf{u}_x &= \mathbf{r}_1(\mathbf{k}, \mathbf{z}, \omega) e^{i(\mathbf{kx} - \omega t)} \\ \mathbf{u}_y &= \mathbf{0} \\ \mathbf{u}_z &= i\mathbf{r}_2(\mathbf{k}, \mathbf{z}, \omega) e^{i(\mathbf{kx} - \omega t)} \end{aligned} \tag{6.11}$$

where r_1 and r_2 are the complex amplitude, for positive and real r_1 , r_2 the phase shift between these components \mathbf{u}_x \mathbf{u}_z can be computed. At angular frequency ω , the Rayleigh waves velocity is $V_R = \omega/k$. The phase shift between r_1 and r_2 is $\pm \frac{\pi}{2}$. When this phase shift is positive the motion is termed as prograde, while retrograde if the phase shift is negative. The stress components corresponding to this situation are given by

$$\begin{aligned} \tau_{yz} &= \tau_{xy} = \mathbf{0} \\ \tau_{xx} &= i \left(\lambda(\mathbf{z}) \frac{d\mathbf{r}_2}{d\mathbf{z}} + \mathbf{k}(\lambda(\mathbf{z}) + 2\mu(\mathbf{z}))\mathbf{r}_1 \right) e^{i(\mathbf{kx} - \omega t)} \end{aligned}$$

$$\tau_{yy} = \mathbf{i} \left(\lambda(\mathbf{z}) \frac{d\mathbf{r}_2}{dz} + \mathbf{k}(\lambda(\mathbf{z})\mathbf{r}_1) \right) \mathbf{e}^{i(\mathbf{kx}-\omega t)} \quad (6.12)$$

$$\tau_{zz} = \mathbf{i} \left((\lambda(\mathbf{z}) + 2\mu(\mathbf{z})) \frac{d\mathbf{r}_2}{dz} + \mathbf{k}(\lambda(\mathbf{z})\mathbf{r}_1) \right) \mathbf{e}^{i(\mathbf{kx}-\omega t)}$$

$$\tau_{xz} = \mu(\mathbf{z}) \left(\frac{d\mathbf{r}_2}{dz} - \mathbf{k}\mathbf{r}_2 \right) \mathbf{e}^{i(\mathbf{kx}-\omega t)}$$

where $\lambda(\mathbf{z}), \mu(\mathbf{z})$ are the Lamé parameters $\mu(\mathbf{z}) \left(\frac{d\mathbf{r}_2}{dz} - \mathbf{k}\mathbf{r}_2 \right) = \mathbf{r}_3(\mathbf{k}, \mathbf{z}, \omega)$ which shows the amplitude of radial shear stress τ_{xz} . Similarly, $\mathbf{i} \left((\lambda(\mathbf{z}) + 2\mu(\mathbf{z})) \frac{d\mathbf{r}_2}{dz} + \mathbf{k}(\lambda(\mathbf{z})\mathbf{r}_1) \right) = \mathbf{r}_4(\mathbf{k}, \mathbf{z}, \omega)$ which shows the amplitude of vertical compression τ_{zz} . Also, another important point to note is that the stress components τ_{xz}, τ_{zz} , should be continuous with respect to z (depth)

$$\tau_{xz} = \mathbf{r}_3(\mathbf{k}, \mathbf{z}, \omega) \mathbf{e}^{i(\mathbf{kx}-\omega t)} \quad (6.13)$$

$$\tau_{zz} = \mathbf{i}\mathbf{r}_4(\mathbf{k}, \mathbf{z}, \omega) \mathbf{e}^{i(\mathbf{kx}-\omega t)} \quad (6.14)$$

By combining Eqs.6.11, 6.12 and 6.13 the motion-stress vector $\mathbf{f}(\mathbf{z})$ for Rayleigh waves can be written as

$$\frac{d}{dz} \begin{pmatrix} \mathbf{r}_1 \\ \mathbf{r}_2 \\ \mathbf{r}_3 \\ \mathbf{r}_4 \end{pmatrix} = \begin{pmatrix} \mathbf{0} & \mathbf{k} & \mathbf{u}(\mathbf{z})^{-1} & \mathbf{0} \\ -\mathbf{k}\lambda(\mathbf{z})[\lambda(\mathbf{z}) + 2\mu(\mathbf{z})^{-1}] & \mathbf{0} & \mathbf{0} & [\lambda(\mathbf{z}) + 2\mu(\mathbf{z})^{-1}] \\ \mathbf{k}\xi(\mathbf{z}) - \omega^2 \mathbf{f}(\mathbf{z}) & \mathbf{0} & \mathbf{0} & -\mathbf{k}\lambda(\mathbf{z})[\lambda(\mathbf{z}) + 2\mu(\mathbf{z})^{-1}] \\ \mathbf{0} & -\omega^2 \rho(\mathbf{z}) & -\mathbf{k} & \mathbf{0} \end{pmatrix} \begin{pmatrix} \mathbf{r}_1 \\ \mathbf{r}_2 \\ \mathbf{r}_3 \\ \mathbf{r}_4 \end{pmatrix} \quad (6.15)$$

where $\xi(\mathbf{z}) = 4\mu(\mathbf{z}) [\lambda(\mathbf{z}) + \mu(\mathbf{z})] / [\lambda(\mathbf{z}) + 2\mu(\mathbf{z})]$, Aki and Richards (2002).

The boundary conditions for Rayleigh waves are (disappearance of stress at the free surface $z = 0$, and no motion at infinity) such as

$$\mathbf{r}_1, \mathbf{r}_2 \rightarrow \mathbf{0} \text{ as } z \rightarrow \infty \quad (6.16)$$

$$\mathbf{r}_3 = \mathbf{r}_4 = \mathbf{0} \text{ at the free surface } (z = z_0) \quad (6.17)$$

The interaction of incident P and SV waves with the free surface gives rise to an interference wave travelling along the surface as a Rayleigh wave (Lay and Wallace, 1995).

The computation of forward modelling of dispersion curve and ellipticity from Eq 6.15 is based on the eigenvalue problem solved through propagator matrix described by Thomson (1950) and Haskell (1953), subsequently modified by Knopoff (1964), Dunkin (1965) and Herrmann (1994). We are employing a code which is based on the Dunkin's notations (see for detail Sesame report No. D14.07 (2003)). For Rayleigh waves, the equations of motion are reduced to a system of simple differential with a derivative of the first order in z . To solve this problem numerically the original vertically heterogeneous Earth is modelled and replaced by a large number of horizontal layers ($n+1$) over a homogenous half-space (Fig.6.3). The properties of each layer are characterized by four parameters h , V_s , V_p , ρ as function of depth z (thickness, shear wave velocity, primary wave velocity and density). The homogeneous half space is defined by V_s , V_p and ρ only (shear wave velocity, primary wave velocity and density).

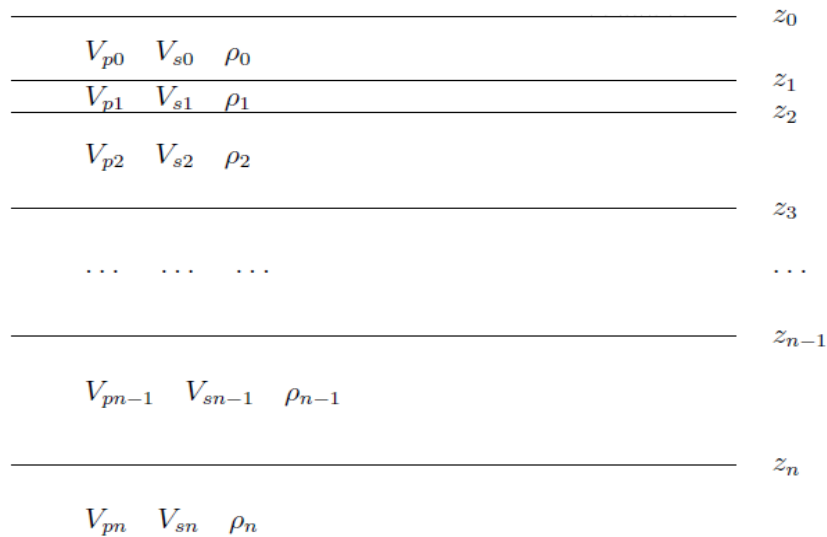


Fig.6. 3 Shows the schematic one-dimensional model defined by a stack of ($n+1$) layers. z_i are the depths of the top of each layer (modified from Aki and Richard, 2002).

For the propagation of wave, in case of a stack of horizontal layers over the half-space, the problem is expressed by the differential Eq. 6.18 as

$$\frac{d}{dz} \mathbf{f}(z) = \mathbf{A}(z) \mathbf{f}(z) \quad (6.18)$$

where f is the general motion-stress vector of n components and A is a $n \times n$ matrix whose elements depend on the elastic parameters of the layers. When displacement is defined at a reference depth z , the vector $f(z_0)$ can be obtained through Eq.6.18. If A is independent of depth z , which is valid inside a layer, then Eq.6.18 provides a freedom of computing the vector $f(z)$ for any arbitrary depth.

$$\mathbf{f}(z) = \mathbf{G}(z, z_0)\mathbf{f}(z_0) \quad (6.19)$$

$\mathbf{G}(z, z_0)$ is called Thomson-Haskell propagator matrix. It is a 4×4 matrix, function of depth at top and bottom of the layer, and matrix A . The $\mathbf{G}(z, z_0)$ elements are calculated by the eigenvalue decomposition of $A(z)$ and expressed in the form as (Aki and Richards, 2002)

$$\mathbf{G}(z, z_0) = e^{(z-z_0)\mathbf{A}(z)} \quad (6.20)$$

The advantage of this approach is that it can be used for a stack of n -layers (levels), where the n -level is related with the reference on (z_0) through the product of the matrix $\mathbf{G}(z_i, z_n)$ relative the whole intermediate layers for any arbitrary depth z_i and expressed as

$$\mathbf{f}(z) = \mathbf{G}(z, z_n)\mathbf{G}(z_n, z_{n-1}) \dots \mathbf{G}(z_1, z_0)\mathbf{f}(z_0) \quad (6.21)$$

Eq.6.21 allows to determine the vector $f(z)$ at each arbitrary depth, under the following conditions: the stress component being null at the surface ($z = 0$); both displacement and stress are assumed continuous on the correspondence of each surface between the layers and the one between the last layer and the half-space. The propagator matrix G is the functions of the depth at the top and at the bottom of each layer, and of the matrix A , which depends upon layer properties. It allows simulating the wave propagation into each layer of the model solving the series of equations (like Eq.6.21). However, the boundary conditions at infinite depth for Rayleigh waves (Eq. 6.15 and 6.16) can't be solved directly. At first this problem is transform into a radiation condition that no up-going waves are found in the bottom half-space and then Eq.6.21 is used to solved the motion stress vector for Rayleigh waves Eq.6.15.

Ellipticity of Rayleigh waves is evaluated as the displacement ratio of horizontal and vertical component $\mathbf{u}_x(z_0)/\mathbf{u}_z(z_0)$ at surface, which is estimated for a wave propagated from the bedrock to surface (see for detail, Aki and Richard, 2002). The solution (non-vanishing) for Rayleigh waves cases exist only at certain discrete wave numbers for a given frequency, which are termed

as eigenvalue for that specific frequency. The solution of Eq.6.15 for the specific eigenvalue is an eigenfunction of the problem. The pairs of eigenvalues and eigenfunction, $\{k_i, r_k(z, k, \omega)\}$ where $i=1, M, rk=1, 2, 3, 4$ for Rayleigh wave, each set of $\{k_i, r_k(z, k, \omega)\}$ defines a mode of propagation and, in general, there are M normal modes of propagation at any given frequency ω .

The ellipticity for IAG borehole model for the first 4 modes is shown in Fig 6.4. Note that ellipticity for fundamental mode exists for all the frequencies, while that one of higher mode exists beyond a certain frequency. So, usually it is suggested that the shape of H/V curve is dominated by fundamental mode of Rayleigh waves ellipticity up to the first minimum (Hobiger et al., 2013). Beyond the trough frequency, the influence of higher Rayleigh mode dominates the H/V curve. The peak and trough of the H/V curve mostly coincide with Rayleigh waves ellipticity peak and trough, however, there is a disagreement in amplitude between the H/V curve and ellipticity curve (see Fig.6.2). This discrepancy in amplitudes of both the curves is associated to the presence of Love waves on the horizontal component of noise wave field. In modelling prospective of ellipticity, it is easy to model a tabulated layered Earth case with thickness, density, V_p and V_s information. However, when dealing with experimental data there is always a chance of presence of other seismic phases (body and Love waves) contributing to the noise wave field. Therefore, taking experimental H/V spectral ratio as true representative of Rayleigh waves ellipticity might cause biased results. Hence, it is necessary to remove or minimize the effect of Love and body waves before considering a H/V spectral curve as closer representative of ellipticity curve for subsurface structure retrieval. We will list the available procedures for the minimization of Love waves effect from experimental curve in a final chapter with some experimental data. In next section, we will discuss the modelling of H/V curve considering both Rayleigh and Love waves.

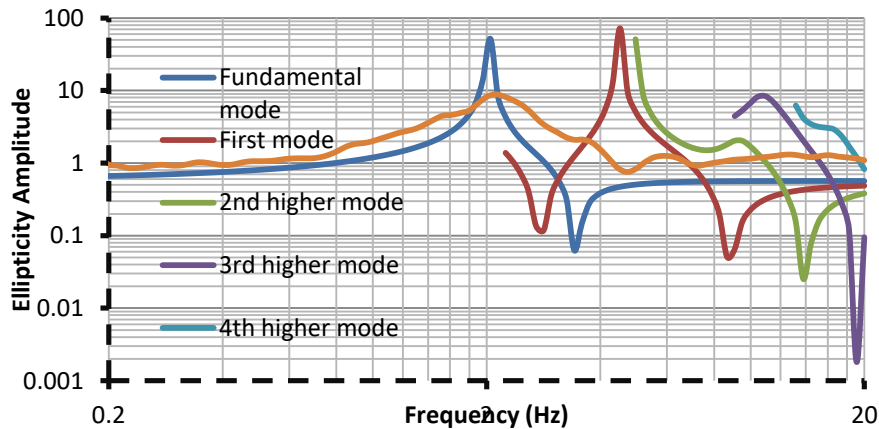


Fig.6. 4 Show the ellipticity curve for the first four mode of IAG bore model, yellow line show the experimental H/V recorded at site..

6.3 H/V modelling on the basis of surface wave

As described above, the shape variation of the fundamental mode of Rayleigh wave ellipticity up to the trough is responsible for experimental variation of H/V shape curve, while the amplitude of H/V curve deviation from the ellipticity is attributed to the fraction of Love waves presence in the noise wave field. So, what is the consequence if we model the H/V curve by considering the noise wave field is dominated only by surface wave? The first attempt in this direction was made by Arai and Tokimatsu (2000). In this procedure, total average spectral power is estimated by the integration on the horizontal plane. This integration is estimated analytically (Malischewsky, 2015). Almost the similar approach was adapted, latter, by Lunedei & Albarello (2009) to model the H/V curve by total average spectral power. However, we will use the Arai & Tokimatsu (2000, 2004) procedure for modelling H/V curve as both gives almost the same results. Arai & Tokimatsu (2000, 2004) considered a model of N-parallel layers made-up from semi-infinite elastic medium, isotropic, solid, homogenous, where each layer is characterized by thickness H_i , S-wave velocity, V_{si} , P-wave Velocity, V_{pi} , and density, ρ_i (Fig.6.5). For the numerical simulation of surface waves, they used Harikrider (1964) procedure. The authors also utilized Lachet and Bard (1994) procedure, such as Fourier transform of vertical $L_V(\omega)$ and horizontal $L_H(\omega)$, point source having angular frequency (ω) and randomly distributed over the surface. From each of these points, waves are generated and propagated along the medium. As body waves attenuate quickly than the surface waves (Tokimatsu & Tamura, 1995), the displacement at an origin is considered to be produced by surface waves under far field source situation, which is, each distance between a source and origin (r_i) is greater than the one wavelength of both Rayleigh and Love waves.

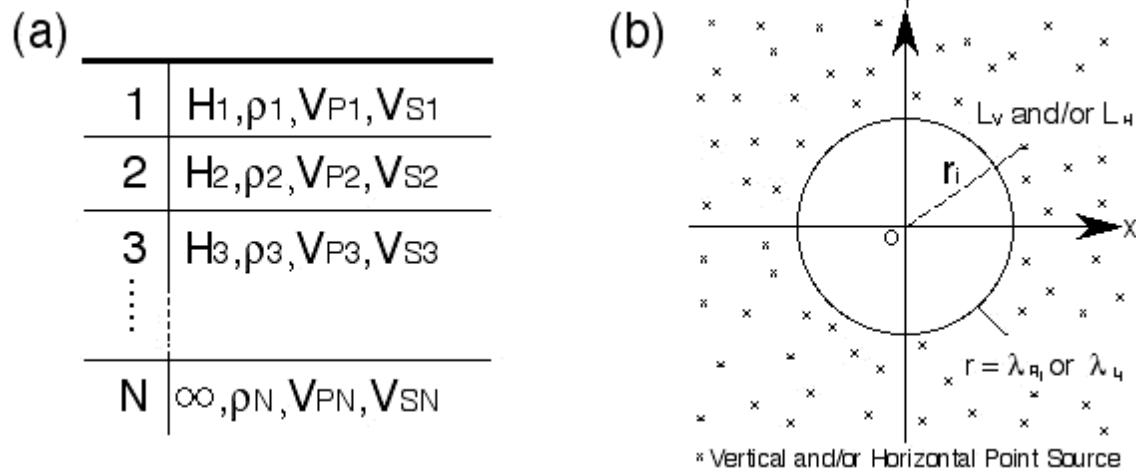


Fig.6. 5 Shows the geometry of (a) soil layer and (b) microtremor source models to formulate the theoretical H/V spectrum of surface waves considering the effects of fundamental and higher modes (from Arai and Tokimatsu, 2004).

Considering the i th vertical point force, $L_V(\omega)$, at a frequency ω , the vertical (demonstrated here by superscript (V)) and horizontal powers (P) (demonstrated by superscript (H)), the m th mode of Rayleigh waves (r) can be expressed as

$$P_{VRmi}^V(\omega) = L_V^2(\omega) A_{Rm}^2(\omega) |H_0^2(K_{Rm}r_i)|^2 \exp(-2h_{sc}K_{Rm}r_i) \quad (6.22)$$

$$P_{HRmi}^V(\omega) = L_V^2(\omega) A_{Rm}^2(\omega) (x_m^2 |H_1^2(K_{Rm}r_i)|^2 \exp(-2h_{sc}K_{Rm}r_i)) \quad (6.23)$$

where A_{Rm} is the medium response factor (Harkrider, 1964), k is the wavenumber, x_m is the ellipticity curve of the m th mode of Rayleigh waves on the free surface (Haskell, 1953), r is the distance between the origin and the point force, $H_0^{(2)}$ and $H_1^{(2)}$ are the Hankel functions of the second kind of zero and first order, and h_{sc} is the scattering damping ratio of soil ($h_{sc} > 0$).

In the same manner by considering the i th horizontal point force, $L_H(\omega)$, at a frequency ω , the vertical and horizontal powers of the m th mode of Rayleigh waves and m th mode of Love waves (r) may be expressed as

$$P_{VRmi}^H(\omega) = \frac{1}{2} L_H^2(\omega) A_{Rm}^2(\omega) (x_m^2 |H_1^2(K_{Rm}r_i)|^2 \exp(-2h_{sc}K_{Rm}r_i)) \quad (6.24)$$

$$P_{HRmi}^H(\omega) = \frac{1}{2} L_H^2(\omega) A_{Rm}^2(\omega) (x_m^4 |H_0^2(K_{Rm}r_i)|^2 \exp(-2h_{sc}K_{Rm}r_i)) \quad (6.25)$$

$$P_{HLmi}^H(\omega) = \frac{1}{2} L_H^2(\omega) A_{Lm}^2(\omega) (x_m^4 |H_0^2(K_{Lm}r_i)|^2 \exp(-2h_{sc}K_{Lm}r_i)) \quad (6.26)$$

A_{Lm} is the medium response for Love waves. Under the assumption that sources work independently, being randomly activated in time (i.e. the phases of all the sources are statistically independent), the vertical and horizontal power of all the waves (Love or Rayleigh) observed at the origin at a frequency ω can be computed by integration of each of equation (6.22) to (6.26) for all point sources and expressed in the form

$$P_{VR}^V(\omega) = \sum_{m=0}^M \int_0^{2\pi} d\varphi \int_{\lambda=0}^{\infty} P_{VRmi}^V(\omega) r_i dr_i \quad (6.27)$$

$$P_{HR}^V(\omega) = \sum_{m=0}^M \int_0^{2\pi} d\varphi \int_{\lambda=0}^{\infty} P_{HRmi}^V(\omega) r_i dr_i \quad (6.28)$$

$$P_{VR}^H(\omega) = \sum_{m=0}^M \int_0^{2\pi} d\varphi \int_{\lambda=0}^{\infty} P_{VRmi}^H(\omega) r_i dr_i \quad (6.29)$$

$$P_{HR}^H(\omega) = \sum_{m=0}^M \int_0^{2\pi} d\varphi \int_{\lambda=0}^{\infty} P_{HRmi}^H(\omega) r_i dr_i \quad (6.30)$$

$$\mathbf{P}_{HL}^H(\omega) = \sum_{m=0}^M \int_0^{2\pi} d\varphi \int_{\lambda=0}^{\infty} \mathbf{P}_{HLmi}^H(\omega) \mathbf{r}_i d\mathbf{r}_i \quad (6.31)$$

The highest mode considered is represented by M here. Considering far-field case $r_i > \lambda_{RmLm}$ (where the distance between source and origin is longer than wavelength of both Rayleigh and Love waves), Hankel function simplify to $H_n^2=2/\pi z$. The approximated form of the integral in Eq.6.27-31 becomes as:

$$\mathbf{P}_{VR}^V(\omega) = \kappa L_v^2 \sum_{m=0}^M \left(\frac{A_{Rm}}{K_{Rm}} \right)^2 \quad (6.32)$$

$$\mathbf{P}_{HR}^V(\omega) = \kappa L_v^2 \sum_{m=0}^M \left(\frac{A_{Rm}}{K_{Rm}} \right)^2 (x)_m^2 \quad (6.33)$$

$$\mathbf{P}_{VR}^H(\omega) = \kappa \frac{L_H^2}{2} \sum_{m=0}^M \left(\frac{A_{Rm}}{K_{Rm}} \right)^2 (x)_m^2 \quad (6.34)$$

$$\mathbf{P}_{HR}^H(\omega) = \kappa \frac{L_H^2}{2} \sum_{m=0}^M \left(\frac{A_{Rm}}{K_{Rm}} \right)^2 (x)_m^4 \quad (6.35)$$

$$\mathbf{P}_{HL}^H(\omega) = \kappa \frac{L_H^2}{2} \sum_{m=0}^M \left(\frac{A_{Rm}}{K_{Rm}} \right)^2 \quad (6.36)$$

where $\kappa=(2/h_{sc}) \exp(-4\pi h_{sc})$.

Once these estimations are made, surface waves power of all the horizontal and vertical components at frequency ω on origin can be estimated as

$$\mathbf{P}_{VS}(\omega) = \mathbf{P}_{VR(\omega)} = \mathbf{P}_{VR}^V(\omega) + \mathbf{P}_{VR}^H(\omega)$$

$$\mathbf{P}_{VS}(\omega) = \kappa L_v^2 \sum_{m=0}^M \left(\frac{A_{Rm}}{K_{Rm}} \right)^2 (x)_m^2 \left[\left(1 + \left(\frac{\alpha^2}{2} \right) (x)_m \right)^2 \right] \quad (6.37)$$

$$\mathbf{P}_{HS}(\omega) = \mathbf{P}_{HR(\omega)} + \mathbf{P}_{HL(\omega)} = (\mathbf{P}_{HR}^V(\omega) + \mathbf{P}_{HR}^H(\omega) + \mathbf{P}_{HL}(\omega)) \quad (6.38)$$

$$= \kappa L_v^2 \sum_{m=0}^M \left\{ \left(\frac{A_{Rm}}{K_{Rm}} \right) ((x)_m^2) \right\} \left(1 + \left(\frac{\alpha^2}{2} \right) (x)_m \right)^2$$

$$\mathbf{P}_{HL(\omega)=P_{HL}^H(\omega)} = \kappa L_v^2 \sum_{m=0}^M \left(\frac{\alpha^2}{2} \right) \left(\frac{A_{Rm}}{K_{Rm}} \right)^2 \quad (6.39)$$

Here, H/V ratio of the loading forces (L_H/L_V) is represented by α . This is unknown, so for the most cases it is considered constant here $\alpha=0.7$. The H/V curve for surface waves can be obtained as

$$\left(\frac{H}{V}\right)_S = \sqrt{\frac{P_{HS}(\omega)}{P_{VS}(\omega)}} = \sqrt{\frac{P_{HR}(\omega) + P_{HL}(\omega)}{P_{VR}(\omega)}} \quad (6.40)$$

Arai & Tokimatsu (2004) used these formulations (Eq.6.40) to estimate the theoretical H/V curves at two-test sites in Japan, where S-wave velocities were known from borehole measurements. Theoretical and experimental H/V curves (Fig 6.6) are in good agreement with each other. Indeed, while the ellipticity curves of the fundamental mode of Rayleigh waves, $(H/V)_{R_0}$ (shown in dashed line in Fig 6.6) are definitely unable to reproduce the H/V amplitude values of the experimental curves from microtremor recordings, $(H/V)_m$, the theoretical surface wave curves, $(H/V)_S$, show a good harmony. For IAG borehole model, the H/V curve for this surface wave case is given for 10 Rayleigh and Love higher modes (Fig 6.7).

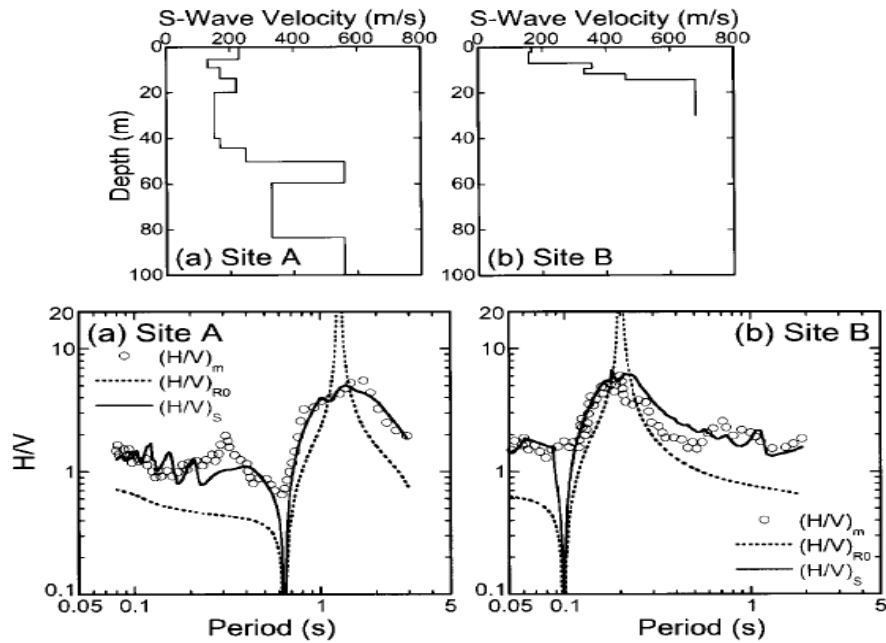


Fig.6. 6 Top panel show S-wave velocity profiles based on the results of PS logs at two sites A and B in Tokyo. Comparison of the H/V spectra of microtremors $(H/V)_m$ (open circles) with those of fundamental-mode Rayleigh wave and surface waves, $(H/V)_R$ and $(H/V)_S$ (broken and solid lines), respectively, computed for the soil profiles at sites A and B (Arai & Tokimatsu, 2004).

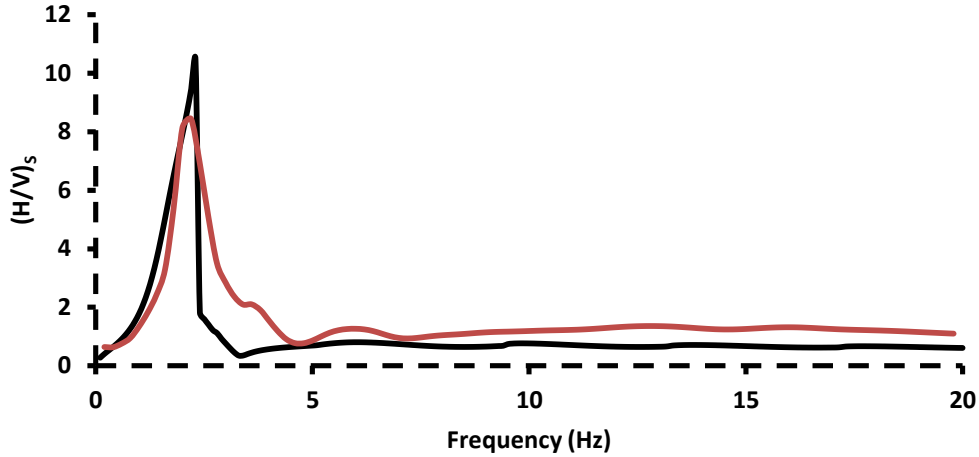


Fig.6. 7 Shows the IAG model curve by considering the contribution of surface waves (Rayleigh and Love waves) using Arai & Tokimatsu (2004) procedure, red line show the experimental H/V recorded at the borehole site (IAG).

6.4 Diffuse field assumption technique

Starting the H/V modelling from the Nakamura QTS (SH waves incident) and later outlining it modelling with the ellipticity and surface wave domination, it seems that there was a constant desire to include body waves effect in the modelling. A very recent development in the modelling of the H/V curve is the combination of all the previous three explanations in terms of all elastic wave inclusion and considered noise wave field as a diffused field arises from the multiple scattering. Sanchez-Sesma et al. (2011) proposed to consider ambient noise wave field as a diffuse wave field, which contain all the different types of waves (surface and body). The ambient noise wave field is generated by multiple random uncorrelated forces/sources near to or at the Earth surface. The wave field may contain the scattering effect of various elastic modes. The field intensities could be better described by a diffuse like situation. To assume that the noise wave field is diffuse, the H/V curve can be estimated for a receiver at Earth surface in terms of Green tensor imaginary part at the source (source and receiver are assumed to be at same location). The work of Sanchez-Sesma provides an idea of linkage between energy density and imaginary part of GF in 3D (energy densities of the noise wave field is proportional to the imaginary part of Green tensor). The H/V curve, obtained from the square root ratio of imaginary parts of GF (horizontal and vertical components), Eq.6.42, serves as an intrinsic property of the medium and therefore, its inversion can be used to retrieved subsurface soil profile. The detailed analysis of the procedure can be easily found in Sanchez-Sesma et al. (2011), García-Jerez et al., (2016) and Piña-Flores et al., (2017). A brief summary of this procedure is that autocorrelation of motion at a receiver sensor in a given direction is proportional to directional energy density (DED), and this DED is proportional to the imaginary part of Green tensor at that sensor (Sanchez-Sesma et al., 2011).

Patron et al. (2009) showed that in case of 3D homogeneous elastic half space, the horizontal displacement (radial and transverse) has fix energy proportion (e.g., $E_1(x, x, \omega) = E_2(x, x, \omega)$ and also $ImG_{11}(x, x, \omega) = ImG_{22}(x, x, \omega)$). For a diffused wave

field the H/V can be represented in terms of directional energy densities, assuming that source and receiver lies at same location (\mathbf{x}) on the surface of Earth as

$$\frac{H}{V}(\boldsymbol{\omega}) = \sqrt{\left(\frac{E_1(\mathbf{x},\mathbf{x},\boldsymbol{\omega})+E_2(\mathbf{x},\mathbf{x},\boldsymbol{\omega})}{E_3(\mathbf{x},\mathbf{x},\boldsymbol{\omega})}\right)} \quad (6.41)$$

$$\frac{H}{V}(\boldsymbol{\omega}) = \sqrt{\left(\frac{ImG_{11}(\mathbf{x},\mathbf{x},\boldsymbol{\omega})+ImG_{22}(\mathbf{x},\mathbf{x},\boldsymbol{\omega})}{ImG_{33}(\mathbf{x},\mathbf{x},\boldsymbol{\omega})}\right)} \quad (6.42)$$

where in (6.41)

$$E_m(\mathbf{x}, \boldsymbol{\omega}) = \rho\omega^2 \langle \mathbf{u}_m(\mathbf{x}, \boldsymbol{\omega}) \mathbf{u}_m^*(\mathbf{x}, \boldsymbol{\omega}) \rangle = -2\pi\mu E_s \mathbf{k}_s^{-1} Im[G_{mm}(\mathbf{x}, \mathbf{x}, \boldsymbol{\omega})] \text{ where } \mathbf{m} = 1, 2, 3$$

$E_1(\mathbf{x}, \mathbf{x}, \boldsymbol{\omega})$, $E_2(\mathbf{x}, \mathbf{x}, \boldsymbol{\omega})$ and $E_3(\mathbf{x}, \mathbf{x}, \boldsymbol{\omega})$ are the energy densities at coincident source and receiver (\mathbf{x}, \mathbf{x}), at frequency $\boldsymbol{\omega}$, and subscripts 1,2,3 show the horizontals (east-west, and north south) and the vertical components, respectively. Energy density is found at point \mathbf{x} in direction \mathbf{m} . $\boldsymbol{\omega}$, ρ and \mathbf{u}_m are angular frequency, layer density and displacement at point \mathbf{x} , respectively. $E_s = \rho\omega^2 s^2$ is the strength of diffuse illumination in terms of shear wave average energy density, μ is shear wave modulus, $\langle \dots \rangle$ bracket shows the azimuthal average, $\mathbf{k}_s = \frac{\boldsymbol{\omega}}{V_s}$ shear wave number, V_s shows medium S-wave velocity. The symbol $(.*)$ shows complex conjugate process. The medium response in a direction \mathbf{m} (of impulse load and acting in same direction) is indicated by G_{mm} . The H/V curve obtained in this manner is linked to the intrinsic property of medium. The resulted H/V curve from the diffuse-field approach might allow its inversion without considering any supplemented information (dispersion curve).

Integration in the horizontal wave number domain at specific frequency ($k, \boldsymbol{\omega}$) is evaluated to imaginary part of Green function (Sanchez-Sesma et al., 2011). This integration in horizontal wave number domain was done to separate different elastic waves. Similarly, the contribution from surface and body waves is achieved by discrete wave number method like Bouchon's (2007). However, recently, García-Jerez et al. (2016) adopted a new procedure to evaluate the integral. We are following García-Jerez et al (2016) procedure, here. In this procedure, the horizontal wave number components are extended to complex wave number domain. Latter, Cauchy's residue theorem was utilized to estimate the surface wave contribution at simple pole along the real k axis (see for detail García-Jerez et al., 2016). The contribution of body waves to imaginary part of Green function are estimated by integration but at discrete intervals $(\mathbf{0}, \boldsymbol{\omega}/V_{HS})$ where V_{HS} represent the half-space shear wave velocity. For the situation of

coincident source and receiver, the imaginary part of Green function is given by García-Jerez et al. (2013; 2016) as

$$\begin{aligned} \text{Im}G_{11}(\mathbf{0}, \mathbf{0}, \omega) = \text{Im}G_{22}(\mathbf{0}, \mathbf{0}, \omega) = \\ -\frac{1}{4}(\sum_m x_m^2 A_{Rm} + \sum_m A_{Lm}) + \frac{1}{4\pi} \int_0^{\omega/V_{HS}} \text{Re}(f_{P-SV}^H + f_{SH}) dk \end{aligned} \quad (6.43)$$

$$\text{Im}G_{33}(\mathbf{0}, \mathbf{0}, \omega) = -\frac{1}{2}(\sum_m A_{Rm}) + \frac{1}{2\pi} \int_0^{\omega/V_{HS}} \text{Re}(f_{P-SV}^V) dk \quad (6.44)$$

$f_{P-SV}^H, f_{P-SV}^V, f_{SH}$ are data kernel for body waves, x_m is Rayleigh waves ellipticity curve. The accurate locations of poles for the estimation of A_{Rm}, x_m, A_{Lm} are found by dispersion curve in (k, ω) domain (see for detail García-Jerez et al., 2016, Piña-Flores et al., 2017). For IAG borehole model, the H/V curve, under diffused field assumption from the given imaginary Green function ratios, are shown in Fig.6.8. The values of Green function given in Eq 6.43 and 6.44 are shown in Fig.6.9 for the same model.

It is noted that, in this case of DFA, the H/V modelling is resting on the assumption that noise wave field is diffused. So, the question arise naturally that, is noise wave field really diffused? If the ambient noise wave field is diffused, it should fulfill the three criteria of general diffused field, which are: 1) The wave field (phases) should be random; 2) Waves should come from all the directions toward the receiver, which means that the wavefield must be isotropic with azimuth; 3) The amplitude of incident waves should be same at a given point anywhere for a specific spatial domain. Mulagia (2012) followed these three criteria to seek its answer and statistically check these assumptions of diffused wavefield for seismic noise at 65 different geographic locations of diverse geological conditions and recording environments. He showed, statistically, that the seismic noise wave field is not diffused and the noise wave field is not azimuthally isotropic in all these cases.

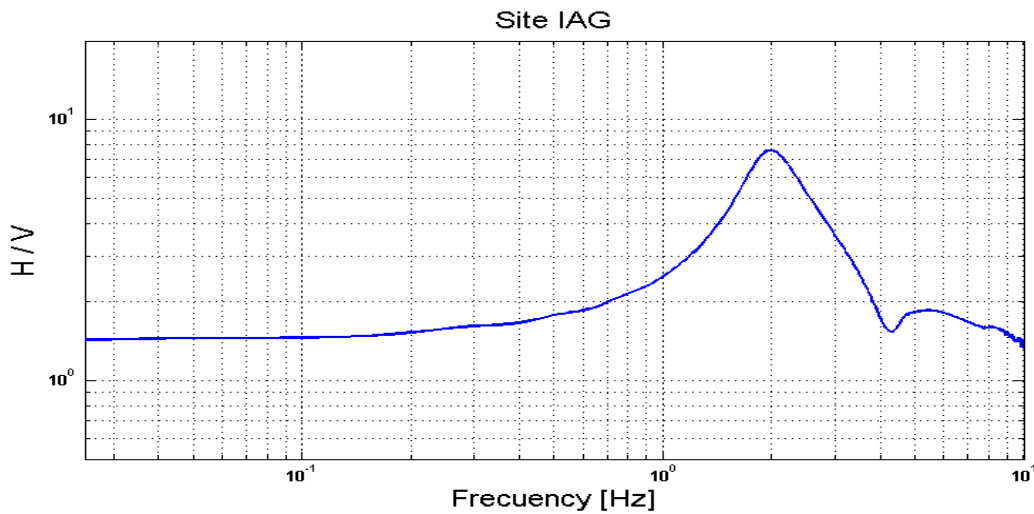


Fig.6. 8 Shows the H/V curve for the IAG borehole model by using full wavefield under diffused field assumption.

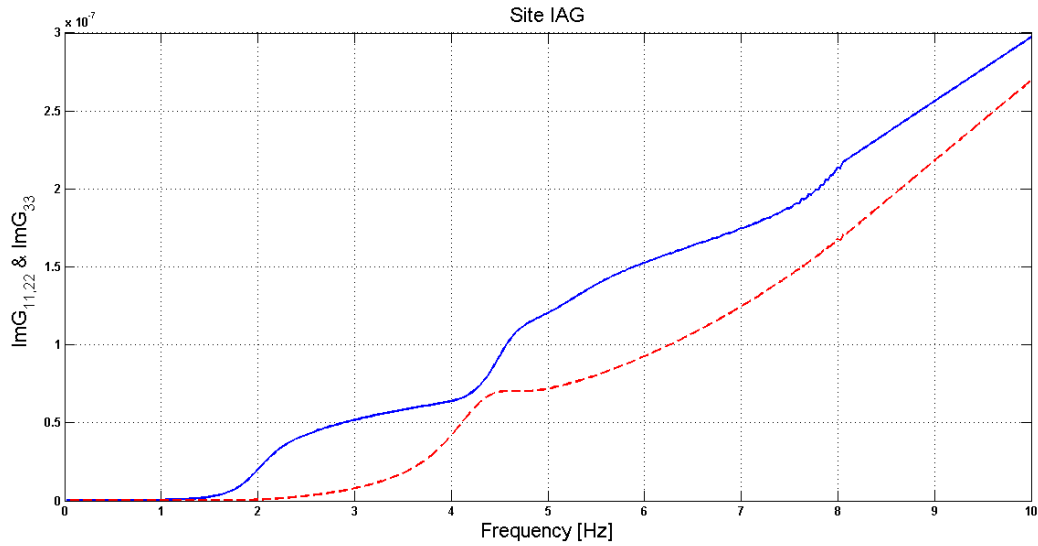


Fig.6. 9 Shows the imaginary part of Green function for both horizontal component ImG_{11}, ImG_{22} in blue, and imaginary part of Green function for vertical component for ImG_{33} .

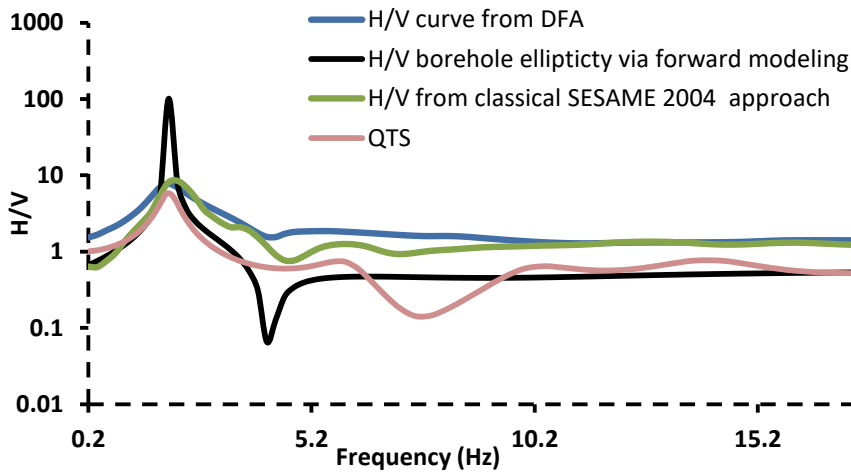


Fig.6. 10 Show different curve comparison with that of H/V obtained from the noise data recorded at IAG borehole site.

To draw the conclusion from the above analysis, we can easily observe that to model the H/V curve with surface wave domination noise field case gives a better result in a comparison with all other modeling techniques of the H/V curve (Fig 6.7). However, the shape of the H/V curve is dominated mostly by the fundamental mode of Rayleigh waves (as it present for all the frequency range, while higher mode occurs only for specific frequencies, Fig 6.4). Hence, for the inversion of the H/V curve, it necessary to remove the effect of Love waves presence. To find the fraction of Love waves that contributes to the noise wave field, it can be done from the 3 component sensors array analysis (SPAC and FK method). However, for a single 3 component

station case, we need some Love waves effect removal technique. In last chapter, we will discuss two techniques, which are used to remove the effect of Love waves from the H/V curve for single 3C sensor.

Chapter7: The peak frequency (f_0) and shape of the H/V curve

7. Introduction

In the previous section, we outlined all the different theoretical developments that serve as an explanation for the H/V curve modelling. Although all these theories and explanations are used to interpret the H/V curves of experimental practices somehow equally, However, the ellipticity and DFA theory are those which require most attention. As indicated by Mulagia (2012), the noise field is not diffused and any assumption based on such hypotheses will lead to a biased interpretation of the data. However, any suggested theory to a physical model is an idea which is tested against reality (Piña-Flores et al., 2017). It can be said that every modelling technique of the H/V is footed on some assumption, for example, Nakamura's (QTS, 1989) explanation is based on the assumption that wave field is dominated by body waves and that horizontal and vertical motions are same at bedrock level. The Rayleigh waves ellipticity theory of the H/V modelling is supported with the supposition of noise wave field domination by the Rayleigh waves. The surface waves dominancy of noise wave field (Arai & Tokimatsu, 2000-2004) exempt any body waves contribution. Recently, Lunedei & Malischewsky (2015) reviewed the development of the H/V modelling theories over time and concluded that the two main research lines are the ellipticity of Rayleigh wave and diffused field assumption for the explanation of the H/V curve technique. The H/V curve was first utilized only for the H/V peak frequency association with the fundamental frequency f_0 of the site (Nakamura 1989, 2000). The peak frequency of the experimental curve match with S-resonance frequency of site when high S-wave velocity contrasts exists between soil and bedrock (SESAME, 2004). However, the overall shape of the experimental H/V curve is generally higher than the ellipticity curve, except at the peak of the H/V curve (Tokimatsu, 1997; also see Fig.7.1). At the peak of the ellipticity, the vertical component vanishes and the peak of the ellipticity curve is elevated as compared to the experimental curve. This mismatch between the amplitude of the curves is attributed to the presence of body waves around the peak frequency f_0 . As in the case of Rayleigh waves domination, the horizontal component vanishes, which gives rise to sufficiently higher peak, therefore this discrepancy in peak can be associated with the effect of body and Love waves presence on the horizontal component (Parolai et al., 2005). Sánchez-Sesma et al. (2010; 2011a) comes with a solution to consider the noise wave field as diffuse field and assumed equipartition of energy between two horizontal and vertical components or between P-waves and two polarized component of S-waves (P, S_v, S_h) carrying 1/3 of total available energy. In this situation, the H/V can be obtained from the ratio of the Green function imaginary part of the horizontal and vertical components, which are obtained by the autocorrelation of the coinciding source and receiver over a layered medium. In the coming section, we will check the deviation of peak frequency of the H/V curve from S-wave resonance frequency based on these two main theories.

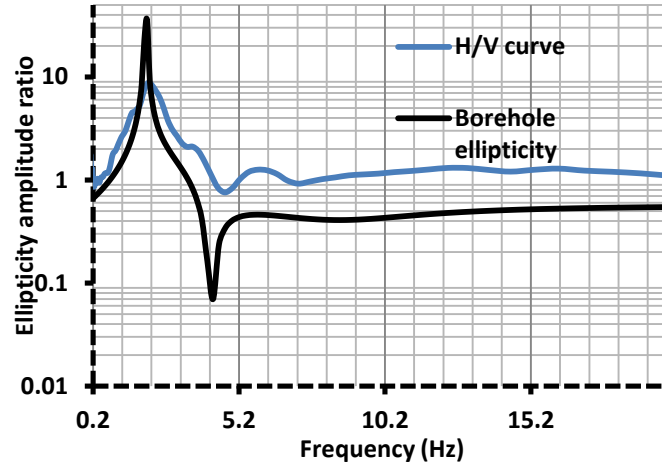


Fig.7. 1 Shows the comparison of H/V curve and the theoretical borehole ellipticity curve for the IAG site; the blue shows the experimental H/V curve, while black line shows the borehole ellipticity curve.

7.2 Peak frequency (f_0) of the H/V curve

As described above, one of the main uses of the H/V curve is to identify the resonance frequency f_0 of S-wave (fundamental period of a site that maximum S-wave displacement amplification occurs). The H/V curve generally results in a peak which corresponds to the S-wave resonance frequency for high S-wave contrast between soil and rock. This peak frequency is used to obtain the average velocity within the sediment package if the depth to the bedrock is known by relation $f_0 = Vs_0/4h$. In the same way, the fundamental frequency of the site is obtained if thickness or S-wave velocity of soil layer is known in advance. We observed that the peak frequencies of H/V curves strongly depends on the average travel time of the S-wave to reach from bedrock to the surface ($f_0 = 1/4T$). Analogous travel time for different models will result on the same peak frequency. This is elaborated for a simple case of one layer model with six different cases. For the six models in Fig 7.2, model A ($h=400$ m, $V_{soil}=800$ m/s, $T=0.5$ second), model B ($h=200$ m, $V_{soil}=400$ m/s, $T=0.5$ second) and C ($h=100$ m, $V_{soil}=200$ m/s, $T=0.5$ second) results on a fundamental frequency at 0.5 Hz (Fig 7.3). Similarly, the other three models, model D ($h=100$ m, $V_{soil}=400$ m/s, $T=0.25$ second), model E ($h=50$ m, $V_{soil}=200$ m/s, $T=0.25$ second) and model F ($h=40$ m, $V_{soil}=160$ m/s, $T=0.25$ second) results on a peak with frequency of 1.01 Hz. These curves were obtained by the ellipticity and DFA based forward modelling. The dispersion curves of the model A, B, C and D, E, F are also shown in Fig 7.2., which demonstrate that the dispersion of the Rayleigh waves begin at the frequency above the fundamental frequencies of 0.5 and 1.01 Hz, respectively. This phenomenon was firstly observed by Tazime (1957) and Scherbaum (2003), that is, at the fundamental frequency of the site the medium act as filter and all the lower frequencies are filter out. Therefore, the dispersion of Rayleigh waves is only visible above the fundamental frequency of the site.

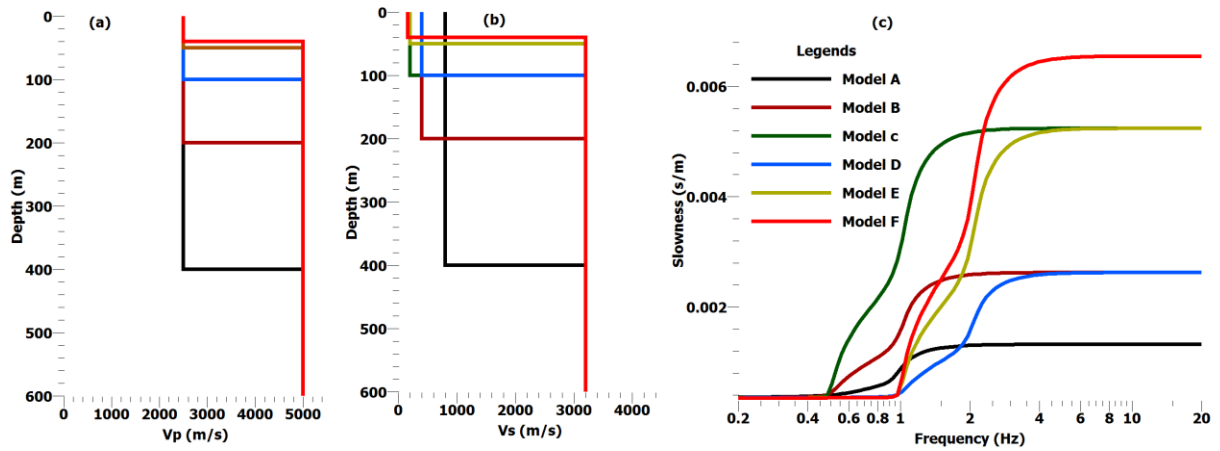


Fig.7. 2 Shows the (a) Vp and (b) Vs profiles for six different models. The corresponding dispersion curves are also given for the six models (c).

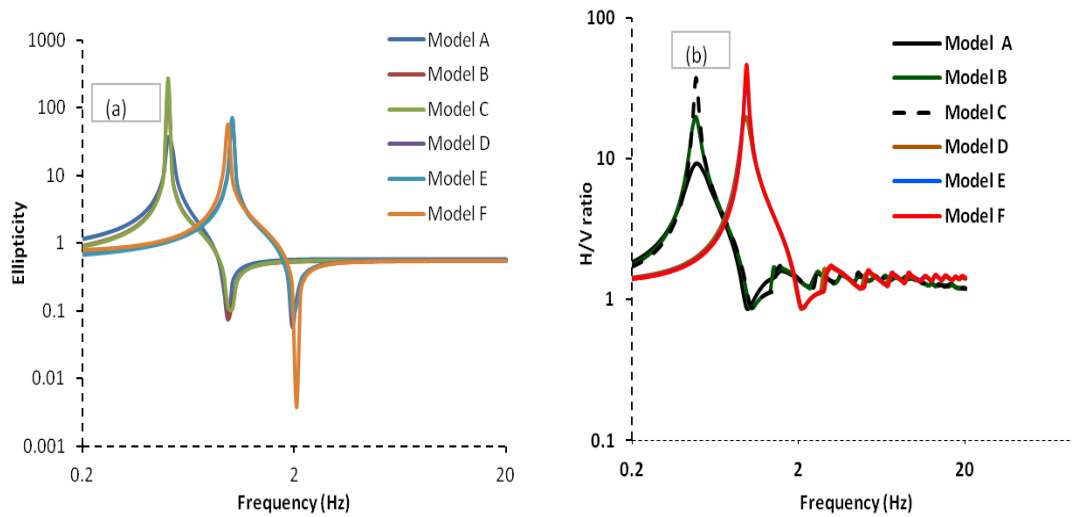


Fig.7. 3 Shows the H/V curve obtained via ellipticity (a) and DFA approach (b) for six different models shown in Fig.7.2.

We analysed the effects of different seismic wave field contributions around the peak frequency and their deviations from the S-wave resonance frequency, by considering three different situations: (a) only the presence of the Rayleigh waves; (b) the effect of both the Rayleigh and Love waves; (c) the equal contribution from all the seismic wave types. In case (a) the exact ellipticity is estimated for layered Earth case by the Dunkin (1965) formulation, following the eigenvalue problem described in Thomson (1950) and Haskell (1953). Ellipticity is computed from the full stack of the eigenvalues and the fast root search algorithm by Wathelet (2005). In case (b), for the surface waves, the H/V is estimated by a method proposed by Arai & Tokimatsu (2000, 2004). In this case, the seismic sources, that generate the waves, are assumed to be continuously distributed on the surface of the Earth with independent phases. The total spectral power is estimated by integration analytically on the horizontal plane. The sources that generates

seismic waves are assumed to be located one wavelength (both surface) away to ensure surface wave arrival at the receiver. For the convergence of the power integral, Arai & Tokimatsu (2000, 2004) considered an exponential damping factor generated by the scattering of surface waves in the subsoil layered model. In case (c) the DFA and H/V are estimated from the autocorrelation of a coinciding source and receiver (Sánchez-Sesma et al., 2010; 2011a). This autocorrelation results on the imaginary part of the Green function. The H/V is obtained from the square root ratio of the combined horizontal and vertical imaginary part of the Green function.

The deviation of the peak frequency from S-wave resonance is demonstrated for IAG and a second model is taken from Hobiger et al. (2013). The peak frequency shift is obtained for the Poisson ratio ranges from 0 to 0.5. The Poisson ratio varied by changing the shear wave velocity of the first layer, V_{s0} . For this range of Poisson ratios, the H/V curves were obtained by forward modelling by considering the seismic wave field of the three previous cases. The peak frequencies deviation from the S-wave resonance frequency is shown in Fig 7.5a. The relative errors of the frequencies peak for each case with S-wave resonance frequency are shown in Fig 7.5b. It can be observed in Fig 7.5b that by considering the contribution from all the type of waves around, the peak shows little relative error with S-wave resonance frequency for all Poisson ratio range. However, the relative error in frequency estimated for Rayleigh and surface waves case is less than 10% for the Poisson ratio range 0.4 to 0.5. Similarly, the relative error between the S-wave frequencies is shown at Hobiger et al (2013) model in Fig.7.6c. Again, the relative error in frequencies estimated for Poisson ratio 0.4 to 0.5 is lesser. The typical range of Poisson ratio for the soil of engineering importance is 0.4 to 0.5 (Sharma et al., 1990, Davidovici, 1985). The Poisson ratio of 0.4 of the soil layer signify that V_p in the soil layer should be 2.4 times higher than V_{s0} . In general, this V_p is three-four times higher than S-wave velocity in the soil layer (Nakamura 2000). So, if this is the case then even Rayleigh waves domination of noise wave field closely match the S-wave resonance frequency.

This analysis showed that, incorporating the contribution of body waves into the main peak of the H/V curve, the relative error of the S-wave resonance frequency is lesser, comparatively. However, it still does not match completely with the S-wave resonance frequency. The reason might be the proportion of body waves considered, which might not be the true one as in the case of DFA, where an equal contribution is considered for all the seismic waves. Concerning the experimental procedure of the H/V, mismatch with Rayleigh waves ellipticity indicates that the peak of the H/V curve contains the effect of both body and surface waves (Hobiger et al., 2009). That is why the peak of the H/V curve closely follows S-wave resonance frequency (SESAME 2004) as compared to the other case of wave dominance around the peak.

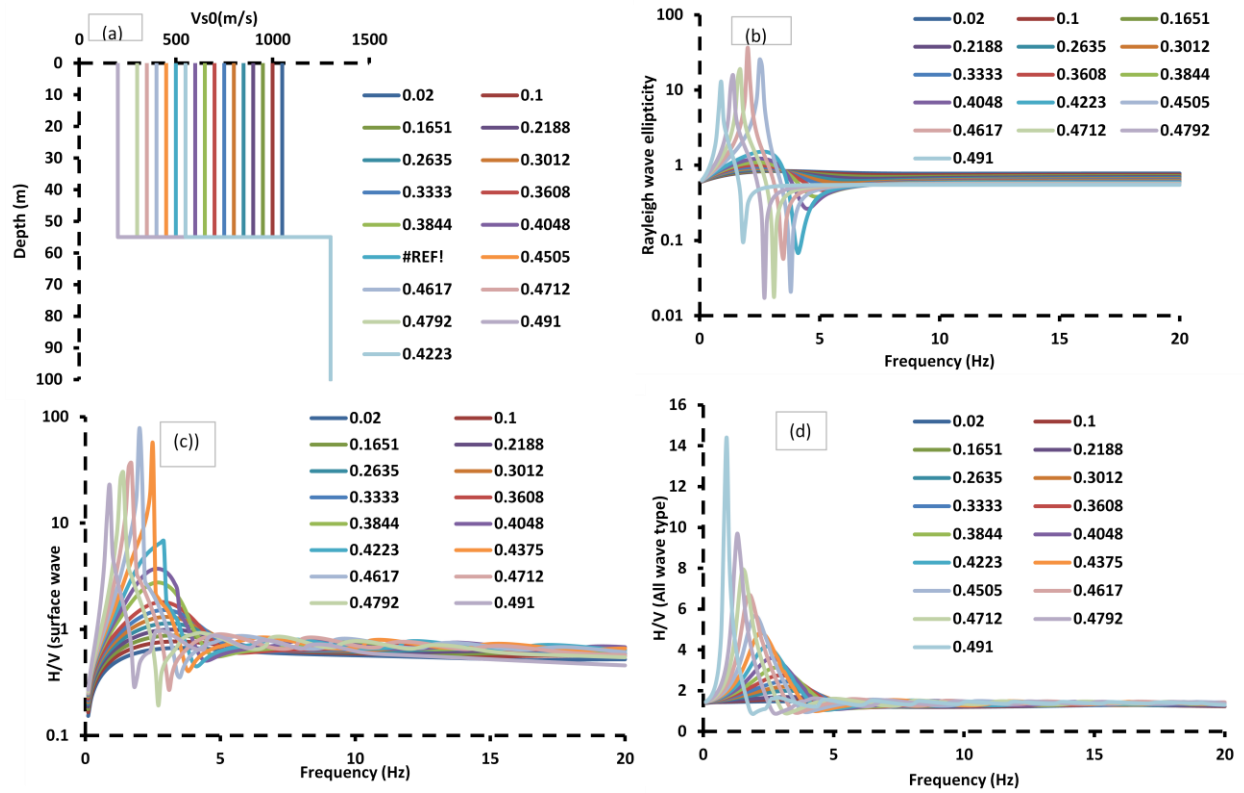


Fig.7. 4 Shows (a) the change in Poisson values by changing V_{s0} value of soil layer by considering Rayleigh waves (a) ; (b) Surface wave contribution only ; (b) shows the peak frequency of all wave.

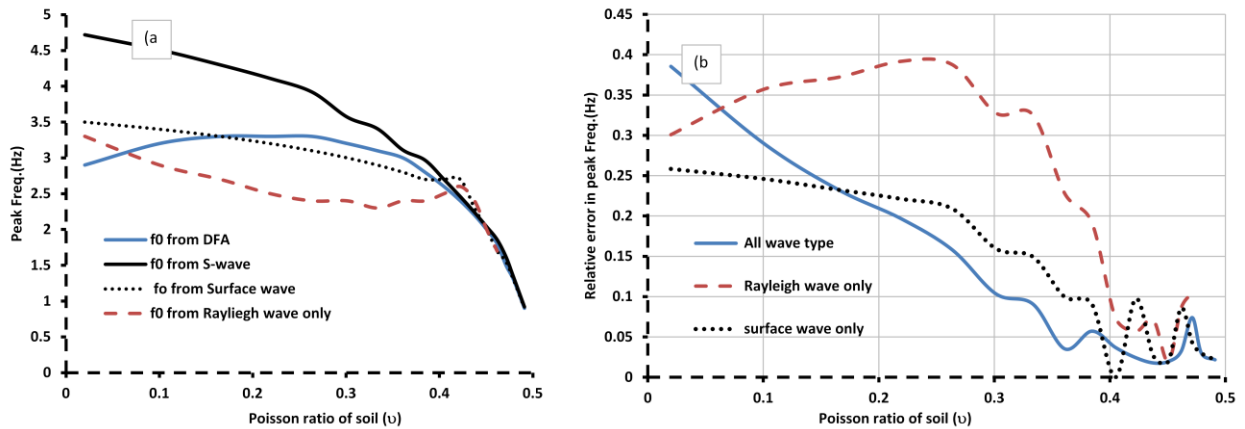


Fig.7. 5 Shows the (a) the peak frequencies deviation from S-wave resonance; (b) the relative error between different wave contributed H/V curve and S-wave resonance.

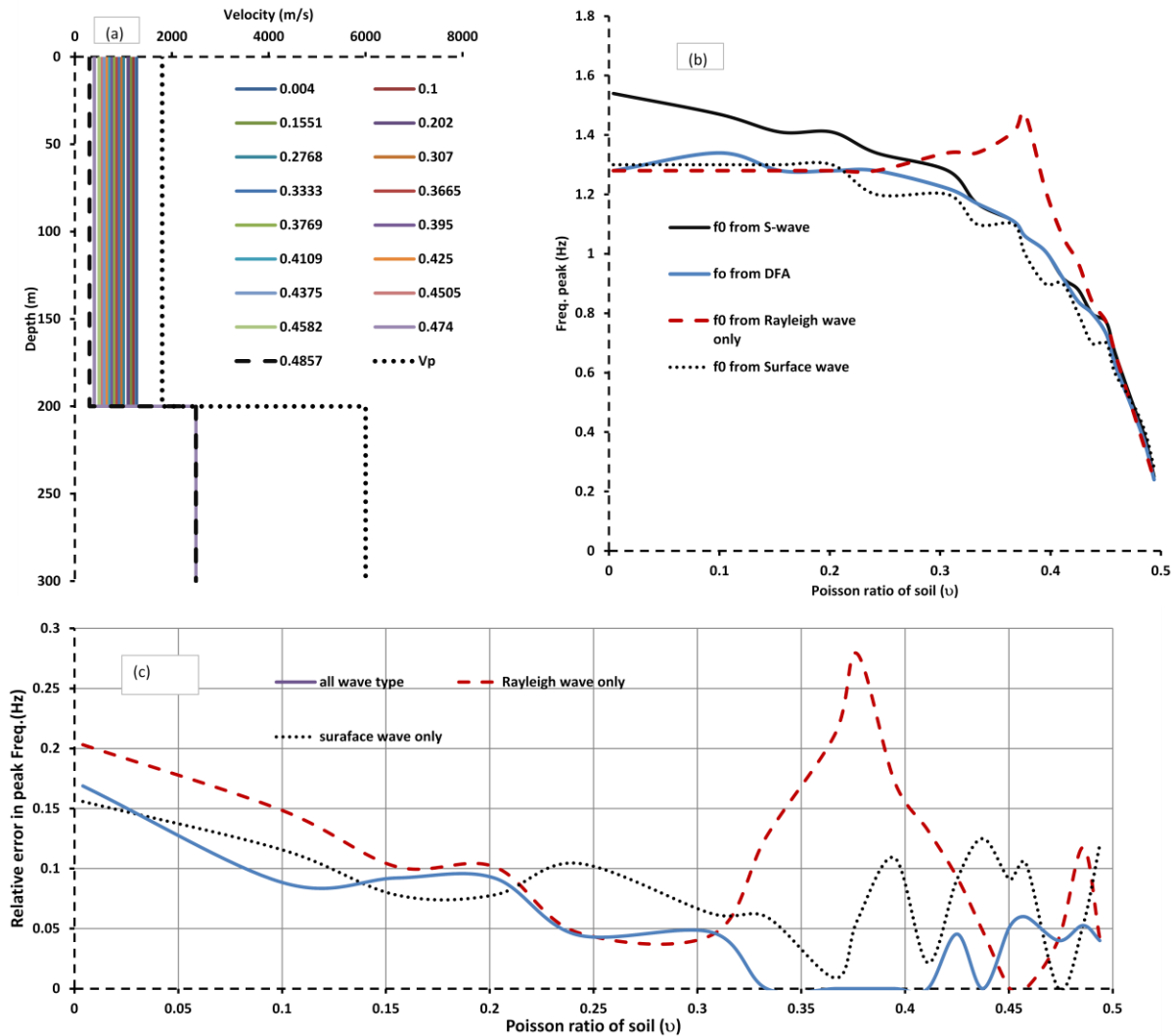


Fig.7. 6 Shows the (a) V_p and V_{s0} of the soil layer changing which corresponded to Poisson ratio variation (b) the peak frequencies as a function of Poisson ratio (c) the relative error between different wave contributed H/V curve and S-wave resonance.

7.3 Sensitivity analysis of the peak frequency f_0 for ellipticity and DFA H/V curves

As described above, at present the two main modelling techniques commonly used for the experimental H/V curve modelling are ellipticity and DFA (diffused field assumption). We have also discussed that the most important information derived from the H/V curve is the peak frequency of the curve, and hence, important information about the site are estimated from this peak frequency such as thickness and V_{s0} (Parolai, 2002, Ibs-von Seht, 1999, Tuan, 2015). It is of prime importance to check the sensitivity of these peaks for both ellipticity and DFA H/V curves to the layer parameters V_p, V_s, h and ρ (P-wave velocity, S-wave velocity, thickness and density of mass). This analysis is done under the assumption that, apart from modelling a physical problem, it is of equal importance that the modelling solution should be sensitive to the real Earth properties as well. So, our aim was to check which of the H/V modelling techniques

(DFA or ellipticity) give more sensitivity to the Earth parameters that it should be more suited to be adopted for the inversion for H/V curve.

Xia (1999) analysed different layer parameters (V_s , V_p , ρ and h) that can affect the shape of the Rayleigh waves dispersion curve for a given model. The goal was to find that parameter which affects less or more the dispersion curve. By knowing the less affecting parameter, it can be omitted from the inversion analysis to reduce the number of the unknown during the inversion. The Rayleigh-wave phase velocity (dispersion curve) is the complicated function of four parameters: S -wave velocity, P -wave velocity, density ρ and thickness of the layer h . Xia (1999) observed that the most affecting parameters influencing the Rayleigh-wave phase velocity curve are the shear wave velocity, thickness, density and primary wave velocity, respectively. Here, we modified Xia (1999) dispersion curve and re-plotted it as slowness vs frequency (slowness is used to clearly observed the effect of parameters variation on higher frequencies). The frequency range used for the analysis is 0.2 Hz to 20 Hz (this range of frequencies is commonly used for H/V curve for the near surface engineering application). The model used for demonstration is taken from Xia (1999, Fig7.7). The effect of these four parameter changes is displayed in Fig 7.8.

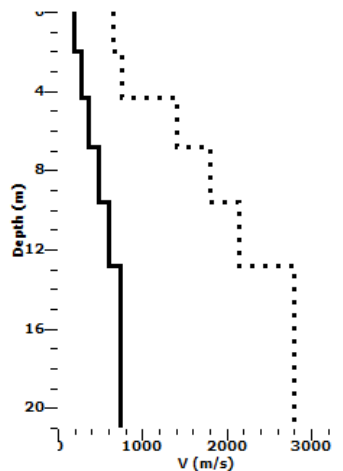


Fig.7. 7 Model used by Xia (1999) for finding out the sensitivity of Rayleigh wave dispersion curve for different parameters (solid line shows the profile of V_s , while dotted line the V_p profile).

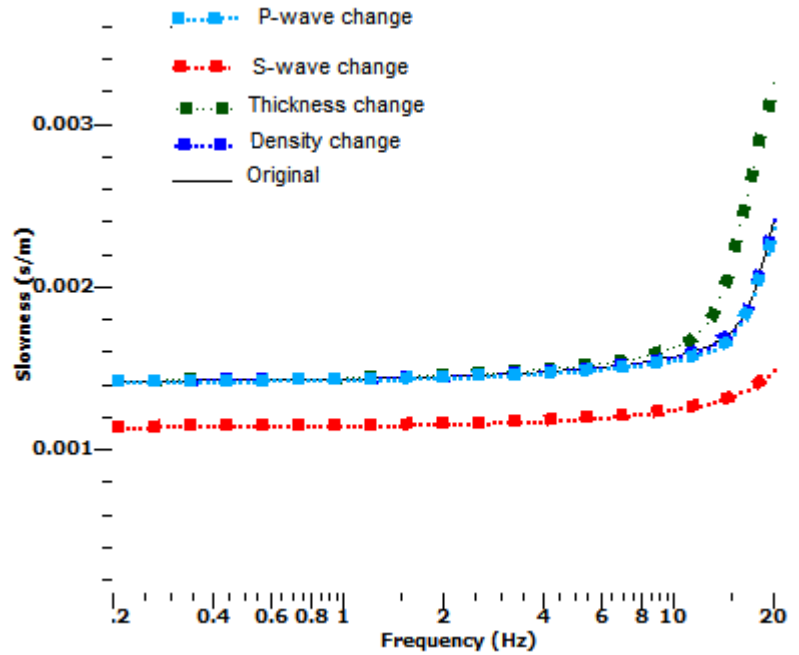


Fig.7. 8 Shows the contributions to Rayleigh-wave phase velocity by 25% changes in each model parameter (V_s , V_p , ρ and h). The solid black line (not visible clearly due to overlapping of density and P-wave change based dispersion curve) is Rayleigh-wave phase slowness attributed to the Earth model. The dispersion of each parameter change is shown in with different colours (modified from Xia 1999).

In the same manner, the modelling of the H/V curve is done for layered Earth model where each layer are characterized by properties of V_s , V_p , ρ and h . Checking the most affecting parameters on the peak frequency of the H/V (ellipticity and DFA approach) that will be detailed in this section. Usually, the analysis should be done with real data to check the sensitivity of these four parameters (shear wave velocity, thickness, density and primary wave velocity) on the peak of the curve. However, to test the effect of one parameter on the peak frequency (i.e., V_s) the other parameters (V_p , h , ρ) should be kept constant to observe its influence clearly. However, in real, such a preferred situation is approximately impossible. Therefore, the only scenario left is to check the effect of this parameter for different models with forward modelling and simulation with the two mostly used procedures for the H/V modelling/inversion. The positive side of such analysis is that at a single time one of the parameters (V_s , V_p , ρ and h) of the ground model is altered, while keeping all the other properties fixed. The change with H/V peak and shape is documented for this parameter variation and a general behaviour identification for later use. The IAG and Hobiger et al. (2013) models are used for this analysis, too. The models have four layers over the bedrock at 55 m and 200 m (Fig7.9). These four layers velocity were reduced to a sediment package of one layer over the bedrock to easily handle different parameters change analysis and also for the fact that H/V analysis are sensitive to the travel time taken by S-wave to reach the surface from bedrock (Fig 7.9).

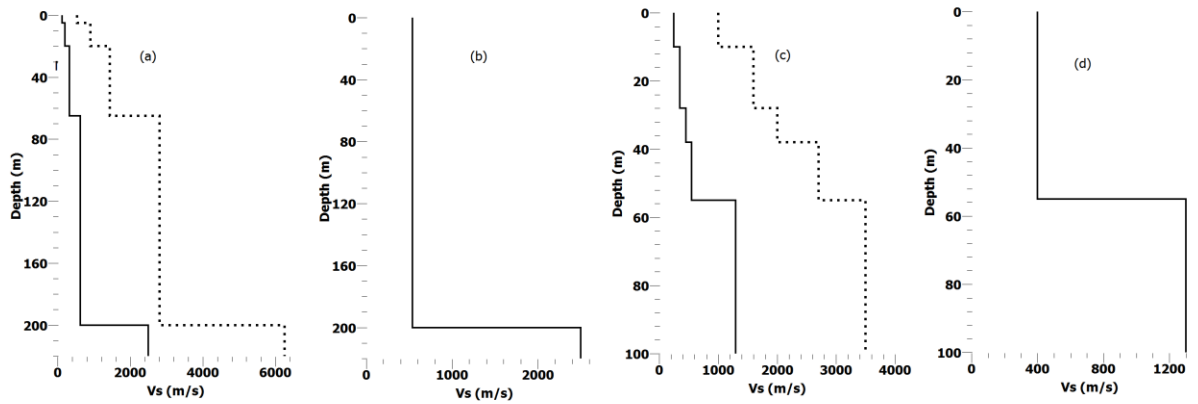


Fig.7. 9 Shows IAG-and Hobiger models, (a) and (c); solid line shows Vs profiles, while dashed lines show Vp profiles. (b) and (d) are the IAG and Hobiger models reduced to one layer above the bedrock (Vs profiles only).

7.3.1 Thickness (h), density, P-wave and S-wave velocities effects on the peak frequency

From the sensitivity analysis, we found that the first parameter, which affects the peak frequency of the H/V curve (for both ellipticity and DFA) the most, is the thickness (h) of the soft sediment package. This effect of thickness on the peak frequency (fundamental frequency) has been observed extensively by Scherbaum (2003). Here, we extended this analysis to the deviation of the H/V peak frequency from the S-wave resonance and also included the DFA based H/V curve in the analysis. The scheme is to change (increase and decrease, respectively) the sediments package thickness by 50%, 25%, 20%, 15%, 10% and 5% of the original thickness (IAG model, 55 m and Hobiger model, 200 m; Fig.7.10). The peak frequency of the H/V curve is observed to shift toward the lower frequencies in case of increasing thickness, while shifted toward higher frequencies in case of decreasing thickness of the sediment package for both ellipticity and DFA approach H/V curves (Fig. 7.11). Both the Rayleigh waves ellipticity and DFA approach H/V show a similar trend in shifting the peak trend. The shift of peak frequency from that S-wave resonance frequencies are shown in Fig. 7.12. The deviation in peak frequencies from the S-wave resonance frequencies in case of IAG is greater compared to the Hobiger model case (Fig 7.12a,b). This shift of ellipticity peak from S-wave resonance frequencies is higher almost 11% for different thicknesses. However, we observed that the peak frequencies of the ellipticity curve closely match the S-wave resonance frequencies when the Vs-contrast between soil and bedrock is 3.6 or higher (see, for example, Fig 7.19). The Vs value for the rock of IAG model we used is 1300 m/s, while for the soil we used 400 m/s, which give a Vs contrast of 3.25 lesser than the 3.6. So, we increased the Vs contrast up to 3.6 by taking bedrock velocity at 1440 m/s. This Vs contrast increase when checked for the thickness variation and compared with S-wave resonance frequency gives a deviation of almost less than 5% overall (Fig 7.13c). The deviation in peak frequencies between ellipticity curve and that of the S-wave resonance frequency is even less than 3% in Hobiger model case, where the Vs-contrast is 4.6 between soil and bedrock velocities. This analysis shows that for high-velocity contrast (3.6 or higher) the deviation of ellipticity peak from S-wave resonance frequency is less than 5%. So, we can say

that in the case of high-velocity contrast the ellipticity modelling of H/V gives a satisfactory result for the S-wave resonance frequency.

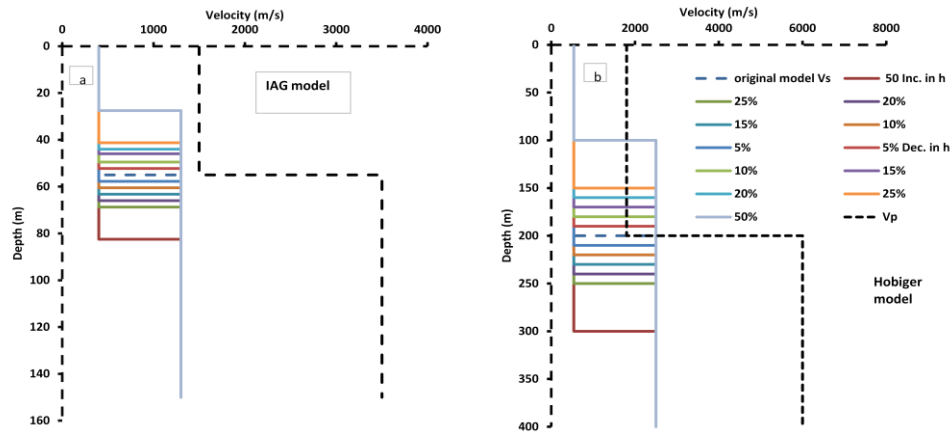


Fig.7. 10 Shows the thickness variation for IAG and Hobiger models.

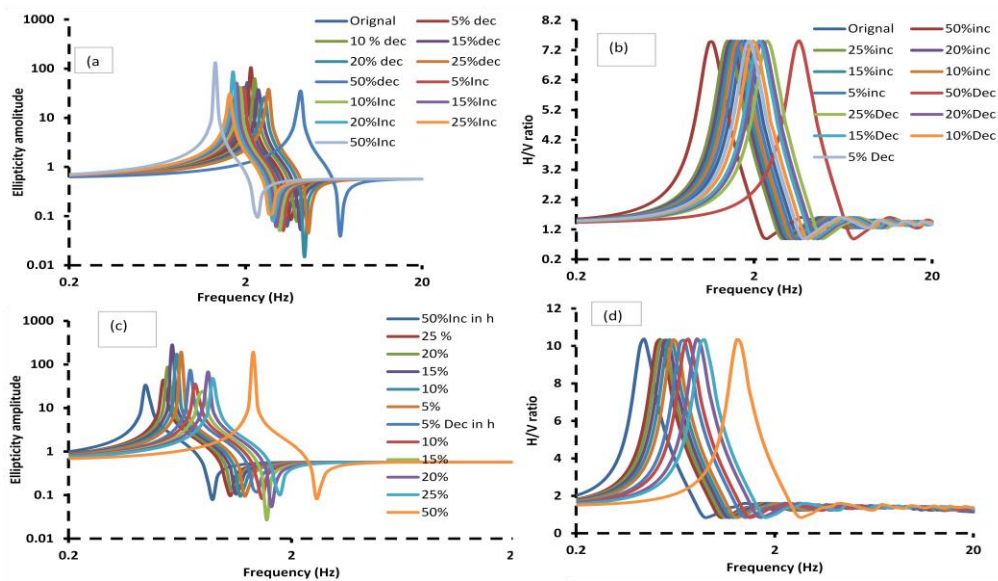


Fig.7. 11 Shows changes in thickness vs change in frequency peak of ellipticity curve; the peak shifted toward the lower and high frequencies with increase and decrease of thickness, respectively, for both ellipticity DFA approaches. Colours are assigned to each increase and decrease along with Vs profile.

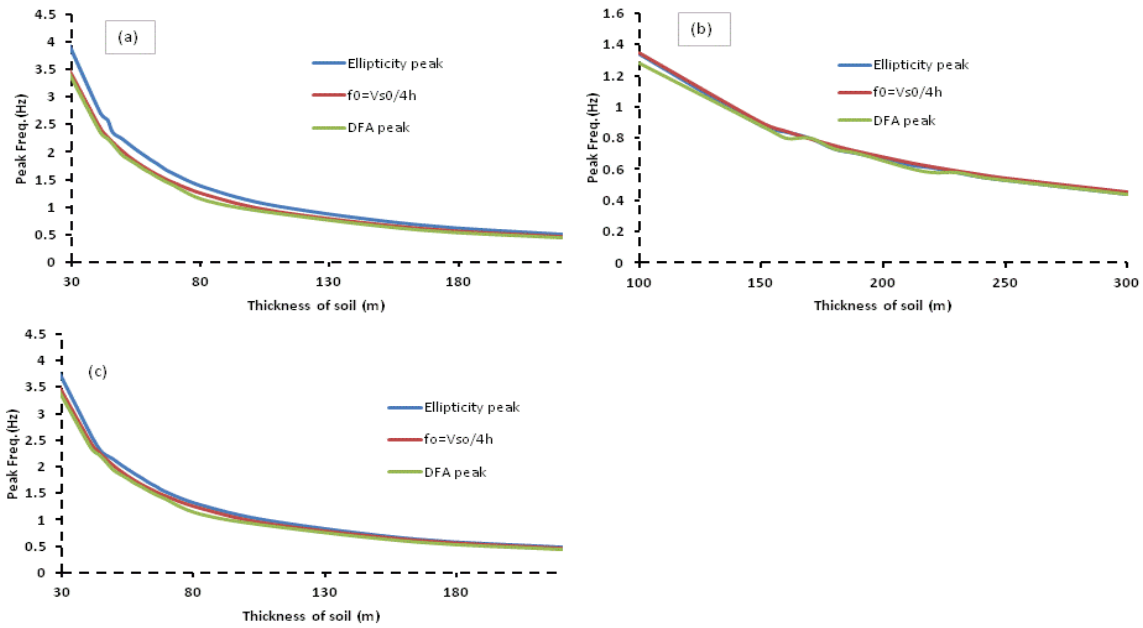


Fig.7. 12 Shows the deviation from fundamental frequencies of S-wave with that of ellipticity curve and DFA based H/V curve. (a) IAG model, (b) Hobiger model and (c) IAG with high Vs-contrast 3.6.

The second and third checked parameters which effect on the peak frequency, for both the approaches, were density (ρ) and P-wave velocity contrast (Fig. 7.14 and 7.16). The P-wave velocity contrast and density contrast changes have no effect on the peak frequency of both ellipticity and DFA curves (it is shown at IAG model).

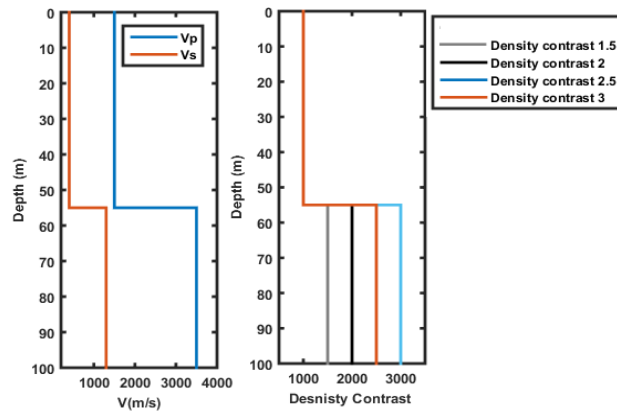


Fig.7. 13 Shows the V_p , V_s and density profiles of IAG-borehole.

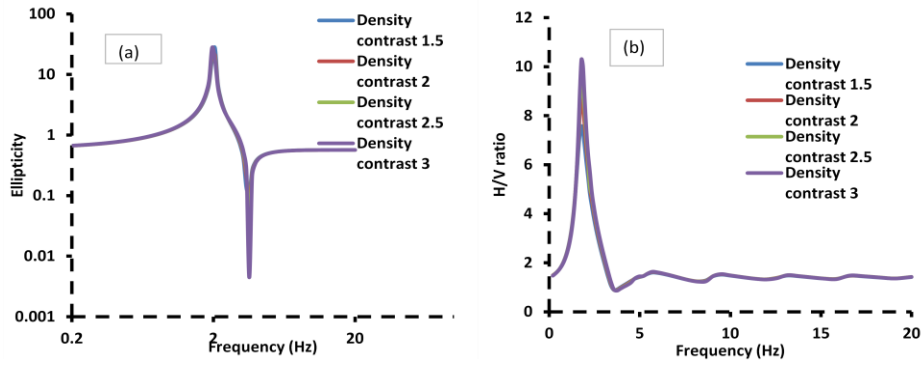


Fig.7. 14 Shows H/V curve obtained via Rayleigh wave ellipticity (a) and DFA approaches (b) against density changes between soil and rock interface.

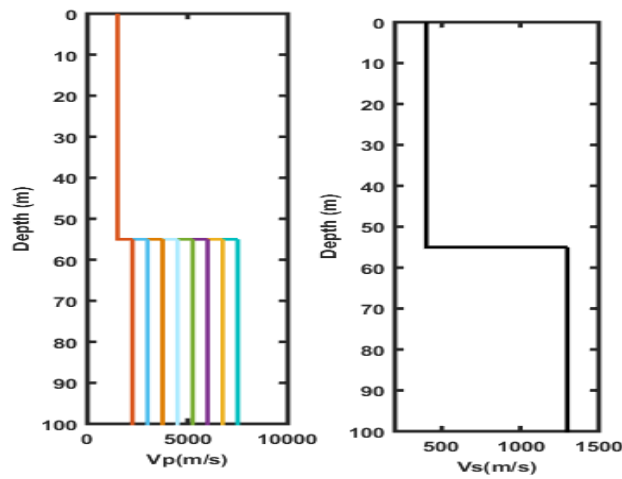


Fig.7. 15 Shows the Vp velocity contrast profile of IAG-borehole.

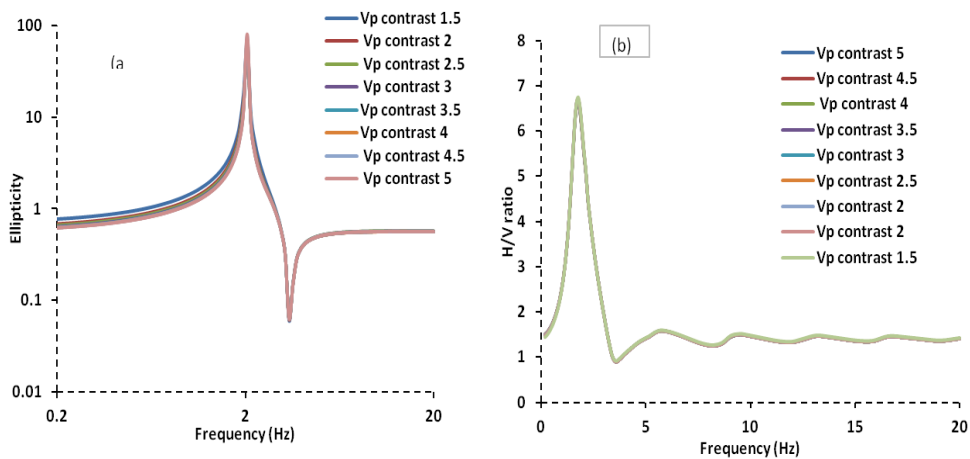


Fig.7. 16 H/V curve obtained via Rayleigh wave ellipticity (a) and DFA approaches (b) against P-wave velocity contrast changes between soil and rock interface.

The last parameter checked for the effect on the peak frequency was shear-wave velocity contrast for both the Rayleigh waves ellipticity and DFA approaches. Velocity contrast was changed relatively between sediment package and bedrock (Fig.7.17). The shear wave velocity ratio between bedrock and sediments packages were kept 10, 9, 8, 7, 6, 5, 4, 3, 2.5, 2, 1.5 and 1.2, respectively. The peak frequency of the H/V against Vs contrast is having a clear peak when the Vs ratio of sediment and bedrock is 2.5 or higher, for both the cases. The ellipticity peak frequency deviation from the S-wave resonance frequency is less than 7% when the Vs contrast between soil and bedrock is 3.6 or higher. We observed for both the cases of thickness variation and velocity contrast variation, that the deviation from the S-wave resonance frequency are lesser (less than 5% of thickness variation and less than 7% for Vs-contrast) when the Vs contrast is 3.6 or higher. Though, experimental H/V curves, most of the time, failed to reproduce the amplitude of the ellipticity curve. However, the analysis showed that, in the case of high-velocity contrast (3.6 or higher), the ellipticity modelling of H/V curve matched with S-wave resonance frequency closely, except at peak amplitude (Fig 7.1).

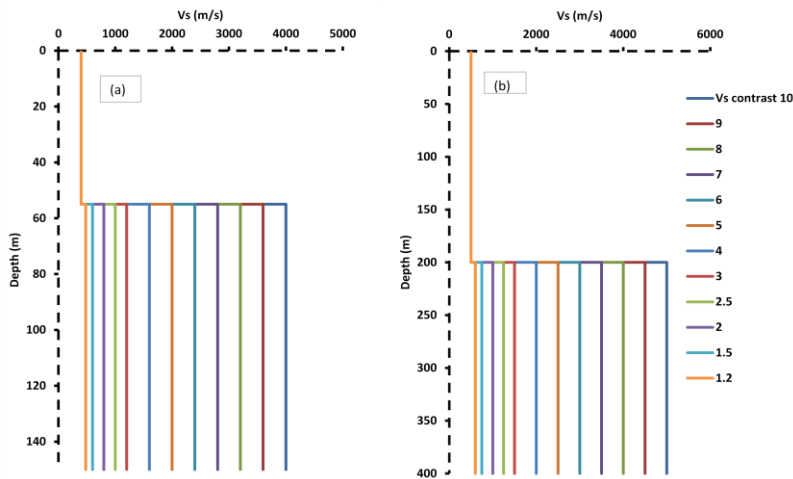


Fig.7. 17 Shows the Vs profile along with Vs velocity contrast profile with Vs contrast among soil and bedrock: (a) IAG-model; (b) Hobiger model.

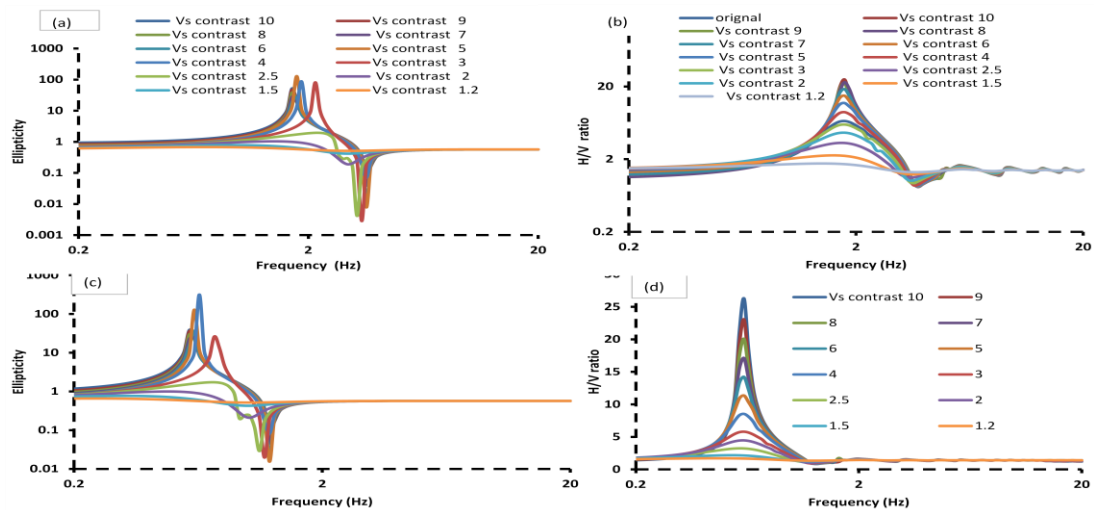


Fig.7. 18 Shows the shape of the H/V curve obtained via Rayleigh wave ellipticity for IAG model (a), for Hobiger model (c), and DFA approach for IAG (b) and for the Hobiger model (d), against S-wave velocity contrast changes between soil and rock interface.

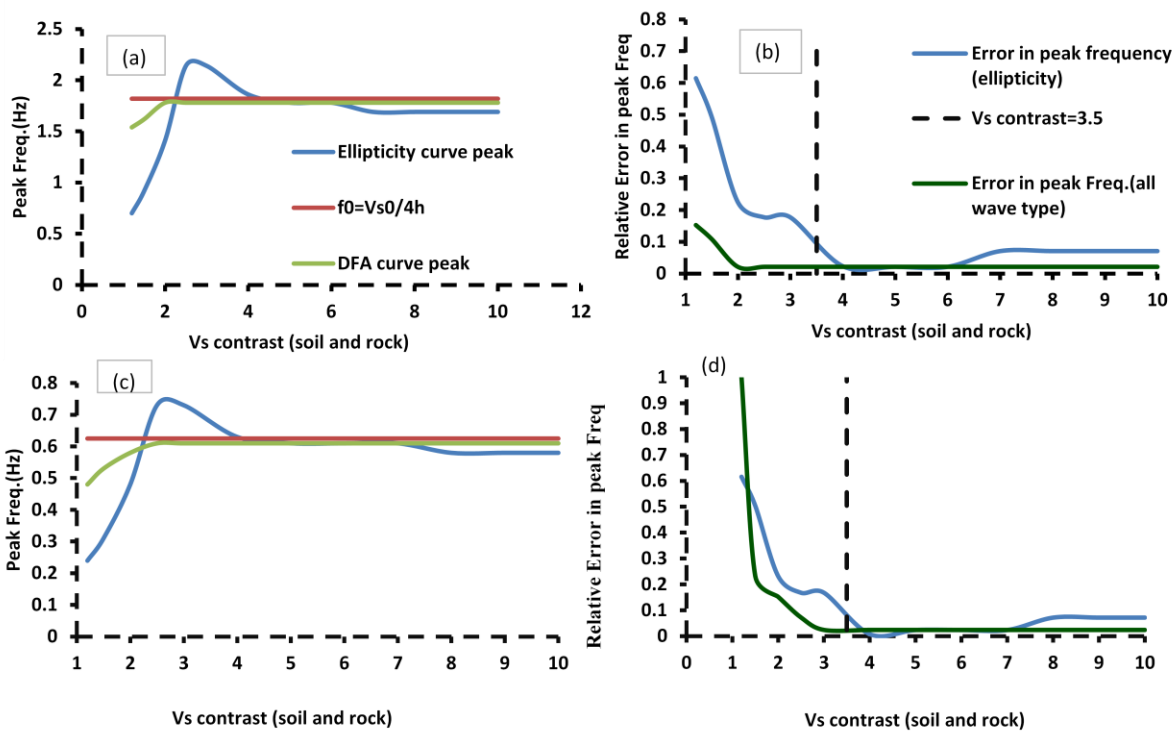


Fig.7. 19 (a) shows the plot of ellipticity peak frequency shift with Vs contrast increase; (b) shows the ratio of trough frequency to that of peak frequency of ellipticity; (c) shows the combined plot; the vertical black line shows the Vs ratio 2.6 from where the effect Vs contribute smoothly.

We observed that another strange behaviour of peak frequency is the shift of the peak frequency with Vs contrast (Fig.7.20). The trend of the peak frequency shift showed that when the Vs contrast is lower than 2.61, the peak frequency of H/V increases rapidly until the Vs contrast of

2.61. Afterward, the frequency of the peak decreases and stabilizes to a constant value with increasing V_s contrast. Similarly, another observation made by Konno & Ohmachi (1998) that peak to trough frequency ratio is almost 2 for high V_s contrast and higher Poisson value soil layer. The peak to trough ratio decreases with V_s contrast until 2.61, and then stabilizes to a constant value of 2.1 above V_s contrast 3.6.

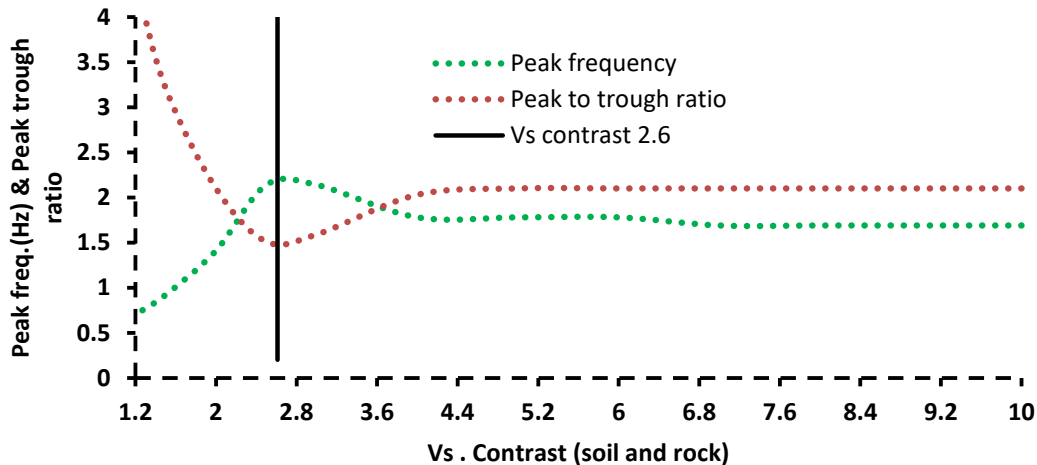


Fig.7. 20 Shows the combined plot of ellipticity peak frequency shift with V_s contrast increase (green) and the ratio of peak to trough frequency (red). The vertical bar indicates the V_s contrast 2.61 from where both curve stabilize.

The peak frequency analysis of these parameters variation and their deviation from the resonance frequency show that, in the case of considering the contribution of all the seismic phases around the peak frequency, a very little deviation from the S-wave resonance frequency is expected. Similarly, in the case of higher V_s velocity contrast (3.6 or higher), the ellipticity peak deviation from the S-resonance frequency is very little. For the inversion procedure, this peak frequency region contains very undefined contributed seismic phases and should not be considered for the inversion around this peak frequency of the experimental H/V curve.

7.4 The shape of the H/V curve

As we discussed in the previous section, around the peak of H/V, the contribution to the horizontal component might be attributed to the Love and body waves presences due to the reason that the amplitude of the curve never reproduce the ellipticity curve at peak (Tazime, 1957) (Scherbaum, 2003). In this case, it follows the shear wave resonance frequency closely. Now, to view the whole shape of the H/V that what type of wave dominates the shape of the H/V curves, we took five models from the different areas and estimated the H/V curve for all the major modelling techniques discussed in chapter 6. The shapes of the curves for these different modeling cases are compared at Fig. 7.22. It is clear that in all the cases the modelled curve is following the Rayleigh waves fundamental mode ellipticity shape. It is, therefore, very straightforward to say that the overall shape of the H/V curve is controlled by the Rayleigh wave ellipticity, while deviation of amplitude at peak is controlled by the presence of body/Love waves on horizontal component. The discrepancy in amplitude for the whole curve is controlled

by the presence of Love wave on the horizontal component. Recently, Pina-Flores et al., (2017) showed that the H/V curve is dominated by the surface waves above the peak frequency, while below the peak frequency the effect of body waves dominate the noise wavefield. The idea of the importance of the Rayleigh wave ellipticity can be easily established by observing the shape of the H/V curve in terms of peak and trough coincidence (Fig 7.22). The DFA based H/V curve in all the model's cases closely follow the shape of Rayleigh waves ellipticity peak and trough (Fig 7.22).

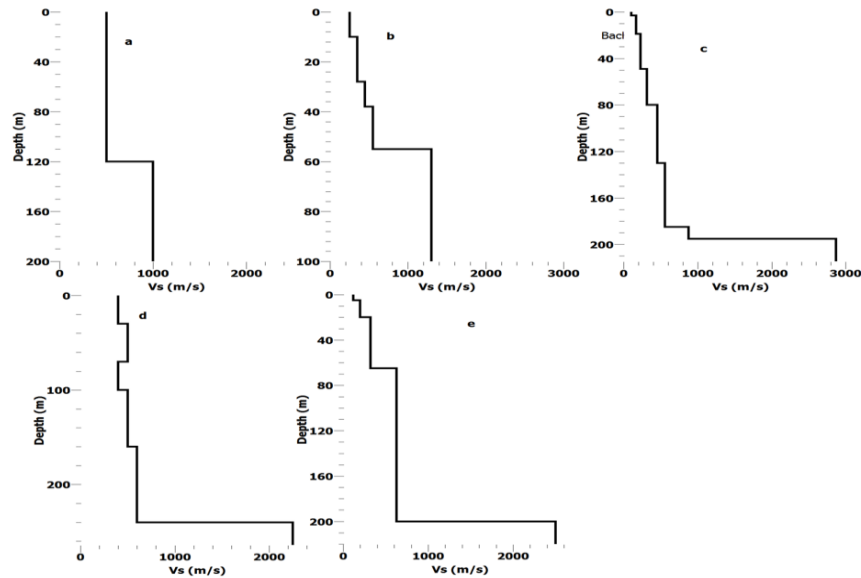


Fig.7. 21 Shows the Vs profiles of the models used for the comparison of H/V curve for Rayleigh wave ellipticity modeling and Diffuse field assumptions modeling for Green function. (a) Model Jose Pina-Flores (2016); (b) IAG borehole generic model; (c) Greece model (Lontsi, 2015); (d) Piccozi (2005) model; (e) Hobiger model (2013).

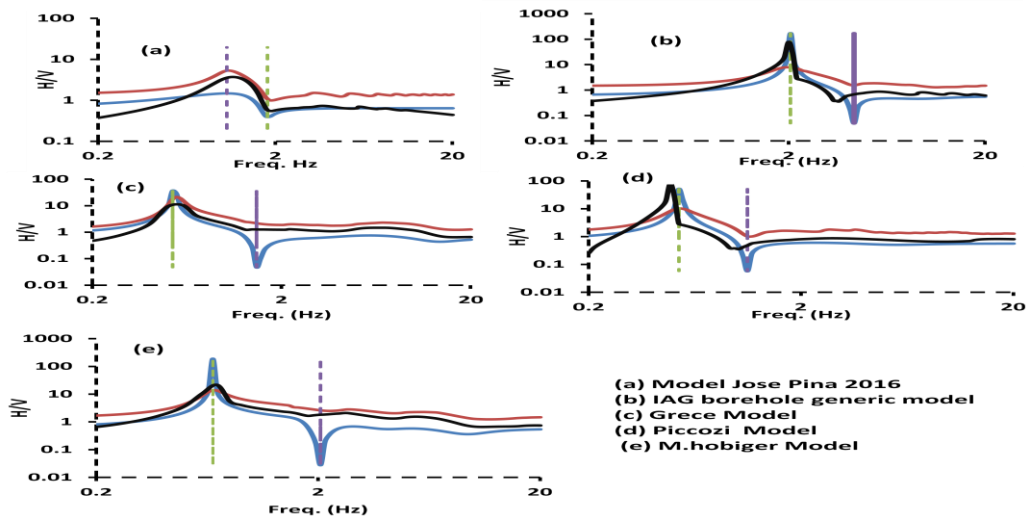


Fig.7. 22 Shows the H/V curve obtained for different models through the ellipticity of Rayleigh wave (blue line), Diffuse field assumption (red line). The vertical lines indicate the peak and trough of the curve as indicated by the ellipticity.

7.5 The numbers of layers and effect on the shape of H/V curve

The most intriguing question to ask is: does the H/V curve shape changes with the number of Vs contrasting interfaces within the structure of the subsurface target? If the shapes are changing, what is the number of layers, up to which the H/V curve for both the DFA and ellipticity approaches, is sensitive to the subsurface layer structure till the bedrock? The two H/V modelling techniques were utilized (ellipticity of Rayleigh wave and DFA) to demonstrate this. The models used for this forward modelling analysis are IAG-borehole and one taken from Greece (Lontsi, 2015; Fig 7.21). The Greece model was taken because it has the maximum number of layers among the models (Fig 7.21). The number of layers of both the models is increased in such way that peak frequency of the curves should not vary more than $\pm 5\%$ of the original peak frequency of the one layer model by adjusting the S-wave average travel time. The number of layers is increased from 1 layer over half space to 10 layers over half space (bedrock) for both the models. The deviation of the curve shape from one layer model upon increasing the number of the layer are found as

$$\mathbf{Deviation}_{curve\ shape} = \frac{1}{N} \sum \left(\frac{\left(\frac{H/V_{1L}(fi) - \frac{H}{V_{nL}}(fi)}{H/V_{1L}(fi)} \right)^2}{H/V_{1L}(fi)^2} \right) \quad (7.1)$$

where $H/V_{1L}(fi)$ is H/V curve at frequency fi for one layer model, $\frac{H}{V_{nL}}(fi)$ is H/V curve at frequency fi for n layer model ($n=2,3,4,\dots,10$), N is the number of data point, 100 in this case. Eq. 7.1 measures the mean deviation of n-layer model relative to one-layer model. Higher is the **Deviation**_{curve shape} mean more sensitivity to the number of layers. For both modelling techniques, the **deviation**_{curve shape} is estimated with different number of layers. The results are shown in Fig 7.24 and 7.25. They show that the deviation between for different number of layers relative to one-layer model is higher in case of Rayleigh waves ellipticity case, while lower in DFA based on H/V curves for different layers model.

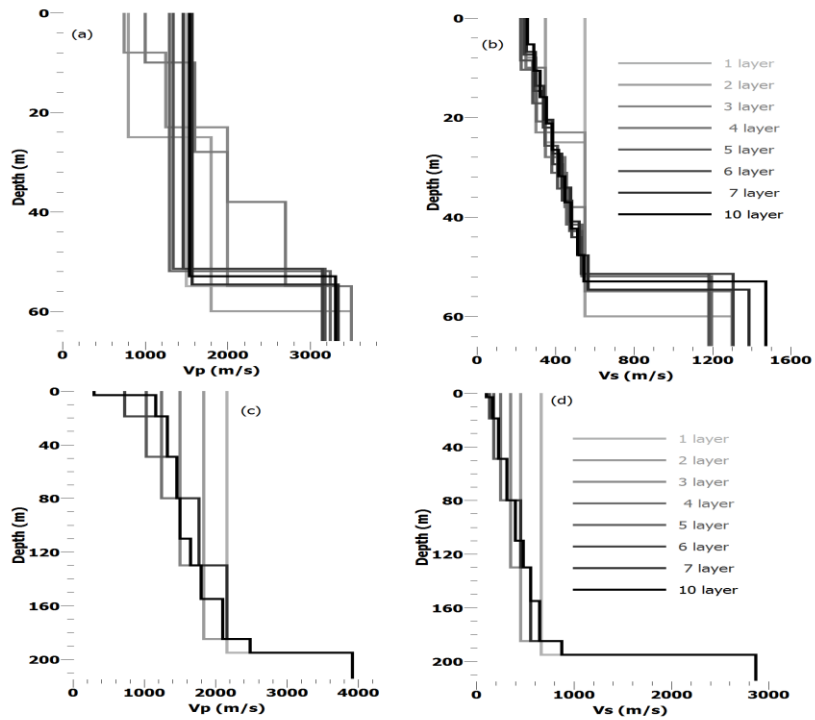


Fig.7. 23 ows the IAG and Greece models with a different number of layers.

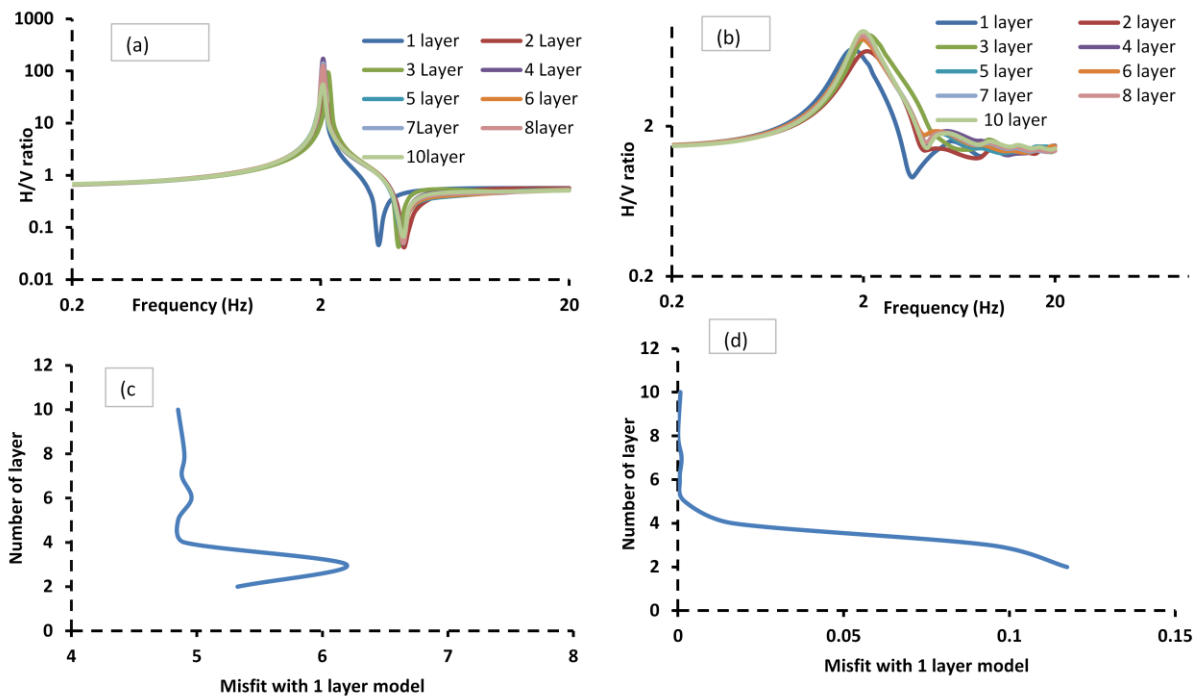


Fig.7. 24 Shows IAG model with a different number of layers for both ellipticity (a) DFA H/V modelling approaches (b) with corresponding shape deviation from one layer model in (c) and (d).

This analysis indicated that maximum deviation between the shape of the H/V curve relative to one-layer model when the number of layers of the subsurface target is 3 and 6 for both ellipticity and DFA based H/V curve for IAG model (Fig.7.24) and 6 for ellipticity and DFA for Greece model. Beyond this threshold number of layers, the deviation of the shape curve relative to one-layer model again decreased. Based on this analysis we can say that the maximum possible number of layers up to which the H/V curve is capable of carrying information and could be retrievable is 6. However, this does not mean that it should be fixed to the number of layers to be 6 layers in each of the H/V inversion case (when considering H/V curve as ellipticity curve). The number of layers for each inversion case should be started with a simple case of one layer, and then increased to the number of the layer by looking at the misfit. A general layers number used, for almost all the case till now, for the H/V and dispersion curve inversion is 4 (Hobiger, 2013 and Wathelet, 2008). It is recommended that, in the case when there is no prior information about the subsurface structure, the usual number of the subsurface layers to be chosen for the inversion is 4.

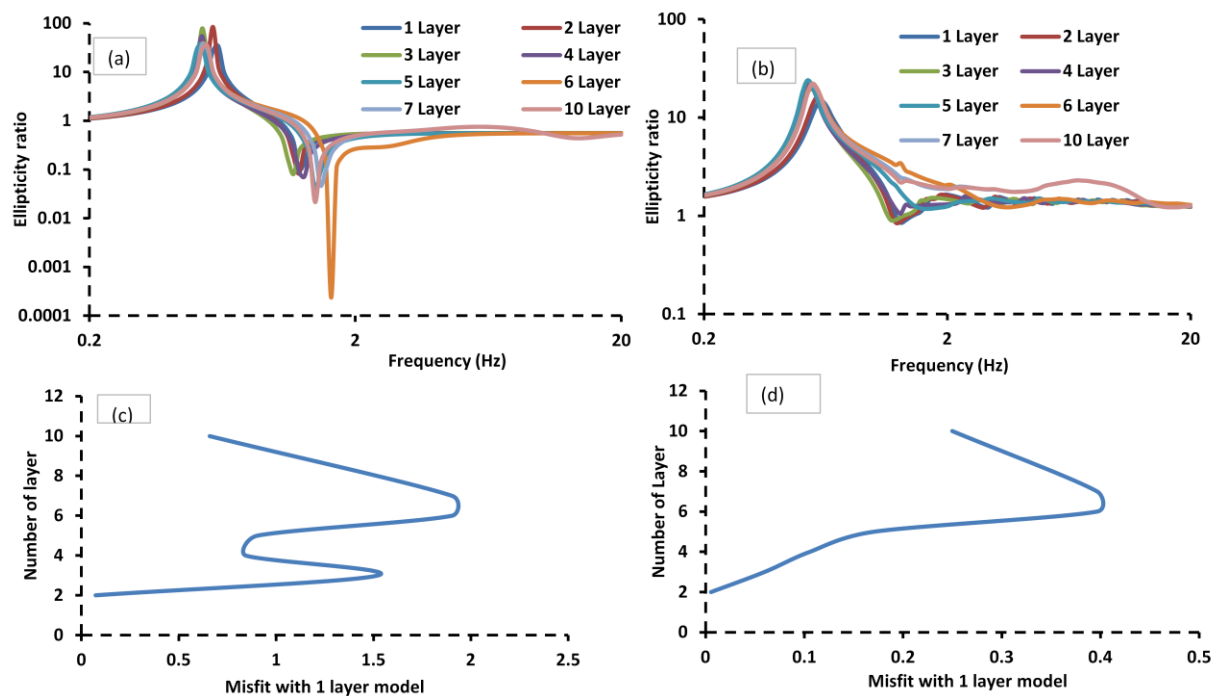


Fig.7. 25 Shows Greece model with a different number of layers for both ellipticity and DFA H/V modelling approaches (b) with corresponding shape deviation from one layer model in (c) and (d).

Chapter 8: The use of peak frequency of the H/V curve

8. Thickness frequency relation

The characteristic site period, that depends on the thickness and shear wave velocity of the soil (as described in the previous chapter), provides a very useful sign of the vibration period at which the most significant amplification can be expected. Despite of the knowledge of types of wave which dominates the result of the H/V curve around the peak, luckily, for the purposes of estimating the soft sediment thickness, the H/V technique can be employed for the measurement of resonance frequency (Konno & Omachi, 1998; Ibs-von Seht & Wohlenberg, 1999; SESAME 2004; Bonnefoy-Claudet et al., 2008; Tuan et al., 2011) which can be used to obtain sediment thickness above the seismic bedrock. In the case of the H/V curves, as it has been observed extensively, the peak of H/V curve corresponds to the shear wave resonance with good accuracy (SESAME, 2004). This simple method of ambient seismic noise recording provides us information about the fundamental period or fundamental frequency (f_0) of a site, which plays a very important role in hazard mitigation analysis such as earthquake microzonation. A relation between the fundamental resonance frequency and thickness of the soft soil can be estimated for the control point (borehole), which later can be utilized for a larger area. This thickness frequency relationship is usually found out by the regression analysis of thickness and peak frequencies obtained for those borehole sites. This $f - h$ relationship strongly depends on the shear wave velocity and thickness of soil and, hence, relies on the average travel time of shear wave in the soil package (as shown for six different models in chapter 7). To obtain this $f - h$ relationship for an area, there should be borehole control points scattered in the study area, where it should measure the ambient noise and estimate the H/V curve for peak frequency retrieval to make a relation between thickness of soil from boreholes and these peak frequencies. However, these desired situations often do not meet. Here, in this section, we are suggesting to estimate this $f - h$ relation with the help of dispersion curve (obtained with any active source technique SASW or MASW). This new procedure is highlighted for the two theoretical models and used latter for the Bebedouro area, where we have ambient noise measurements at seven borehole sites and have six MASW survey profiles to utilize the dispersion curves.

In most cases, the trend of velocity increases with depth in recent deposit sediments. This increase in the velocity is associated with the compaction caused by lithostatic load increase. Faust (1951) analysed experimental data and proposed a non-linear relationship between V_p (P-wave velocity), Z (depth) and α (age of the strata).

$$V_p(z) = \kappa(Z\alpha)^{\frac{1}{6}} \quad (8.1)$$

Chandler (2005) generalized it for the shallow sedimentary structure (< 4 km) on the basis of the experimental data. The Chandler empirical relationship can be written with little modification as

$$V_s(z) = \frac{1}{Z^4} V_0 \quad (8.2)$$

where $V_s(z)$ is the average shear wave velocity with depth Z and V_0 is the velocity at one meter depth. Usually, the trend velocity is estimated from one meter depth onward. Therefore, the depth Z , to put $Z=z+1$ in eq.8.2, it becomes as

$$V_s(z) = V_0(1 + z)^{0.25} \quad (8.3)$$

In general form, eq.8.3 can be written as

$$V_s(z) = V_0(1 + z)^x \quad (8.4)$$

where x is the shear wave velocity increase its dependence according to depth. As it is obvious from Eq.8.4, the values of V_0 and x are required to get the general increase trend of shear wave velocity. Usually, these values are estimated from the borehole data analysis. Both these values vary from site to site. The literature review on this topic provide three general relations (Albarelo, 2011) for the different geological setting

- $V_0 = 210$ m/s and $x = 0.20$ for compact soils
- $V_0 = 170$ m/s and $x = 0.25$ for sands
- $V_0 = 110$ m/s and $x = 0.40$ for rework or very recent soils

Deriving the formula for thickness frequency relationship, let's assume that a trend velocity increase in the unconsolidated soil deposit it is in the form of Eq. 8.4. Let h be the thickness of the soft soil, then the travel time T required for S waves to travel through distance h is given as

$$T = \int_0^h \frac{dz}{V_s(z)} \quad (8.5)$$

Replacing $V_s(z)$ with its value from Eq8.4 and integrating with the limits, result as

$$T = \frac{1}{V_0} \left(\frac{(1+h)^{1-x} - 1}{(1-x)} \right) \quad (8.6)$$

$$f_0 = \frac{\langle V_s(z) \rangle}{4h} = \frac{1}{4T} = \frac{V_0(1-x)}{4[(1+h)^{1-x}-1]} \quad (8.7)$$

Eq.8.7 can be written in the form of

$$h = \left[\frac{V_0(1-x)}{4f_0} + 1 \right]^{\frac{1}{1-x}} - 1 \quad (8.8)$$

if $h \gg 1$ and $V_0(1-x) \gg 4f_0$, has an approximate relation as follow

$$h \cong \left[\frac{V_0(1-x)}{4} \right]^{\frac{1}{1-x}} f_0^{\frac{-1}{1-x}} = a f_0^b \quad (8.9)$$

where $a = \left[\frac{V_0(1-x)}{4} \right]^{\frac{1}{1-x}}$ and $b = \frac{-1}{1-x}$ are empirical constants. As Eq.8.9 is derived based on average time taken by shear wave velocity to travel through the soil deposit of thickness h , so let's call this relation as time based thickness frequency relation. The appearance of V_0, x in Eq 8.9 suggest the idea that the relation between thickness and frequency will have different a and b values for different areas (as V_0, x will have different values for each site). For example, the two thickness-frequency relation developed for Cologne, Germany and the western Lower Rhine Embayment, Germany are given as

$$h = 108 f_0^{-1.551} \quad (\text{Parolai 2002}) \quad (8.10)$$

$$h = 96 f_0^{-1.338} \quad (\text{Ibs-von Seht 1999}) \quad (8.11)$$

Eq. (8.10 and 8.11) are developed from the regression analysis of the H/V peaks and the depth of the bedrock from the borehole control points. As described above, the thickness frequency relationship for different localities will have different a and b values because of the different V_0, x . Therefore, in general, fixing values of these constants a and b will be certainly bias to each geological setting. Another thickness frequency relationship was recently derived by Tuan et al. (2015). He used the transfer matrix (Haskel, 1953) method to derive an explicit equation for the multi layered situations with fixed bottom. These approximate equations are

then generalized for the model of a functionally graded material (FGM) layer over the half-space (Eq.8.12). The positive side of this formulation is considered by deriving the effect of density and the position of sub-layers (for more detail, look at Tuan, 2015).

$$\mathbf{h} = \left(\frac{V_0^2(1-x)}{2\pi^2} \right)^{\frac{1}{2(1-x)}} \mathbf{f}_0^{\frac{-1}{1-x}} \quad (8.12)$$

8.1 How to estimate the value of V_0, x

Both in Eq.8.9 and 8.12, the two unknowns are the shear wave velocity at one-meter depth and the shear wave velocity increase trend (x), which is generally find out from the borehole velocity analysis. However, it is difficult to have a calibration of borehole for these values at each site. Here, we are suggesting and estimating these values (V_0, x) from the phase velocity dispersion curve. To elaborate the procedure, the analysis is initially made for the two theoretical 1D models (A and B, Fig.8.1). The values of V_0, x can be indirectly obtained from the interpretation of the effective Rayleigh wave dispersion curve. The fundamental mode of Rayleigh wave dispersion curve coincides with the above framework of rough idea of estimation parameter V_0, x (Albarelo et. al., 2011). Some authors have suggested, on the basis of empirical evidence, that the average S-wave velocity up to a depth of h roughly corresponds to the relative Rayleigh waves phase velocity to a fixed wavelength of the order of $1 \div 3$ times h (Konno & Kataoka, 2000; Martin & Diehl, 2004; Albarelo & Gargani, 2010). According to relation, the Rayleigh wave velocity approximately matches with S-wave average velocity up to bedrock depth (Albarelo, 2011)

$$\mathbf{VS}(z)_h = 1.1\mathbf{VR}(f) \text{ as } h = \left(\frac{0.3}{0.5} \frac{\mathbf{VR}(f)}{f} \right) \quad (8.13)$$

Eq.8.13 gives an idea that dispersion curve obtained from the MASW, or any other array technique, can be utilized to infer the values of V_0, x . In this case, we are using the best fitting technique between shear wave velocity and depth obtained from the dispersion curve directly for the two models (A, B). For each point of the dispersion curve, shear wave velocity and depth are estimated by using a rough approximation

$$\mathbf{VS}_h = 1.1\mathbf{VR}(f) \quad \text{Depth } h = \frac{\mathbf{VR}(f)}{2f} \quad (8.14)$$

The model A contains four layers over the half space at 200 meter (the composite thickness of soft sediments is 200 m, Fig 8.1.a), while model B is considered to have the same number of layers over the half space at 100 meter depth (Fig 8.1b). The number of layers above the half space is arbitrary, as our focus is to find the composite thickness of soil over the bedrock (half space in this case).

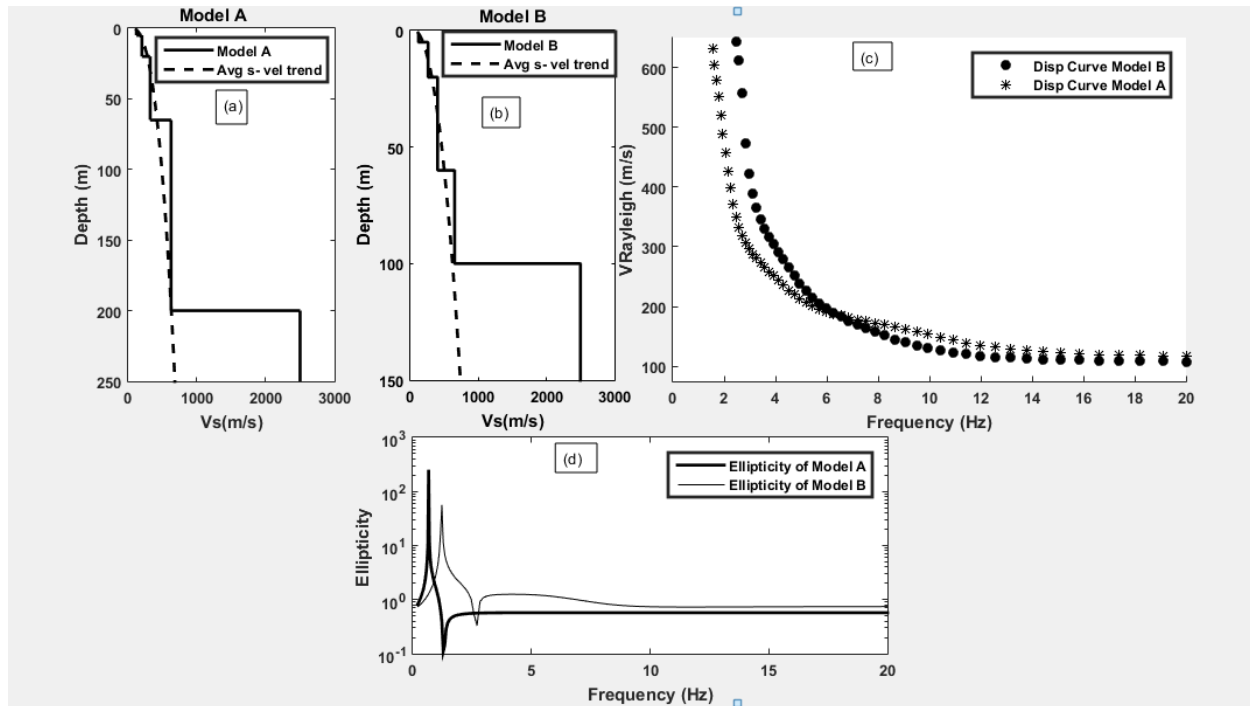


Fig.8.1 Model A and B. (a) and (b) show Vs profiles (solid lines) while dash line show average S-velocity trend obtained from best-fitting; (c) shows fundamental mode dispersion curve for models A and B; (d) shows the fundamental mode ellipticity curve for both models.

The theoretical dispersion curve of the fundamental mode was estimated using Dunkin (1965) formulation, which was modified from Thomson (1950) and Haskell (1953) following an eigenvalue problem. The theoretical ellipticity curve is estimated for the models A and B (Fig 8.1d) from a stack of eigenvalues for each layer. The stepwise procedure adopted were: 1. The dispersion and ellipticity were estimated for the models A and B (Fig 8.1c,d); 2. The shear waves velocity and depth were estimated for each Rayleigh-frequency points (100 points are considered for theoretical models) of dispersion curve using Eq. 8.13; additionally, peaks of ellipticities curves for model A and B are considered as fundamental frequency (f_0 : **A = 0.67 Hz** , **B = 1.20 Hz**, Fig.8.1d); 3. The best fit was passed through shear wave velocity and depth points and the rate of increase of the shear wave velocity with depth x was obtained (Fig

8.2); 4. The V_0 values were estimated from $V_0 = V(1 + z)^x$, where V was the velocity at the surface estimated from the best fit (it can also be roughly approximated from the VRayleigh dispersion curve values at higher frequency when available).

The values obtained from this procedure for the theoretical models (A: $(V_0, x) = 118, 0.35$, B: $(V_0, x) = 112, 0.40$) were input to the Eq.8.12, and composite thickness for soft sediment over bedrock were estimated (A: $h=205.8$ m, B: $h=104.5$ m by Tuan relation Eq8.12 and A: $h=174$ m, B: $h=81$ m by average time based on relation Eq 8.9). The analysis of the theoretical models results for the thickness estimations suggest that Tuan (2015) relation provides a better estimate in contrast to the average time travel based relation. The same procedure can be adopted for actual field cases, and will be further investigated in the coming section.

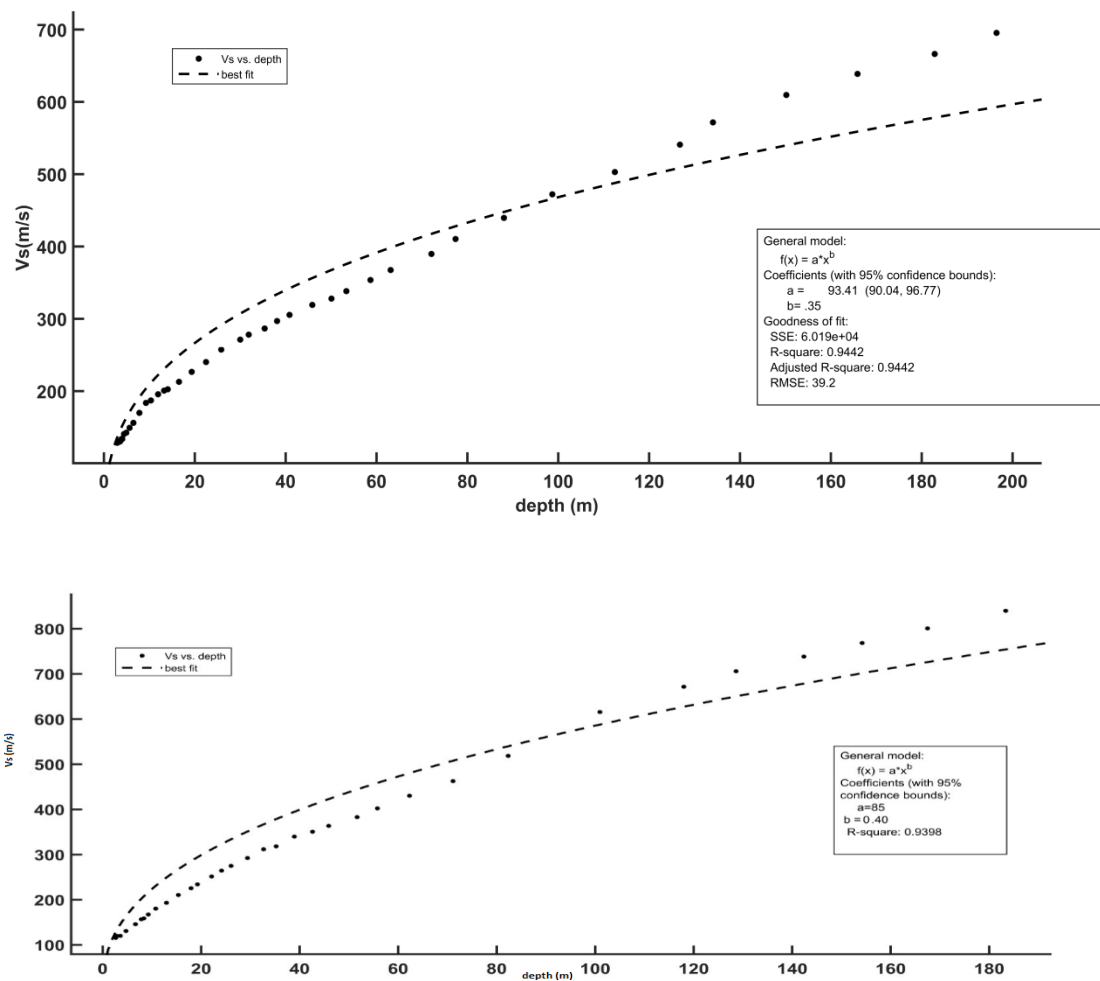


Fig.8.2 The best-fit line through V_s -depth plot for model A (top) and (B) bottom; the rate of increase of average shear wave velocity obtained is $b=0.35$ for A (top); the same procedure is done for model B which result in $b =0.40$ (bottom).

8.2 Thickness frequency relation for the Bebedouro area

In the Bebedouro area, the seismic noise measurement was made next to seven water wells where we know the exact depth of sandstone and basalt interfaces from the drilling information. The seismic noise measurement was made next to these water wells. The fundamental frequencies of these water wells sites were estimated from the H/V analysis (Fig.8.3, Table 8.1) and linked to the sandstone top by the regression analysis to find the thickness frequency relation for the Bebedouro area (Fig 8.4). The Bebedouro area contains two geological interfaces near the surface, soft sediments followed by sandstone layer and fractured basalt. However, we could not find any prominent peak for the basalt interface as the velocity contrast were not might sufficient to result in a peak for the basalt sandstone interface. Therefore, we limited the $h - f_0$ relation of the soil and top of the sandstone layer (Fig.8. 4). The regression analysis equation has an average error of $\pm 8\%$ (minimum 1% and maximum 15%) with actual thickness estimated from the wells. This result will be compared with the results of Eq 8.9 and Eq.8.12. Prior to that, let's find out the V_0, x for the sites.

Table 8. 1 Peak frequencies of noise recording made next to water wells.

Well name	Prominent peak of H/V f_0 (Hz)	Top of sandstone (m) from well
P11	3	27
P09	2.6	42
P04	4.2	22
P02	7.5	7
P03	7.2	7
PST2	6	12
StaAna1	6	11

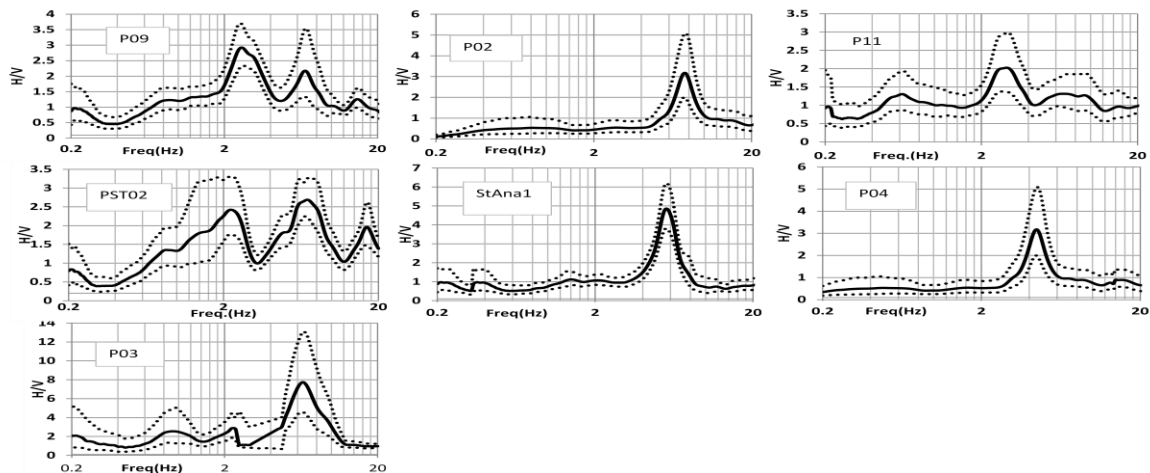


Fig.8.3 Shows the H/V curves measured at borehole sites given in Table 8.1.

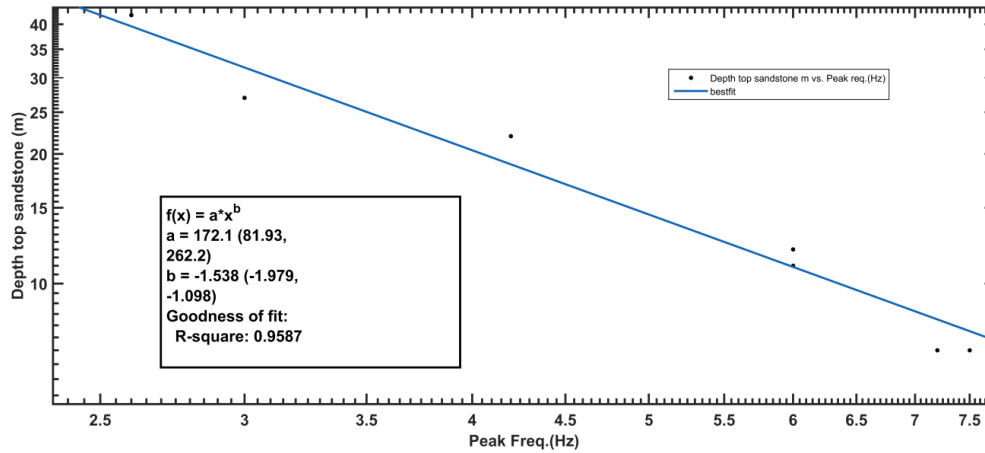


Fig.8.4 Shows the regression plot for H/V curve peaks and depth to bedrock (sandstone) in Bebedouro area (x is resonance frequency, R-Square is the coefficient of determination, f(x) thickness to soil deposit).

8.3 V_0, x values estimation for the Bebedouro area from MASW dispersion curve

To find the values of V_0, x for the Bebedouro area we used six MASW profiles. Four of the MASW profiles were recorded in 2008, being them BEB 4a, BEB7, BEB 11 and BEB1, and two new profiles BEB 4b and BEB 16b were acquired in 2015 (Fig.8.5a). The dispersion curves from these MASW profiles were used to estimate the shear wave velocity increase trend for the region. The BEB 4b MASW profile was used to obtain three dispersion curves for different source intervals (Fig.8.7). We tried to directly invert these data from the Rayleigh wave velocity-frequency to shear wave velocity-depth through the relations $V_s = 1.1V_r$ and $depth = \frac{V}{2f}$, for each frequency point. The shear wave velocity is linked to Rayleigh wave phase velocity through Poisson ratio such as $\frac{V_r}{V_s} = \frac{0.862+1.14\nu}{1+\nu}$ (where V_r is the Rayleigh wave phase velocity, V_s is the shear wave velocity and ν is the Poisson ratio). The Poisson ratio for the near surface application varies from 0.4 to 0.5. Therefore, let's consider the Poisson ratio is changing from 0 to 0.5. The corresponding $\frac{V_r}{V_s}$ ratio to this range of Poisson ratio increases from 0.862 to 0.955. The shear wave velocity trend obtained through the best fit line of the V_s -depth points are given in Fig 8.7. An important point to note is that, if the V_s increases, the depth trend should not vary if the surface geology of the area is not changing abruptly. All the three curves shown in Fig.8.7 were obtained from different source-receiver intervals of the same BEB 4b site from active source 30 meter forward (a), 15 m reverse (b), and passive source curve (c).

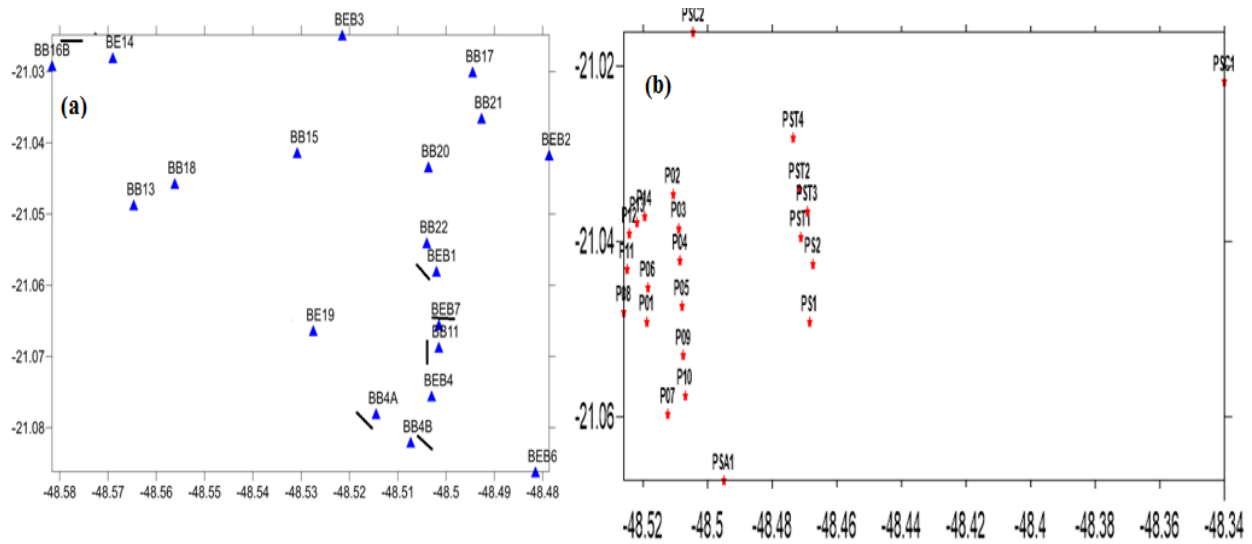


Fig.8. 5 (a) The location of the seismic stations in Bebedouro area. The triangles show the location of seismic sensors where the noise measurement are made for the H/V analysis, black lines show the MASW profiles. (b) The stars show the location of water wells; the wells used for a thickness frequency relationship are shown in Table 8.1.

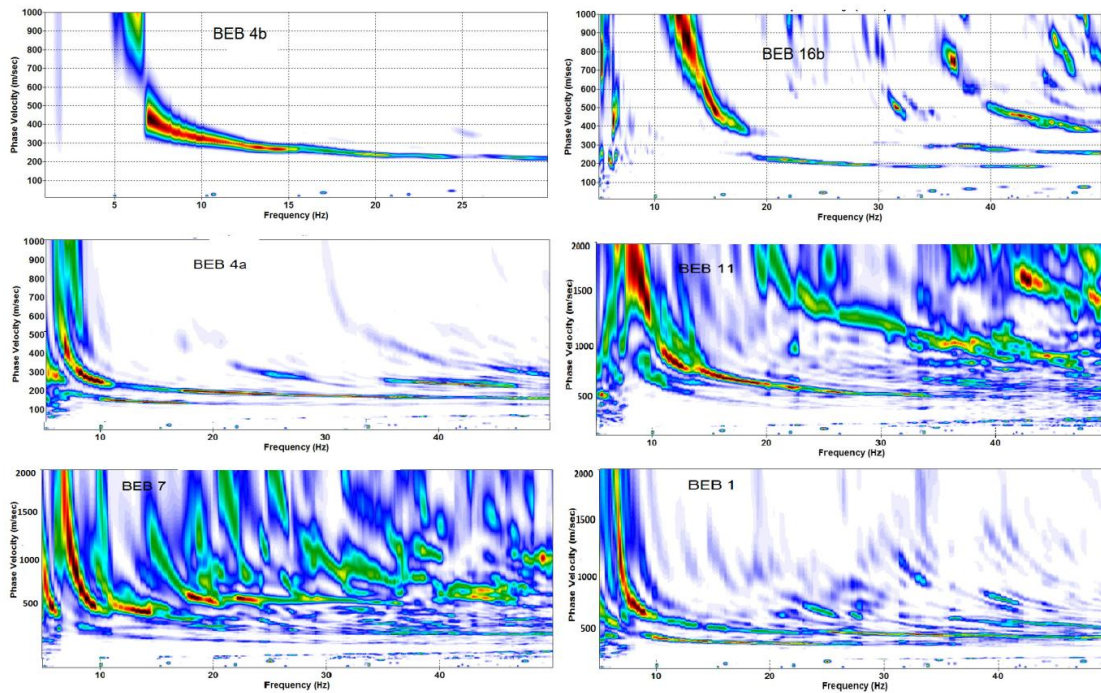


Fig.8.6 Shows the dispersion images of all the MASW profiles (Fig.8. 5) black lines.

To observe the effect of the Poisson ratio variation on the velocity increase trend, we analysed the same dispersion curve of BEB 4b and changed the Poisson ratio from 0 to 0.5. The velocity increase trend was kept constant at 0.3369 in all the cases (Fig 8.8). This analysis showed that

the change of Poisson ratio only affect the velocity at the surface ($a=V$ in best-fit relation) and hence, have no effect on the velocity increase trend.

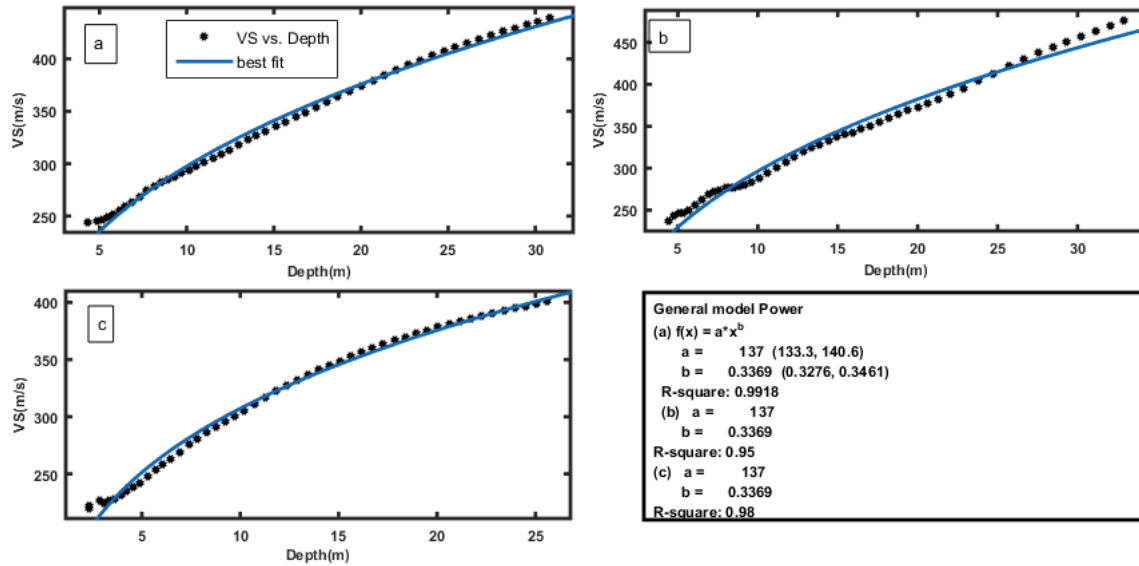


Fig.8.7 Shows Vs-depth data fit for the three curves (a) active 30 meter forward (b) 15 m reverse, and (c) passive source curve; on the lower right statistical robustness and values of data fit are given. The values of (V_0) and x are same as all these curves are taken from same site MASW.

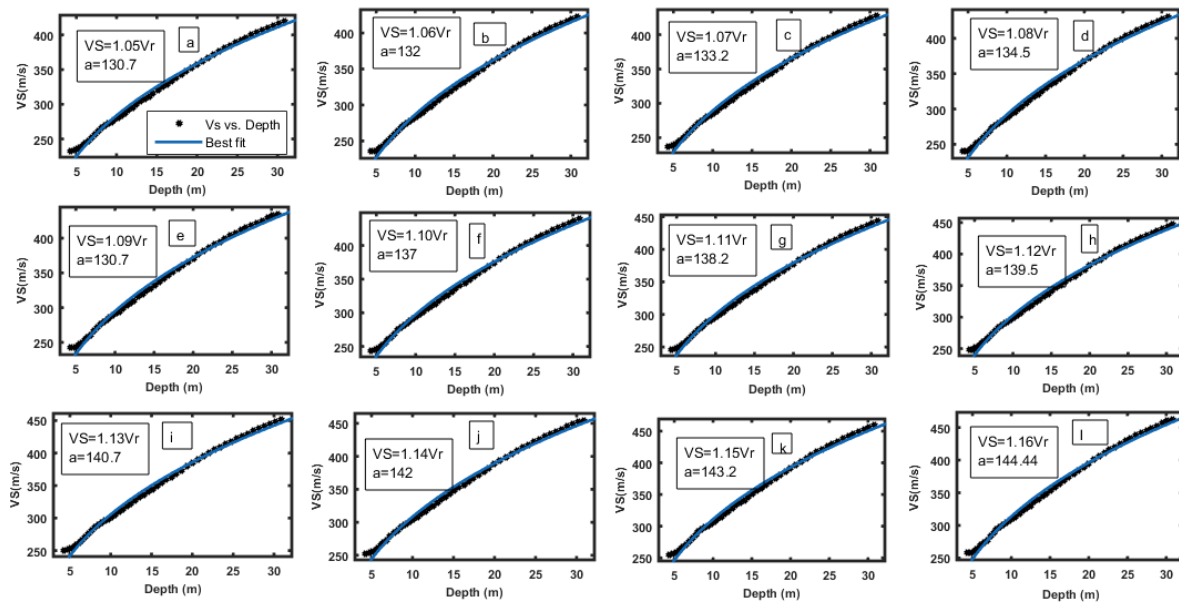


Fig.8.8 Shows the effect of Poisson ratio changes on velocity increase trend with depth for different Poisson ratios. The black dots shows the Vs-depth data while the blue line shows the best fit to the data. The value of x remains constant at 0.3369.

The value of the V_o variation for the Poisson ratio range 0 to 0.5 was found out for the IAG borehole model. The Poisson ratio was changed by changing the velocity of the soil layer and V_o values were estimated by Eq8.4 for the whole range of Poisson values. These values of V_o for different Poisson ratios and the corresponding velocity increase trend with depth are shown in Fig.8.9. Note that the value of the x used, 0.42, was estimated from the best-fit of Rayleigh wave dispersion curve for IAG model.

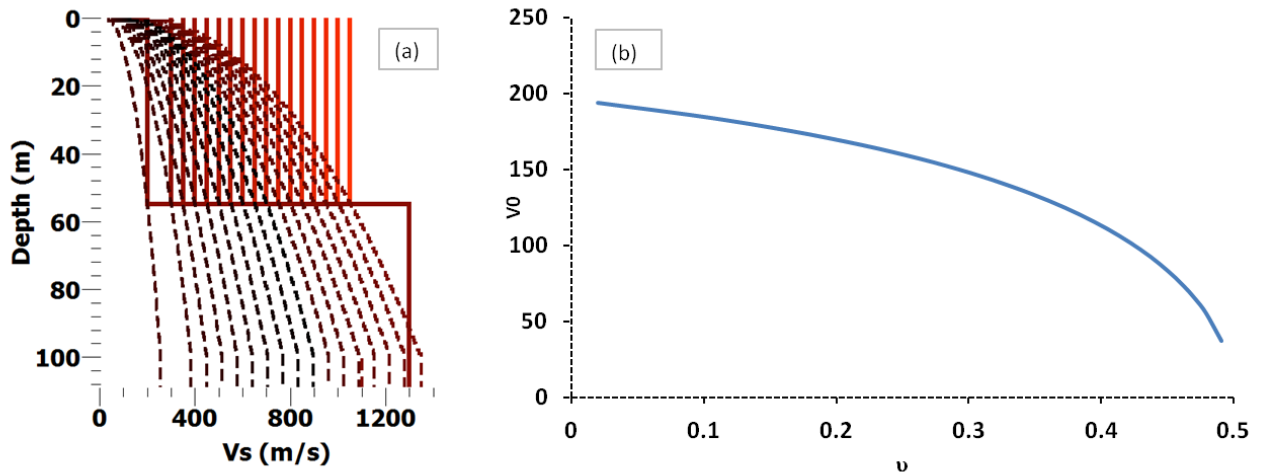


Fig.8.9 Shows the IAG model and the corresponding velocity increase trend ($x = 0.42$) for different Poisson ratio (ν) of the soil layer. The V_o values as a function of Poisson ratio are given in (b).

Similarly, like BEB 4b, four other dispersion curves were obtained for different source intervals: (a) 30 meter forward, (b) 30-meter reverse (c) 10 meter forward and (d) 10-meter reverse at BEB 16b, shown in the Fig 8.10. The same procedure was applied and the best fit was passed to get a sense of increase velocity trend with depth. It is clear from the analysis of Fig 8.10 (a, b, c) that the velocity increases with depth trend is around 0.33. However, a little increase to 0.38 in depth dependence of velocity Fig 8.10(c) is observed. This deviation in x is most probably associated with erroneous picking off the dispersion curves. The interesting fact, which can be noted here, is that the distance between these two sites (BEB 4b and BEB 16b) is almost 10 km from each other and still the values of x (velocity dependence on depth) are almost similar. Similarly, at the other sites (BEB 1, BEB 4a, BEB 7 and BEB 11), the dispersion curves were directly inverted and the V_s -depth trend were obtained (Fig 8.11). The fundamental mode of the dispersion curve is considered in all these cases to obtain the shear wave velocity increase trend with the depth. The velocity dependence on depth value is the same for almost all the six MASW acquired sites. The values of a depend on the local setting and they are highly varying only among the two sites BEB 4a and BEB 11. The four rest sites showed almost similar velocity at the very near surface.

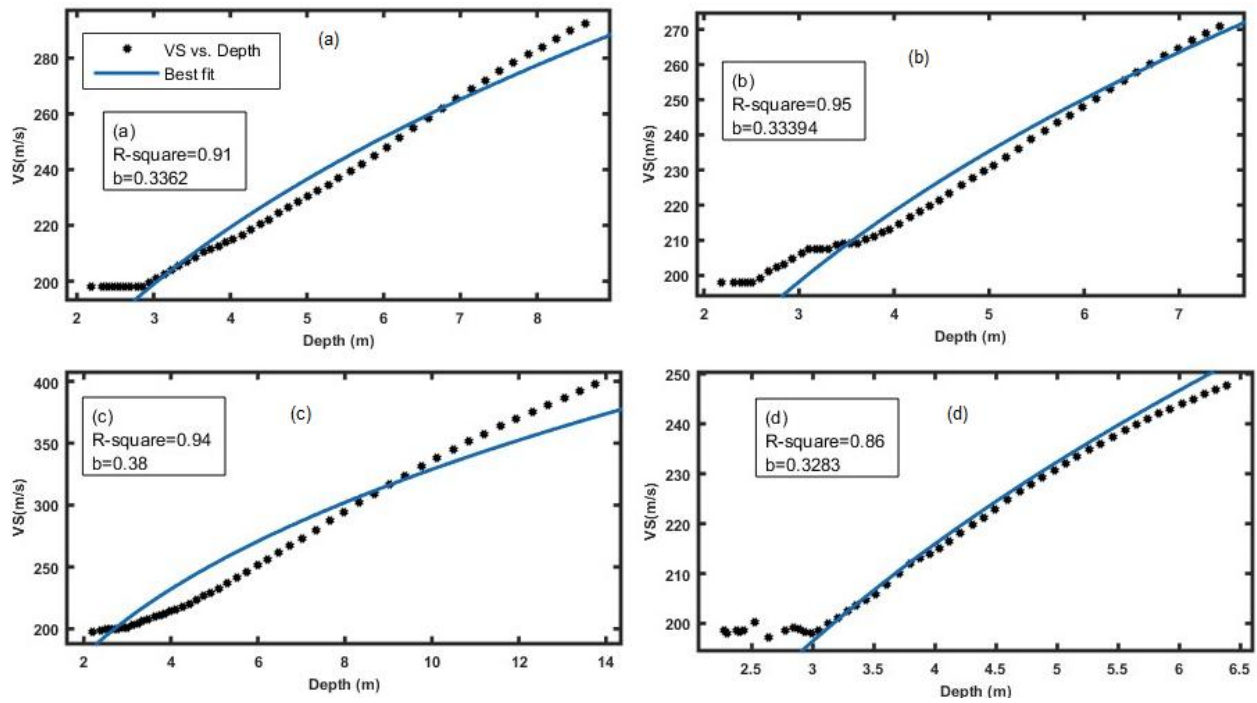


Fig.8.10 Shows the velocity-depth increase trend for different source intervals a) 30 meter forward, (b) 30-meter reverse, (c) 10 meter forward and (d) 10-meter reverse. The value of in power law relationship obtained from Fig 8.7 is kept constant at $a=137$.

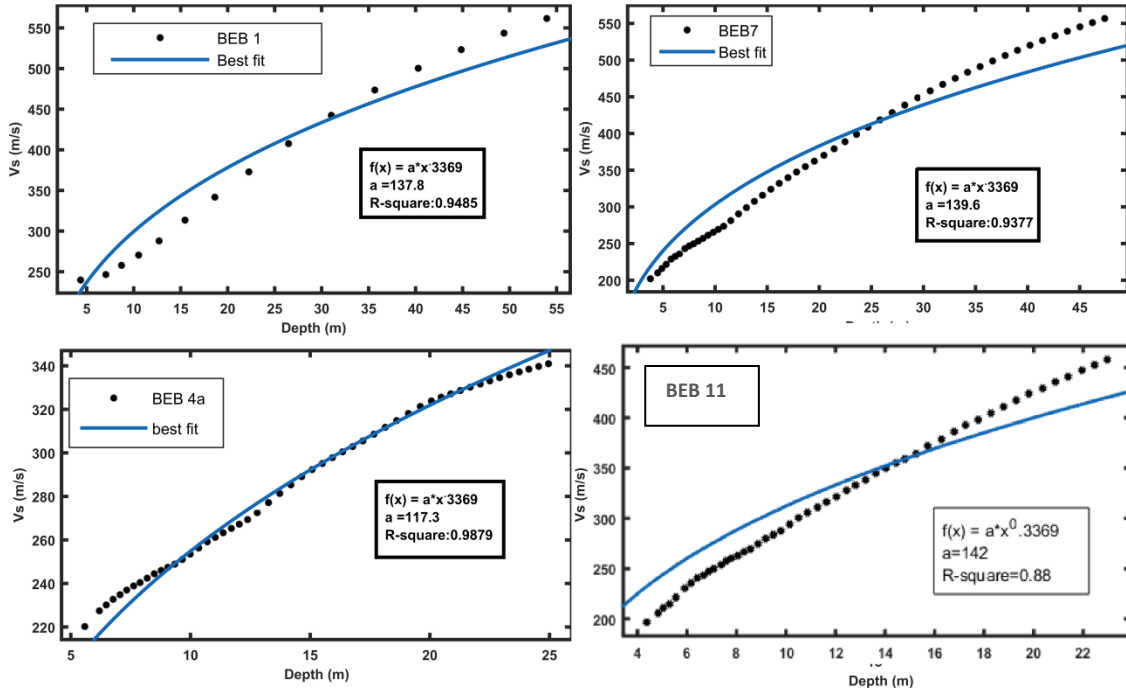


Fig.8.11 Shows the velocity-depth increase trend for BEB 1, BEB 4a, BEB 7 and BEB 11; shear wave velocity increase trend with depth are kept constant at $x=0.3369$; the value of a are shown in each case.

To estimate the thickness frequency relation from Eq 8.9 and 8.12, we need the values of V_0 , x , this is desirable for later comparison to see the deviation in both of experimental thickness-frequency relation. The values approximated from the dispersion curve indirect inversion and fitting are taken as $x=0.34$ and $V_0=171$. These values were used in Eq 8.9 and 8.11 and thickness frequency relation were obtained by

$$h_{time-based} = 158f_0^{-1.515} \quad (8.15)$$

$$h_{T.Tuan\ relationship} = 184f_0^{-1.515} \quad (8.16)$$

Both of these equations results were plotted along with the experimentally derived relation in Fig 8.12. To observe the error produced in thickness estimation of all these three relations, we have plotted the estimated thickness, with the \pm one standard deviation at each frequency points (Fig.8.13). The standard deviations were found out in the three thickness estimates at an each given frequency (0.2 to 20 Hz). The plot was rescaled for various frequency ranges vs. the corresponding thickness to clearly observe the deviation in different thickness estimates frequency range.

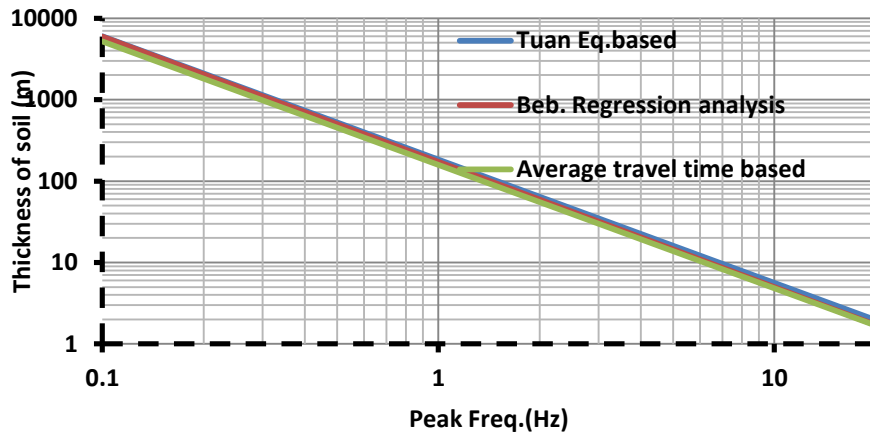


Fig.8.12 Shows the plot of all the three thickness-frequency relationships obtained for the Bebedouro area.

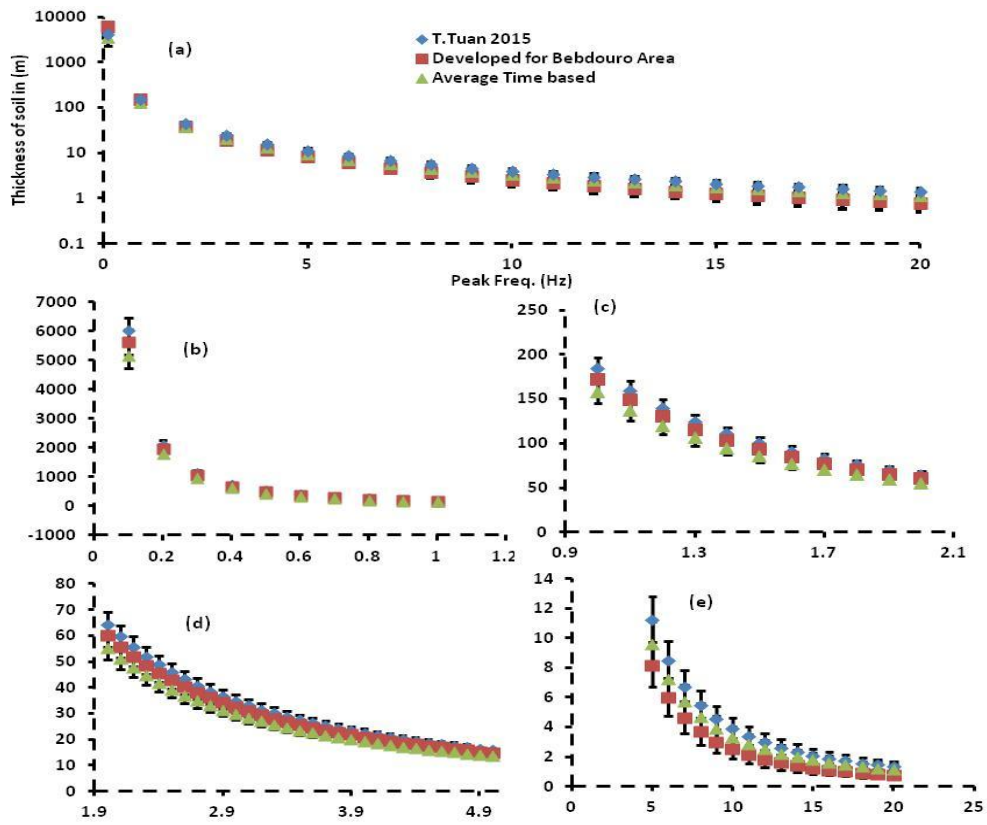


Fig.8.13 Shows the plot of thickness estimate vs. frequency with an error bar of \pm one standard deviation. The plot is reproduced for various frequency ranges to clearly view the deviation in thickness estimate.

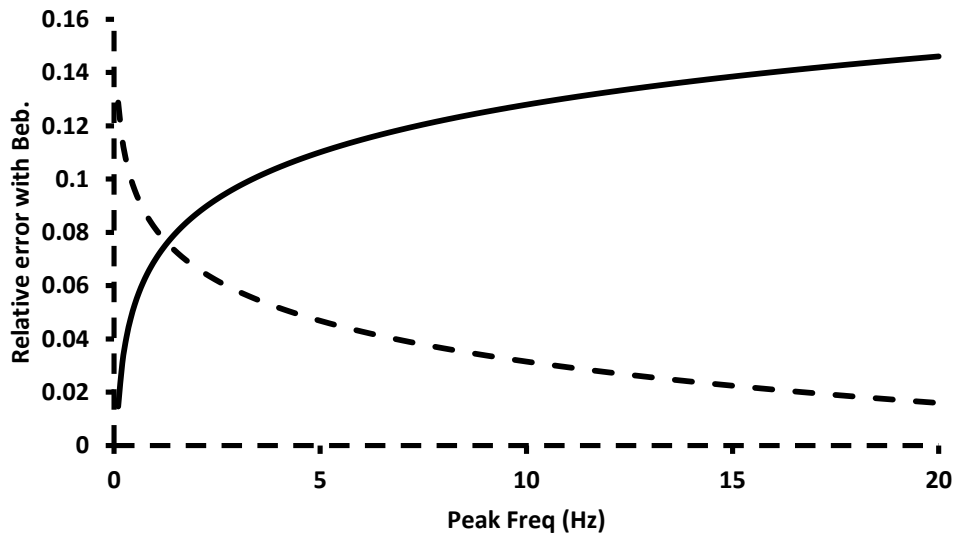


Fig.8.14 Shows the relative error plot of thickness relationship of travel time based (dashed line) and Tuan relation based (solid line).

8.4 Deviations in thickness estimates among the three equations

The thickness estimated from all the three relations are shown in Fig.8.13 with an error bar of \pm one standard deviation. The thickness estimate values lies almost within the error bar of each other. The observation of the error estimates in thickness measurement are done by finding out the relative error between a reference equation and the other two relations. Here, we have considered the average time based and Tuan (2015) relations as a reference as its derivation are based on the mathematical background rather than empirical analysis, like regression analysis in the Bebedouro case. Then, the relative errors were found out in the Bebedouro thickness-frequency relation by considering as reference either the Tuan or time average equations. The relative error are shown in Fig.8.14. The relative error plot in thickness estimates shows the different zone of frequencies where the relative error of either Tuan or average time relation is giving good results when compared to the regression-based relation.

The analysis of the relative error demonstrates an error of 1.5 % in thickness estimated at 0.1 Hz, and 15% at 20 Hz with regression relation for Tuan thickness estimate (Eq8.12) and 13 % at 0.1 Hz to 2 % at 20 Hz with regression for average time relation (Eq8.9). At a glance, the average thickness estimates with time-based relation are in close proximity with regression relation. However, we used the Tuan relation for the situation where the dominant frequency (fundamental) of the site is 0.3 Hz up to 1.2 Hz otherwise the average time base relation for the higher frequencies. The relative error between Tuan and average time-based relation shows a constant error of 11% when Tuan is used as reference measure for thickness and a constant error of 12% when the average time-based relation is used as reference measure. The point where the relative errors with regression analysis are changing is actually the point where the Tuan and the average time-based lines cut the regression analysis equation line.

In conclusion, it can be said that in situation where the thickness frequency relation is not in hand due to the unavailability of control (borehole) points, a dispersion curve can be used to obtain these values of \mathbf{V}_0, \mathbf{x} , which can be utilized to obtain the local thickness frequency relation for a site using Eq.8.9 and 8.12. The range of frequencies of dispersion curve used for \mathbf{V}_0, \mathbf{x} retrieval values are site dependent. To ensure a better result in fields, two different dispersion curve should be obtained for the two nearby sites. If the dispersion curves of both the sites show the dispersion in the same frequency range, then any of the dispersion curves can be used for \mathbf{V}_0, \mathbf{x} retrieval values, otherwise, if one dispersion curve shows a spread in wider frequency range compared to the other, the curve with wider frequency range should be used for this velocity and increase trend with depth estimation for regression analysis.

Chapter 9: Part of ellipticity and misfit function

9.1 Which part of ellipticity curve should be used for inversion?

In the previous two chapters, the shape and the peak frequency were analyzed in terms of wave field and also, the importance of the peak frequency for the thickness-frequency relation. As we have shown, the shape of the H/V curve is dominated by the Rayleigh wave ellipticity, especially fundamental mode till the first trough, thus ellipticity curve is of great interest for the subsurface structure retrieval. However, it is first necessary to infer which part of ellipticity is carrying the most relevant information regarding the velocity structure. In particular, the resonance frequency f_0 is of great concern for inversion because it carries information about the depth of bedrock. However, as we have seen in the previous chapter, a constant travels time for the shear wave in soft sediment has same fundamental frequency peak regardless of thickness and velocity. So, the peak of H/V curve depends on the ratio between the thickness of the soft layer and the average S-wave velocity of the sediment package. Therefore, to get the thickness of soft sediment or the average velocity of soft soil from the H/V curve, we must have either information about the shear wave velocity of the soil or the thickness. This direct estimates obtained via f_0 helps to constrain the thickness of the sedimentary cover when some information such as h - f_0 relationship for the given area is available or knowledge about the local Vs profile are in hand. In this section we will analyze which part of the ellipticity is carrying the most relevant information of the subsurface. We will use the same model of the borehole of IAG site for this analysis. It should be noted that ellipticity curve alone does not provide sufficient information about the subsurface soil structure (Scherbaum, 2003). The inversion of the dispersion and ellipticity curve alone give very differing results (Fig 9.1). The dispersion curve inversion misfit has a clear minimum while that of ellipticity inversion gives a clear trade-off between the velocity and thickness of soil (the dispersion and H/V curves have different sensitivity for the layer parameter (S-wave velocity, thickness of soil)).

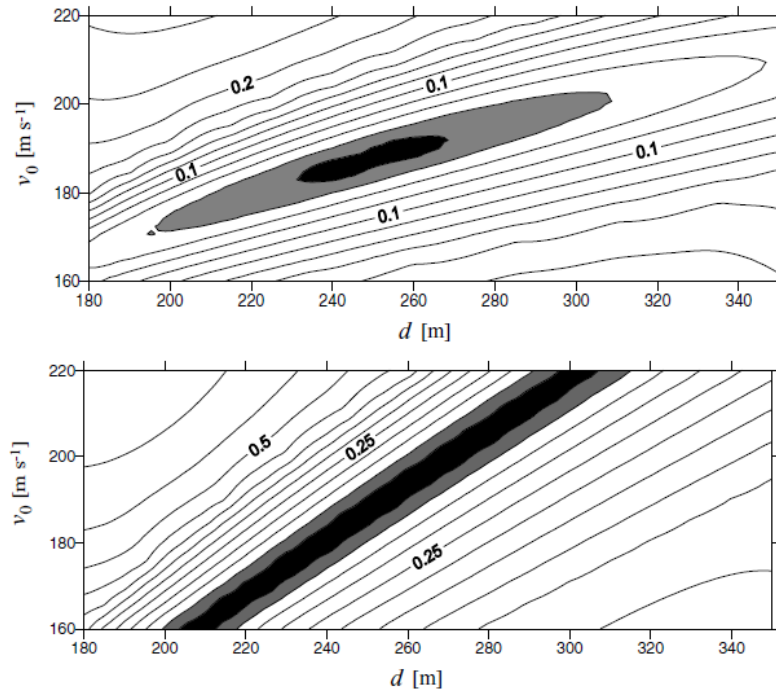


Fig.9.1 Shows the distribution of the misfits as a function of the surface velocity (v_0) and layer thickness (d). The upper panel corresponds to the dispersion curve misfits while the lower panel corresponds to the ellipticity misfits (Scherbaum, 2003).

This trade-off in ellipticity approach can be observed by changing the number of layers of IAG model while keeping the same velocity contrast between the soil and bedrock. A similar ellipticity curve (having a peak $\pm 5\%$ of one-layer frequency peak) were obtained (Fig 9.2). The velocity structure was changed by having one to four layers in the soil above the bedrock. This gives an idea that if we try to utilize the peak frequency only for the inversion, it will provide a biased result. The only visible deviation at these different models ellipticities is at the right limb, which shows that the right flank till the minimum of the ellipticity is the important part which is controlled by the velocity structure of site within the soil. So, one can qualitatively guess that the right limb of ellipticity (from peak to trough) should be used for the inversion, because it is the only portion of the ellipticity varying with altering the number of layers and hence, velocity structure within the soil. Another important point to make here is that, at the horizontal component of seismic noise wavefield the Love effect is present. The Love wave effect is more prominent at singularities (peak and trough) of the H/V. At peak frequency, the vertical component of noise wavefield vanish (Bard, 1998). The total contribution around the peak is then from the horizontal component of Rayleigh, Love and body waves. At the trough frequency, the horizontal components of Rayleigh wave vanish, so the total horizontal energy is attributed to the Love wave and body waves contribution. Beyond the trough frequency, the influence of higher modes might lead to misestimating of the different Rayleigh mode ellipticities (Bard,

1998). So, the right flank till the trough of the ellipticity seems the most reliable part of an ellipticity curve for the inversion along with other information like the dispersion curve.

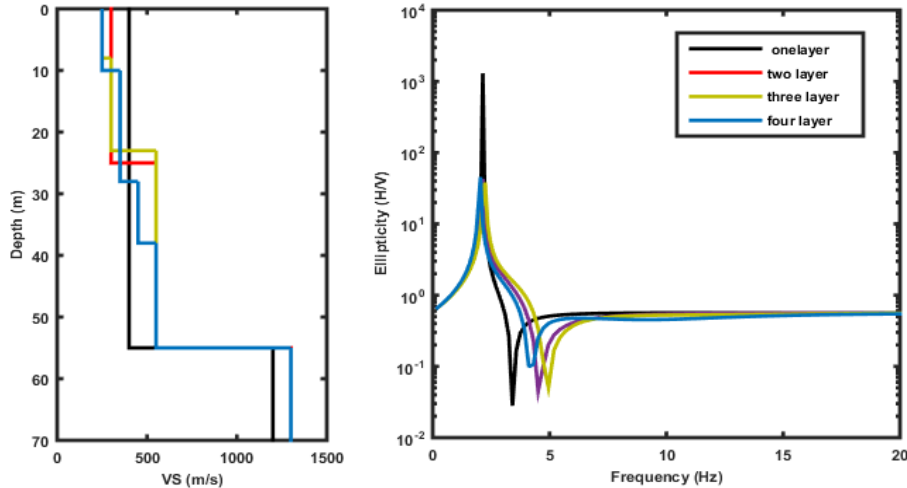


Fig.9.2 Shows the four models and their corresponding ellipticity curves. The same model of the IAG borehole by considering one, two, three and four layers above the bedrock.

The H/V curve techniques are strongly conditioned by the properties (thickness of sediment package and impedance contrast) of the interface between the sediment and the bedrock (Parolai et al., 2005), while it is poorly informative about the S-wave velocity of the sedimentary layers (Fig 9.1). On the other hand, the dispersion curves of the array technique (i.e., MASW) constraint mainly the S-wave velocity structure of the subsurface soil. However, the dispersion curve provides very uncertain information about the deep subsurface velocity structure, especially below the fundamental frequency of a site due to the filtering effect of the media. Therefore, when either H/V or dispersion curves are used singularly for the subsurface structure retrieval, there is a un-resolvable trade-off between the model parameters (velocity and thickness of the soil layers) that hampers the inversion analysis results. So, it is usually suggested to invert H/V and the dispersion curve jointly (Fig 9.3). However, it is a cumbersome process to map out a large area by acquiring both the ambient noise and MASW measurement at each location. Sometimes one (i.e., noise recording) measurement is acquired easily while the other are difficult to acquire because of accessibility limitation (i.e., the Colônia site swampy condition).

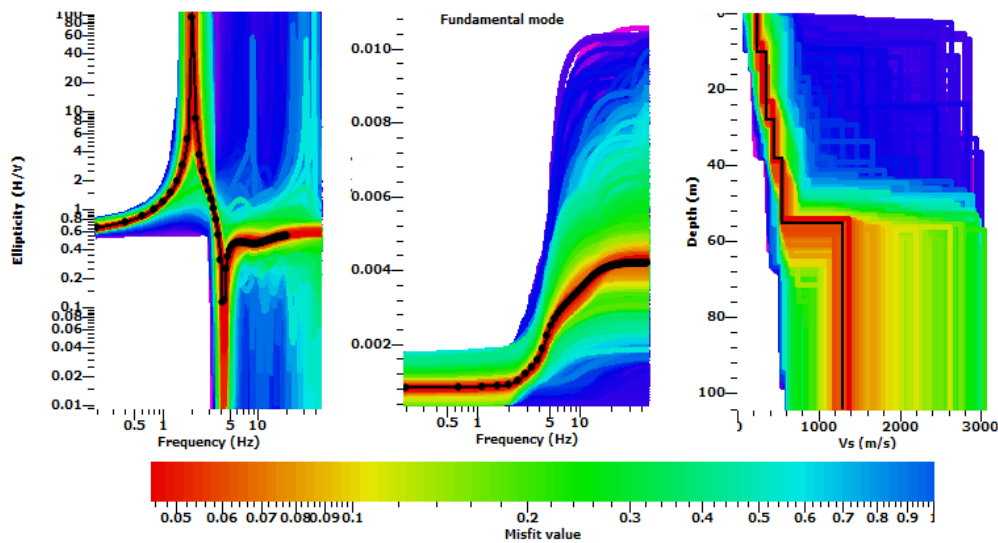


Fig.9.3 Showing joint inversion of ellipticity and dispersion curves. The black dotted line shows the IAG borehole data ellipticity and dispersion curve. On the right, the result of inversion is shown; the black line shows the true model.

If the geology of the area where V_s measurement up to the bedrock desired has a smooth geological setting, then we can expect that the shear wave velocity will increase smoothly with depth (i.e., Bebedouro). The MASW measurement at some of the locations of the whole investigation area can be utilized to obtain this shear wave velocity increase trend for that area. This shear wave velocity increase trend can then be used to invert the H/V curves obtained in the whole area by using this information of V_s increase trend and velocity at near surface information or information about the thickness of the sediments package obtained via $h - f$ relation. As we have discussed above, the ellipticity inversion alone always gives ambiguous result, therefore, this additional information of velocity (shear wave) or thickness will reduce the unresolvable trade-off between thickness and V_s velocity.

Forward modelling is performed to obtain the dispersion curve of the of the borehole model. This dispersion curve is indirectly inverted by using each point of dispersion curve to obtain depth and V_s values. Each point of the dispersion curve gives depth and S-wave estimate. These data are used to plot the best fit and to obtain the general trend of S-wave velocity with depth. The values obtained for the IAG model were $V_0=134$ m/s and $x=0.42$ (Fig 9.4). These values ($V_0=134$ m/s, $x=0.42$) are used to get velocity at 55 meter (around 750 m/s). Similarly, we have seen that the most affecting parameter on the ellipticity curve is the thickness of the sediment package following by effect of shear wave velocity. If the sediment thickness and H/V peak relation for an area is not available, then the values ($V_0=134$ m/s, $x=0.42$) are used to estimate this relation. The relation can be use to find out the thickness of the sediment package (see, for example, the previous chapter for detailed procedure). This information of thikness and V_s help to resolve this trade-off between thickness and velocity during the inversion.

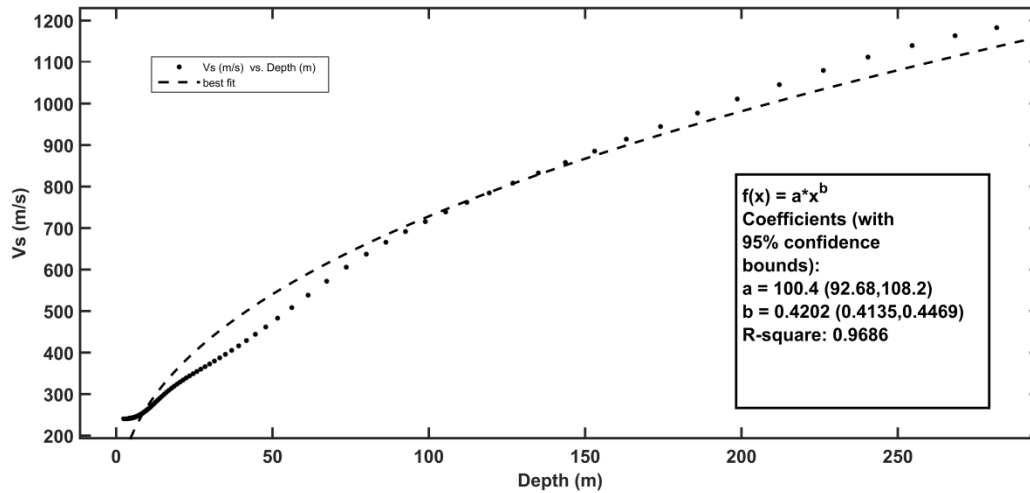


Fig.9.4 Shows the shear wave velocity vs. depth trend for the theoretical model dispersion curve of IAG borehole curve.

9.2 Inversion of the ellipticity curve with velocity trend and thickness information

For the inversion in this section, the number of layers is chosen to be four. For simple ground structure, the inversion converges very soon after the generation of very fewer numbers of models. We are not studying in detail the parameterization effect on the inversion, which was already done by Sambrige (2002) and Wathelet (2005, 2008). The parameter space for the inversion of the ellipticity curve is chosen such that shear and P-wave are allowed to change in a wide range. At the top of the sediment package, the velocity is selected as the velocity of one meter 50-250 m/s (in case of 134 m/s) and velocity at bottom is chosen on the basis of shear wave velocity increase trend by taking thickness information into account (750 m/s). We chose this velocity to be around 900 m/s. The velocity of bedrock is chosen to vary between 900 to 3500 m/s. The number of layers from the top to the bottom of sediments package is chosen to be four. The density is fixed at 2000 kg/m³. The Poisson ratio is chosen to lie between 0.2 to 0.5 for the whole sediment package. For this case of four layers model over the homogeneous half-space, the parameter space is 14 dimensional (five Vs, five Vp and 4 thickness). The original theoretical model is always included in ground model profiles with the misfit = 0 for the comparison. The theoretical inversion of this or any model will converge after a long time. For an inversion algorithm, even faster than Monte Carlo, it will requires infinite time to explore the complete parameter space. However, the usual goal of all the inversion processes is to find a model with acceptable fit to the data in some practical time. The number of models generated in all the theoretical section and later in the experimental data is kept limited to 25000, as in most of the cases. The inversion convergence was good after such number of model generation. The check of which part of the ellipticity is carrying the most important information is done by inverting different parts of ellipticity with the supplemented information regarding thickness and velocity at top and bottom of the sediment package. As we have the complete knowledge of the ground structure, it is easy to check the quality of inversion, that is, how good the model is

retrieved. So, it is essential to check and define a parameter to evaluate the quality (integrity of fit) of the inversion (Hobiger et al., 2013). If this integrity of fit is computed by comparing the theoretical Vs-profile to that of lower misfit inverted model, it will be problematic because of non-uniqueness. The inverted model may not have same layer thickness and bedrock depth with that of the theoretical one, but will have same phase velocity dispersion curve. Hobiger et al. (2013) suggested a parameter to check the quality of inversion with that of the theoretical model, termed it as the proximity value (T). They used this parameter to find the quality of joint inversion of autocorrelation curve with different parts of the ellipticity curve. The proximity value (T) is actually comparing the Rayleigh wave dispersion curve calculated for the lower misfit (best fitted inverted) model with the reference dispersion curve of the theoretical model. This reference dispersion curve is calculated for the given IAG theoretical model. The proximity value can be defined as

$$T = \sqrt{\frac{1}{N} \sum_{i=1}^N \left(\frac{Mod(f) - Inv(f)}{Mod(f)} \right)^2} \quad (9.1)$$

Mod(f) is the theoretical model dispersion curve, **Inv(f)** is the best fitted inverted model at frequency (f), N is the number of frequency points. As the theoretical model dispersion curve do not has any measuring error, the measuring error present in misfit function is replaced by **Mod(f)**. The value of T gives, somehow, a mean deviation of the inversion model from the reference model. Hobiger et al. (2013) suggested the T value to be around 90% match with reference model (theoretical model). However, a value of less than 0.1 can considered good fit to the model.

We checked which part of the ellipticity should be inverted to retrieve the theoretical model from the inversion by using velocity trend and thickness information. Fig 9.5 to 9.9 show the inversion of ellipticity full (0.2Hz to 20 Hz), left limb (0.2 to 2.04 Hz), left limb-peak-right limb (1Hz-to-3Hz) , right-limb up to trough (2Hz-to-4.5 Hz) and part beyond the trough of the ellipticity curve (4.5Hz-to-20Hz). The corresponding fit of the inverted models to that of theoretical and final model are shown in each corresponding figures (Fig. 9.6 to 9.10). Table 9.2 summarizes the results of all these parts of inversion along with misfit and T values.

Fig 9.3 shows the joint inversion of both ellipticity and dispersion curves, after the generation of 25000 models. The ground model is very well retrieved. Almost all the layers and velocity are very well retrieved. Fig 9.5 shows the inversion of the ellipticity curve only along with the shear wave velocity at the top and bottom of the sediment package obtained through dispersion curve direct inversion. The information for the thickness of the sediment package was obtained via thickness-frequency relation. In this case, the theoretical profile is not very well retrieved as that of joint inversion case in Fig 9.3, especially the depth of first and 3rd layers. However, as the

main purpose of utilization of the different techniques recommended for microzonation is to find the average velocity of sediment package and depth of bedrock, which is of great importance for seismic motion amplification and hazard mitigation for a site, the use of shear wave velocity trend, thickness information along with the ellipticity curve inversion serve to fulfill this desired goal (to find average shear wave velocity of sediment package and its thickness above the seismic bedrock). The velocity of the bedrock (at 55 meters is 1300 m/s) is very well retrieved by lower misfit model.

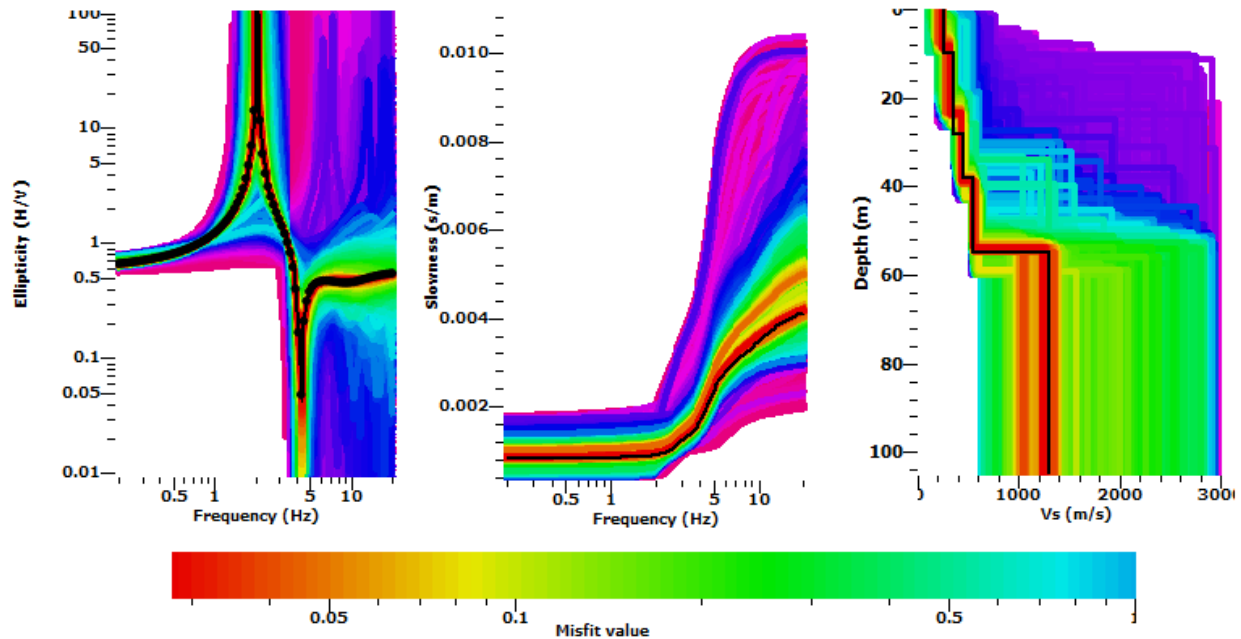


Fig.9.5 Shows the inversion of ellipticity curve along with S-velocity increase trend and thickness information.

Fig 9.6 shows the inversion of the left limb (0.2Hz to 2.04Hz) of the ellipticity curve. In this case, the ground structure is not very well retrieved, although the inverted profile is very well fitted by the data of ellipticity with the lower misfit. However, the T values are high, which show a bad retrieval of the model. Fig 9.7 shows the left and right limbs along with the peak of ellipticity (1Hz to 3Hz). As the peak of ellipticity carries important information about the thickness of sediments, this peak frequency can be used to find sediment thickness if the local thickness-frequency relation exists. We found that the inversion result of this part is very essential for the utilization of inversion of ellipticity alone if the near surface velocity and thickness information are known in priority. Fig 9.8 shows the inversion of right limb of ellipticity. The T values are lesser and the model fit to the inverted model also shows a good fit. Fig 9.9 shows the inversion of the ellipticity curve above the trough. Although the data above the trough are very well fitted by ellipticity curve, the model and T-values retrieved shows a deviation.

This analysis shows that by incorporating both limbs around the peak frequency along with velocity trend and thickness information, the minimum misfit model is closer to the subsurface model. We tested the same procedure for another model taken from Picozzi et al. (2005) and from Lontsi (2015). The Picozzi et al. (2005) model is composed of five layers over the bedrock at depth of 240m. The frequency-thickness and S-velocity increase trend relation for the area was already developed by Parolai et al. (2002), which was used to estimate the thickness (280 m), the top and bottom of sediment package velocity values (50 m/s to 150 m/s and 950 m/s to 1200 m/s). The velocity of half space was considered to vary between 950 m/s-to-3500 m/s, the density was considered constant and the number of layers equal to eight (the number of layers were chosen as it was used in the original study of Piccozi, 2005 and Lontsi, 2015). The inversion result is shown in Fig 9.10. The reference model of Picozzi et al. (2005) is retrieved but not in the absolute scale. The model integrity is tested by comparing the reference model dispersion curve to the best fit model dispersion curve to get the proximity value, $T=0.04$ suggests a very good retrieval of the model. Lontsi (2015) model has seven layers above the bedrock at 195 meters depth. The velocity increase trend is obtained by using the dispersion curve obtained via forward modelling of this model ($V_0 = 85$, $\alpha = 0.37$). This velocity increase trend and V_0 values were used to estimate the thickness-frequency relationship for the area ($h = 74f_0^{-1.587}$). The thickness and velocity trend information were supplemented with ellipticity of the model for inversion. The inversion result is shown in Fig. 9.11. The T value for the best model is 0.13. In this case, the model is not truly retrieved beyond the 80 meter depth, however, the overall velocity structure has a deviation of 18% of velocity below the 80 m between inverted and theoretical model. The surface wave methods are not sensitivity to map all the small contrasting interfaces but sensitive to map only interfaces with high contrast. The Lontsi (2015) model has interfaces whose velocities change very little bit among the first six layers. As mentioned earlier, the technique adopted to perform microzonation are required to provide the average shear wave velocity of soft sediment package and depth of bedrock. This velocity and thickness information supplemented based ellipticity inversion achieve the goal of that task very well.

Table 9. 1 Shows the misfit and T values for the ellipticity different part inversions.

Part used for inversion	Minimum misfit	T-Value
Ellipticity +Disperison curve	0.02	-----
Complete ell. + (velocity trend and thickness information)	0.03	0.008
Left limb of ell. + (velocity trend and thickness information)	0.03	0.15
Left and right limb of ell. + (velocity trend and thickness information)	0.009	0.007
right limb of ell. + (velocity trend and thickness information)	0.008	0.007
Above the trough of ell. + (velocity trend and thickness information)	0.08	0.25

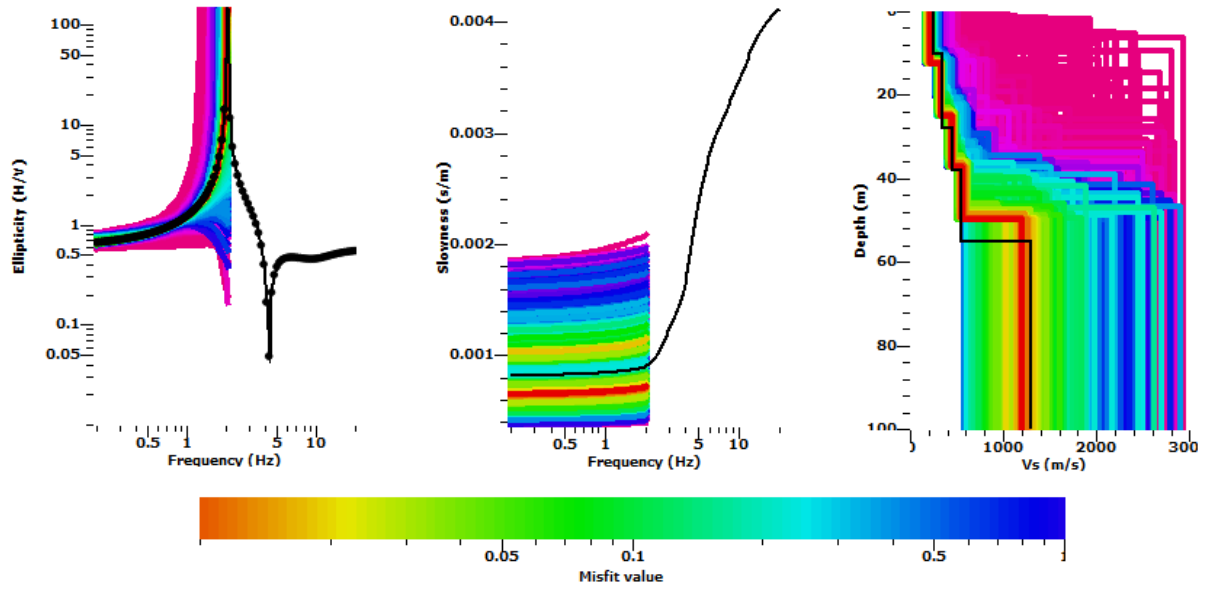


Fig.9.6 Shows the inversion of a left limb of ellipticity curve along with S-velocity increase trend and thickness information.

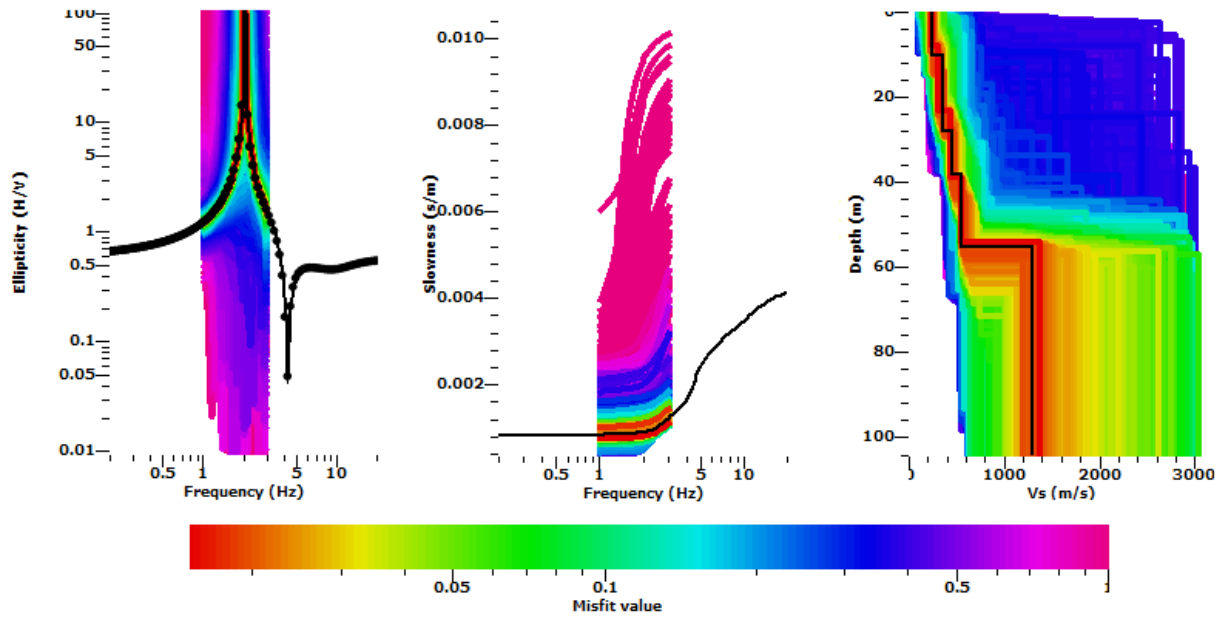


Fig.9.7 Shows the inversion of a left-peak-right limb of ellipticity curve along with S-velocity increase trend and thickness information.

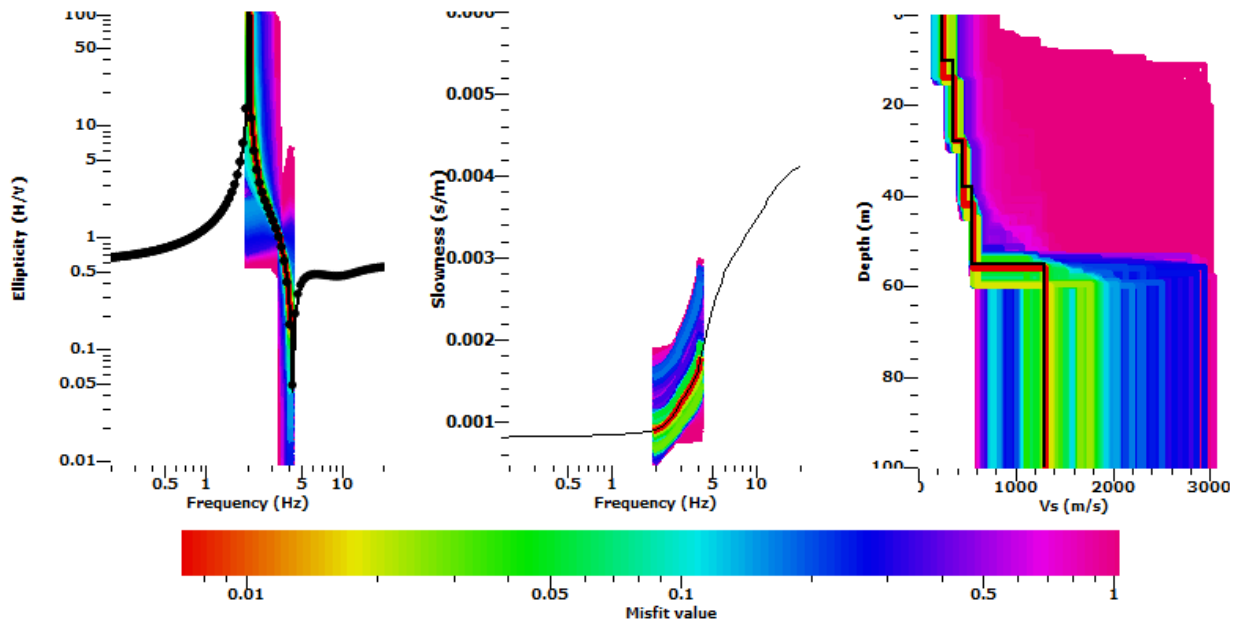


Fig.9.8 Shows the inversion of right limb of ellipticity curve along with S-velocity increase trend and thickness information.

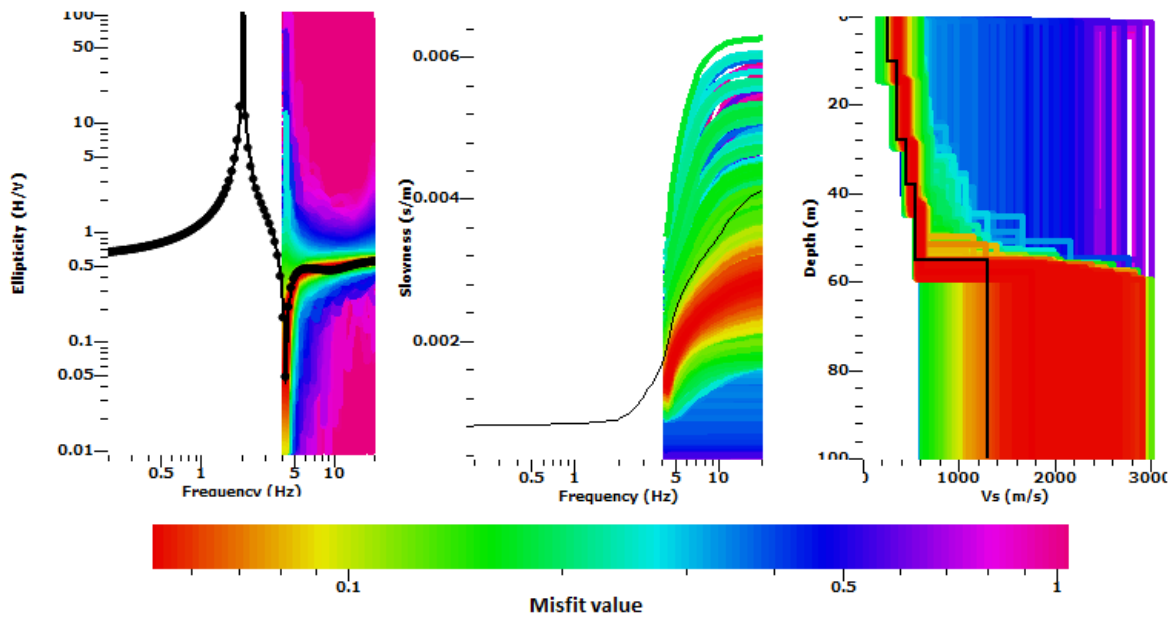


Fig.9.9 Shows the inversion of beyond the trough of ellipticity curve along with S-velocity increase trend and thickness information.

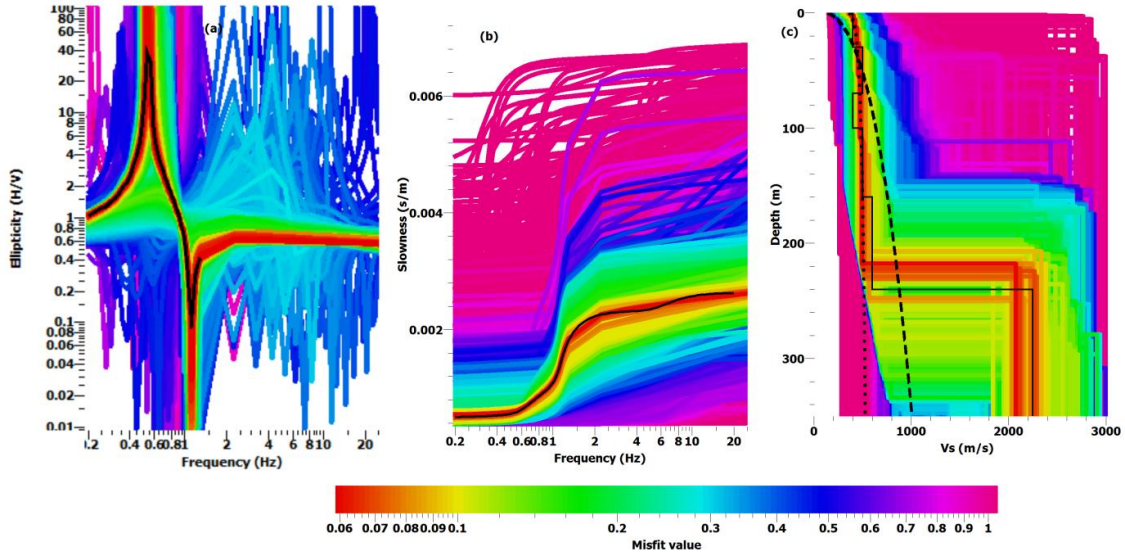


Fig.9.10 Shows the inversion result of Picozzi model: (a) ellipticity curve along (b) shows the proximity value is given with narrow black line the dispersion curve of the original model; (c) shows the inversion results; the dotted line shows the velocity increase trend obtained from dispersion curve, dashed line shows Parolai (2002) velocity trend for the area, and the narrow black line shows the original model.

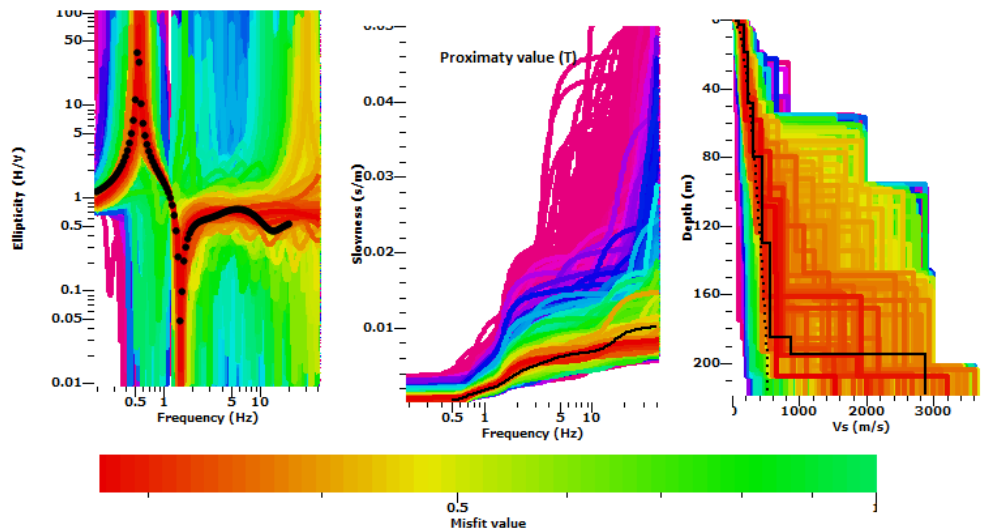


Fig.9.11 Shows the inversion result of Greece model (Lontsi, 2015) from full ellipticity curve along with S-velocity increase trend; dash line show the velocity increase trend for the model, at the center the proximity value is given with narrow black line.

This analysis showed that the trade-off between velocity and thickness for the ellipticity inversion can be minimized by the incorporation of S-wave velocity increase trend and thickness information. If the S-wave wave velocity increase trend is used with the ellipticity, this can, in a better way, replicate the subsurfaces-wave velocity structure.

9.6 Misfit function for the joint inversion

Generally, an inversion process can be divided into three steps: an computational algorithm to compute the initial set of models, a mathematical procedure to estimate the theoretical target curve (dispersion or ellipticity) utilizing a prior range of parameters (V_s, V_p, h, ρ) for layered Earth model, and a computation procedure to minimize the misfit (this will be explained in coming section). As in the all random inversion algorithm processes (i.e., genetic, simulated annealing and neighbourhood) the number of models generated are quite large. The test all of these models, that how close the response curves of these generated models are to the original target is done by a function known as misfit or cost function. The misfit is a quality control factor which pedals the performance of the inversion. Its value measures the deviation between the experimental and theoretically calculated values for the generated model for a layered Earth model. In case of uncertainty in the target curve data, the misfit function for the dispersion curve inversion is given as

$$\mathbf{Misfit}_{disp} = \sqrt{\left(\sum_{i=1}^N \frac{(\mathit{disp}_{exp}(f_i) - \mathit{disp}_{calculated}(f_i))^2}{\sigma^2(f_i)} \right) / N} \quad (9.2)$$

where $\mathit{disp}_{exp}(f_i)$ is the experimental dispersion curve at frequency f_i , $\mathit{disp}_{cal}(f_i)$ is the estimated dispersion curve for the model under consideration at frequency f_i , $\sigma(f_i)$ is the uncertainty in the experimental curve measurement at frequency f_i and N is the number of data points for which this comparison between experimental and estimated curve is made. Similarly, the misfit value for the ellipticity (H/V) inversion is given as

$$\mathbf{Misfit}_{ellip} = \sqrt{\sum_{i=1}^N \frac{(\mathit{ellip}_{exp}(f_i) - \mathit{ellip}_{theo}(f_i))^2}{\sigma^2(f_i)} / N} \quad (9.3)$$

where $\mathit{ellip}_{exp}(f_i)$ is the experimental ellipticity curve at frequency f_i , $\mathit{ellip}_{theo}(f_i)$ is the estimated (theoretical) ellipticity curve for the model under consideration at frequency f_i , $\sigma(f_i)$ is the uncertainty in the experimental curve measurement at frequency f_i and N is the number of points for which this comparison between experimental and estimated curve is made. Both the equations (9.2 and 9.3) will result 1 if all the models fall within the standard deviation of experimental data (dispersion or ellipticity). This signify that the \mathbf{Misfit}_{disp} and \mathbf{Misfit}_{ellip} usuall acceptable value is 1 (Sambridge, 2001), which mean that a calculated model ellipticity or

dispersion curves must lie within the one standard deviation of experimental ellipticity and dispersion curves. An important point to remember here is that in case of no uncertainty in experimental curve, specially when active source is used for the theoretical measurement such as performed in this study, the term $\sigma^2(\mathbf{fi})$ in both equation 9.2 and 9.3 is replaced by the $\mathbf{disp}_{exp}^2(\mathbf{fi})$, $\mathbf{ellip}_{exp}^2(\mathbf{fi})$. In case of joint inversion, the misfit at the end of the inversion is average for both ellipticity and dispersion curves such as

$$\mathbf{Misfit}_{\mathbf{ellip}+\mathbf{disp}} = \frac{(\mathbf{Misfit}_{\mathbf{ellip}}+\mathbf{Misfit}_{\mathbf{disp}})}{2} \quad (9.4)$$

However, this does not seem a very interesting approach, because it weights both the targets equally. Earlier, the joint inversion of H/V and dispersion curves was suggested around the peak and trough of the H/V curve due to the Love and body wave effects presence within the curve. For peak and trough consideration case only, the misfit of H/V curve was suggested by Scherbaum (2003) and Wathelet (2005) is given by

$$\mathbf{Misfit}_{\mathbf{ellip-extrema}} = \sqrt{\frac{(\mathbf{f}_{\mathbf{exp-max}}(\mathbf{ellip})-\mathbf{f}_{\mathbf{theo-max}}(\mathbf{ellip}))^2}{\sigma^2(\mathbf{maxima})}} \quad (9.5)$$

while for minima such as

$$\mathbf{Misfit}_{\mathbf{ellip-minima}} = \sqrt{\frac{(\mathbf{f}_{\mathbf{exp-mini}}(\mathbf{ellip})-\mathbf{f}_{\mathbf{theo-mini}}(\mathbf{ellip}))^2}{\sigma^2(\mathbf{minima})}} \quad (9.6)$$

where the $\mathbf{f}_{\mathbf{exp-max}}(\mathbf{ellip})$ and $\mathbf{f}_{\mathbf{exp-mini}}(\mathbf{ellip})$ show the experimental ellipticity maximum and minimum values, while $\mathbf{f}_{\mathbf{theo-max}}(\mathbf{ellip})$ and $\mathbf{f}_{\mathbf{theo-mini}}(\mathbf{ellip})$ show the modelled ellipticity maximum and minimum values and $\sigma^2(\mathbf{maxima})$ and $\sigma^2(\mathbf{minima})$ show the uncertainty at these maximum and minimum experimental ellipticity curve. The final misfit for these singularities points of ellipticity curve is average as

$$\mathbf{Misfit}_{\mathbf{ellip-peaks}} = \frac{(\mathbf{Misfit}_{\mathbf{ellip-extrema}}+\mathbf{Misfit}_{\mathbf{ellip-minima}})}{2} \quad (9.7)$$

However, a new problem arises here, which is how to weight this $Misfit_{\text{ellip-peaks}}$ with the dispersion curve, which usually contains multiple data points. Two procedures are generally adopted for weighting each target in joint inversion. One is the averaging of the individuals misfit for both the dispersion and ellipticity (Hobiger, 2013), while the other is suggested by Wathelet (2005) is given as

$$Misfit_{\text{ellip+disp}} = (1 - \alpha)Misfit_{\text{disp}} + \alpha Misfit_{\text{ellip}} \quad (9.8)$$

In this case, the usual values of the α is 0.5, which means to assign an equal weight to both of the dispersion targets. Similarly, $\alpha = 0$ means the inversion is completely based on the dispersion curve, while $\alpha = 1$ means the inversion relies only on ellipticity curve. However, as the numbers of data sample for both the target are not usually the same, it is difficult to assign an equal weight to of both the targets. Piccozi et al. (2005) suggested a procedure to lower the values of α for one target at the expense of the other (reducing one target weight while increasing the other). By applying this trial and error method, we can choose the value for α which results in a lower misfit. We checked this procedure here for different values of α and found generally a good result of α ranges from 0.2 to 0.015. However, the disadvantage of this procedure is that the range of α changes for case to case and has no such common range of α values which could be recommended for the general usage.

So, defining the misfit function seems very cumbersome. Usually, the Sambridge (2001) idea of an acceptance level for misfit is used to overcome this hindrance in the weighting of a different target. Sambridge (2001) suggested an acceptance level of misfit, which is, within certain misfit value, all the models in parameter space are taken from the model generated for the different target (dispersion and ellipticity curves). As acceptance level, Sambridge (2001) suggested that all the generated models should lie within one standard deviation of the target curve, $Misfit_{\text{disp or ellip}(fi)} = \text{disp or ellip}_{\text{exp}}(fi) \pm \sigma(fi)=1$. For joint inversion of different targets (dispersion and ellipticity curves) the misfit weight is set to 1 for both the targets at the start of inversion, which will compel the algorithm to generate models within one standard deviation. The misfit values at the end are averaged out for both of the targets. The drawback of this approach arises simply from the question: are the standard deviations for both targets the same? The simple answer is no, because both the targets are obtained differently as the H/V curve is obtained from the ambient noise recording (will certainly have higher standard deviation), while the dispersion curve is obtained from active source, and will have little standard deviation (specially in our case).

Therefore, it is clearly required to define a weighting function for this joint misfit function. This new weighting function should use the span of data points for the different targets (dispersion and ellipticity curves) as a controlling parameter. We tried to obtain this weighting function from a simple proportion formula such as $W_{HV} * n = W_{disp} * m$, where n is the number of data points for ellipticity curve, m is the number of data points for dispersion curve, W_{HV}, W_{disp} are weighting functions of ellipticity and dispersion curves, respectively. The values of these weights are chosen such that their sum should be equal to 1 ($W_{HV} + W_{disp} = 1$). This lead to define the weighting factor for both the targets as $W_{disp} = \frac{n}{n+m}$ and $W_{ellip} = \frac{m}{n+m}$. Now, the joint misfit function for both the targets can be defined with their respective weighting functions as

$$Misfitt = W_{HV} * \sqrt{\left(\sum_i^n \frac{(elliptarget(f) - ellipmodeled(f))^2}{\sigma^2(f)_{target}}\right)} + W_{disp} * \sqrt{\left(\sum_i^m \frac{(disptarget(f) - dispmodeled(f))^2}{\sigma^2(f)_{target}}\right)} \quad (9.9)$$

where $disptarget(f)$ and $elliptarget(f)$ are the target curves for both targets (theoretical or experimental), $ellipmodeled(f)$ and $dispmodeled(f)$ are the modelled curves for both the targets at frequency f , $\sigma^2(f)_{target}$ is the deviation in data measurement. If not available, it can be replaced with $elliptarget(f)$ and $disptarget(f)$ in either case.

We used the IAG model to demonstrate how this misfit function work for joint inversion of ellipticity and dispersion curves considering a different number of data points for both the targets and the result was compared in terms of target curves and the original model. Initially, the data points of both the targets were considered to be equal, $n=m=50$, followed by $n=25$ and $m=50$ (Fig 9.12). This weighting function for both the targets W_{HV}, W_{disp} has an advantage which ensures higher weights for the target curve having less number of data sample, while the target having higher number of points get lower weight. This can be observed more clearly when the data points for ellipticity are reduced. The weight it gets higher as compared to dispersion curve (Fig 9.13).

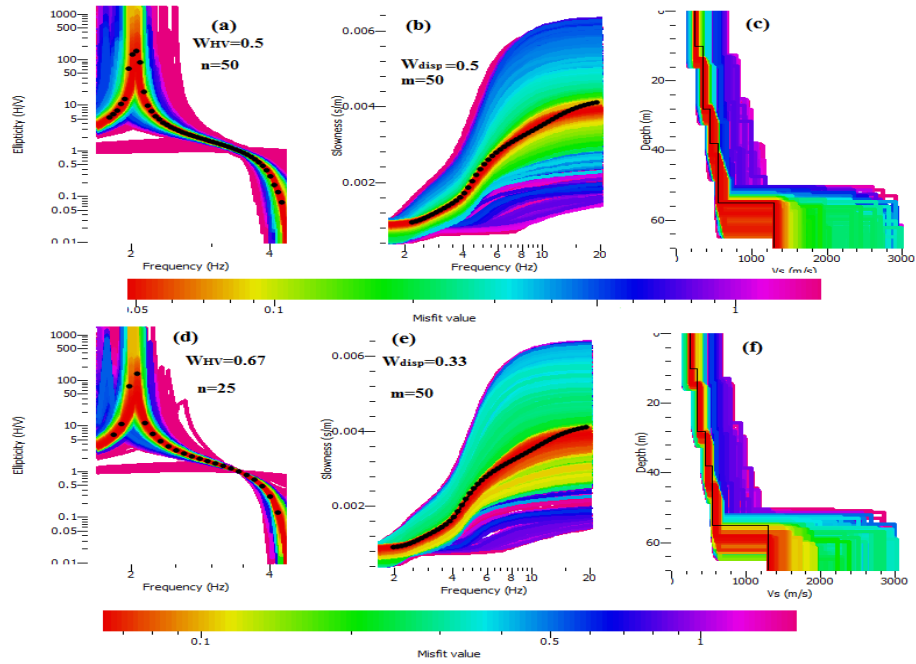


Fig.9.12 Shows the inversion results for misfit function defined in Eq.9.9 for a different number of data points for ellipticity and dispersion curves. Shear wave velocity profiles of all the generated models are shown; the original model has included (black line).

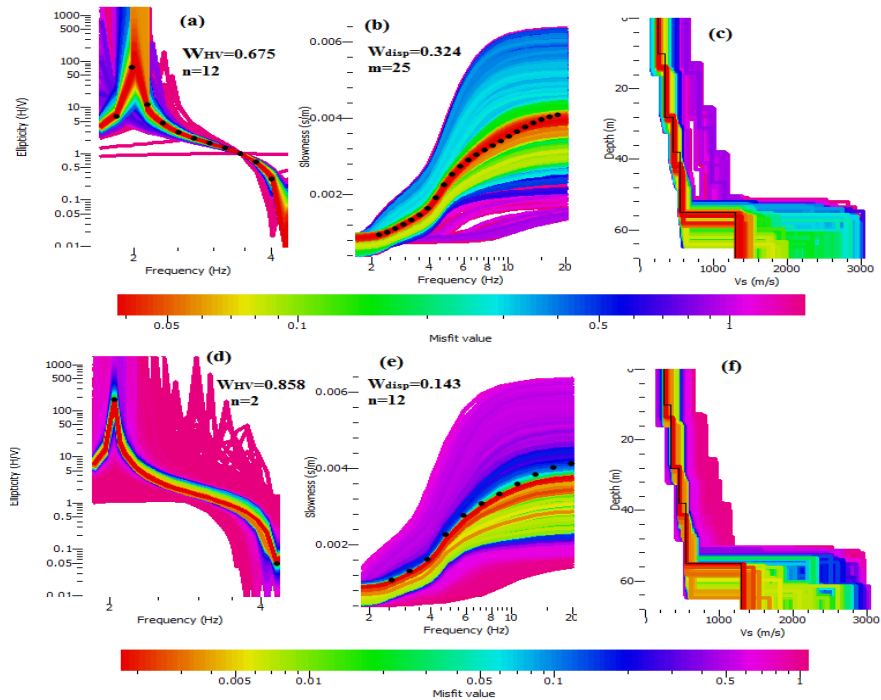


Fig.9.13 Shows the inversion results for misfit function defined in Eq 9.9 for a different number of data points for ellipticity and dispersion curves. Shear wave velocity profiles of all the generated models are shown; the original model has included (black line).

Until now this newly defined misfit works well for the theoretical joint curves inversions as shown in Fig 9.12 and Fig 9.13. However, this new misfit does not give a satisfactory result for the experimental data inversion. We used Eq.9.8 for the experimental curves for our inversion, where the weights of ellipticity curve were chosen to vary between $\alpha = \mathbf{0.2 to 0.015}$.

Chapter 10: The inversion of ellipticity and dispersion curves

10.1 Inversion of the experimental data

To check the lessons learned from the investigations of chapters 7, 8 and 9, we processed some experimental data. The three different sites chosen for this are located at the state of São Paulo, Brazil (Fig 10.1). The three sites, University of São Paulo (USP), the Colônia and the Bebedouro were chosen while keeping in mind some distinct properties of each site. The USP site (in front of the IAG - Instituto de Astronomia, Geofísica e Ciências Atmosféricas, cited here frequently as IAG and another site next to the IGc - Instituto de Geociências, cited here as IGC) has the advantage of the borehole data availability for the calibration and for the quality check of the inversion result. The Colônia site was chosen because of its geological significance, such as its bowl shape structure that is almost swampy and most of the conventional geophysical methods are difficult to be employed there because of the surface water and mud (there are some small patches of dry land which make it possible to install seismometer for noise recording and hence, the H/V analysis). The Bebedouro site was chosen because of the availability of seismic noise data recording as well as the multiple water wells subsurface interfaces data, from which the information about the subsurface interfaces were accessible and it was easy to test the thickness-frequency relation. Among all these three sites, the two IAG-IGC and Colônia have a strong bedrock laying below the unconsolidated soft sediments. This is true for the Bebedouro area too, however, the surface sediments are stronger as compared to the pre-mentioned sites. The detailed geological description of these sites are beyond the scope of this chapter, however, a concise introduction will be presented for each of the sites here. In this chapter, initially, the geology of the sites will be briefly discussed, followed by the removal of Love waves contribution from the H/V curve, to make it a truer representative of the Rayleigh waves ellipticity, and then the use of its inversion with dispersion curve. At the end, it will be showed some new aspects for which the simple H/V could be utilized.

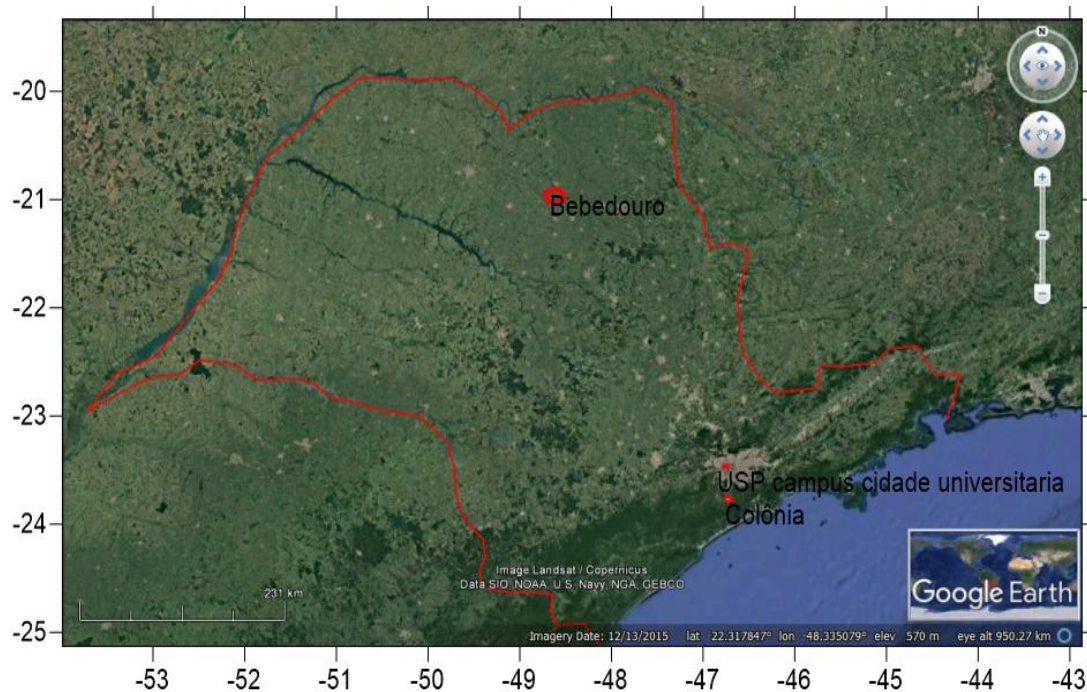


Fig.10.1 Shows the boundary (in red) of Sao Paulo state. Locations where the MASW and H/V analysis were made are shown in the red circles ((taken from Google earth. Imagery date April 2015. Access at March 2017).

The IAG-IGC-USP site is located in the continental rift part of south-eastern Brazilian basins, specifically in the São Paulo basin. The São Paulo basin has an irregular shape comprised of an area of almost 1000 sq. km. It is mainly drained by the Tietê river and secondarily by Pinheiros and Tamanduatei rivers plus their tributaries (Riccomini, 1989, 1992). The São Paulo basin is geotechnical and geologically extensively investigated because most of it lies under the urbanized part of São Paulo city. The geology of the site presents predominance of clay-sand sediments of Resende and São Paulo formations, superimposed on the crystalline basement augen-gneisses composed of Precambrian age (Riccomini, 1989). The lithological information from the wells (Porsani et al., 2003) shows a sandy-clay backfill layer predominantly dark, sometimes with organic matter, with a variable thickness between 4.5 and 6 m. Sedimentary units of the Resende formation have two levels. The top consists of interbedded silty clay with coarse-grained sand that has thickness ranging from 11 to 14.5 m. The lower unit is composed of sandy-clay superimposed to a clay horizon, with thickness between 29 and 32 m, the sandy layer is 18 m thick and the clay layer 13 m thick at the end. The crystalline basement is composed of augen-gneiss with feldspar crystals. The top of the basement is fractured. The bedrock is at 52-55 m depth in the site.

The Colônia site is located in the southern suburbs of São Paulo city, Brazil (Fig.10.2). In the area, there is a structure with a circular geometry (diameter of 3,6 km) comprising an annular ring of hills surrounding a depression. The structure is mostly a swamp. Its origin is attributed to an impact of meteorite (Riccomini et al., 1989). The structure was formed in crystalline basement rocks of Neoproterozoic age and the depression is mainly filled with organic-rich

sediments of Quaternary age. The main rock types of the basement comprise schist, quartzite, gneiss, migmatite, diorite, quartz diorite (Sadowski et al., 1974). The upper sediments of the sedimentary infill of the depression described from a shallow drilling (Ledru et al., 2005, 2009) showed black, organic-rich, clayey sediment (peat) with some intercalations of fine sand. A core recovery of a groundwater borehole (Riccomini et al., 1991) showed the follows sedimentary column: i) predominantly organic-rich silty clay up to 200 m deep, approximately, with minor intercalations of sandy mud with quartz grains after 90 m deep; ii) from 200 m up to 260 m occurs intercalations of sandy mud with quartz grains and sandy mud with quartz pebbles; iii) starting from 260 m, approximately, occurs pebbly mud with some presence of Precambrian rock fragments suggesting to be a fanglomerate deposit derived from the elevated parts of the ring (Ledru et al., 2005), a representation of the initial filling, or to occurrence of a crater-fill breccia. The total depth, estimated by seismic reflection investigation (shown in Fig 10.2) which does not reach the central part of the structure (Riccomini et al., 2011) is around 340 m (sedimentary infill plus breccia).

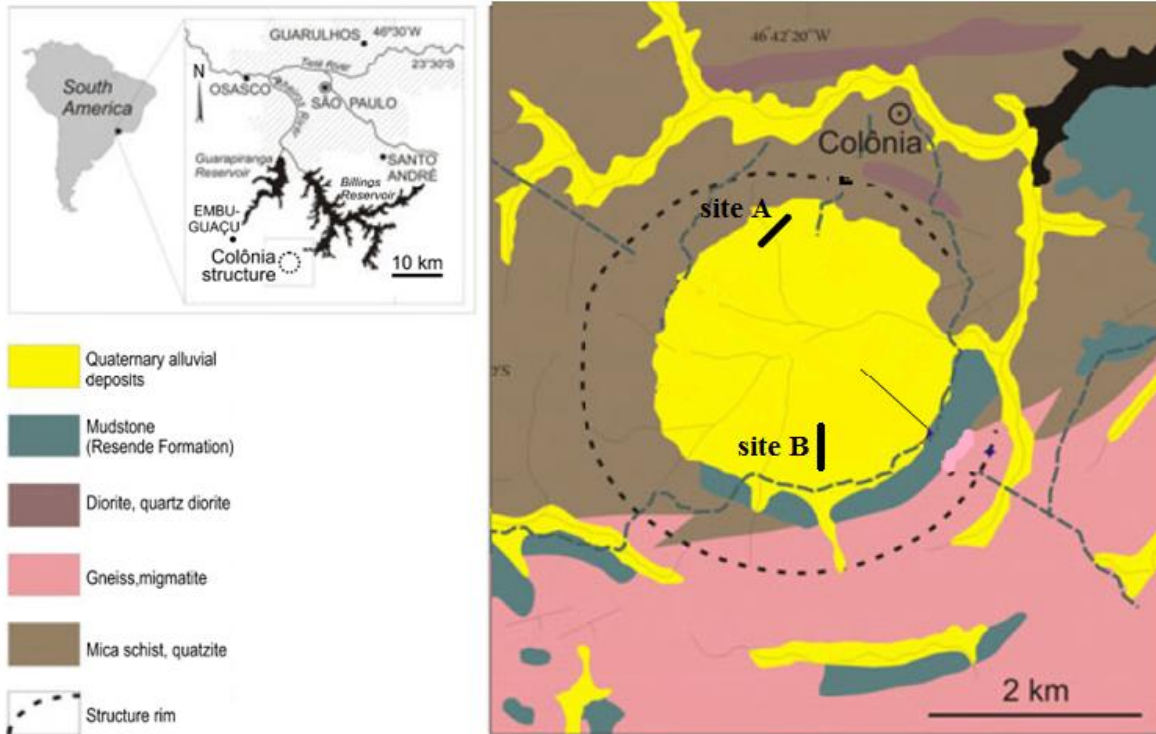


Fig.10.2 Location (left) and geological map of the Colonia structure. The black thick lines indicate the locations of MASW tests, while thin line indicates reflection line (modified from Riccomini et al., 2011).

The Bebedouro site is covered by a layer of sandstone (Adamantina formation) with, usually, 50 to 100 m thick. Below the sandstone is a basalt layer (Serra Geral formation) with a thickness of approximately 500m (Assumpcao, 2007). The geological map of the site is shown in Fig. 10.3, which shows the main geological units of the region. The sandstones overlie, in unconformity, the basalts of the Serra Geral Formation (Lower Cretaceous). In between, basalt sequence may

also occur with thin layers of sandstones. The surface of the terrain is smooth, in general, with elevation varying from 480 to 520 meters.

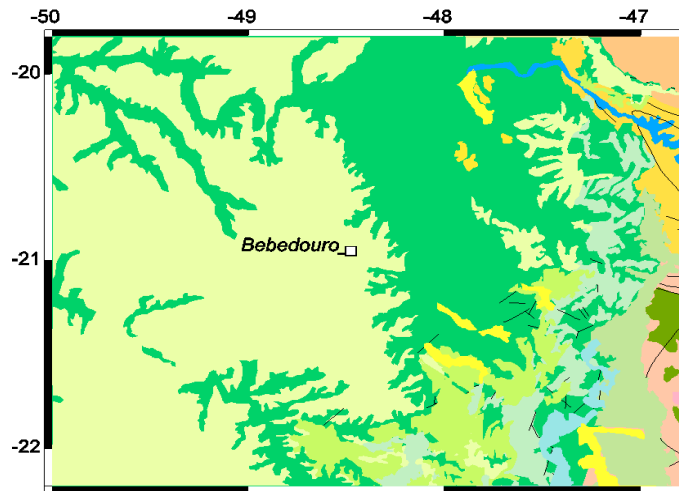


Fig.10.3 Shows the geological map of the NE region of São Paulo State. The area is dominated geologically by the sedimentary rocks of the Bauru Group and basalts.

In Bebedouro, sandstones predominate Adamantina Formation and the underlied basalts of the Serra Geral Formation; these basalt layers extends westward under sediments (sandstones) of the Bauru Group. In Bebedouro and neighboring municipalities, fractured aquifers in this basalt layer are quite explored (Assumpção, 2007).

10.2 Data acquisition parameters

MASW and the H/V analysis were made at two sites in USP campus (São Paulo city) (Fig 10.4). One of the acquisitions was made in front of Instituto de Astronomia, Geofísica e Ciências Atmosféricas (IAG) while the other in front of Instituto de Geociências (IGC). The measurements were made with a broadband 3 component sensor (Nanometrics Trillium Compact 120-s) and the ambient noise wavefield recordings were made for 24 continuous hours on weekends to ensure minimum cultural noise influence. The ambient noise data acquisitions were done following the guidelines developed under the SESAME (2004) recommendations. For the fundamental resonance frequency estimation through H/V curve, the SESAMES's (2004) processing recommendations were followed. Three sensors were used to record the seismic noise data at IAG site while two sensors were used at IGC site. IAG site contains three boreholes. The noise measurements were made next to each borehole (Fig 10.5). The H/V curves of IAG and IGC site are given in Fig 10.6.

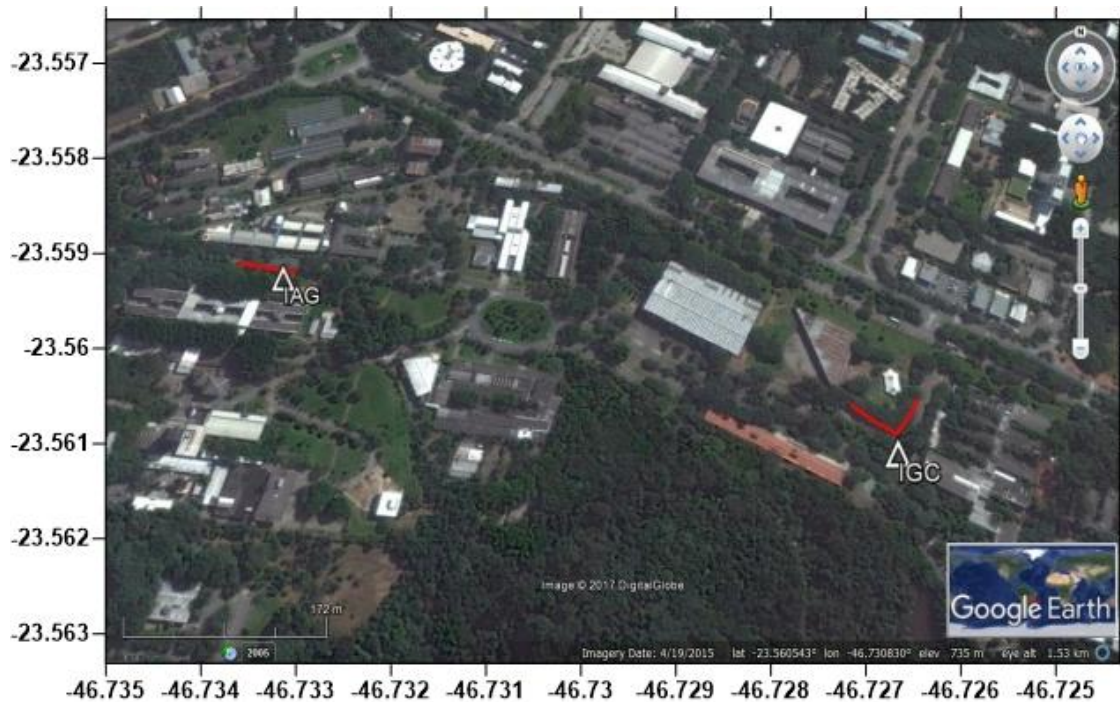


Fig.10.4 Shows the locations of IAG-IGC-USP site where the MASW (in red) and H/V analysis were made (triangle) (taken from Google earth. Imagery date April 2015. Access at March 2017)..

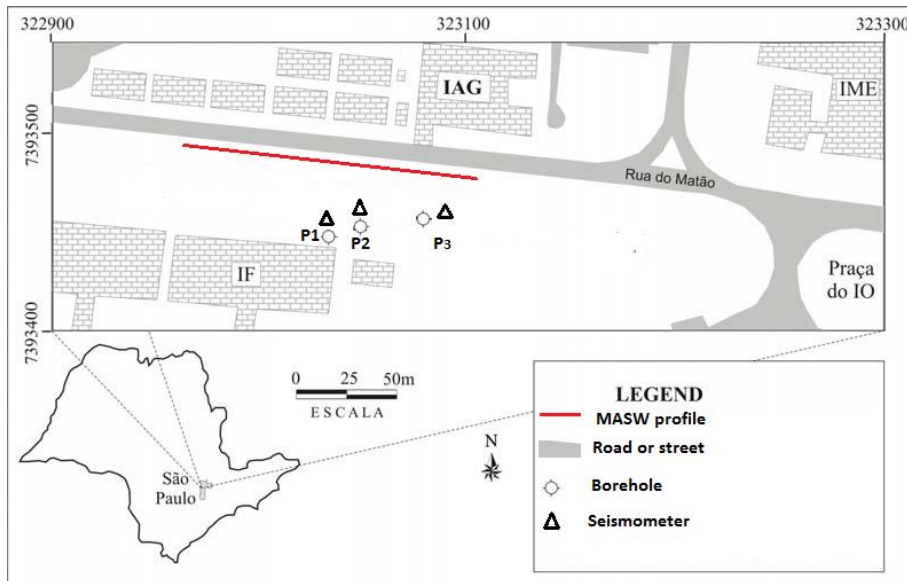


Fig.10.5 Shows the detailed location map of IAG site; legends explain the different symbols (modified from Porsani 2004).

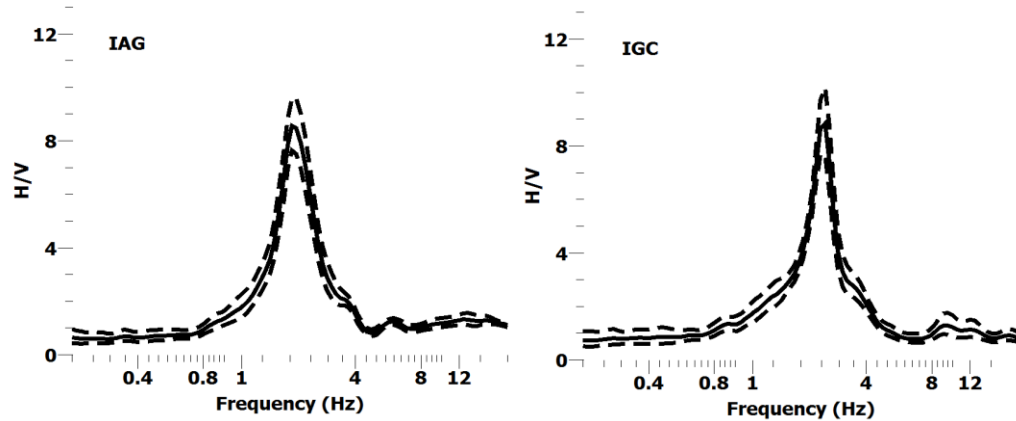


Fig.10.6 Shows the H/V curve of IAG and IGC sites.

At the Colônia site, seismic noise recording was made at six sites (Fig 10.7) with the same sensors. The seismic noise recordings were made at different locations and similar processing was followed to find the H/V curve for each site. The two MASW profiles were recorded near to sensor 7 and 4 (Fig 10.7). The recording parameters of these and all the others MASWs are given in chapter 4. The H/V curves obtained for these sites are shown in Fig 10.8.

The Bebedouro site has been monitored through seismometers installed for source characterization of induced seismic activity in the area. The locations of these stations and water wells are shown in Fig 8.5 (chapter 8). The H/V curves obtained from seismic noise recording next to 6 MASW profile are shown in Fig 10.9.

The H/V curves obtained at these three sites could be considered a good approximate of the fundamental resonance frequency of these three sites. However, to invert these curves for the shear wave velocity, the contribution of the other seismic phases should be removed, as suggested by Bonnefoy et al. (2008). To make this analysis we will demonstrate this Love waves effect removal for seismic noise recorded at IAG site only, it is due to the borehole velocity (V_s) availability for calibration via forward modelling.

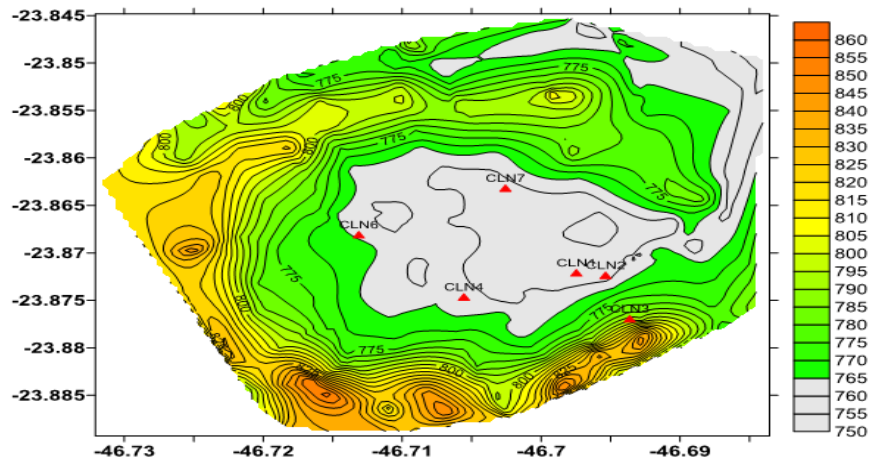


Fig.10.7 Shows the elevation contour map of the Colonia area; the red triangle shows the location of seismic noise recordings.

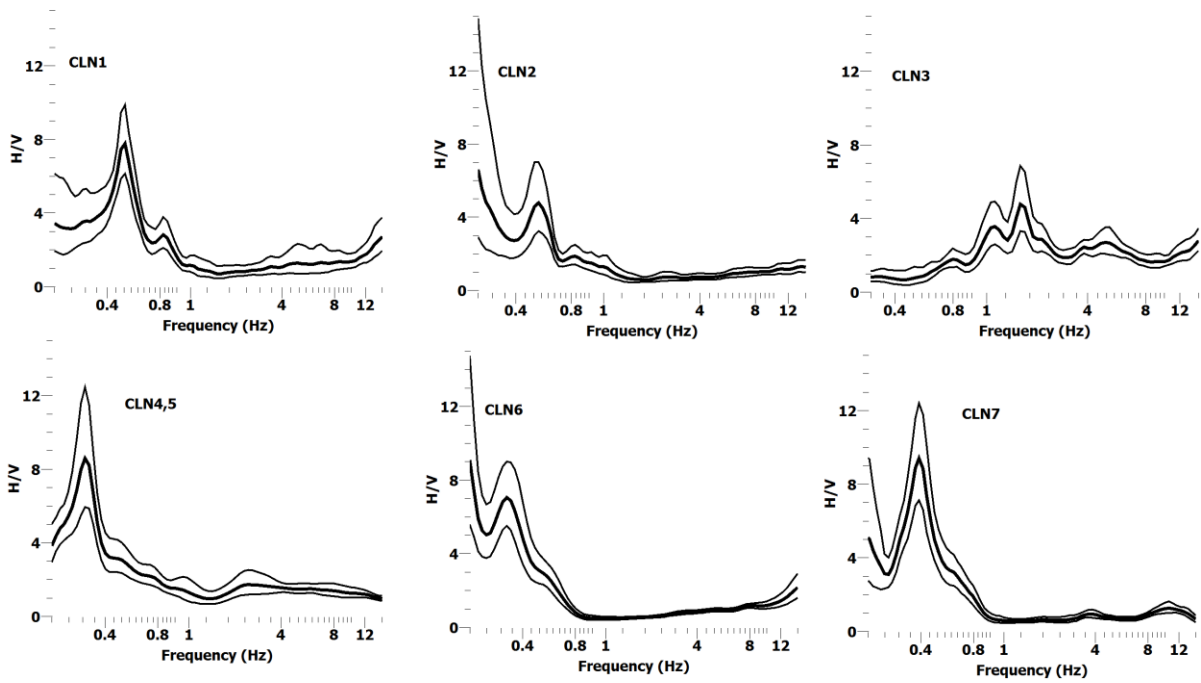


Fig.10.8 Shows the H/V curves obtained for the Colonia site (Fig 10.7).

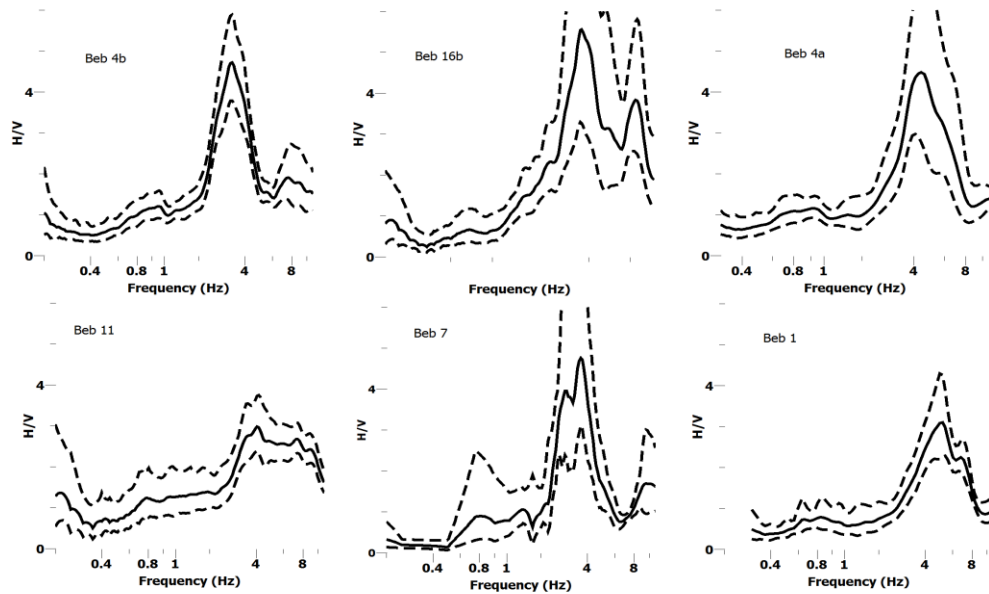


Fig.10. 9 Shows the H/V curves of Bebedouro area next to each MASW profile.

10.3 The retrieval of ellipticity from single 3c-station recording

The H/V curve peak frequency alone can provide three distinct informations, fundamental site resonance frequency, the thickness of the soil package and the average shear wave velocity of the soil package above the seismic bedrock. These information's can be directly obtained from the H/V curve peak. To obtained the thickness and average shear wave velocity information of the soil package, the knowledge of V_0 and the velocity increase trend with depth (x) are needed. For example, the IAG site fundamental frequency obtained from the H/V peak is 2.1 Hz. The values of $V_0 = 134\text{m/s}$ and $x=0.42$ were obtained from the dispersion curve direct inversion. These values were used to obtained the thickness of the soil package at the site (54 m) and the average shear wave velocity of the soil package (455 m/s). The depth of bedrock found from the borehole data is 53-55 m, while the average shear wave velocity of the soil above bedrock is around 393 m/s (only 15% deviation from the V_s values obtained from the H/V curve peak). This procedure shows the direct utilization of the H/V curve. However, for more sophisticated inversion and better subsurface information retrieval, we, usually, employ an inversion procedure. In this procedure, the H/V curve is linked to some physical phenomenon, which is latter utilized for the inversion. For example, the H/V curve is closely linked with the Rayleigh waves ellipticity and these Rayleigh waves ellipticity characteristics are used to obtain the subsurface information.

Most of the studies performed on the joint inversion of the H/V and dispersion curves were based on the assumption that H/V the curve truly replicates the ellipticity of Rayleigh waves. However, some earlier studies showed that the surface waves contribution to the horizontal components dominates over all the other phases of seismic waves, which constitute noise wavefield (Yamamoto, 2000; and Arai & Tokimatsu, 2000). Similarly, another observation established

from these studies is that Love waves contribution to the horizontal component may be higher than that of the Rayleigh waves. The same conclusion was endorsed by Bonnefoy-Claudet (2008). This fraction of Love waves contribution to the horizontal component is not constant and varies with time and from site to site (Kohler et al., 2006; Endrun, 2011) (also outlined in chapter 2). Hence, a prior assumption (if not close to the real value) about the Love waves fraction at the horizontal component of the H/V curve might lead to erroneous results. So, it is of prime interest to remove the Love waves contribution from the H/V curve to make it closer to the true Rayleigh waves ellipticity and then proceed to the inversion.

As described earlier, the H/V inversion was based on the conjecture that H/V completely corresponds to the Rayleigh waves ellipticity. The experimental H/V curve is usually unable to reproduce all the ellipticity curve characteristics (Tokimatsu, 1997). Tokimatsu (1997) observed that, except at the peak of the H/V and ellipticity curves, the H/V curve amplitude is generally higher than that of Rayleigh waves ellipticity (Fig 10.10). This deviation between the curves can be easily linked to the presence of the Love and other body waves phases to the noise wavefield at the horizontal component. The ellipticity peak ratio is amplifying more as compared to the H/V curve. Tazime (1957) and Scherbaum (2003) tried to link this Rayleigh ellipticity higher amplitude to the vanishing of the vertical component, around the site, fundamental frequency. Such as the fundamental resonance frequency, the medium acts as a filter which attenuates all vertical component contributions from the seismic noise wavefield. However, the H/V curve amplitude never reaches to match the ellipticity curve around this peak, but always remains finite. To explain this, one might link the non-vanishing of the vertical component around the site fundamental period to the presence of other seismic phases like refracted, reflected and converted body waves. The lowering of vertical component spectral amplitude around the resonance frequency can be easily observed. However, like the ellipticity curve, the vertical component spectra does not vanish; this makes sense if we assume that the body waves contribution to the vertical component. The Fig 10.10 shows the theoretical Rayleigh ellipticity obtained for the borehole P2 (Fig 10.5) and the H/V curve obtained from the noise measurement at the same site. The trough of both curves (ellipticity and H/V) does not perfectly match. This might be due to the argument that the borehole model is a representative single point while the H/V curve shape and peak is affected by the whole site local structure. Generally, the ellipticity curve is not considered for the inversion beyond the trough frequency due to the fact that from the trough onwards the influence of higher modes might dominate the curve (Hobiger et al., 2013).

The removal of the Love waves effect can be done by characterizing the distinctive properties of Rayleigh waves, which are different from the Love waves. This distinct feature can be later used for Love waves effect removal. Surface waves resulted from the polarized body waves coupled near to or at the surface, for instance, the coupling of P-wave and the vertically polarized shear wave (S_V) produces Rayleigh waves (Aki 2002). A phase shift of $\pm\pi/2$ exists between the

particle motion induced by this P-waves and vertically polarized shear wave (S_V). This coupling depicts an ellipse at the surface. The phase shift can either be positive or negative producing prograde or retrograde motion. Hence, the Rayleigh wave ellipticity can be defined as the ratio of horizontal and vertical displacement eigen-function at each frequency (at the surface) of the particle motion under Rayleigh waves influence. Love waves are horizontally polarized shear waves (S_h) trapped within the soft layer above a rock of high shear wave velocity due to multiple reflections. This distinction can be utilized to minimize or even remove the effect of Love waves fraction from the horizontal components of the experimental H/V curve and make it closer to the ellipticity curve (Hobiger et al., 2009).

As discussed, the presence of both surface wave types fraction has to be considered for inversion algorithms. The first technique proposed for this analysis is the classical polarization, where the H/V ratio obtained from the noise analysis is used for the Love waves effect minimization. The main assumptions on which this technique is based on are that, around the peak frequency of the H/V curve, the vertical component is mainly dominated by Rayleigh waves fundamental mode and the spectral content of the Love waves contributes equally to the horizontal components of the H/V curve. Hence, the H/V ratio amplitude should be divided by the $\sqrt{2}$ to remove the effect of Love waves (Fig 10.10). However, the Rayleigh/Love contribution, within the noise wavefield varies from site to site and its fraction, also strongly depends on frequency (Cornou, 2002). Hence, this equal contribution approach for Love waves effect removal from the horizontal component might lead to biased results. Therefore, to remove the Love waves effect, it should be used some more sophisticated approaches rather than a prior assumption about the Love waves fraction. Two procedures are suggested for this task of single 3c-station recording case: the time-frequency analysis (Fah et al., 2009) and RayDec (Hobiger et al., 2009). We adopted both techniques in this thesis, to remove the Love waves contribution from the horizontal components of single station noise recording. A concise introduction of this technique is presented here. The interested readers are referred to Fah et al. (2009) and Hobiger (2009) for more details.

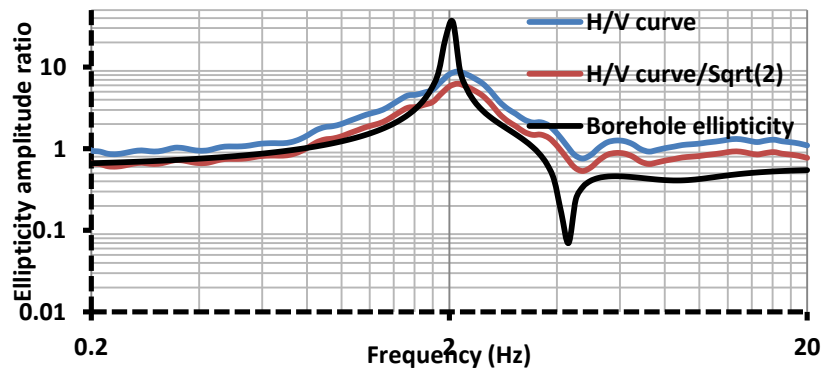


Fig.10.10 The comparison between H/V curve and the theoretical borehole ellipticity curve for the same site. The H/V curve in case of equal contribution of Rayleigh and Love waves as $(H/V)/\sqrt{2}$.

10.3.1 Time-frequency analysis

As described in the introduction of this section, the main features that can be used, in a systematic way, for Love waves effect minimization are the polarization properties of both surface waves (Rayleigh and Love). The first technique employed for this job is the time-frequency analysis. In this procedure, the Rayleigh waves vertical component is used as a distinctive property indicator of Rayleigh waves, which is lacking in the Love waves case. The vertical component energy level is estimated from the continuous wavelet transformation, which is later correlated with combined horizontal components energy maxima for the Rayleigh waves. The continuous wavelet transformation (CWT) is performed for all the three components of noise recording. This transformation projects the real-valued signal $x(t)$ into a time-scale plane, where both the duration and bandwidth of the noise signal are controlled by this single parameter called scale. CWT can be defined as

$$\text{CWT}_{x(t)}(\mathbf{a}, \mathbf{b}) = \frac{1}{\sqrt{\mathbf{a}}} \int_{-\infty}^{\infty} x(\mathbf{t}) \psi^* \left(\frac{\mathbf{t}-\mathbf{b}}{\mathbf{a}} \right) d\mathbf{t} \quad (10.1)$$

where $x(t)$ represents the noise record (vertical or horizontal), $\psi(t)$ is the mother wavelet, * illustrates a complex conjugation process, \mathbf{a} is the scale parameter, and if t is the time then b is a translation in time. The wavelet generally chosen for CWT transformation is Morelet wavelet.

The original Morelet wavelet was modified for the H/V analysis by Fah et al. (2009) as the original wavelet was not suitable for this analysis. This new modified Morelet wavelet is narrower in the frequency domain, which is better for the noise time-frequency analysis as frequency resolution is more substantial in this analysis (Fah et al., 2009). The modified Morelet wavelet is defined as

$$\psi(\mathbf{t}) = \frac{1}{\sqrt[4]{\pi}} (-\mathbf{a}\omega - \omega_0)^2 \mathbf{m} \text{ for } \omega > 0 \quad (10.2)$$

Here, m serves as a single parameter that controls both time and frequency resolutions. The central frequency of the wavelet is ω_0 at scale $a=1$. Higher values for m means higher frequency resolution while low time control/resolution. Similarly, low value for m ensures more time resolution at the expense of frequency resolution. The value of $m=1/2$ corresponds to the classical Morelet wavelet.

When the CWT is performed on the signal, its amplitude is obtained as a function of both time and frequency. The energetic arrival at the vertical component is chosen and the corresponding maxima on the horizontal components for the Rayleigh waves arrival is picked for the same time and frequency (Fig 10.11). The horizontal component selected response is delayed and advances at quarter of the period to compensate the theoretical phase shift $\pm \frac{\pi}{2}$ between the vertical and horizontal components. The ratio between these vertical and horizontal responses is taken as the ratio for this specific time and frequency and is stored. The process is repeated for all the frequency and time translations, and the wavelet coefficients are statistically analyzed through

histogram. The detailed time-frequency procedure analysis can be found in Fah et al. (2009). Here, we checked the effect of two parameters, duration of the signal and m of the time-frequency results with the borehole ellipticity.

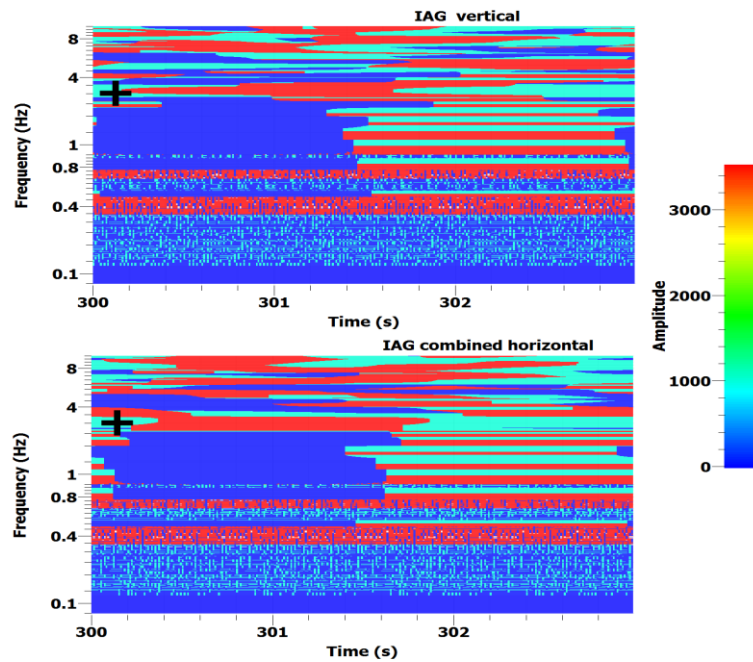


Fig 10.11 A graphic outline of the time-frequency method showing the CWT results of the vertical (top) and combined horizontal (bottom) signals from noise record. The plus sign is taken as an example of maxima on the vertical component for Rayleigh wave detections. The ellipticity of these detected Rayleigh waves is estimated using the ratio between the horizontal and vertical maxima at this time and frequency, \pm shifting the horizontal component by a quarter period at each analyzed frequency f .

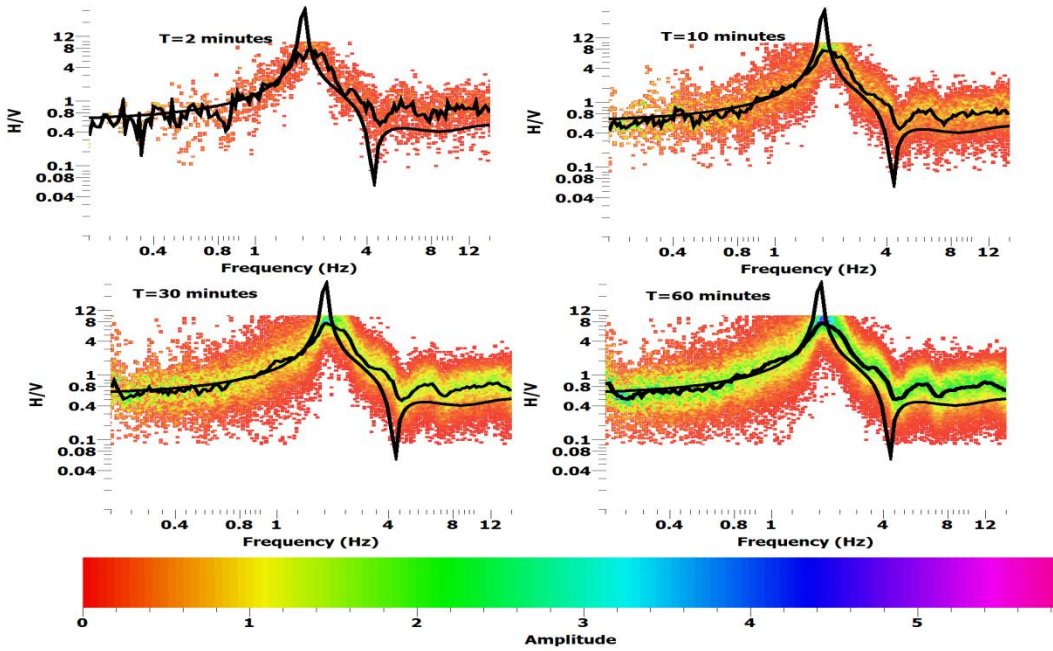


Fig.10.12 Shows the ellipticity (H/V) obtained from continuous wavelet transformation CWT for different duration of the signal with value of $m=2$; a histogram is drawn for each frequency; the colour within the histogram indicates the energy level; curly line shows the ellipticity obtained from CWT while solid smooth line shows the ellipticity curve obtained from the borehole data at the same location (IAG site).

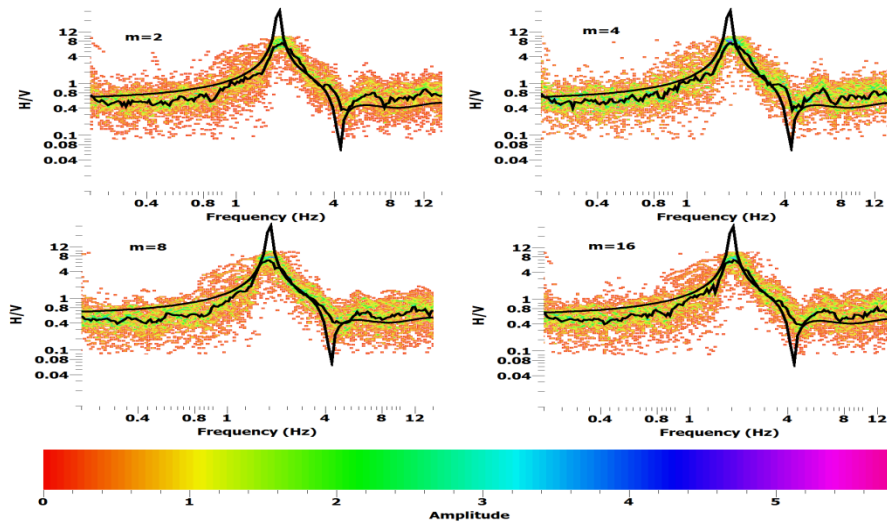


Fig.10.13 Shows the ellipticity (H/V) obtained from the continuous wavelet transformation (CWT) for different values of m for one hour signal. The curly line shows ellipticity obtained from CWT while solid smooth line shows the ellipticity curve obtained from the borehole data at the same location (IAG site).

From a comparison of the result with the borehole ellipticity at the site, we can suggest that for a better correlation with the right limb of the borehole ellipticity curve (Fig.10.13 c-d), the value of m (scale) should be in the range of 8-16.

10.3.2 Random decrement technique (RayDec)

The other major technique used for the Love waves effect removal/minimization to make the H/V curve a truer representative of the Rayleigh ellipticity is RayDec (random decrement technique). RayDec is classically used to find the building dynamic properties using a single component signal. Hobiger et al. (2009) extended this technique to the three component signal analysis. The ellipticity retrieved from the single station noise recording through RayDec is nearer to ellipticity curve than the classical H/V division by $\sqrt{2}$ for the Love waves effect minimization. A brief outline of the method will be discussed here (for more detail procedure, see Hobiger et al., 2009).

Consider a three component signal having N data point for each component, each of length T; the signal is, at first, filtered of bandwidth df centred at frequency f. The vertical component is considered as a master trigger similar to time-frequency analysis for the distinction of Rayleigh wave arrival. The vertical component of noise record is a search for all the times where the signal changes its sign from negative to positive; at each of these points, a signal of length segment Δ is stored for all the three components. The length of this segment Δ is chosen to ensure 20 significant cycles at each analyzed frequency ($\Delta=20/f$, where f is the analyzed frequency; frequency range 0.2 to 20 Hz is used).

Both horizontal components are shifted by $1/4f$ to compensate the theoretical phase shift of $\frac{\pi}{2}$ between vertical and horizontal components. The ratio between these stored segmented signals is found as

$$\mathbf{E} = \sqrt{\frac{\int_0^{\Delta} hf^2 \cdot s(t) \cdot dt}{\int_0^{\Delta} vf^2 \cdot s(t) \cdot dt}} \quad (10.3)$$

The term hf.s (t) shows the average horizontal signal while Vf.s(t) shows the vertical component. For our recorded data, we analyzed a one-hour noise record similar to the one used for the previous analysis in the section above. There are two control parameters on which this analysis of RayDec depends, one is the choice of window length (Δ) and the other is the bandwidth (df) of filtering. The effects of these parameters along with the duration of the signal are shown in Fig 10.14. The one-hour record is divided into 6 windows of 10 minutes each. Each one of these windows is analyzed separately and the ellipticity is discovered. At the end, the ellipticity for all these 6 windows is averaged out (Fig 10.14d). The ellipticity obtained is shown in Fig 10.14d along with the averaging error bar. The result shows a better match with the borehole's ellipticity especially around the peak and some part of the ellipticity left and right limb. The choice of window length (Δ) and bandwidth (df) for which we found better result are $\Delta = \frac{20}{f}$, **and** df=0.4f.

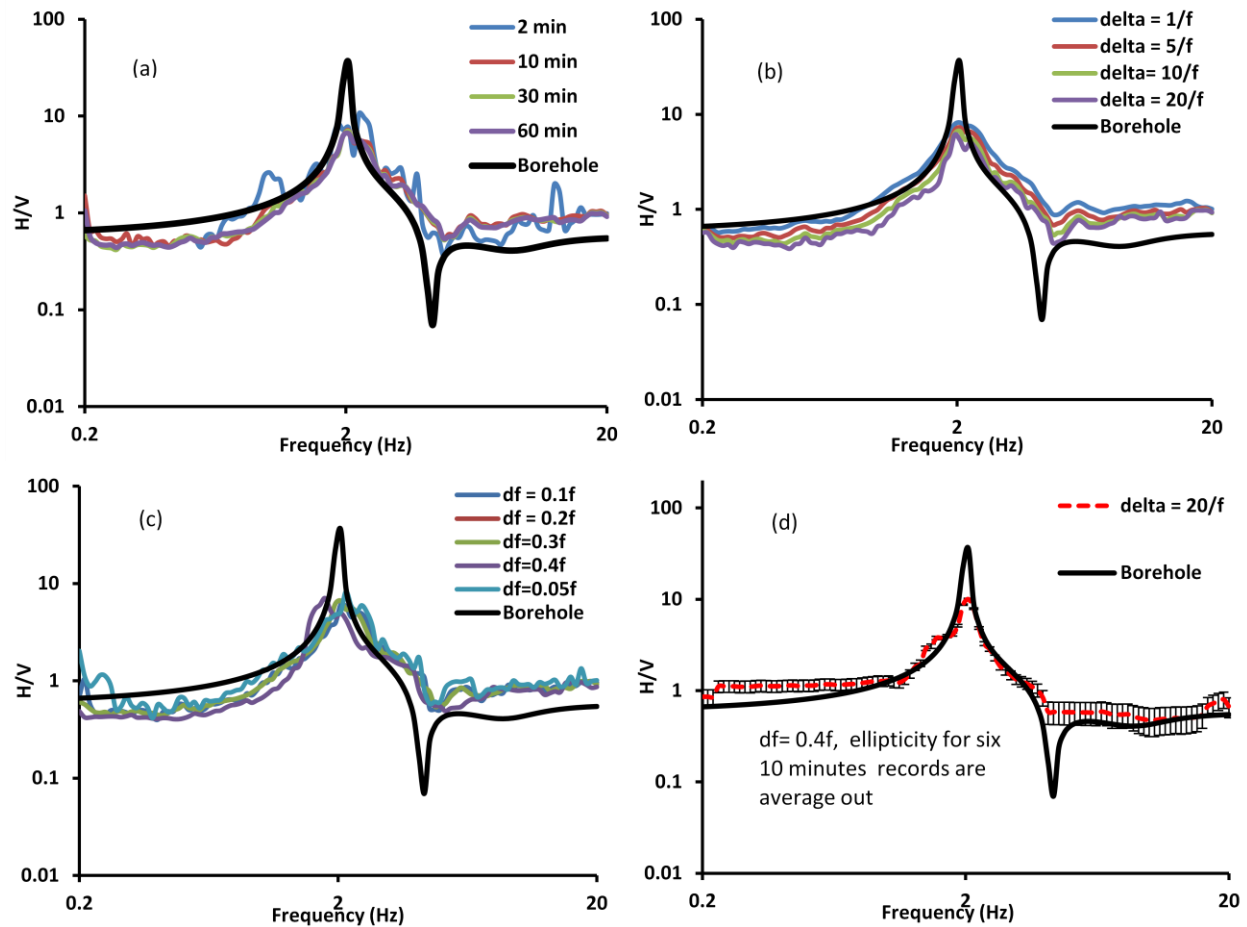


Fig.10.14 Shows the ellipticity obtained via RayDec technique; (a) shows the effect of recorded signal duration on ellipticity retrieval $df=0.2$ and $\delta=20/f$; (b) shows the effect of δ on ellipticity retrieval for $T=1$ hour and for $df=0.2$; (c) shows the effect of filtering for different df values with $T=1$ hour and $\delta=20/f$; (d) shows the ellipticity for six 10 minutes windows, the result is averaged out and compared with the borehole ellipticity.

10.4 Joint inversion of the ellipticity and dispersion curve for USP, Colonia and Bebedouro

The ultimate goal of most of the near surface geotechnical and earthquake engineering is to evaluate the stiffness of an area. The stiffness direct relation with shear-wave velocity makes it possible to measure V_s -profile with some geophysical techniques from the surface recording. The retrieval of ellipticity from the seismic ambient noise for a single station recording by removing/minimizing the effect of Love waves made it possible to obtain the V_s - profile with little bit more accuracy than the all previous inversion of H/V and dispersion curves. To check this, we needed to jointly invert the dispersion and ellipticity curves for all the three sites, starting from the IAG site as it has borehole data available for quality check of the inversion result. The ellipticity of all three studied area were obtained through the RayDec technique. As shown, in both the case of time-frequency analysis and RayDec techniques, that the ellipticity is

well retrieved for the right limb of the borehole ellipticity (Fig 10.13d and 10.14d), the same observation is made by Hobiger et al. (2013) for the right limb. As the peak amplitude of the retrieved ellipticity does not match the theoretical ellipticity peak of the site, the data points around the peak are not considered in the three cases. However, as the peak frequency provides a better estimate of the proximal depth of the bedrock, some part of the left limb of the ellipticity is considered for inversion to confine and utilize this peak frequency. The experimental dispersion curve of the IAG site, along with the theoretical dispersion curve from the Vs profile of the borehole P2, is shown in Fig 10.15. The experimental dispersion curve was obtained from 4.6 Hz till 33 Hz, while the borehole model dispersion curve was obtained for the frequency range 0.2 Hz to 50 Hz. However, it deviates from the experimental curve around 7 to 17 Hz. This deviation might be due to the fact that the borehole model dispersion curve represents a single point while the experimental dispersion is affected by the Vs structure of the whole area. The joint inversion of both the targets curve is shown in Fig.10.16.

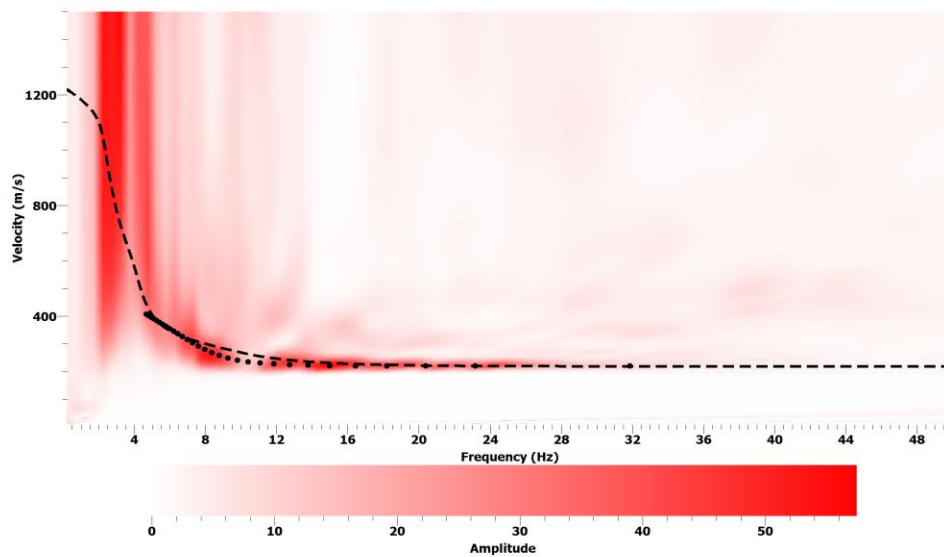


Fig.10.15 Shows the dispersion image of MASW recording line (Fig10.5). The dotted line shows the dispersion curve obtained from dispersion image while the dashed line shows the borehole's model dispersion curve.

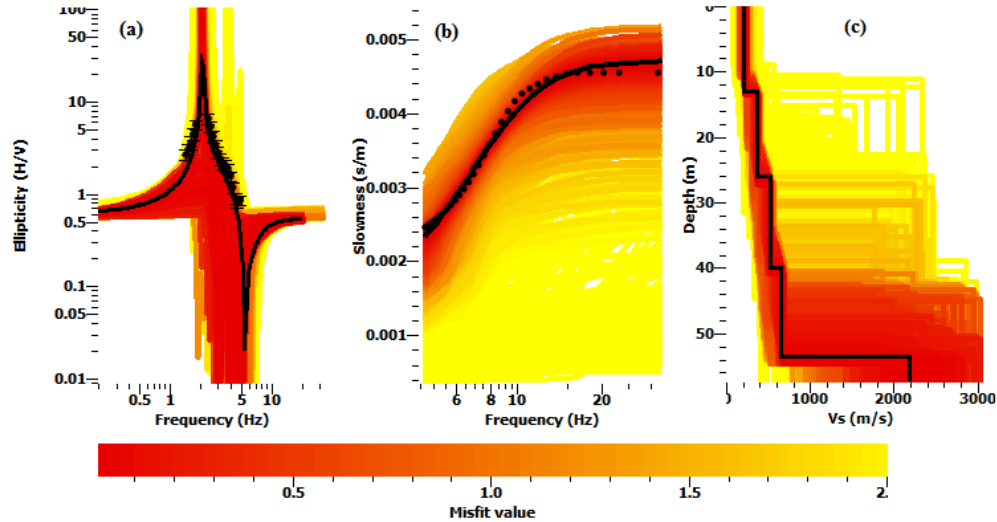


Fig.10.16 The inversion result of ellipticity and dispersion curves at IAG site; (a) shows the fitting ellipticity curve of IAG site with the dotted line while the black line shows the lower misfit ellipticity curve model; (b) shows the fitting to the experimental curve with the dotted line and lower misfit model dispersion curve with the black line; (c) shows all the generated models, the black line shows the lower misfit model.

The inversions of different parts of ellipticity and velocity increase trend provide a better estimate of the bedrock velocity in the theoretical section (chapter 9), however, in the experimental ellipticity and dispersion curve inversion, despite of the better depth estimate of the bedrock, it failed to provide a good estimate of bedrock velocity (Fig 10.17). The reason for this might be the unavailability of the experimental dispersion curve for the lower frequency range to better constrained the bedrock velocity.

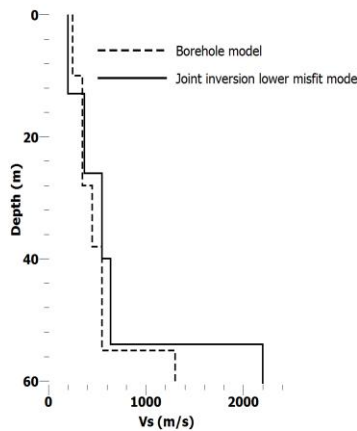


Fig.10.17 Shows the lower misfit Vs model (solid line) of the joint inversion (Fig.10.16) and borehole Vs model (dashed line).

We compared our recent results to the previous investigation at the site (Porsani et al., 2004). For all the models with misfit lower than 0.5, the bedrock depth retrieved from the joint inversion are

around 44-55 m, which is in very good correspondence with borehole (P2) depth 55 m. Additionally, lower misfit model shows bedrock at 53 m (Fig 10.17). The lower misfit model of joint inversion when compared to the borehole model (Fig 10.17) shows a maximum of 17% deviation in the velocity from the borehole model within the soil package. The bedrock velocity is not well constrained and has a 41% deviation with the borehole model velocity (Fig 10.17). Probably, the ellipticity curve joint inversion with a higher mode dispersion curve might provide a better constraint to the bedrock velocity as shown by Piccozi et al. (2005). However, it is not very common to observe higher mode dispersion curve and, even if one is able to retrieve the higher mode dispersion curve, the order of the picked curve remained always a mystery as higher mode appearance generally does not follow a certain order. As we do not have a clear higher mode dispersion appearance in our experimental curve (Fig 10.15), we limited to the fundamental mode dispersion curve only. The joint inversion performed here showed good average velocity trend retrieval with that of borehole shear-wave velocity. This velocity deviation within soil package between the borehole and joint inversion results might be due to the fact that the borehole result is confined to a single point, while the ellipticity and dispersion curve results are influenced by the whole local subsurface structure. The short summary of this site results shows that if we are able to minimize the Love waves contribution to the horizontal noise wavefield, the joint inversion will give good results in a very cost effective and easy way. The joint inversion of IGC ellipticity and dispersion curves are shown in the Fig 10.18. The bedrock depth for the lower misfit model in IGC case is a bit shallower (46 m). This shallower bedrock depth could also be inferred directly from the peak frequency of the H/V which is 2.5 Hz as compared to 2.1 Hz at IAG case.

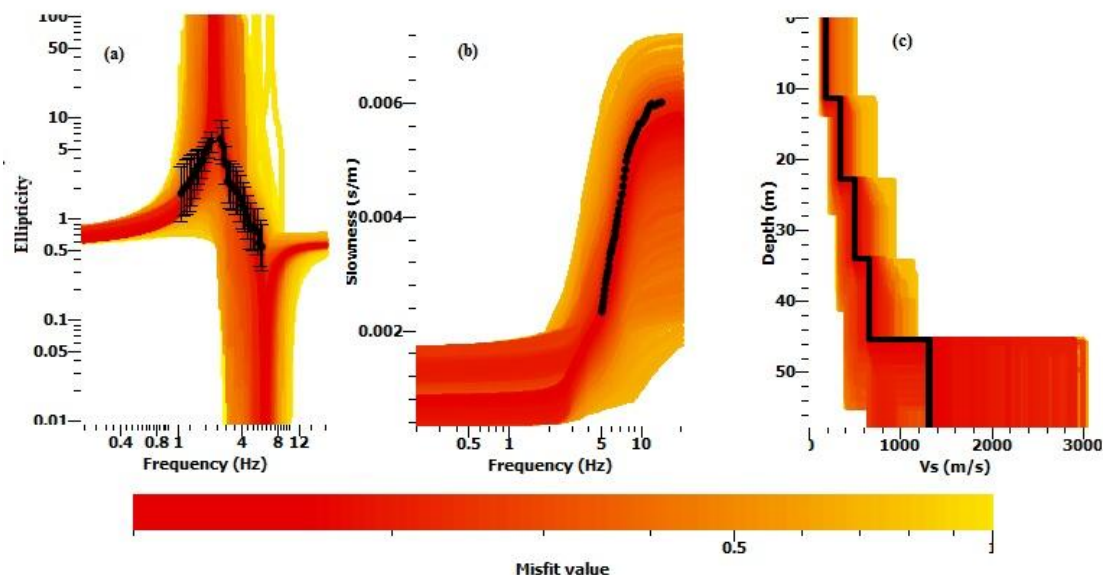


Fig.10.18 Shows the inversion result of the ellipticity and dispersion curves at IGC site; (a) shows the fitting ellipticity curve of IGC site with the dotted line while the black line shows the lower misfit model ellipticity curve; (b) shows the fitting to the experimental curve with the dotted line and lower misfit model dispersion curve with the black line; (c) shows all the generated models, the black line shows the lower misfit model.

The Colônia experimental data recording had some limitation, especially in the dispersion curves, where it was very difficult to retrieve it for a broad range of frequencies. This disappearance of dispersion in Colônia could be linked to the presence of muddy clay with very lower cohesion. However, the dispersion curve was still obtained for a small frequency range (1.1 to 3.8 Hz). We have assumed this dispersion information to be the representative of shear-wave velocity increase within the soil package and have inverted this information directly to V_s and depth values. These V_s and depth estimates were used to obtain velocity increase trend with depth (Fig 10.19). The velocity increase trend along with the velocity (V_s) at one-meter depth was input into Eq 8.12 and the depth of the bedrock at each sensor locations were estimated (Table 10.1). This sediment package thickness and velocity increase trend were used along with ellipticity curve for inversion and shear wave velocity profile retrieval (Fig 10.20).

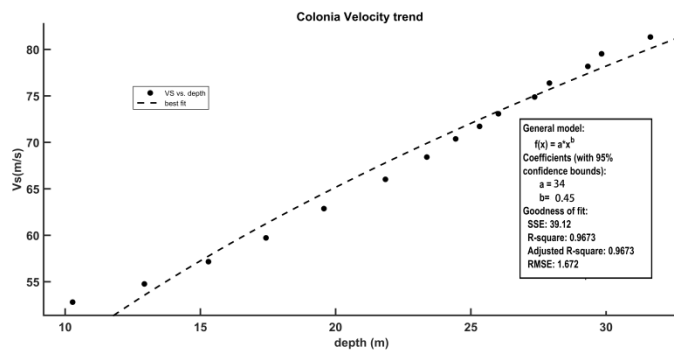


Fig.10.19 Shows the velocity increase trend via best-fit through shear wave velocity and depth which give value of $V_0 = 50 \text{ m/s}$ and $x=0.45$ (b here is x in other relation of chapter 7).

Table 10. 1 Shows the fundamental frequency of each station and their corresponding thickness estimated from (8.12).

Station name	Fundamental resonance frequency f_0 (Hz)	$f_0^{-\frac{1}{1-b}}$	$\left(\frac{V_0^2(1-b)}{2\pi^2}\right)^{\frac{1}{2(1-b)}}$	h (m)
CLN1	0.50	3.52	47.3	166
CLN2	0.52	3.28	47.3	155
CLN3	1.9	0.31	47.3	15
CLN4,5	0.31	8.40	47.3	397
CLN6	0.31	8.40	47.3	397
CLN7	0.38	5.8	47.3	274

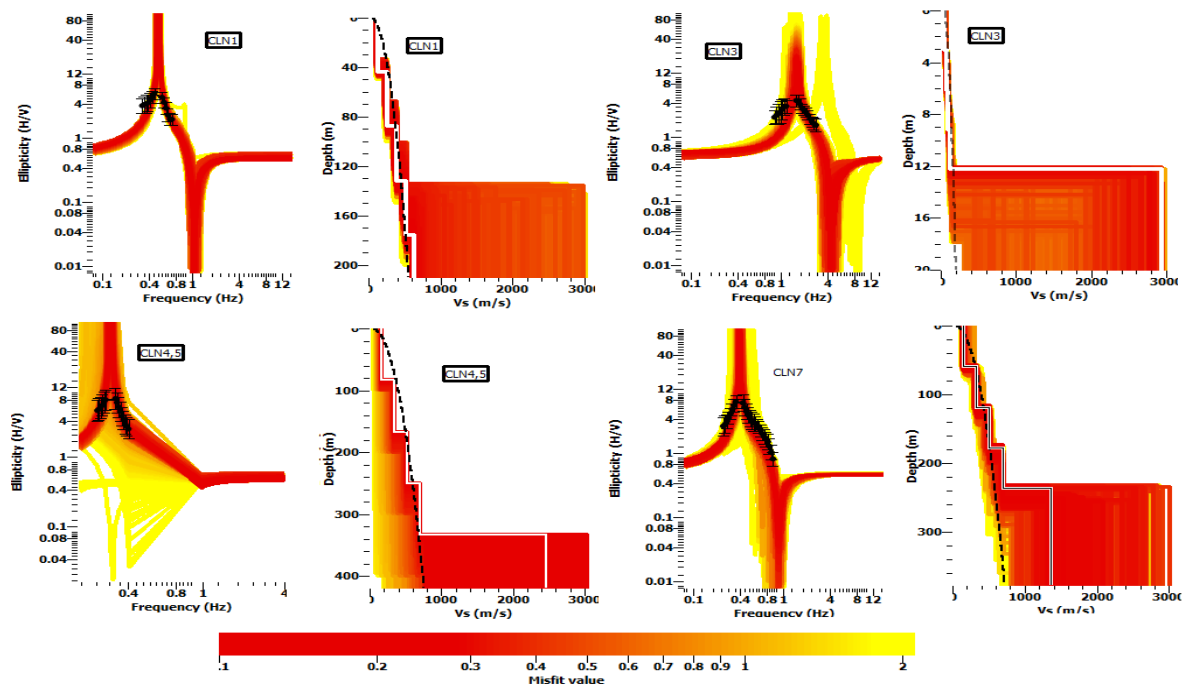


Fig.10.20 Shows the inversion of ellipticity curve supplemented by the sediment thickness and velocity increase trend shown in dashed line.

In Bebedouro area, ellipticity curves were obtained from each of the 6 sensors installed next to MASW profiles. The joint inversions were made for all these six locations. The results are shown in Fig 10.21- 10.23. The velocity increase trend was obtained from all the six dispersion curve direct inversions. This velocity increase trend was used along with ellipticity curve obtained for the 4 sensors where the dispersion curves were not available (Fig 10.24). The velocity increase trend was overlaid on the inversion result which shows a very good velocity increase trend match with lower misfit velocity profile (Fig 10.24).

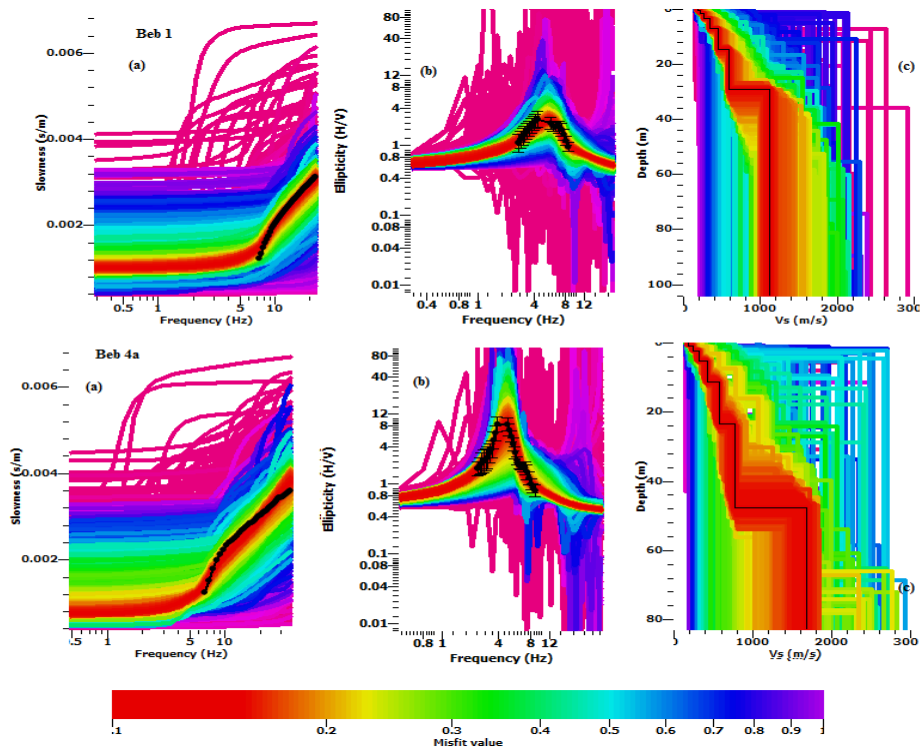


Fig.10.21 Shows the inversion results of the dispersion and ellipticity curves for Bebedouro site, areas Beb1 and Beb 4a.

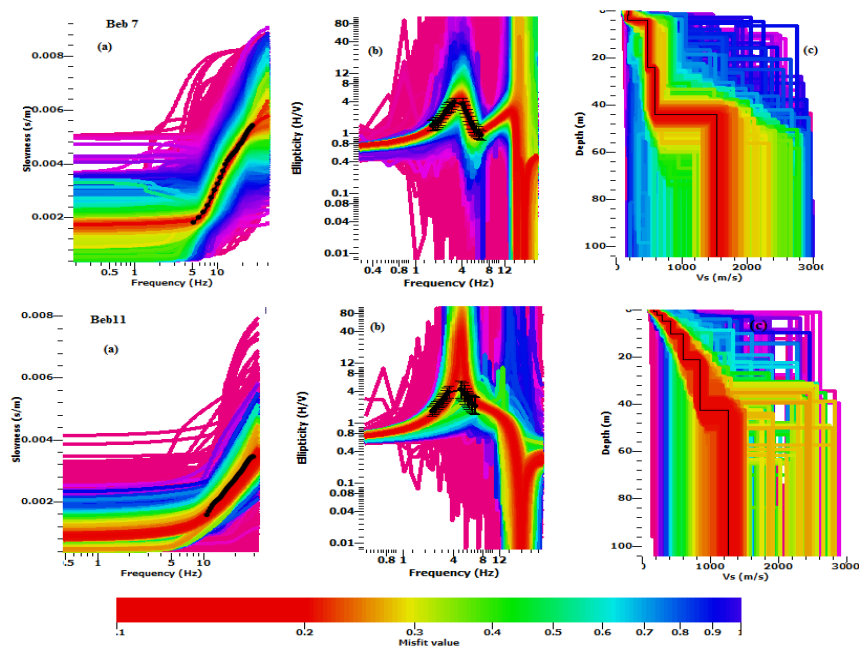


Fig.10.22 Shows the inversion results of the dispersion and ellipticity curves for Bebedouro site, areas Beb7 and Beb 11.

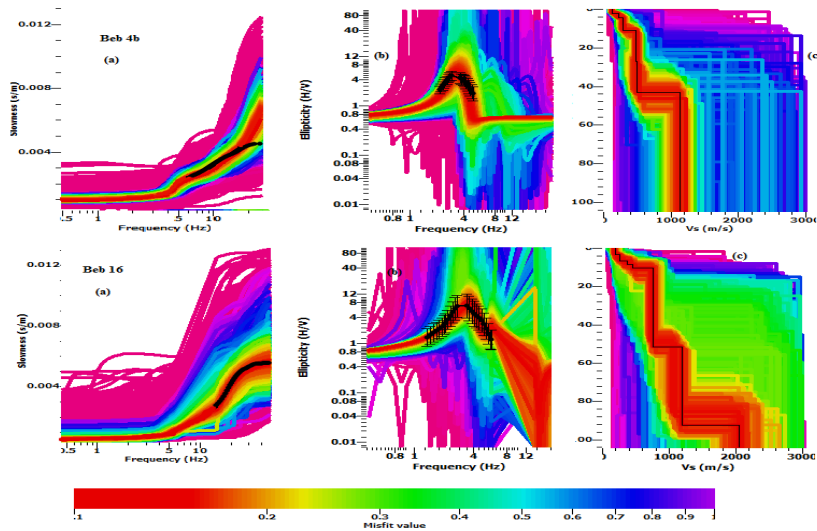


Fig.10.23 Shows the inversion results of the dispersion and ellipticity curves for Bebedouro site, areas Beb 4b and Beb 16.

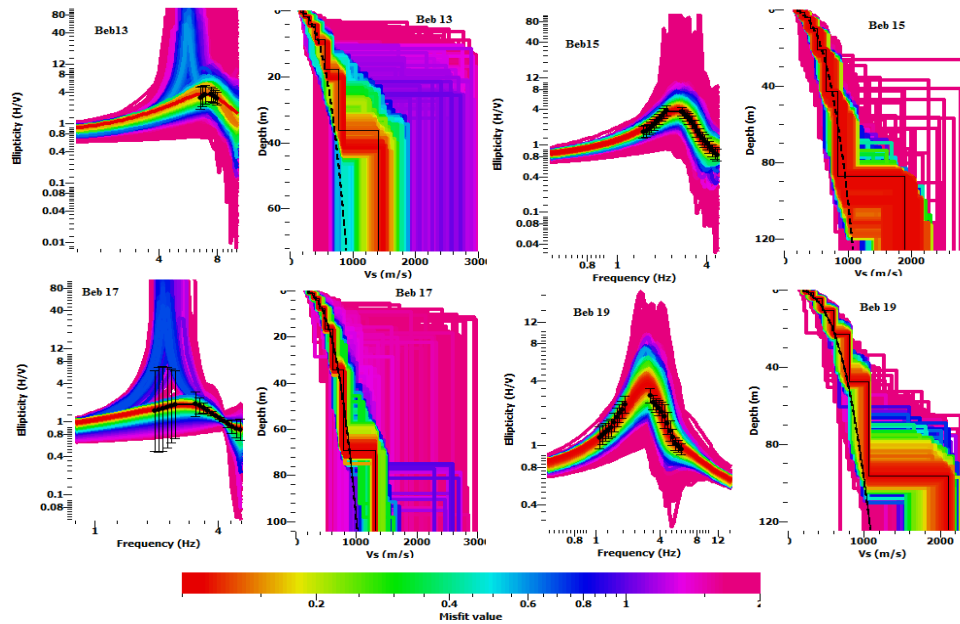


Fig.10.24 Shows the inversion results of ellipticity curves supplemented with velocity trend (shown in dashed line of all models) for Bebedouro site, areas Beb 13, Beb 17, Beb 17 and Beb 19.

10.5 The application of H/V curve for some new aspects

Apart from the site resonance frequency, thickness, average shear wave velocity for soil package estimation and also 1D shear wave velocity profile from its inversion with dispersion curve, the H/V curve can be used for some other application as well. The shear wave velocity obtained from the MASW survey is considered as 1D Vs representative structure of the investigation site. As we showed in this study, the peak frequency of the H/V provides a very good approximation of the bedrock depth if the thickness-frequency relation for a locality is available. The dispersion

curve at IAG site has been used to estimate thickness-frequency relation and to evaluate whether the bedrock topography at the site is isotropic or there is some azimuth variation. We rotated the horizontal components of the seismic noise recording at 10^0 steps from 0^0 at North to 180^0 at South. The rotated horizontal components are divided by the vertical Fourier spectral amplitude. This rotated H/V curves are documented for this azimuth (Fig 10.25). The shift of peak frequencies with azimuth is used to estimate the thickness of soft sediment package for that azimuth from the thickness-frequency relation (Fig 10.26).

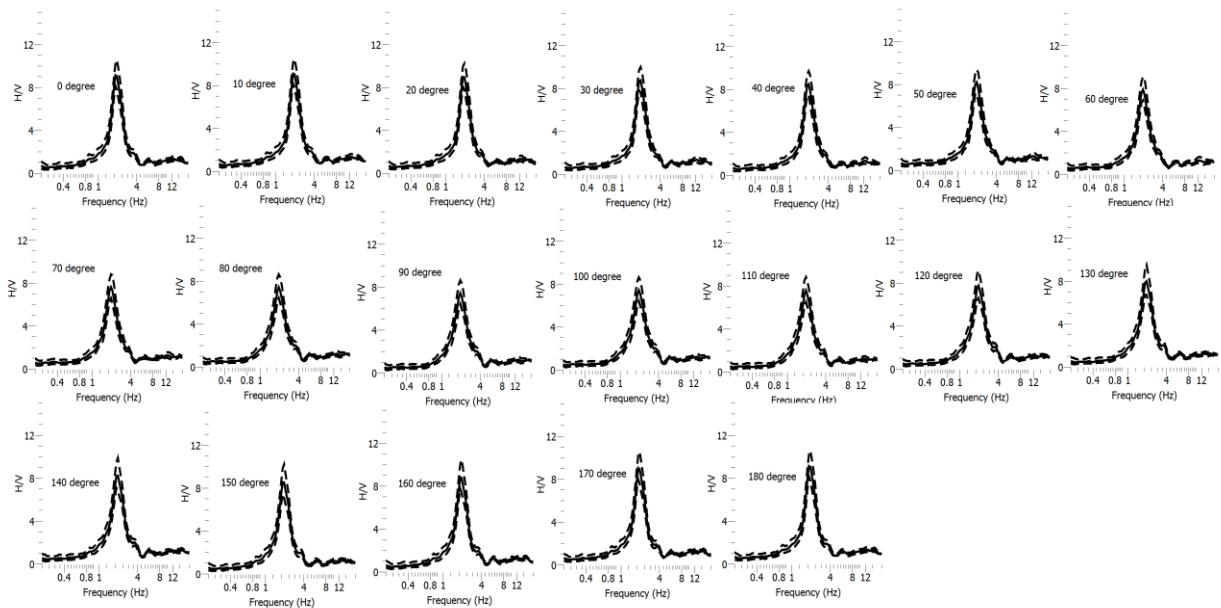


Fig.10.25. Shows the shift of the peak frequency of H/V curves for rotating horizontal components for IAG site.

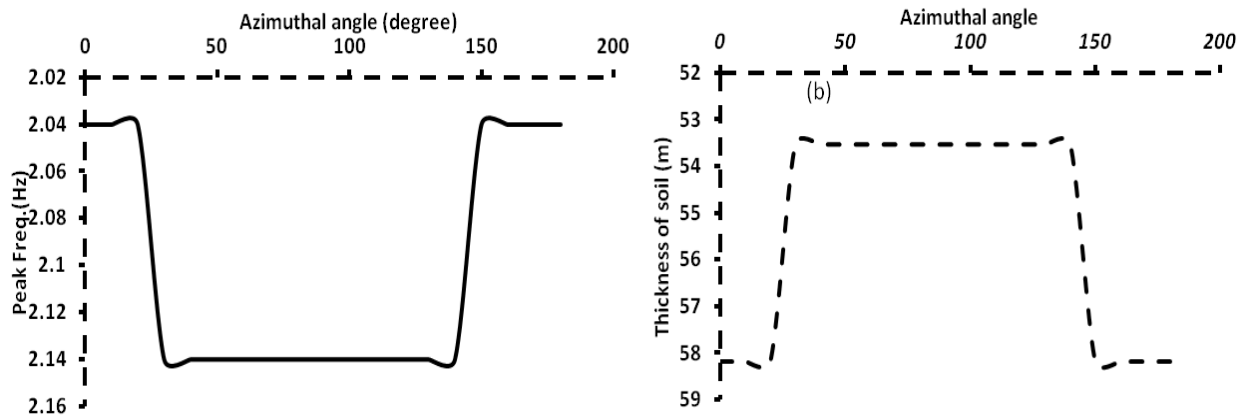


Fig.10.26 Shows the shift of peak frequency with the azimuth (left), while on the right shows the thickness of sediment package estimated from the peak frequency shift with azimuth (for IAG site).

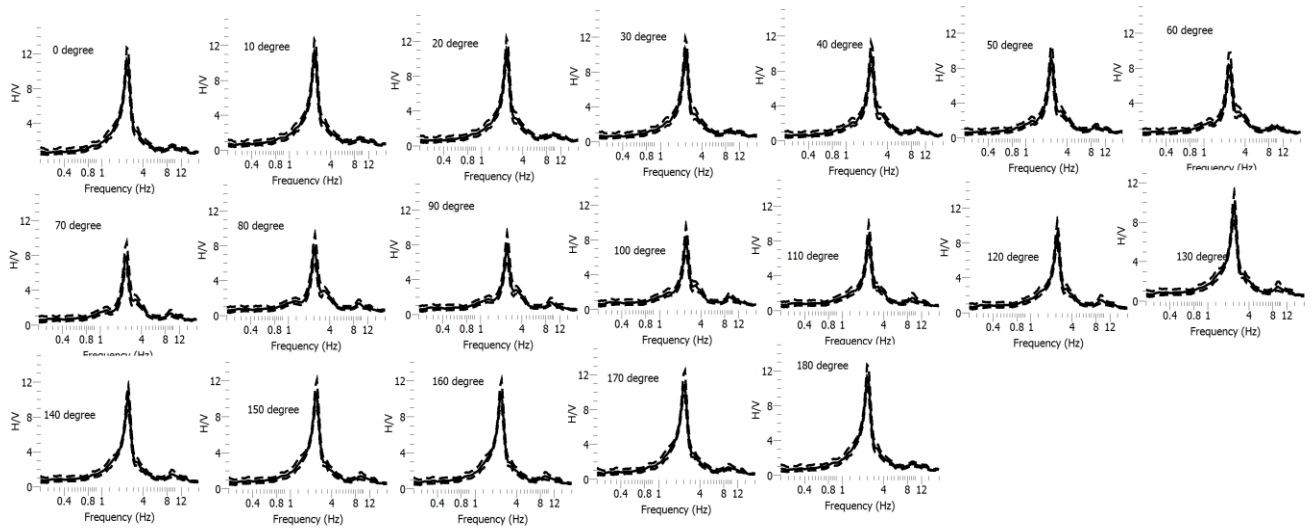


Fig.10.27 Shows the shift of the peak frequency of H/V curves for rotating horizontal component for IGC site.

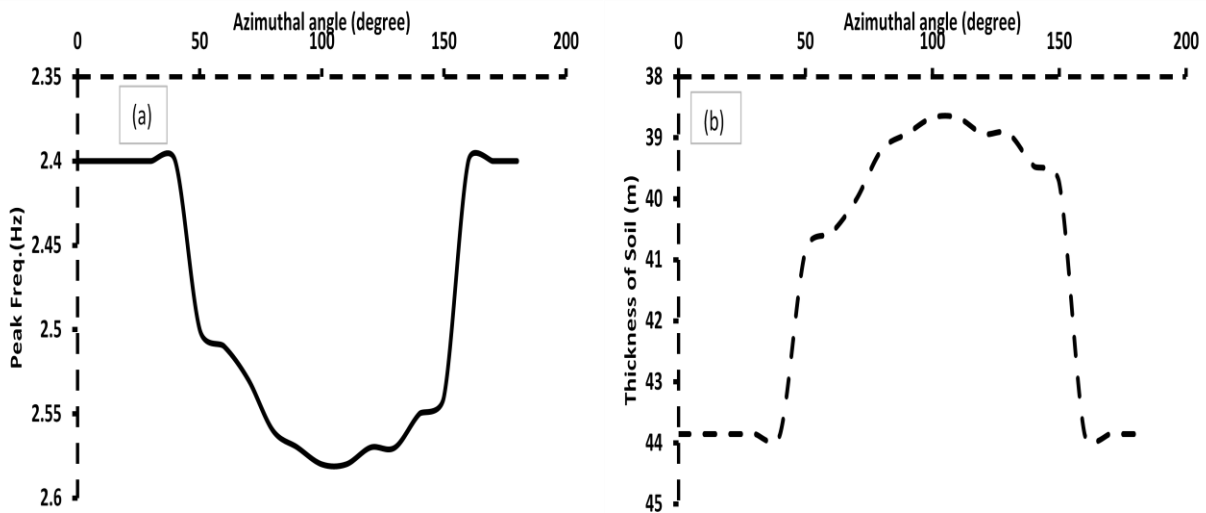


Fig.10.28 Shows the shift of peak frequency with the azimuth (left), while on the right shows the thickness of sediment package estimated from the peak frequency shift with azimuth (for IGC site).

These analysis indicate that there is a upwelling of the bedrock topography within the subsurface along these azimuth range 40° – 130° . We tried to link this to the surface topography of the USP site (Fig 10.29). The increase of elevation and bedrock appearance toward the westward direction might be an indication of the bedrock topography continuation within the subsurface.

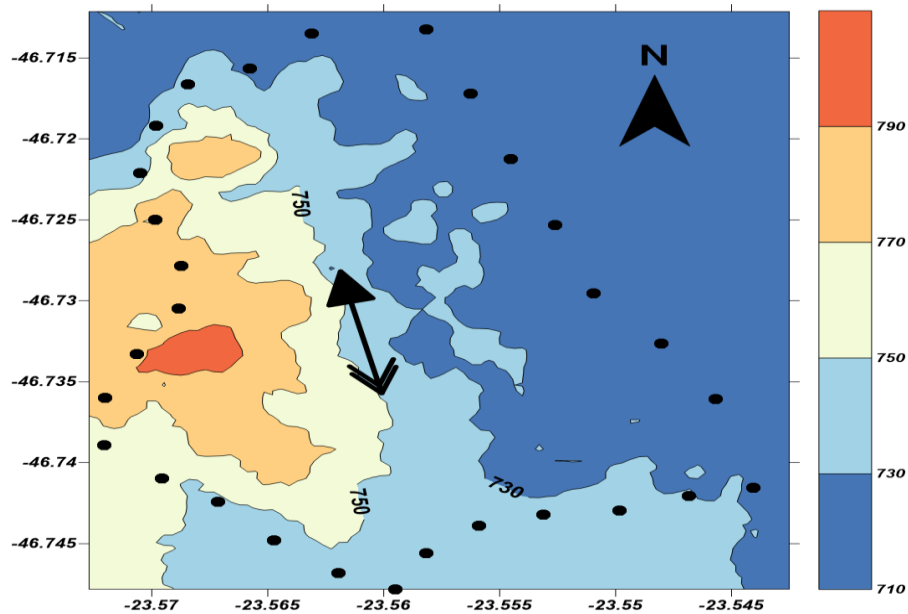


Fig.10.29 Shows the topographical map of USP (the boundary of campus are shown in dotted line); filled arrow shows IAG site while two-headed arrow show IGC site.

The second aspect that could be investigated by the simple H/V curve analysis is the dominance of a higher mode of Rayleigh waves at a site. The dispersion curves of the six MASW profiles at the Bebedouro site are shown in the Fig 10.30. The dispersion images of these six profiles show higher mode appearance in Beb 16, Beb 4a, Beb 11 and Beb 7 (Fig 10.30). The six H/V curves at these sites are shown in Fig (10.9). A link could be established between the shape of the H/V curve and higher mode dominance in the dispersion images by this observation that, when there is one clear peak and trough and there is no such other peak comparable to the prominent peak of the H/V curve, the dispersion image shows the dispersion curve and most probably fundamental mode such as in Beb 4b in Fig (10.9). However, when there is either a flat or two peaks within the H/V curve, the dispersion image is dominated by higher mode Rayleigh waves. The similar observation were extended for the other two sites with two MASW profiles each one at IAG and IGC and two at Colônia site (Fig 10.31). The H/V curves of these sites (Fig 10.32) shows only one clear peak and trough while the dispersion images recorded at these sites shows only one prominent dispersion curve on the dispersion image. Though this observation was verified at 10 sites, we still believe that this behaviour of H/V need more detailed analysis to conclude it in detail. However, the results from these sites dispersion images and the H/V curves shape comparison shows that if the H/V curve shape shows a single peak and trough with no flat or second comparable peak, the site characteristics do not allow the higher mode dominance of Rayleigh waves.

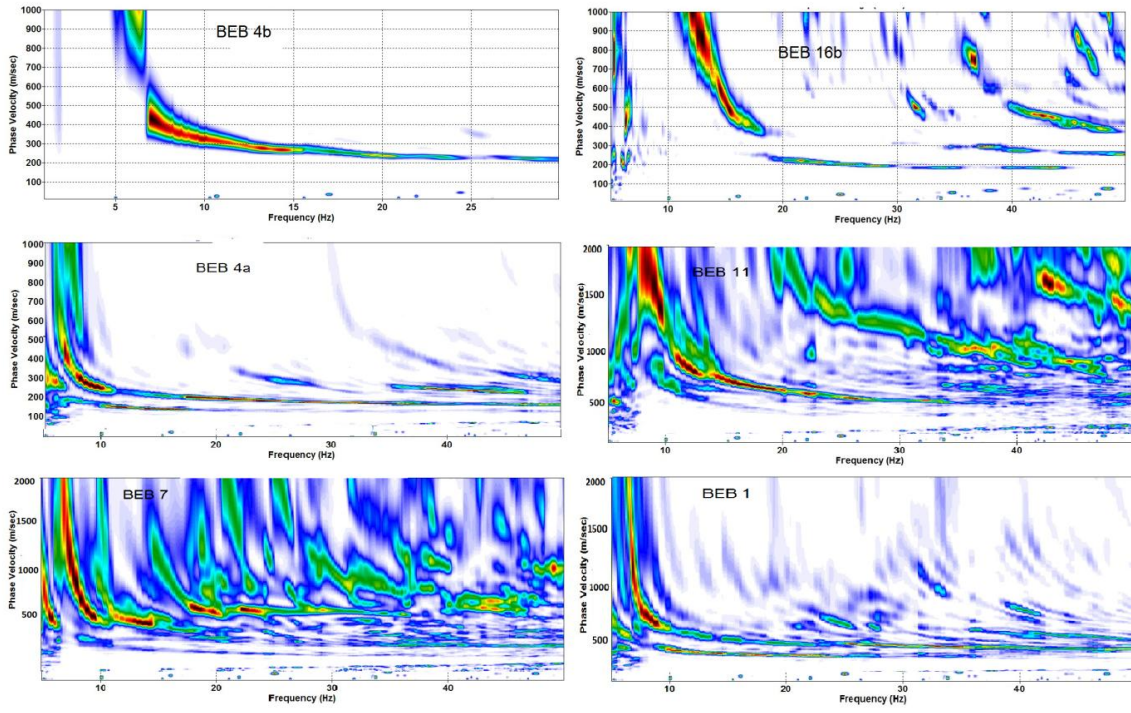


Fig.10.30 Shows the dispersion images of six locations at Bebedouro area.

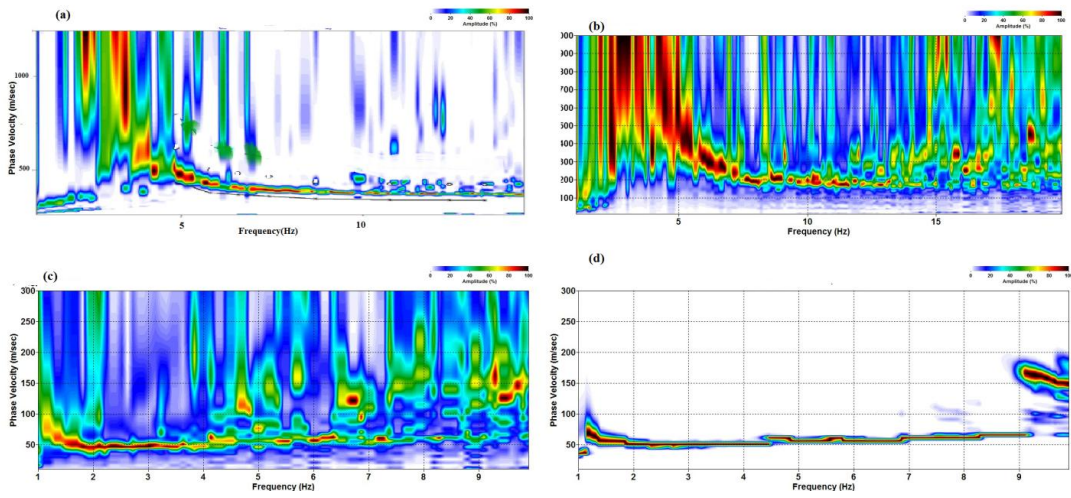


Fig.10.31 Shows the dispersion images (a) IAG site (b) IGC site (c) Colonia 1 and (d) Colonia 2

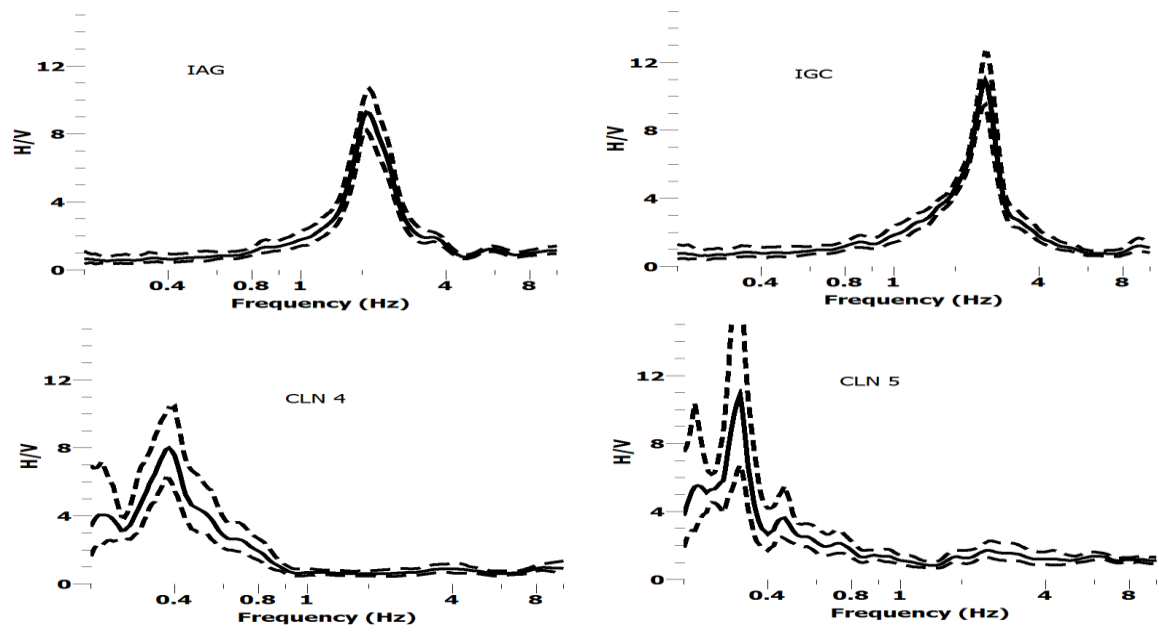


Fig.10.32 Shows the H/V curves for IAG, IGC and Colonia sites of the MASW profiles shown in Fig 10.31.

Chapter 11: Conclusions

The most important part of any study is to draw the conclusion. However, to draw the conclusion about an analyzed phenomenon might always need improvement and further testing. So here, it will be tried to note down only those phenomena which we have found by analyzing our theoretical and experimental data.

The modelling of the H/V curve and its linkage with a physical phenomenon remained always the prime concern for all the study performed using the H/V spectral ratio curves. We have analyzed all the available and presented so far techniques for the modeling of the H/V curve and compared the result of each modelling technique with the experimental H/V curve measured at the borehole site. The technique which gives the best correlation with experimental data is the surface wave modelling of the H/V curve. However, the shape of H/V curve is mainly controlled by the Rayleigh ellipticity fundamental mode. The Nakamura and Diffused field assumption are excluded from the inversion analysis due to the results of some previous studies and also due to the deviation of the experimental curve from the model curve by these techniques for our site.

The main advantage of the H/V curve techniques is that it provides the shear resonance frequency of the site. The technique provides an easy, cheap and fast method to obtain this fundamental resonance frequency. The type of waves around the peak of the H/V curve always remained the topic of discussion. Our analysis showed that the H/V curve peak provides a better representation of the shear wave resonance frequency because of all the elastic seismic waves contributed around the peak. The other technique of surface waves and Rayleigh waves dominance shows better replication of fundamental resonance frequency but only for a higher Poisson ratio. Similarly, the deviations from the shear resonance frequencies were checked for the velocity contrast between the soil and bedrock. The H/V curve for the mostly used modelling techniques shows that peak frequency changes its behavior when the shear wave velocity contrast is 2.6. At the contrast velocity of the 3.6, the peak frequency deviation of the H/V curve from the shear resonance frequency is lesser. Similarly, the thickness of soil variations were checked for the peak frequency deviation from shear wave resonance frequency and it was found that when the shear wave contrast is 3.6 or higher the deviation from the shear wave resonance frequency is greatly reduced. The P wave contrast and density contrast show no effect on the peak frequency deviation of the H/V curve.

The shape of the H/V curve was checked with the three main techniques and it was found that the shape of the H/V curve is mainly dominated by the fundamental mode of the Rayleigh wave ellipticity curve. Also the shape deviation of the H/V curve from the one layer model was analyzed for different number of contrasting interfaces (layers) within the subsurface. It gives a

dubious and unclear result, however, the shape deviation for the H/V curve was found to be sensitive to a maximum number of 6 layers within the subsurface.

The peak frequency of the H/V curve provides a good idea about the thickness of the soft sediment packages if the shear wave velocity information at the near surface is known. The peak of the H/V curve is strongly depended on the ratio between the thickness of the soil to the shear wave velocity (average shear wave travel time). The same average travel time gives an analogous peak. The peak and thickness relation is mostly utilized for a larger area to get quickly the idea of the soft sediment thickness from the H/V curve peak. We have compared the results of experimental H/V curve peak frequency relations for the Bebedouro area with two equations obtained mathematically. These two equations showed very close results to one another. We demonstrated that the dispersion curve can be directly inverted to shear and depth values in which will result in the velocity at one-meter depth and the shear wave velocity increase trend with depth upon regression analysis. These two values can be used to obtain the thickness-frequency relation and also, these values can be used for the ellipticity curve alone inversion to obtain the subsurface 1D shear wave velocity profile.

The part of ellipticity which carries the most important information about the subsurface was also checked. The only part of the ellipticity which it changes its shape with the subsurface velocity contrast is the right limb of the ellipticity curve. The dispersion and ellipticity curves have different sensitivities to the different layer parameters. The inversion of each of the target curves alone (dispersion and ellipticity curve) provides a trade-off between shear wave velocity and soft sediment thickness. To invert the ellipticity curve alone, some supplementary information was required. We analyzed the different parts of the ellipticity curve inversion with velocity increase trend information. We found that right limb of the ellipticity curve provides a better result of the inversion. However, as the peak frequency contains information regarding to the depth of the contrasting interface between soft sediment and seismic bedrock cover, the left limb of the ellipticity curve was also included in the inversion to constrained the sediments thickness. The misfit function was analyzed for both the targets (dispersion and ellipticity curve) to weight properly both of the target during the inversion. We had defined a new strategy to weight both the targets and had shown that it provides a better result for the theoretical case. Unfortunately, it did not provide a better result for the experimental data inversion. It might need some more terms (conditions) to be included which will be analyzed in a future work. To improve the result of joint of inversion, we have adopted trial and error procedure by adjusting the weight of one target at the expense of the other.

Lessons were learned from the theoretical analysis tested on data of the three sites, where the dispersion and seismic ambient noise recording were made. It has been extensively observed that H/V curves always contain the effects of Love and body waves, especially around the peak, but the Love wave effect extends for the whole frequency range. This contamination drives the shape of the H/V curve to deviates from the Rayleigh ellipticity curve. Two techniques were tested to remove the effect of Love waves from the horizontal component of noise wavefield and make

the shape of the H/V curve closer and true representative of the fundamental mode of Rayleigh wave ellipticity. The methods were tested for a theoretical curve by comparing with an experimental curve at the borehole site (USP area). The result of joint inversion of ellipticity and dispersion curves at a borehole site was compared with direct measurements which gave a very good correlation. Similarly, the joint inversion result was made for the other areas too. The velocity increase trend at the Bebedouro and Colônia areas were used along with ellipticity curves to obtain the shear wave velocity profiles.

The H/V curve was checked for the peak frequency variation with azimuth. If the peak frequency is varying, we can infer that soil thickness is also varying with azimuth.

The shape of the H/V curve was checked with dispersion curve for ten different acquisition points, which showed that when the H/V curve has one peak and the dispersion curve shows trough a single dispersion curve, it is most probably the fundamental mode. However, when there were two or a flat peak, the H/V dispersion image at the same site showed higher mode appearance and existence.

The future work includes some more detail insights of the H/V curve variation with azimuth and its linkage with site geological setting. This could be potentially utilized in the area of land sliding to identify the direction of maximum slope. The shape of the H/V curve linkage with Rayleigh waves fundamental and higher modes dominancy needs further testing too. Three component sensors array analysis (SPAC) is under consideration to find out the fraction of Love wave contribution to horizontal component of noise wavefield. If this fraction is somehow find out with time and site variability, this will help to simply reduce the effect of Love by dividing the H/V spectral ratio with that factor and ready to go for inversion with dispersion curve. The misfit function are desired to be modified to give better result for experimental curves joint inversion.

Articles

Journal Publication

1. Ullah, I., Prado, R.L. Soft sediment thickness and shear-wave velocity estimation from the H/V technique up to the bedrock at meteorite impact crater site, Sao Paulo city, Brazil. *Soil Dynamics and Earthquake Engineering*, 2017. <https://doi.org/10.1016/j.soildyn.2017.01.015>.
2. Ullah, I., Prado, R.L. & M.Lisa, (2017) . Single-station ellipticity retrieval and its joint inversion with dispersion curve, for a borehole test site . *Arab J Geosci* 10: 316. <https://doi.org/10.1007/s12517-017-3106-x>.
3. Ullah, I., Prado, R.L. Some new aspect of H/V spectral ratio method, abstract accepted and extended paper submitted to a special issue of *Urban Geophysics Special Issue Near Surface Geophysics journal*.

Review and discussion paper

1. Ullah, I., Prado, R. L. The analysis of H/V curve from different ellipticity retrieval technique for a single 3c-station recording, *Nat. Hazards Earth Syst. Sci. Discuss.*, <https://doi.org/10.5194/nhess-2016-370>, 2016.

Conference papers

1. Ullah, I., Prado, R.L. Estimation of shear wave velocity from MASW and H/V joint inversion in a noisy area of Sao Paulo. Oral presentation at 1st Brazilian Symposium on seismology 6-9 December 2015, Brasilia.
2. Ullah, I., Prado, R.L. A relationship between the resonance frequency of Horizontal-to-Vertical Spectral Ratio (HVSR) curve and depth of bedrock for Bebedouro area, Brazil. Poster presentation at 1st Brazilian Symposium on seismology 6-9, December 2015, Brasilia. Poster presentation.
3. Ullah, I., Prado, R.L. Estimation of Shear Wave Velocity from MASW and H/V Joint Inversion in a Noisy Area of Sao Paulo City, Brazil, AGU Fall Meeting, 14-18 December 2015, in San Francisco, California. Poster presentation.
4. Irfan Ullah, Renato Luiz Prado, Yawar Hayat, Thickness and shear wave velocity measurement of sediment package at meteorite impact crater site of Colonia, Sao Paulo City, Brazil. 2016, VII SimBGf SIMPÓSIO BRASILEIRO DE GEOFÍSICA, At Ouro Preto Minas Gerais, Brazil.
5. Prado, R.L., Ullah, I. Investigation with seismic methods of the sedimentary cover of an astrobleme at outskirts of Sao Paulo City, Brazil. 22nd European Meeting of Environmental and Engineering Geophysics Near Surface Geoscience, 2016
6. Ullah, I., Prado, R.L. Near Surface shear wave velocity increase trend estimation from dispersion curve and its utilization for H/V curve technique at a sediment filled crater site, Sao Paulo Brazil. IASPEI Regional Assembly Latin - American and Caribbean Seismological Commission - LACSC, 2016 - San Jose, Costa Rica. Poster presentation.

References

- A. P. Singh (2015). Seismic hazard evaluation in Anjar city area of western India: Microtremor array measurement, *Soil Dynamics and Earthquake Engineering*, 71, 143-150 .
- A. P. Singh, A. Shukla, M. Ravi Kumar (2017). Characterizing surface geology, liquefaction potential and maximum intensity in the Kachchh seismic zone, Western India through Microtremor analysis, *Bulletin of the Seismological Society of America*, 107(3)
- A.P. Singh, N. Annam, and Santosh Kumar (2014). Assessment of predominant frequencies using ambient vibration in the Kachchh region of western India: Implications for earthquake hazards, *Natural Hazards*, 73 (3), 1291-1309: DOI 10.1007/s11069-014-1135-2
- Akamatsu K., (1961). On microseisms in the frequency range from 1c/s to 200c/s. *Bull. Earthquake Res. Inst., Tokyo Univ.*, 39, 23-75.
- Aki, K. (1957). Space and time spectra of stationary stochastic waves, with special reference to microtremors, *Bull. Earth. Res. Inst.*, 35, 415-456.
- Aki, K. (1964). A note on the use of microseisms in determining the shallow structures of the earth's crust. *Geophysics*, 30, 665-666.
- Aki, K. (1965). A note on the use of microseisms in determining the shallow structures of the Earth's crust. *Geophysics*, 30, 665-666.
- Aki, K., and P.G. Richards (2002). *Quantitative seismology*, Second Edition, University Science Books.
- Albarello D. and Gargani F.; (2010): Providing NEHRP soil classification from the direct interpretation of effective Rayleigh waves dispersion curves. *Bull. Seismol. Soc. Am.*, 100, 3284–3294, doi: 10.1785/0120100052.
- Albarello, C. Cesi, V.Eulilli, F. Guerrini, E. Lunedei, E. Paolucci, D. Pileggi and L.M.Puzzilli (2011). The contribution of the ambient vibration prospecting in seismic microzoning: an example from the area damaged by the April 6, 2009 L'Aquila (Italy) earthquake, *Bollettino di Geofisica Teorica ed Applicata* Vol. 52, n. 3, pp. 513-538;
- Arai and Tokimatsu , (2004) S-Wave Velocity Profiling by Inversion of Microtremor H/V Spectrum, *Bulletin of the Seismological Society of America*, Vol. 94, No. 1, pp. 53–63.
- Arai, H. and K. Tokimatsu , (2000). Effects of Rayleigh and Love waves on microtremor H/V spectra, *Proc. 12th World Conf. On Earthquake Engineering*, 2232/4/A.

- Arai, H., and K. Tokimatsu (1998). Evaluation of local site effects based on microtremor H/V spectra. *Proceeding of the Second International Symposium on the Effects of Surface Geology on Seismic Motion*. Yokohama, Japan. 2 673-680.
- Assumpção, M. (2007) Atividade Sísmica no Distrito de Andes, Bebedouro, 2005-2006, e sua Relação com a Perfuração de Poços Tubulares, (<http://www.iag.usp.br/~marcelo/bebedouro>).
- Asten, M.W. (1978). Geological control of the three-component spectra of rayleigh-wave microseisms. *Bull. Seism. Soc. Am.*, 68, 1623-1636.
- Asten, M.W. and J.D. Henstridge (1984). Array estimators and use of microseisms for reconnaissance of sedimentary basins, *Geophysics*, 49, 1828-1837.
- Aster, R. C., McNamara, D. E. & Bromirski, P. D., (2008). Multidecadal climate-induced variability in microseism. *Seismological Research Letters*, 79, 194-202.
- Backus, G. E., and J. F. Gilbert (1967). Numerical applications of a formalism for geophysical inverse problems, *Geophys. J. R. Astron. Soc.*, 13, 247-276.
- Backus, G. E., and J. F. Gilbert (1968). The resolving power of gross Earth data, *Geophys. J. R. Astron. Soc.*, 16, 169-205.
- Backus, G. E., and J. F. Gilbert (1970). Uniqueness in the inversion of inaccurate gross Earth data, *Philos. Trans. R. Soc. London, Ser. A.*, 266, 123-192.
- Bard P.Y. (1999) [Balkema, Rotterdam] Irikura K, Kudo K, Okada H, Sasatani T, editors. *Microtremor measurements: a tool for site effect estimation? The Effects of Surface Geology on Seismic Motion*, p. 1251-79.
- Besson, B., & Erlingsson, S. (2011). Shear wave velocity in surface sediments. *Jökull*, 61, 51-64.
- Bonnefoy-Claudet et al., (2006), The nature of noise wavefield and its applications for site effects studies, *Earth Science Reviews* doi:10.1016/j.earscirev.2006.07.004.
- Bonnefoy-Claudet, S. (2004). *Nature du bruit de fond sismique : implication pour les études des effets de site*, PhD thesis Université Joseph Fourier (LGIT), Grenoble, France.
- Bonnefoy-Claudet, S., Köhler, A., Cornou, C., Wathelet, M. & Bard, P.-Y., (2008). Effects of love waves on microtremor H/V Ratio, *Bull. Seism. Soc. Am.*, 98(1), 288-300.
- Bormann, P. (Ed.) (2012). *New Manual of Seismological Observatory Practice (NMSOP-2)*, IASPEI, GFZ German Research Centre for Geosciences, Potsdam; <http://nmsop.gfz-potsdam.de>; DOI: 10.2312/GFZ.NMSOP-2.
- Bouchon, M. & Sanchez-Sesma, F.J., (2007). Boundary integral equations and boundary elements methods in elastodynamics, *Adv. Geophys.*, 48, 157-189.

- Brenguier, F., Campillo, M., Hadziioannou, C., Shapiro, N. M., Nadeau, R. M. & Larose, E., (2008b). Postseismic relaxation along the San Andreas fault at Parkfield from continuous seismological observations. *Science*, 321, 1478-1481.
- Brenguier, F., Shapiro, N. M., Campillo, M., Ferrazzini, V., Duputel, Z., Coutant, O. & Nercessian, A., (2008a). Towards forecasting volcanic eruptions using seismic noise. *Nature Geoscience*, 1, 1-5.
- Brooks, L. A., Townend, J., Gerstoft, P., Bannister, S. & Lionel, C., (2009). Fundamental and higher-mode Rayleigh wave characteristics of ambient seismic noise in New Zealand. *Geophysical Research Letters*, 36, L23303.
- Burtin, A., Bollinger, L., Vergne, J., Cattin, R. & Nábělek, J. L., (2008). Spectral analysis of seismic noise induced by rivers: A new tool to monitor spatiotemporal changes in stream hydrodynamics. *Journal of Geophysical Research*, 113, B05301.
- Capon, J., Greenfield, R.J., Kolker, R.J. (1967). Multidimensional Maximum-Likelihood Processing of a Large Aperture Seismic Array. *Proceedings of the IEEE*, vol.55, N.2.
- Chandler A.M., Lam N.T.K. and Tsang H.H.; (2005): Shear wave velocity modelling in crustal rock for seismic hazard analysis. *Soil Dyn. Earthq. Eng.*, 25, 167–185.
- Chavez-Garcia, Miguel Rodriguez, and William R. Stephenson (2005)" An Alternative Approach to the SPAC Analysis of Microtremors Exploiting Stationarity of Noise. *Bulletin of the Seismological Society of America*, Vol. 95, No. 1, pp. 277–293, February 2005, doi: 10.1785/0120030179.
- Chouet, B., De Luca, G., Milana, G., Dawson, P., Martini, M., Scarpa, R. (1998). Shallow velocity of Stromboli volcano, Italy, derived from small-aperture array measurements of Strombolian tremor. *Bull. Seism. Soc. Am.*, 88-3, 653-666.
- Cornou, C. (2002). Traitement d'antenne et imagerie sismique dans l'agglomération grenobloise (Alpes françaises): implications pour les effets de site (In french). *Université Joseph Fourier*, 260..
- Davidovici, V. (1985) Génie parasismique. *École Nationale des Ponts et Chaussées*, Paris,
- Donohue, S., Forristal, D., & Donohue, L. A. (2013). Detection of soil compaction using seismic surface waves. *Soil and Tillage Research*, 128 , 54–60.
- Dorman J., and M. Ewing (1962). Numerical inversion of seismic surface wave dispersion data and crust-mantle structure in the New York-Pennsylvania Area. *J. Geophysical Research*, 67 (13), 5227-5241.
- Douze, E.J., (1964). Rayleigh waves in short-period seismic noise. *Bulletin of the Seismological Society of America* 54 (4), 1197–1212.
- Douze, E.J., (1967). Short-period seismic noise. *Bulletin of the Seismological Society of America* 57 (1), 55–81.
- Dunkin, J.W. (1965). Computation of modal solutions in layered, elastic media at high frequencies. *Bull. Seism. Soc. Am.*, 55, 335-358.

ects, *Journal of Seismology* 7, 449.

Emad K. Mohamed , M.M.F. Shokry, Awad Hassoupa, A.M.A. Helal (2016). Evaluation of local site effect in the western side of the Suez Canal area by applying H/V and MASW techniques, 10.1016/j.jafrearsci.2016.07.004

Endrun, B., Ohrnberger, M. & Savvaidis, A., (2011) On the repeatability and consistency of three-component ambient vibration array measurements. *Bulletin of Earthquake Engineering*, 8, 535-570.

Fäh, D, Stamm, G. & Havenith, H. B., (2008). Analysis of three-component ambient vibration measurements. *Geophys. J. Int.*, 172, 199–213.

Fäh, D., F. Kind and D. Giardini (2003). Inversion of local S-wave velocity structures from average H/V ratios, and their use for the estimation of site-e

Fäh, D., Kind, F., and Giardini, D. (2001). A theoretical investigation of average H/V ratios. *Geophys. J. Int.* 145, 535-549.

Fäh, D., Wathelet, M. , Kristekova, M., Havenith, H. Endrun, B., Stamm, G. , Poggi, V. , Burjanek, J. , Cornou, C. Report (2009) Using Ellipticity Information for Site Characterisation, Software on inversion of H/V ellipticity (version 1) Deliverable number:D4.

Faust LY.; 1951: Seismic velocity as a function of depth and geologic time. *Geophysics*, 16, 192–206.

Gallagher, K., and M. Sambridge (1994). Genetic algorithms: A powerful tool for large-scale non-linear optimization problems. *Comput. Geosci.*, 20(7/8), 1229–1236.

García-Jerez A., Luzón F., Sánchez-Sesma F. J., Lunedei E., Albarello D., Santoyo M. A., Almendros J. (2013) Diffuse elastic wavefield within a simple crustal model. Some consequences for low and high frequencies. *Journal of Geophysical Research* 118(10), 5577–5595. [doi:10.1002/2013JB010107].

García-Jerez A., Piña-Flores J., Sánchez-Sesma F.J., Luzón F., Perton M. (2016). A computer code for forward calculation and inversion of the H/V spectral ratio under the diffuse field assumption, *Computers & Geosciences* 97, 67–78. [doi:10.1016/j.cageo.2016.06.016]

Goldberg, D. E. (1989). *Genetic Algorithms in Search, Optimization, and Machine Learning*. Addison-Wesley, Reading, Mass.

Golub G.H., and C. Reinsch (1970). Singular Value Decomposition and Least Square Solutions. In J. H. Wilkinson and C. Reinsch, editors, *Linear Algebra*, volume II of *Handbook for Automatic Computations*, chapter I/10, pages 134-151. Springer Verlag.

Gouédard, P., Stehly, L., Brenguier, F., Campillo, M., Colin de Verdière, Y., Larose, E., Margerin, L., Roux, P., Sánchez-Sesma, F. J., Shapiro, N. M. & Weaver R. L., (2008a). Cross-correlation of random fields: mathematical approach and applications. *Geophysical Prospecting*, 56, 375-393.

Grevemeyer, I., Herber, R. & Essen, H.-H., (2000). Microseismological evidence for a changing wave climate in the northeast Atlantic Ocean. *Nature*, 408, 349-352.

- Groos, J. C. & Ritter, J. R. R., (2009). Time domain classification and quantification of seismic noise in an urban environment. *Geophysical Journal International*, 179, 1213–1231.
- Gutenberg, (1958) " Two types of microseisms" *JCR V63* 595–597 DOI: 10.1029/JZ063i003p00595.
- Gutenberg, B., (1911). *Die seismische Bodenunruhe*. Doctoral thesis, Universität Göttingen, Germany.
- H.M. Mooney, B.A. Bolt, (1966) Dispersive characteristics of the first three Rayleigh modes for a single surface layer, *Bull. Seism. Soc. Am.* 56 43–67.
- Hanssen, P. & Bussat, S., (2008). Pitfalls in the analysis of low frequency passive seismic data. *First Break*, 26, June, 111-119.
- Harkrider D.G. (1964), Surface waves in multilayered elastic media. Rayleigh and Loves waves from buried sources in a multilayered elastic half-space. *Bull. Seism. Soc. Am.*, 54, 627-679.
- Haskell, N.A. (1953). The dispersion of surface waves on multilayered media. *Bull. Seism. Soc. Am.*, 43, 17-34.
- Heisey, J. S., Stokoe, K. H., and Meyer, A. H.!. (1982) “Moduli of pavement systems from spectral analysis of surface waves.” *Transportation Research Record 852*, Transportation Research Board, Washington, , D.C., 22–31.
- Herrmann, R.B. (1994). *Computer programs in seismology*, vol IV, St Louis University..
- Hobiger, M., P.-Y. Bard, C. Cornou, and N. Le Bihan (2009), Single station determination of Rayleigh wave ellipticity by using the random decrement technique (RayDec), *Geophys. Res. Lett.*, 36, L14303, doi:10.1029/2009GL038863.
- Hobiger,, C. Cornou,¹ M. Wathelet,G. Di Giulio,B. Knapmeyer Endrun, F. Renalier,P.-Y. Bard,¹ A.Savvaidis, S. Hailemikael,N. Le Bihan,M. Ohrnberger and N. Theodoulidis (2013) Ground structure imaging by inversions of Rayleigh wave ellipticity sensitivity analysis and application to European strong-motion sites *Geophys. J. Int.* 192, 207–229.
- Hobiger. (2011) *Polarization of surface waves : characterization, inversion and application to seismic hazard assessment*. Earth Sciences. Universite de Grenoble.
- Holland, J. H. (1975). *Adaptation in Natural and Artificial Systems*. Univ. of Mich. Press, Ann Arbor, Mich.
- Horike, M. (1985). Inversion of phase velocity of long period microtremors to the S-wave-velocity structure down to the basement in urbanized areas. *J. Phys. Earth*, 33, 59-96.
- Ibs-von Seht and Jtirgen Wohlenberg, (1999). Microtremor Measurements Used to Map Thickness of Soft Sediments, , *Bulletin of the Seismological Society of America*, Vol. 89, No. 1, pp. 250-259,
- Kanai, K. and T. Tanaka.1961. On microtremors, VIII, *Bull. Earthq. Res. Inst.* 39: 97-114.
- Kanai, K., T. Tanaka. and K. Osada. (1954). Measurements of microtremors. *Bulletin of Earthquake Research Institute, Tokyo University* 32: 199-210.

- Kirkpatrick, S. C., D. Gelatt, and M. P. Vecchi (1983). Optimization by simulated annealing. *Science*, 220, 671–680.
- Knopoff, L. (1964). A matrix method for elastic wave problems. *Bull. Seism. Soc. Am.*, 54, 431-438.
- Köhler, A., M. Ohrnberger, and F. Scherbaum (2006). The relative fraction of Rayleigh and Love waves in ambient vibration wave fields at different European sites, in 3rd Int. Symposium on the Effects of Surface Geology on Seismic Motion, Grenoble, France, paper 83.
- Köhler, A., Ohrnberger, M., Scherbaum, F., Wathelet, M., and Cornou, C. (2007). Assessing the reliability of the modified three-component spatial autocorrelation technique, *Geophysical Journal International* 168 (2), 779-796, 10.1111/j.1365-246X.2006.03253.x
- Konno K. and Kataoka S.; (2000): An estimating method for the average S-wave velocity of ground from the phase velocity of Rayleigh wave. *Proceedings of JSCE.*, 647, 415–423.
- Konno, K., and T. Ohmachi (1998). Ground-Motion Characteristic Estimated from Spectral Ratio between Horizontal and Vertical Components of Microtremor. *Bull. Seism. Soc. Am.*, 88, 228-241.
- Koper, K. D., Seats, K. & Benz, H., (2010). On the composition of Earth's short-period seismic noise field. *Bulletin of the Seismological Society of America*, 100, 606-617.
- Kramer, S.L. (1996). *Geotechnical Earthquake Engineering*, Prentice Hall, Inc., Upper Saddle River, New Jersey, 653 pp.
- Kurrle, D. & Widmer-Schmidrig, R., (2008). The horizontal hum of the Earth: A global background of spheroidal and toroidal modes. *Geophysical Research Letters*, 35, L06304.
- Lachet, C. and Bard, P-Y. (1994). Numerical and theoretical investigations on the possibilities and limitations of Nakamura's technique. *J. Phys. Earth*, 42, 377-397.
- Lacoss, R. T., Kelly, E. J. & Toksöz, M. N., (1969). Estimation of seismic noise structure using arrays. *Geophysics*, 34, 21-38.
- Lai, C.G. (1998). Simultaneous inversion of Rayleigh phase velocity and attenuation for near-surface site characterization. PhD Diss., Georgia Inst. of Techn., Atlanta (Georgia, USA)
- Lay, T., and T.C. Wallace (1995). *Modern Global Seismology*. Academic Press.
- Ledru M-P, Mourguiart P, Riccomini C. (2009). Related changes in biodiversity, insolation and climate in the Atlantic rainforest since the last interglacial. *Palaeogeogr, Palaeoclimatol, Palaeoecol*:140–52.
- Ledru M-P, Rousseau D-D, Cruz FWJ, Karmann I, Riccomini C, Martin L. (2005) Paleoclimate changes during the last 100 ka from a record in the Brazilian Atlantic rainforest region and interhemispheric comparison. *Quat Res*:444–50.
- Li, T. M. C., Ferguson, J. F., Herrin, E., D. H. B. (1984). High-frequency seismic noise at Lajitas, Texas. *Bull. Seism. Soc. Am.*, 74-5, 2015-2033.

- Longuet-Higgins, M. S., (1950). A theory of the origin of microseism. *Phil. Trans. Roy. Soc. London, Ser. A*, 243, 1-35.
- Lontsi A.M, Francisco José Sánchez-Sesma Juan Camillo Molina-Villegas Matthias Ohrnberger Frank Krüger (2015) Full microtremor H/V(z, f) inversion for shallow subsurface characterization *Geophys J Int* 202 (1): 298-312. DOI: <https://doi.org/10.1093/gji/ggv132>
- Malischewsky P.G Auning, Cinna Lomnitz, Frank Wuttke (2006), " Prograde Rayleigh-wave motion in the valley of Mexico" *Geofísica Internacional* Vol. 45, Num. 3, pp. 149-162.
- Malischewsky P.G., Frank Sherbaum (2004). Love's formula and H/V-ratio (ellipticity) of Rayleigh waves, *Wave Motion* 40, 57-67.
- Malischewsky PG, Scherbaum F, Lomnitz C, Thanh Tuan T, Wuttke F, Shamir G (2008) The domain of existence of prograde Rayleigh-wave particle motion for simple models. *Wave Motion* 45: 556–564.
- Martin A.J. and Diehl J.G.; (2004): Practical experience using a simplified procedure to measure average shear wave velocity to a depth of 30 meters (VS30). In: 13th World Conference on Earthquake Engineering, Vancouver, B.C., Canada, August 1–6, 2004, paper n. 952.
- McMechan, G. A., & Yedlin, M. J. (1981). Analysis of dispersive waves by wave field transformation. *Geophysics*, 46 (6), 869–874.
- Mohammed, A. Y., Berteussen, K. A., Small, J. & Barkat, B., (2007). A low frequency, passive seismic experiment over a carbonate reservoir in Abu Dhabi. *First Break*, 25, November, 71-73.
- Nakamura, Y. (1996), " Real Time Information Systems for Seismic Hazards Mitigation UrEDAS, HERAS and PIC", *Quarterly Report of RTRI*, Vol. 37, No. 3, 112-127.
- Nakamura, Y. (1997), "Seismic Vulnerability Indices For Ground and Structures Using Microtremor", *World Congress on Railway Research in Florence, Italy*, November 1997.
- Nakamura, Y., (1989). A method for dynamic characteristics estimation of subsurface using microtremor on the ground surface. *QR Railway Tech. Res. Inst.* 30, 25-33.
- Nogoshi, M. & Igarashi, T. (1971)'On the amplitude characteristics of microtremor (part 2)', *Journal Seismological Society of Japan* 24,26–40.
- Okada, H., (2003). *The Microtremor Survey Method*. *Geophys. Monograph Series, SEG*, 129 pp.
- Ólafsdóttir, (2016), *Multichannel Analysis of Surface Waves for assessing soil stiffness*, M.Sc. thesis, Faculty of Civil and Environmental Engineering, University of Iceland.
- Ólafsdóttir, E. Á., Bessason, B., & Erlingsson, S. (2014). *Multichannel Analysis of Surface Waves for Estimation of Soils Stiffness Profiles*. In M. Arroyo & A. Gens (Eds.), *Proceedings of the 23rd European Young Geotechnical Engineers Conference*, 2–5 September, Barcelona, Spain (pp. 45–48).
- Park, C. B. (2015). Data acquisition. Retrieved, from <http://www.masw.com/DataAcquisition.html>.

- Park, C. B., & Carnevale, M. (2010). Optimum MASW survey—Revisit after a Decade of Use. In D. O. Fratta, A. J. Puppala, & B. Muhunthan (Eds.), *Geo Florida: Advances in Analysis, Modeling & Design* (pp. 1303–1312). Reston, VA: American Society of Civil Engineers.
- Park, C. B., & Shawver, J. B. (2009). MASW Survey Using Multiple Source Offsets. In D. K. Butler (Ed.), *Proceedings of the Symposium on the Application of Geophysics to Engineering and Environmental Problems 2009* (pp. 15–19). Denver, CO: Environment and Engineering Geophysical Society.
- Park, C. B., Miller, R. D., & Miura, H. (2002). Optimum Field Parameters of an MASW Survey [Expanded Abstract]. In *Proceedings of the 6th SEG-J International Symposium, 22–23 May 2002*, Tokyo, Japan.
- Park, C. B., Miller, R. D., & Xia, J. (1998). Imaging dispersion curves of surface waves on multi-channel record. In *68th Annual International Meeting, SEG, Expanded Abstracts* (Vol. 17, pp. 1377–1380).
- Park, C. B., Miller, R. D., & Xia, J. (1999). Multichannel analysis of surface waves. *Geophysics*, 64 (3), 800–808.
- Park, C. B., Miller, R. D., Xia, J., & Ivanov, J. (2007). Multichannel analysis of surface waves (MASW)—active and passive methods. *The Leading Edge*, 26 (1), 60–64.
- Park, C. B., Miller, R. D., Xia, J., & Ivanov, J. (2007). Multichannel analysis of surface waves (MASW)—active and passive methods. *The Leading Edge*, 26 (1), 60–64.
- Parolai, S., Bormann, P. and Milkereit, C. (2002). New Relationships between VS, Thickness of Sediments, and Resonance Frequency Calculated by the H/V Ratio of Seismic Noise for the Cologne Area (Germany). *Bull. Seism. Soc. Am.* 92, 2521-2527.
- Parolai, S., M. Picozzi, S.M. Richwalski, and C. Milkereit (2005). Joint inversion of phase velocity dispersion and H/V ratio curves from seismic noise recordings using a genetic algorithm, considering higher modes. *Geoph. Res. Lett.*, 32, doi: 10.1029/2004GL021115.
- Pavlick Harutoonian,(2012) Geotechnical Characterisation of Compacted Ground by Passive Ambient Vibration Techniques School of Computing, Engineering and Mathematics University of Western Sydney.
- Perton, M., Sanchez-Sesma, F.J., Rodriguez-Castellanos, A., Campillo, M. & Weaver, R.L., (2009). Two perspectives on equipartition in diffuse elastic fields in three dimensions, *J. acoust. Soc. Am.*,126, 1125–1130.
- Picozzi, M., Parolai, S., Richwalski, S.M. (2005) Joint inversion of H/V ratios and dispersion curves from seismic noise: Estimating the S-wave velocity of bedrock. *Geoph. Res. Lett.*, 32, No.11 doi:
- Picozzi.M (2005) Joint inversion of phase velocity dispersion and H/V ratio curves from seismic noise recordings. A PhD thesis submitted to the Università degli Studi di Siena Facoltà di Scienze Matematiche, Fisiche e Naturali Dipartimento di Scienze della Terra.

- Piña-Flores J., Perton M., García-Jerez A., Carmona E., Luzón F., Molina-Villegas J.C., Sánchez-Sesma F.J. (2017). The inversion of spectral ratio H/V in a layered system using the Diffuse Field Assumption (DFA), *Geophysical Journal International*, In press.
- Porsani , Welitom Borges, Vagner Roberto Elis , Liliana Alcazar Diogo (2004) .Investigações geofísicas de superfície e de poço no sítio controlado de geofísica rasa do IAGUSP, *Revista Brasileira de Geofísica*.
- Porsani JL, Borges W, Elis VR, Diogo LA (2004) Investigações geofísicas de superfície e de poço no sítio controlado de geofísica rasa do IAGUSP. *Geofísica, Revista de Brasileira*.
- Press, W.H., Teukolsky, S.A., Vetterling, W.T., Flannery, B.P. (1992).*Numerical Recipes in Fortran*, second edition, Cambridge University Press.
- Riccomini C, Crósta AP, Prado RL, Ledru M-P, Turcq BJ, Sant’Anna LG, Ferrari JA,Reimold WU. (2011) The Colônia Structure, São Paulo, Brazil. *Meteorit Planet Sci*;46:1630–9.
- Riccomini C, Turcq B, Martin L, Moreira MZ, Lorscheitter M (1991). The Colônia astrobleme, Brasil. *Rev do Inst Geológico* 1991:87–94.
- Riccomini C, Turcq B, Martin L. (1989) The Colônia Astrobleme Excursion field guide.
- Richards, Paul G., (1970a) Body wave reflections from velocity gradient anomalies, *Trans. Am. geophys. U.*, 51, 358.
- Sadowski GR. (1974) *Tectonica da Serra de Cubatão, SP. São Paulo [Ph.D. thesis]. São Paulo, SP, Brazil: Instituto de Geociências;. p. 159*
- Saenger,Erik H. et al , (2009), A passive seismic survey over a gas field: Analysis of low-frequency anomalies *GEOPHYSICS*74(2):O29.
- Saito, T (2010), Love-wave excitation due to the interaction between a propagating ocean wave and the sea-bottom topography , *Geophysical Journal International* 182(3):1515 - 1523.
- Sambridge, M. (1999a). Geophysical inversion with a neighbourhood algorithm: I. Searching a parameter space, *Geophys. J. Int.* 138, 479.
- Sambridge, M. (1999b). Geophysical inversion with a neighbourhood algorithm: II. Appraising the ensemble, *Geophys. J. Int.* 138, 727.
- Sambridge, M., and B.L.N. Kennett (2001). Seismic Event Location: Nonlinear Inversion Using a Neighbourhood Algorithm. *Pure and Applied Geophysics*, 158, 241-257.
- Sambridge, M., Mosegaard, K. (2002). Monte Carlo Methods in Geophysical Inverse Problems. *Reviews of Geophysics*, 40, 3.
- Sánchez-Sesma, F. J., Rodríguez, M., Iturrarán-Viveros, U., Rodríguez-Castellanos, A., Suarez, M., Santoyo, M. A., García-Jerez, A. & Luzón, F., (2010). Site effects assessment using seismic noise, *Proc. 9th International Workshop on Seismic Microzoning and Risk Reduction*, 21st -24th February, , Cuernavaca, Mexico.

- Sánchez-Sesma, F. J., Rodríguez, M., Iturrarán-Viveros, U., Rodríguez-Castellanos, A., Suarez, M., Santoyo, M. A., García-Jerez, A. & Luzón, F., (2010). Site effects assessment using seismic noise, Proc. 9th International Workshop on Seismic Microzoning and Risk Reduction, 21st -24th February, 2010, Cuernavaca, Mexico
- Sanchez-Sesma, F.J. et al. (2011), A theory for microtremor H/V spectral ratio: application for a layered medium, *Geophys. J. Int.*, , 186(1), 221–225.
- Scales, J. A. & Snieder, R., (1998). What is noise? *Geophysics*, 63, 1122-1124.
- Scales, J.A., and R. Snieder (2000). The Anatomy of Inverse Problems. *Geophysics*, 65, 1708-1710.
- Scherbaum F., Hinzen K.G. and Ohrnberger M.; (2003): Determination of shallow shearwave velocity profiles in Cologne, Germany area using ambient vibrations. *Geophys. J. Int.*, 152, 597–612.
- Sen, M. K., and P. L. Stoffa (1992). Rapid sampling of model space using genetic algorithms. *Geophys. J. Int.*, 108, 281–292.
- SESAME European project. (2004). Guidelines for the implementation of the H/V spectral ratio technique on ambient vibrations measurements, processing and interpretation. Deliverable D23.12. http://sesame.geopsy.org/SES_TechnicalDoc.htm
- Sesame report (2003)' Report No. D14.07 ' On the inversion of velocity profile and Version 0 of the inversion software,(http://sesame.geopsy.org/SES_TechnicalDoc.htm).
- Sharma, H.D., Dukes, M.T. and Olsen, D.M. (1990) Field Measurement of Dynamic Moduli and Poisson's Ratios of Refuse and Underlying Soils at a Landfill Site. In: Landva, A. and Knowles, G.D., Eds., *Geotechnics of Waste Landfills: Theory and Practice*, American Society for Testing and Materials, Philadelphia, 57-70.
- Snieder, R. (1998). The role of nonlinearity in inverse problems. *Inverse Problems*, 14, 387-404.
- Snoke, J.A., and M. Sambridge (2002). Constraints on the S wave velocity structure in a continental shield from surface wave data: Comparing linearized least squares inversion and the direct search Neighbourhood Algorithm. *Journal of Geophysical Research*, vol. 107, no. B5, 10.1029/2001JB000498.
- Stankoe, Snježana Markušić, Stjepan Strelec , (2017) , HVSR analysis of seismic site effects and soil-structure resonance in Varaždin city (North Croatia) *Soil Dynamics and Earthquake Engineering* 92 666–677 <http://dx.doi.org/10.1016/j.soildyn.2016.10.022>.
- Stephenson, W.R., (2003). Factors bounding prograde Rayleigh-wave particle motion in a soft-soil layer. *Pacific Conference on Earthquake Engineering*.
- Stoffa, P. L., and M. K. Sen (1991). Nonlinear multiparameter optimization using genetic algorithms: Inversion of plane wave seismograms. *Geophys.*, 56, 1794–1810.
- Tazime, K., (1957). Minimum group velocity, maximum amplitude and quarter wavelength law. Love waves in doubly stratified layers. *J. Phys. Earth*, 5, 43-50.

- Thomson, W.T. (1950). Transmission of elastic waves through a stratified solid medium. *J. Applied Physics*, vol. 21 (1), pp. 89-93.
- Tokimatsu, K. (1997). Geotechnical site characterization using surface waves. *Earthquake Geotechnical Engineering*, Ishihara (ed.), Balkema, Rotterdam, 1333-1368.
- Tokimatsu, K., and S. Tamura (1995). Estimation of local site conditions in Kushiro city based on array observation of microtremors. *Proc., 3rd Int. Conf.on Recent Advances in Geotechnical Earthquake Engineering and Soil Dynamics*, 2, 599-602.
- Tuan TT, Vinh Pham Chi, Malischewsky P, and Abdelkrim. A (2015). Approximate Formula of Peak Frequency of H/V Ratio Curve in Multilayered Model and Its Use in H/V Ratio Technique: *Pure Appl. Geophys*; taken from author personal copy;
- Tuan TT. (2011) . The ellipticity (H/V -ratio) of Rayleigh surface waves, PhD thesis submitted to University of Jena , Germany.
- Voronoi, M.G. (1908). Nouvelles applications des paramètres continus à la théorie des formes quadratiques. *J. reine Angew. Math.*, 134, 198–287.
- Wathelet, M. (2008), An improved neighborhood algorithm: Parameter conditions and dynamic scaling, *Geophys. Res. Lett.*, 35, L09301, doi:10.1029/2008GL033256.
- Wathelet. (2005) Array recordings of ambient vibrations: surface-wave inversion. PhD thesis, Université de Liège, Belgium,.
- William G. Wilson, Kris Vasudevan, (1991) Application of the genetic algorithm to residual statics estimation GCR DOI: 10.1029/91GL02537.
- William Menke (2012) *Geophysical Data Analysis: Discrete Inverse Theory* , Academic Press/Elsevier, 330 p.
- Withers, M. M., Aster, R. C., Young, Ch. J., and Chael, E. P. (1996). High-frequency analysis of seismic background noise as a function of wind speed and shallow depth. *Bull. Seism. Soc. Am.*, 86, 5, 1507-1515.
- Woods, R. D. (1968). Screening of surface waves in soils. *Journal of the Soil Mechanics and Foundations Division*, 94 (4), 951–979.
- Xia, J. (2014). Estimation of near-surface shear-wave velocities and quality factors using multichannel analysis of surface-wave methods. *Journal of Applied Geophysics*, 103 , 140–151.
- Xia, J., Miller, R. D., & Park, C. B. (1999). Estimation of near-surface shear-wave velocity by inversion of Rayleigh waves. *Geophysics*, 64 (3), 691–700.
- Xia, J., Miller, R. D., Park, C. B., & Tian, G. (2003). Inversion of high frequency surface waves with fundamental and higher modes. *Journal of Applied Geophysics*, 52 (1), 45–57.

- Xia, J., Miller, R. D., Park, C. B., Hunter, J. A., Harris, J. B., & Ivanov, J. (2002). Comparing shear-wave velocity profiles inverted from multichannel surface wave with borehole measurements. *Soil Dynamics and Earthquake Engineering*, 22 (3), 181–190.
- Xia, J., Miller, R. D., Xu, Y., Luo, Y., Chen, C., Liu, J., Zeng, C. (2009). High Frequency Rayleigh-Wave Method. *Journal of Earth Science*, 20 (3), 563–579.
- Yamamoto, H. (2000). Estimation of shallow S-wave velocity structures from phase velocities of love- and Rayleigh- waves in microtremors. *Proceedings of the 12th World Conference on Earthquake Engineering*. Auckland, New Zealand.
- Yamanaka, H., and H. Ishida (1996). Application of Generic algorithms to an inversion of surface-wave dispersion data. *Bull. Seism. Soc. Am.*, 86, 436-444.
- Yamanaka, H., Takemura, M., Ishida, H, Niwa, M. (1994). Characteristics of long-period microtremors and their applicability in the exploration of deep sedimentary layers. *Bull. Seism. Soc. Am.*, 84, 1831-1841.
- Zeng, C., Xia, J., Miller, R. D., Tsoflias, G. P., & Wang, Z. (2012). Numerical investigation of MASW applications in presence of surface topography. *Journal of Applied Geophysics*, 84, 52–60.

Index A : The forward computation procedure of the ellipticity curve (courtesy to Piccozi, 2005)

As we discussed in chapter 6, Thomson-Haskell propagator matrix is used for solving the eigenvalue-eigenfunctions problem for horizontal stacks of n-layers, which help us to determine the dispersion and ellipticity curve. Considering a special situation of equation 6.18

$$\mathbf{d} / \mathbf{dzf}(z) = \mathbf{A}(z) \mathbf{f}(z) \quad \text{A1}$$

where \mathbf{f} is a column vector of n components (2 for Love waves, and 4 for Rayleigh waves) that gives the depth dependence of particle displacement and stress, and \mathbf{A} is an nxn matrix that depends both on the elastic properties of the medium and by horizontal slowness p ($p = 1/v = k_n(k\omega)/\omega$ sec/m) and frequency ω . \mathbf{A} for Love waves takes the form (Aki and Richards, 2002)

$$\mathbf{A} = \begin{pmatrix} \mathbf{0} & \mathbf{u}(z)^{-1} \\ k^2 \mathbf{u}(z) - \omega^2 \mathbf{f}(z) & \mathbf{0} \end{pmatrix} \quad \text{A2}$$

and similarly, \mathbf{A} for Rayleigh waves takes the form

$$\mathbf{A} = \begin{pmatrix} \mathbf{0} & k & \mathbf{u}(z)^{-1} & \mathbf{0} \\ -k\lambda(z)[\lambda(z) + 2\mu(z)^{-1}] & \mathbf{0} & \mathbf{0} & [\lambda(z) + 2\mu(z)^{-1}] \\ k\xi(z) - \omega^2 f(z) & \mathbf{0} & \mathbf{0} & -k\lambda(z)[\lambda(z) + 2\mu(z)^{-1}] \\ \mathbf{0} & -\omega^2 \rho(z) & -k & \mathbf{0} \end{pmatrix} \quad \text{A3}$$

When \mathbf{A} is independent of depth, which is valid inside the layer, then A1 solution can be written in the form as

$$\mathbf{f}(z) = \mathbf{G}(z, z_0) \mathbf{f}(z_0) \quad \text{A3}$$

where $\mathbf{G}(z, z_0)$ is the same as equation 6.21

$$f(z) = G(z, z_n)G(z_n, z_{n-1}) \dots G(z_1, z_0)f(z_0) \quad \text{A4}$$

This equation A4 can be used to determine dispersion phase wave velocity curve and ellipticity curve. However, the boundary condition at infinite depth for both the Love and Rayleigh waves (Eq. 6.16 and 6.17) cannot be solved directly. So, Aki and Richards (2002) proposed that it be transformed into a radiation condition that no up-going waves are found in the bottom of the half-space. Moreover, since it is interesting to define the surface wave curves as a function of the desired $V_s(z)$ and $V_p(z)$ structure, for practical reasons, the link between surface waves and the body waves is expressed explicitly. Therefore, as the first step of the procedure, the motion stress vectors (r_1, r_2, r_3, r_4) or (I_1, I_2) (i.e., \mathbf{r} and \mathbf{I} in vector notation, respectively), are related to the displacement amplitudes. Hereafter \mathbf{w} , of up going (\mathbf{P} for P waves and \mathbf{S} for S waves) and down going (\mathbf{P} for P waves and \mathbf{S} for S waves) waves travelling across the medium, through the Eq.A1. For Love waves (Aki and Richards, 2002) the relationship between the amplitudes of \mathbf{S} and \mathbf{S} waves traveling across the homogeneous half space and the motion stress vector at the top of the half space ($z = z_n$) can be expressed in the form

$$\begin{pmatrix} l1 \\ l2 \end{pmatrix} = \begin{pmatrix} e^{-vz} & e^{vz} \\ -Ve^{vz} & Ve^{vz} \end{pmatrix} \begin{pmatrix} S^d \\ S^u \end{pmatrix} \quad A5$$

or in vector notation ($\mathbf{l} = \mathbf{F}\mathbf{w}$), where $\mathbf{v} = (\mathbf{k}^2 + \omega^2/\beta)^{1/2}$, $\beta = (\mu/\rho)^{1/2}$. While the relation for Rayleigh waves has the form of

$$\begin{pmatrix} r1 \\ r2 \\ r3 \\ r4 \end{pmatrix} = F\mathbf{w} \begin{pmatrix} P^d \\ S^d \\ P^u \\ S^u \end{pmatrix} \quad A6$$

In this equation, the matrix \mathbf{F} is factored as

$$\mathbf{F} = \omega^{-1} \begin{pmatrix} \alpha k & \beta k & \alpha k & \beta k \\ \alpha \gamma & \beta k & -\alpha \gamma & -\alpha \beta \\ -2\mu k \alpha \gamma & -\beta \mu (k^2 + \gamma^2) & 2\mu k \alpha \gamma & \beta \mu (k^2 + \gamma^2) \\ -\alpha \mu (k^2 + v^2) & -\alpha \mu k v & \alpha \mu (k^2 + v^2) & -2\beta \mu k v \end{pmatrix} * \begin{pmatrix} e^{-\gamma z} & 0 & 0 & 0 \\ 0 & e^{-vz} & 0 & 0 \\ 0 & 0 & e^{\gamma z} & 0 \\ 0 & 0 & 0 & e^{vz} \end{pmatrix} \quad A7$$

or in vector notation ($\mathbf{r} = \mathbf{F}\mathbf{w}$), where $\gamma = (\mathbf{k}^2 + \omega^2/\alpha)^{1/2}$ and $\alpha = ((\lambda + 2\mu)/\rho)^{1/2}$.

The main advantage of using this formalization appears when the inversion of the relations $\mathbf{l} = \mathbf{F}\mathbf{w}$ and $\mathbf{r} = \mathbf{F}\mathbf{w}$ ($\mathbf{w} = \mathbf{F}^{-1}\mathbf{l}$ and $\mathbf{w} = \mathbf{F}^{-1}\mathbf{r}$) are computed. Namely, the inverse, \mathbf{F}^{-1} , of \mathbf{F} (and also of each of the matrix factors in A7) can be easily evaluated).

In the second step of this procedure, the Thomson-Haskell method were used to apply the relation $\mathbf{w} = \mathbf{F}^{-1}\mathbf{l}$ and $\mathbf{w} = \mathbf{F}^{-1}\mathbf{r}$ to the motion stress vector at the depth $z = z_n$. Thus, the amplitudes of up going and down going waves in the half-space may be expressed in terms of the motion stress vectors at the depth $z = z_0$. Similarly to the eq. (A4) they assume the form

$$\mathbf{w}_{n+1} = \mathbf{F}_{n+1}^{-1} \mathbf{G}(z_n, z_0) \mathbf{l}(z_0) = \mathbf{B} \mathbf{l}(z_0) \quad A8$$

$$\mathbf{w}_{n+1} = \mathbf{F}_{n+1}^{-1} \mathbf{G}(z_n, z_0) \mathbf{r}(z_0) = \mathbf{B} \mathbf{r}(z_0) \quad A9$$

Finally, considering the radiation/boundary conditions assumed for the surface waves existence [$S_{n+1}^u = 0$ and $l_2(z_0) = 0$ for Love; $P_{n+1}^u = S_{n+1}^u = 0$ and $r_3(z_0) = r_4(z_0) = 0$ for Rayleigh waves we have

$$\begin{pmatrix} S_{d+1}^n \\ \mathbf{0} \end{pmatrix} = \begin{pmatrix} \mathbf{B}_{11} & \mathbf{B}_{12} \\ \mathbf{B}_{21} & \mathbf{B}_{22} \end{pmatrix} = \begin{pmatrix} \mathbf{I}_1(z_0) \\ \mathbf{0} \end{pmatrix} \quad \text{A10}$$

$$\begin{pmatrix} P_{n+1}^d \\ S_{n+1}^d \\ \mathbf{0} \\ \mathbf{0} \end{pmatrix} = \begin{pmatrix} \mathbf{B}_{11}\mathbf{B}_{12}\mathbf{B}_{13}\mathbf{B}_{14} \\ \mathbf{B}_{21}\mathbf{B}_{22}\mathbf{B}_{23}\mathbf{B}_{24} \\ \mathbf{B}_{31}\mathbf{B}_{32}\mathbf{B}_{33}\mathbf{B}_{34} \\ \mathbf{B}_{41}\mathbf{B}_{42}\mathbf{B}_{43}\mathbf{B}_{44} \end{pmatrix} = \begin{pmatrix} r1(z_0) \\ r2(z_0) \\ \mathbf{0} \\ \mathbf{0} \end{pmatrix} \quad \text{A11}$$

Clearly, nontrivial solution \mathbf{l} and \mathbf{r} from the above equations can be obtained when B_{21} in equation A10 and the sub-determinant $(B_{31}B_{42} - B_{41}B_{32})$ in the A11 vanishes.

In conclusion, the equations

$$B_{21} = 0 \quad \text{A12}$$

$$\begin{vmatrix} B_{31} & B_{32} \\ B_{41} & B_{42} \end{vmatrix} = 0 \quad \text{A13}$$

are the eigenvalues of the A10 and A11, respectively.

As a result, for evaluating the dispersion curves it is sufficient to find, for each frequency, $\omega/2\pi$, and in the correct order to clearly identify all modes, all the n roots $k(n)$ of the equations (10 and 11). Moreover, it is clear that since the terms of the matrix \mathbf{B} are related with the elastic parameters of the layers forming the medium, the dispersion curves reflect the mechanical structure of the medium itself. However, Dunkin (1965) stated that the terms B_{ij} of the sub-determinant (13) can become very large during the process of computation. Therefore, the result of their subtraction could not have significant digits enough or even becomes zero. As a result, this computational operation is not easy as it seems at a first glance, and if computers with high precision are not available, the phase velocity estimated could be severely biased. Some ways of solving that problem are either using the Laplace's development by minors (Dunkin, 1965 and Knopoff, 1964), or the layer-reduction method (Schwab and Knopoff, 1970), or the Orthonormalization method (Wang, 1999).

From a practical point of view, for each frequency, $\omega/2\pi$, the roots search is performed along the slowness axis, k , by an iterative procedure of trial k_i . Hence, the parameters k_{\min} and k_{\max} , associated to the $V_{R\max}$ and $V_{R\min}$ or the $V_{L\max}$ and $V_{L\min}$, are identified first. Then, the others roots in the range $(k_{\min} - k_{\max})$ are generally obtained by means of some robust non-linear and non-analytical function, as the bracketing techniques combined with bisection proposed by Hisada (1995). We used a code which is based on the Dunkin's procedure of solving that problem. The reference for further documentation can be found on report number D14.07 of SESAME project (SESAME).

After the terms of the matrix \mathbf{B} (A11) are known, it is possible also to evaluate the ellipticity curves $(r_1(z_0)/r_2(z_0))$ for different modes of the Rayleigh waves. In fact, from the equation (A11) we can see that

$$\mathbf{B}_{31} \mathbf{r}_1(z_0) = \mathbf{B}_{32} \mathbf{r}_2(z_0) \quad \text{A14}$$

and consequently, the ellipticity correspond to the relationship

$$\frac{r_1(z_0)}{r_2(z_1)} = -\frac{B_{32}}{B_{31}} \quad \text{A15}$$

This ratio is an imaginary number and, when it is positive, the particle motion is prograde. Conversely, when it is negative, the motion is retrograde. Since, for each frequency, the terms \mathbf{B}_{ij} reflect the elastic properties of the medium at a different depth and also by the ellipticity curve, the mechanical structure of the medium can be found.